

IDENTIFICATION OF TRANSFER FUNCTIONS FOR
WIND-INDUCED PRESSURES ON PRISMATIC BUILDINGS

by

GEORGE THOMAS, B.E., M.E.

A DISSERTATION

IN

CIVIL ENGINEERING

Submitted to the Graduate Faculty
of Texas Tech University in
Partial Fulfillment of
the Requirements for
the Degree of

DOCTOR OF PHILOSOPHY

Approved



—

—

—

—

—

—

11

August, 1996

801

73

1996

No. 63

C. 2

AKJ 3987

Copyright 1996, George Thomas

ACKNOWLEDGMENTS

I am very thankful to Dr. Partha P. Sarkar for accepting me as his first doctoral student and introducing me to the concept of system identification. The intellectual acumen, basic direction, tremendous patience, and enthusiasm shown by him in guiding this work is highly appreciated. I am thankful to Dr. Kishor C. Mehta for providing me the opportunity and encouragement for pursuing basic research in Wind Engineering as part of the Co-operative Program in Wind Engineering. I am also thankful to Dr. H. Scott Norville, Dr. Surya D. Liman and Dr. Richard E. Peterson for their constructive comments during the review of this work.

Financial support from the Office of the Provost, Texas Tech University and the U.S. National Science Foundation, which made this research possible, is gratefully acknowledged. I would like to express my appreciation to all present and past members of the Wind Engineering Research Team, especially Dr. Douglas Smith, Byron Yeatts, Dr. Gary Tarver, Dr. John Ginger, Dr. Jianming Yin and Chris Unanwa, for their invaluable help in different ways during the course of this work. I am thankful to Dr. P.K. Dasgupta for lending me the sonic anemometer. I am also thankful to Dr. B. Bienkiewicz and Dr. L. Cochran of Colorado State University for making available the wind-tunnel data used in this work. Special thanks are due to Dr. Ahsan Kareem of the University of Notre Dame for encouraging me with valuable suggestions and literature.

I would like to recognize my parents Leela Thomas and Late Col. K.V. Thomas, my in-laws Mr. and Mrs. M.V. Varughese, and my family members Bina, Xavier, Neena, Mini, Mona and Simon for all their love and support. I express my deepest appreciation to my spouse, Mini, whose unconditional love and encouragement made possible the completion of this thesis. I express my special appreciation to Amit Armstrong for extending much needed help and moral support during very crucial stages of this work. I reserve my highest respects for Professor A.R. Santhakumar of Anna University, India who has played a unique role in my life, both as a teacher and a friend. This thesis is dedicated to Professor Santhakumar.

CONTENTS

ACKNOWLEDGMENTS	ii
ABSTRACT	viii
LIST OF TABLES	ix
LIST OF FIGURES	xi
CHAPTER	
1. INTRODUCTION	1
1.1 Motivation	1
1.2 Objectives	4
1.3 Scope of Research	5
2. BACKGROUND LITERATURE	6
2.1 Wind Characteristics	6
2.2 Wind Loads on Low-Rise buildings	9
2.2.1 Bluff Body Aerodynamics	10
2.2.2 Factors Affecting Wind Loads on Low-Rise Buildings: Experimental Results	14
2.3 Assessment of Wind Loads	16
2.3.1 Concept of Aerodynamic Admittance	18
2.3.2 Modified Quasi-Steady Theory	19
2.3.3 Nonlinear Relation Between Velocity and Pressure	21
2.3.4 Concept of Multiple Transfer Functions	23

2.4	System Identification in the Frequency Domain	25
2.4.1	Classification of Systems	26
2.4.2	Bispectrum Concept	28
2.4.3	Modeling of Nonlinear Non-Gaussian Processes	31
3.	FIELD FACILITY AND DATA	42
3.1	Introduction	42
3.2	Field Facility: The WERFL	42
3.2.1	The Test Building	44
3.2.2	Some Definitions	44
3.2.3	Pressure Measuring System and Instrumentation	44
3.2.4	Meteorological Tower and Instrumentation	49
3.2.5	Terrain and Site Characteristics	54
3.2.6	Wind Climate	54
3.2.7	Data Acquisition System	55
3.3	Description of Field Data Used	57
3.3.1	Data Sampling Rate	57
3.3.2	Data for Area-Averaged Wind Loads on a Roof Purlin	57
3.4	Wind Tunnel Data from CSU	57
3.5	Comparison of Velocity Spectra from Different Anemometers	58
3.5.1	General	58
3.5.2	Comparison of Longitudinal Velocity Spectra	62
3.5.3	Comparison of Lateral Velocity Spectra	65

3.5.4 Summary	67
4. PROPOSED MODEL AND METHODOLOGY	68
4.1 Introduction	68
4.2 The Proposed Model	68
4.2.1 Notation	69
4.2.2 Assumptions in the Model	70
4.2.3 Mathematical Representation of the Model	74
4.2.4 Identification of Optimal Transfer Functions	75
4.2.5 Spectral Decomposition and Output Prediction	77
4.2.6 Goodness-of-Fit of the Model	77
4.2.7 Effect of Frequency response of the Anemometer used for Measuring the Input Wind Velocity	78
4.2.8 Implementation of the Model	79
4.3 Physical Interpretation of the Model	82
5. TRANSFER FUNCTIONS FOR WIND NORMAL TO THE BUILDING	85
5.1 Introduction	85
5.2 Identification of Transfer Functions and Spectral Decomposition of of Wind Pressures	86
5.2.1 Windward Wall	86
5.2.2 Separation Region on the Roof	101
5.2.3 Reattachment Region on the Roof	110
5.2.4 Leeward Wall or Wake Region	116
5.2.5 Side Walls	123

5.2.6	Area-averaged Pressures on Roof Purlin	129
5.2.7	Frequency Distribution of the Variance of Measured Pressures	138
5.2.8	Phase of Transfer Functions and Pressure Spectra	139
5.3	Simulation of Pressure-coefficient Spectra	144
5.4	Summary	151
6.	TRANSFER FUNCTIONS AT THE ROOF CORNER FOR QUARTERING WIND	153
6.1	Introduction	153
6.2	Identification of Transfer Functions and Spectral Decomposition for the Roof Corner	154
6.2.1	Individual Taps	155
6.2.2	Area-averaged Cases for the Roof Corner	181
6.2.3	Confidence Interval for Mean Coherence	187
6.2.4	Frequency Distribution of the Variance of Measured Pressures at the Roof Corner	188
6.2.5	Phase of Transfer Functions and Pressure Spectra	190
6.3	Simulation of Pressure-coefficient Spectra	193
6.4	Applicability of the Model	200
6.5	Summary	201
7.	CONCLUDING REMARKS	199
7.1	The Proposed Model	203
7.2	Conclusions	204
7.3	Scope for Further Work	206

REFERENCES	208
APPENDIX: SUMMARY STATISTICS OF DATA USED	218

ABSTRACT

Buildings in the atmospheric boundary layer experience highly fluctuating wind pressures which result from turbulence in the undisturbed upstream flow and building-generated turbulence through the processes of buffeting and interaction. An aerodynamic admittance is usually introduced to relate the spectral characteristics of the pressures to the spectral properties of the impinging turbulence. A modified quasi-steady approach, currently in use for predicting fluctuating wind pressures on low buildings, accounts for the building-generated turbulence by means of a single admittance function $\chi^2(f)$. This approach implies that the longitudinal and lateral wind velocities are modified in the same manner by the presence of the building in the flow, which may not be true physically.

A general linear-quadratic model, using the concept of multiple transfer functions, is proposed to relate the spectra of the fluctuating longitudinal (u) and lateral (v) components of the upstream wind velocity to that of pressures on building surfaces. Four transfer functions are defined: one each associated with the linear and second-order terms of the u and v velocity components. The proposed formulation enables a weighted decomposition of the measured output pressure spectrum into components representing the contributions from the linear and quadratic terms of the input velocity components and the remaining uncorrelated residual and/or noise effects. This approach provides physical insight into the mechanism which produces pressures on building surfaces. The four transfer functions are optimally identified from cross-spectra/cross-bispectra of the velocity and surface pressure fluctuations by minimizing the residual/noise spectrum.

The proposed model is applied to gain an understanding of the form and behavior of the transfer functions associated with the incident wind in producing pressures on surfaces of buildings. The study is primarily based on full-scale wind velocity and pressure data collected on a 13.7 m x 9.1 m x 4 m flat-roof metal test building, located on a flat open terrain, at the Texas Tech Wind Engineering Research Field Laboratory. Results are presented for typical flow regions on the building: windward wall, roof separation and reattachment zones, leeward wall, side wall, roof corner and area-averaged cases.

LIST OF TABLES

3.1	Coordinates of pressure taps and transducer locations	47
3.2	Operating specifications of sonic anemometer	53
3.3	Comparison of sonic anemometer velocity data for two sampling rates	59
3.4	Frequency distribution of field measured wind velocity	60
3.5	Summary of data used in spectral comparison at roof height ($z = 4$ m)	62
4.1	Typical field turbulence intensities at 4 m level at WERFL	74
4.2	Comparison of pressure variance for two sampling rates	81
5.1	Summary statistics of velocity data of concatenated records	86
5.2	Contribution from different components of the model to pressures on the windward wall	97
5.3	Contribution from different components of the model to pressures in the roof separation zone	103
5.4	Contribution from different components of the model to pressures in the roof reattachment zone	116
5.5	Contribution from different components of the model to pressures on the leeward wall	117
5.6	Contribution from different components of the model to pressures on the side walls	129
5.7	Tributary area associated with each pressure tap on roof purlin	130
5.8	Contribution from different components of the model to area-averaged pressures on the purlin	131
5.9	Average frequency distribution of measured pressures ($\theta \approx 270^\circ$)	138
6.1	Summary statistics of velocity data of concatenated records	154

6.2 Contribution from different components of the model to pressures for the roof corner taps	162
6.3 Contribution from different components of the model to area-averaged pressures at the roof corner	187
6.4 Average frequency distribution of measured pressures for the roof corner	189
A.1 Summary statistics of velocity data	218
A.2 Summary statistics of pressure-coefficient data	220

LIST OF FIGURES

2.1	Spectrum of horizontal wind speed for Brookhaven at 100 m above ground	6
2.2	Typical turbulence spectrum	9
2.3	Schematic sketch of different regions of turbulent flow around bluff obstacles	11
2.4	Flow around cuboidal buildings	13
2.5	Flow structure of delta-wing vortices	14
2.6	Wind flow patterns over roofs	16
2.7	Ideal assessment of wind loading	17
2.8	Typical admittance functions obtained from WERFL data	22
2.9	Zero memory square-law system	27
2.10	Finite-memory square-law system	28
2.11	General bilinear model in time and frequency domain	34
2.12	Parallel linear and square-law systems with squarer followed by linear system	39
3.1	The WERFL: test building and meteorological tower	43
3.2	Wind azimuth, building position and angle of attack	43
3.3	Location of pressure taps on the Texas Tech test building	46
3.4	Response characteristics of 3-cup/microvane anemometer	50
3.5	Comparison of longitudinal velocity spectra from different anemometers	64
3.6	Comparison of lateral velocity spectra from different anemometers	66
4.1	Schematic diagram of proposed model	69
4.2	Typical probability density functions for field wind velocity at 4 m	71

4.3	Typical cross-correlation function between u and v velocity components	72
5.1	Transfer functions for windward wall tap 42206	89
5.2	Output prediction for windward wall tap 42206 (CS070)	93
5.3	Decomposition of pressure-coefficient spectrum for windward wall tap 42206 (CS070)	94
5.4	Input and output spectra for tap 42206 (CS070)	95
5.5	Total coherence function for tap 42206 (CS070)	95
5.6	Bispectrum of wind pressures for windward wall tap 42206 (M15N545)	98
5.7	Transfer functions for windward wall tap 42212 (CS070)	99
5.8	Transfer functions for tap 50523 under the separation bubble (C544)	104
5.9	Output prediction for tap 50523 under the separation bubble (C544)	106
5.10	Decomposition of pressure-coefficient spectrum for tap 50523 (C544)	107
5.11	Input and output spectra for tap 50523 (C544)	108
5.12	Total coherence function for tap 50523 (C544)	108
5.13	Bispectrum of wind pressure for taps 50523 under the separation bubble (M15N545)	109
5.14	Transfer functions for tap 52323 in the reattachment zone (C544)	111
5.15	Output prediction for tap 52323 in the reattachment zone (C544)	113
5.16	Decomposition of pressure-coefficient spectrum for tap 52323 (C544)	114
5.17	Bispectrum of wind pressure for tap 52323 in the roof reattachment zone (M15N545)	115
5.18	Transfer functions for tap 22306 on the leeward wall (C544)	118
5.19	Output prediction for tap 22306 on the leeward wall (C544)	120

5.20	Decomposition of pressure-coefficient spectrum for tap 22306 on the leeward wall (C544)	121
5.21	Bispectrum of wind pressure for tap 22306 on the leeward wall (M15N545)	122
5.22	Transfer functions for tap 31407 on the side wall (C544)	124
5.23	Output prediction for tap 31407 on the side wall (C544)	126
5.24	Decomposition of pressure-coefficient spectrum for tap 31407 (C544)	127
5.25	Bispectrum of wind pressure for tap 31407 on the side wall (M15N545)	128
5.26	Location of purlin, instrumented pressure taps and tributary areas	130
5.27	Transfer functions for roof purlin with $\theta \approx 270^\circ$ (C544)	132
5.28	Output prediction for roof purlin with $\theta \approx 270^\circ$ (C544)	134
5.29	Transfer functions for roof purlin with $\theta \approx 0^\circ$ (C325)	135
5.30	Output prediction for roof purlin with $\theta \approx 0^\circ$ (C325)	137
5.31	Phase of transfer functions for tap 42206 on the windward wall (C544)	140
5.32	Phase of transfer functions for tap 50523 under the separation bubble (C544)	141
5.33	Phase of pressure spectra (M15N544)	142
5.34	Pdf of phase of pressure spectra	143
5.35	Input velocity and output pressure-coefficient spectra for tap 42212 on the windward wall	145
5.36	Comparison of transfer functions for tap 42212 on the windward wall	146
5.37	Input velocity spectra and output pressure-coefficient spectrum for tap 42212 (CS073)	148
5.38	Simulated pressure-coefficient spectrum for tap 42212 for record CS073	149

5.39	Simulation of pressure-coefficient spectra for record C544 using transfer functions from record C539	150
6.1	Transfer functions for tap 50101 (C081)	156
6.2	Output prediction for tap 50101 (C081)	158
6.3	Decomposition of pressure-coefficient spectrum for tap 50101 (C081)	159
6.4	Total coherence function for tap 50101 (C081)	160
6.5	Bispectrum of pressure-coefficients for tap 50101 (M15N086)	161
6.6	Transfer functions for tap 50501 (C081)	164
6.7	Output prediction for tap 50501 (C081)	166
6.8	Decomposition of pressure-coefficient spectrum for tap 50501 (C081)	167
6.9	Input and output spectra for tap 50501 (C081)	168
6.10	Bispectrum of pressure-coefficients for tap 50501 (M15N086)	169
6.11	Total coherence function for tap 50501	170
6.12	Comparison of transfer functions between field and wind tunnel for tap 50501	172
6.13	Output prediction for tap 50501 for wind-tunnel data (WT3)	174
6.14	Decomposition of pressure-coefficient spectrum for tap 50501 for wind-tunnel data (WT3)	174
6.15	Coherence function for the u terms for tap 50501 for wind-tunnel data (WT3)	175
6.16	Transfer functions for tap 50901 (C081)	176
6.17	Output prediction for tap 50901 (C081)	178
6.18	Decomposition of pressure-coefficient spectrum for tap 50901 (C081)	179
6.19	Bispectrum of pressure-coefficients for tap 50901 (M15N086)	180

6.20	Pressure taps used for area-averaging for cladding at roof corner	182
6.21	Transfer functions for the 11.2 m ² area-averaged case (C081)	183
6.22	Output prediction for 11.2 m ² area-averaged case (C081)	185
6.23	Decomposition of pressure-coefficient spectrum for the 11.2 m ² area-averaged case (C081)	186
6.24	Phase of transfer functions for tap 50501 (C081)	191
6.25	Phase of pressure spectra for tap 50501 (C081)	192
6.26	Pdf of phase of pressure spectra for tap 50501 (C081)	192
6.27	Comparison of transfer functions from two field records for tap 50501	195
6.28	Comparison of transfer functions from wind-tunnel records for tap 50501	197
6.29	Simulated pressure-coefficient spectrum for tap 50501 for record C478	198
6.30	Simulated pressure-coefficient spectrum for tap 50501 for record C709 using averaged transfer functions of C081 and C478	199
6.31	Simulated pressure-coefficient spectrum for C478 using transfer functions of C081 for the 11.2 m ² area-averaged case at roof corner	199
6.32	Simulated pressure spectrum for tap 50501 for wind-tunnel record WT1 using averaged transfer functions from WT2 and WT3	200

CHAPTER 1

INTRODUCTION

*Who has seen the wind ?
Neither you nor I,
But when the trees bow down their heads,
The wind is passing by.*

- Christina Rossetti (1830-1894).

1.1 Motivation

Strong winds associated with a variety of meteorological phenomena constitute the primary hazard to buildings, structures, lifelines, and agricultural fields. In fact, property losses resulting from windstorms accounted for more of the damage than any other natural hazard in the past decade (Cermak, 1993). We cannot see the wind but it manifests itself by the effect it produces on the environment and man-made structures. Some natural structures, such as trees, have adapted to wind through years of evolution. However, for structures like buildings the adaptation to wind has to be made by engineered design. This goal can only be achieved by gaining a deeper understanding of the way wind interacts with structures to produce critical load effects. Also, it is essential to understand and appreciate the variability and uncertainty of wind loading. The research presented herein aims to contribute to the above ends with emphasis on wind pressures on surfaces of rectangular prismatic buildings. The term ‘prismatic’ refers to a sharp-edged body whose shape is uniform both in plan and profile. The current work is, however, based on full-scale wind velocity and pressure-coefficient data collected at the Wind Engineering Research Field Laboratory (WERFL) of Texas Tech University in Lubbock, Texas. The pressure measurements were made on a 13.7 m x 9.1 m x 4 m (45 ft x 30 ft x 13 ft) flat-roof metal test building located in a flat open terrain. The test building can be classified as a low-rise rectangular prismatic building.

The subject of wind loads on low-rise buildings continues to be an active area of research. A large number of factors affect wind loads on low-rise buildings. Also, a vast

majority of the buildings used for residential, commercial, and industrial purposes fall under the category of “low-rise.” Low-rise buildings are primary casualties to wind hazards (Cermak, 1993). Field investigations conducted in the aftermath of hurricanes Hugo, Andrew, and Iniki, show clearly that cladding and roof failures account for much of the damage to low-rise structures during extreme wind events.

When wind interacts with buildings, it produces both external and internal fluctuating pressures on building surfaces. These fluctuating pressures are caused by the turbulence in the upstream flow as well as by the local building-generated or signature turbulence provoked in the wind flow by the structure itself. Hence, the characteristics of the pressures depend on the characteristics of the approaching wind, the geometry of the structure and the angle of attack of the wind. The spatial and temporal distribution of surface pressures is determined by the aerodynamics of the flow around the structure. Bearman (1978) noted that the incident turbulence influences the aerodynamic forces experienced by buildings and structures in two ways: *buffeting* and *interaction*. Unsteady buffeting forces are induced directly by the unsteady incident flow but there is also a complex interaction between the approach flow and the flow around the body. The interaction process is not accounted for by the quasi-steady theory (Letchford et al., 1993; Cook, 1990; Kawai, 1983).

Stathopoulos et al. (1978) highlighted that the dynamic or fluctuating component of all loading effects is significantly larger than the mean component. This is particularly true of local pressures. When high winds as in a hurricane last for an extended duration, they cause many loading cycles of intense pressures on the wall and roof cladding resulting in fatigue damage to components of the building envelope. The root-mean-square (rms) fluctuating pressure-coefficient measures the general energy level of pressure fluctuations occurring at a particular point. The area under the power spectrum of pressure gives the mean-square (variance) of the pressure fluctuations.

An improved understanding of the dynamics and spatial distribution of wind pressures on structures, including low-rise buildings, can be gained from full-scale data collected in the field. An augmented collection of full-scale data and the development of improved

models for wind loading of buildings are among the research areas emphasized by Jones et al. (1993) in their proposed Wind Hazards Reduction Program. The Texas Tech WERFL, a unique full-scale field research facility with sophisticated instrumentation and data acquisition system, provides tremendous new research opportunities to enhance understanding of wind pressures on surfaces of buildings. A National Science Foundation sponsored Co-operative Program in Wind Engineering (CPWE) between Texas Tech University and Colorado State University (CSU) has been underway since 1989. The field experiments conducted so far at the WERFL under the CPWE has made available a high-quality comprehensive database of real-life wind velocity, pressure and other meteorological data for research. The field facility and data are described in Chapter 3.

One of the major objectives of research in wind engineering is to predict wind-induced pressures on structures and structural cladding. The conversion from wind velocity to pressure is necessary in order to provide input to the structural model and is very sensitive since the pressure is generally proportional to the square or even higher power of velocity. In general, this is a difficult problem and the current efforts are only approximations and limited to cases that may be supported by experimental data. The relationship between the power spectra of wind velocity and wind force acting on a structure is commonly referred to as *aerodynamic admittance*. Generally, this relation is based upon experimentally obtained coefficients since the flow around a structure in turbulent wind is too complex to be dealt with analytically. In the physical sense, the presence of a bluff structure in the flow regime essentially results in the distortion of the frequency characteristics of the upstream flow. Additionally, since the relation between force and wind speed is not memoryless, i.e., it contains some aftereffects, a frequency domain representation as utilized in spectral analysis yields frequency dependent load coefficients. This is so because the wind velocity can be approximated as a stationary Gaussian process. An important property of stationary Gaussian processes is that their Fourier transforms at different frequencies are uncorrelated and independent. Also, the wind force is a non-linear function of the wind velocity which implies that the probability distribution of the wind force is non-Gaussian even if the wind velocity may be known,

verified or assumed to be a Gaussian process. It should be stated that wind pressures, as opposed to wind velocity, do in fact exhibit non-Gaussian properties. This fact has been reported by Peterka and Cermak (1975), Holmes (1981), Letchford et al. (1993) and Yin (1996). Gurley and Kareem (1994) and Kareem et al. (1995) have emphasized the use of higher-order spectra like the bispectrum and trispectrum as a tool to model nonlinear and non-Gaussian processes.

The analysis, modeling and system identification of random data are very important towards improved representation and interpretation of wind loading data. The availability of a high-quality comprehensive data base of wind velocity and pressure data of the test building at the WERFL and recent advances in system-identification techniques provide an excellent opportunity for developing transfer function models for wind pressures on building surfaces. Bendat (1990) has described procedures for identifying, in the frequency domain, optimum non-linear system properties from simultaneous measurement of the input and output data. These procedures enable formulation of the problem of predicting wind pressures from wind velocity data as a non-parametric system identification problem in the frequency domain.

1.2 Objectives

With the above background, the objectives of this research are:

1. To identify and propose a non-linear and non-parametric model to relate the spectral characteristics of fluctuating wind velocity components to the spectral characteristics of fluctuating wind pressures on building surfaces. The model aims at accounting for pressure fluctuations due to turbulence in the natural wind as well as the signature turbulence generated due to the structure itself. In other words, the model should be able to account for both the buffeting and interaction processes. The model will use the concept of multiple transfer functions so that it can provide a physical interpretation.
2. To optimally identify the transfer functions based on full-scale wind velocity and pressure data collected at the WERFL for different flow regions on the test building using a system identification technique from Bendat (1990).

3. To gain an understanding of the form and behavior of the transfer functions and to obtain an assessment of the relative contribution of the different components of the incident wind in producing pressures on surfaces of low buildings and to generate a physical interpretation from them. It is also sought to relate them to the laws and theories governing the wind flow around a bluff body. It is thus the aim of this work to investigate the influence of upstream turbulence on pressure fluctuations on building surfaces by applying system-theoretical principles.

1.3 Scope of Research

This research treats external wind pressures on building surfaces and is based on full-scale wind velocity and pressure data collected at the WERFL on a 13.7 m x 9.1 m x 4 m (45 ft x 30 ft x 13 ft) flat-roof metal test building located in a flat open terrain. The proposed model is used to solve (a) the system identification problem and (b) the spectral decomposition and output prediction problem relating wind velocity to wind pressure on building surfaces. The critical cases considered in this study are as follows. The tap locations are given in Chapter 3.

1. Pressure taps along the building shorter axis and sides for wind normal to the building:
 - a. Windward wall (Taps 42206, 42212),
 - b. Separation region on the roof (Taps 50123, 50523, 50823),
 - c. Reattachment region on the roof (Taps 51423, 52323, 52923),
 - d. Leeward wall (Taps 22312, 22306),
 - d. Side walls (Taps 11407, 31407),
 - e. Transfer functions using wind velocity measurements from a sonic anemometer (Taps 42206, 42212, 22306, 11407, 31407),
 - f. Area-averaged pressures on a roof purlin.
2. Pressure taps at the roof corner for quartering wind:
 - a. Corner taps 50101, 50501, 50505, 50901, 50905 and 50907,
 - b. Comparison with CSU wind-tunnel data for tap 50501,
 - c. Area-averaged pressures on cladding areas at the roof corner.

CHAPTER 2

BACKGROUND LITERATURE

2.1 Wind Characteristics

The motion of atmosphere is a complex blend of air movement of a wide range of scales that are broadly classified into three groups: macroscale, mesoscale, and microscale. The first comprehensive spectrum of the horizontal wind speed showing the contribution from these widely different scales was compiled by Van der Hoven (1957) and is reproduced in Figure 2.1.

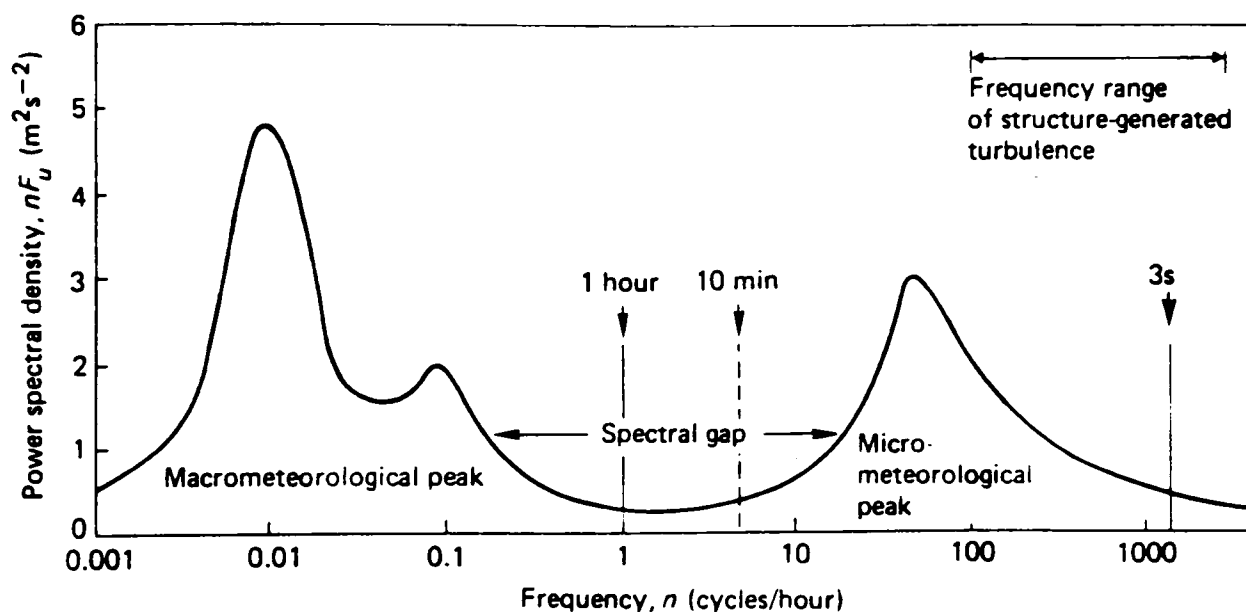


Figure 2.1. Spectrum of horizontal wind speed for Brookhaven at 100 m above ground (after Van der Hoven, 1957).

The macroscale motions are large-scale synoptic fluctuations and are comparable with those of weather maps. The macroscale is thus related to the climatological and orographical character of a site such as storm events or fronts. These have time scales ranging from half a day to several days. The mesoscale motions are the next smaller group that embodies phenomena such as squall lines, sea breeze and mountain valley wind systems. On a still smaller scale, microscale of motion is associated with the turbulent part of the flow. These have time scales ranging from about 10 minutes to less than a second.

The microscale regime of atmospheric motion occurs in the region near the surface of the earth called atmospheric boundary layer. The microscale fluctuations are related to turbulence and aerodynamics of the flow generated by the earth's obstacles on the surface or thermal action in the atmospheric boundary layer. It is the small-scale or microscale fluctuations that are of primary significance for ascertaining wind effects on structures.

The Van der Hoven (1957) spectrum in Figure 2.1 shows three distinct features. A major eddy-energy peak, usually called the *macrometeorological peak*, occurs at a frequency of 0.01 cycles/hour. This corresponds to the typical 4-day transit period of fully developed weather systems. A second major peak, called the *micrometeorological peak*, associated with mechanical and convective turbulence in the boundary layer occurs at a period of about 1 minute. Between these two peaks is a broad well-defined gap, called the *spectral gap*, at a period ranging from about 10 minutes to 1 hour in which there is little fluctuation or energy in the wind.

Van der Hoven (1957) suggests the reason for the spectral gap to be the lack of a physical process that could support wind fluctuations in that frequency range. He observes that there is no indication that the position of the spectral gap is dependent on mean wind speed or occurs at a constant wave number. There is an indication that the position is dependent on the severity of the terrain, the position being at higher frequencies with more rugged terrain. However, the fact that the gap amplitude is consistently low and that the gap is quite broad and flat does not make an exact determination of the center of the gap so vitally important. It is, however, reasonable to assume that the wind spectrum obtained from a time history record of 15 minutes duration contains almost all of the significant frequencies in the micrometeorological range. The large difference in the scales of the wind climate and the boundary layer has ensured that the spectral components of each are separated by the spectral gap. This confirms that there is negligible interaction between the wind climate and the boundary layer, and permits the separate and independent assessment of these two aspects.

From the above arguments, it is feasible to separate the wind into mean wind fluctuations and gust fluctuations (Davenport, 1971). The former are confined to

frequencies much lower than some frequency f_g (called the spectral gap frequency) and the latter to frequencies significantly greater than f_g . The wind may, thus, be treated as a locally stationary process in which the instantaneous velocity of the wind, defined by the vector $\hat{V}(t)$, can be broken down into a very slowly varying mean component, $\bar{V}(t)$, and a turbulent or fluctuating component, $\hat{v}(t)$. For all practical purposes $\bar{V}(t)$ can be considered to be a constant mean over a particular averaging time. Thus,

$$\hat{V}(t) = \bar{V}(t) + \hat{v}(t). \quad (2.1)$$

Dissipation of the wind's energy takes place at the micrometeorological frequencies in the earth's boundary layer. The shear stresses induced at the earth's surface produces eddies having scales of a few hundred meters, the energy of which is derived from the mean flow, and cascades down to smaller scale motions to be finally dissipated through viscosity. The micrometeorological spectrum reflects this dissipation process. The energy level appears to vary directly as the shear stress; consequently the fluctuation amplitudes are proportional to the mean wind strength itself (Davenport, 1971).

The typical shape of the atmospheric turbulence spectrum in the meteorological fS_u versus $\log(f)$ format is shown in Figure 2.2. The area under the curve represents the variance of the turbulence component and can be divided into three subranges by frequency. In the *production subrange* at the low-frequency end, turbulence is generated as large eddies from instabilities of the mean flow. The large eddies have the highest velocities (Cook, 1985) since S_u is largest (although fS_u is small as f tends to zero). In the *inertial subrange* over the middle range of frequency, these large eddies break up, transferring their momentum to smaller ones, then yet smaller ones, and so on forming an *energy cascade*. Finally, in the *dissipation or viscous subrange* the eddies become so small that viscosity becomes significant and their energy is dissipated. Viscous shear stresses perform deformation which increases the internal energy of the fluid at the expense of kinetic energy of the turbulence. It can be deduced that inertia dominates at

low frequencies, thus energy is transferred through the inertial sub-range with little loss, and that viscosity dominates at high frequencies so that the energy supplied from the lower frequencies is dissipated.

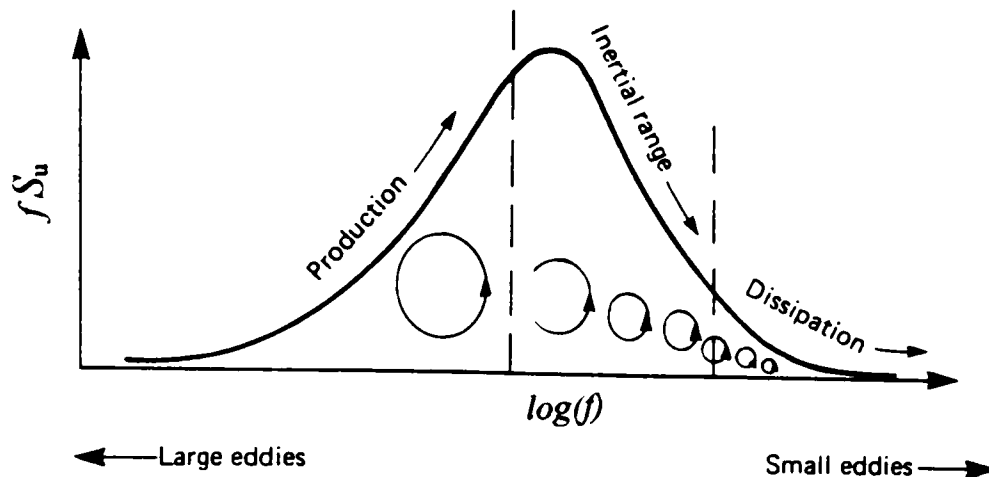


Figure 2.2. Typical turbulence spectrum (after Cook, 1985).

2.2 Wind Loads on Low-rise Buildings

It is difficult to state a precise and formal definition of low-rise buildings, as low-rise buildings cannot simply be defined by the number of stories or by overall height. This is partly due to the fact that low-rise buildings are yet generally not well understood. Low-rise buildings have small height-to-width or aspect ratios. Low buildings have high natural frequencies and are not expected to vibrate under wind action. Because atmospheric turbulence and wind speed gradients are strongest near the ground, the wind loads on low buildings exhibit strong fluctuations.

Pressures on buildings are normally expressed, for generality, in the form of non-dimensional pressure coefficients defined as follows:

$$C_p(t) = \frac{p(t) - p_0}{\frac{1}{2}\rho U^2} \quad (2.2)$$

where, $p(t)$ is the pressure time history, p_0 is a static (ambient, atmospheric) reference pressure, ρ is the air density, and U is the mean longitudinal velocity at a convenient

reference height. In the case of low buildings, this is most often taken to be the eaves height of the building, but away from the influence of the building. The quantity $0.5\rho U^2$ in Eq. 2.2 is referred to as the mean dynamic pressure or velocity pressure.

In this section, the aerodynamics of the flow around bluff structures and the factors that affect wind loading on low buildings are discussed. Aerodynamics is concerned with the study of forces arising from the relative motion of a fluid with respect to a body. The aerodynamics of the flow around bluff bodies have been discussed in detail by Cook (1985), ASCE Committee (1987), and Kareem (1987). Exhaustive state-of-the art reviews on the subject of wind loading on low buildings have been made by Holmes (1982), Stathopoulos (1984), ASCE Committee (1987) and Krishna (1995). Much of the literature presented in this section has been extracted from the above references.

2.2.1 Bluff Body Aerodynamics

A brief review of the rudiments of fluid-structure interaction is presented to appreciate the mechanisms responsible for aerodynamic loads. Aerodynamic loads applied on the roof and walls of a low building are determined by the interaction of wind flow with the surface of the building. Bearman (1978) noted that the incident turbulence influences the aerodynamic forces experienced by buildings and structures in two ways: *buffeting* and *interaction*. Unsteady buffeting forces are induced directly by the unsteady incident flow but there is also a complex interaction between the approach flow and the flow around the body. This interaction depends primarily on the geometry of the building and the flow characteristics.

A schematic sketch of different regions of turbulent flow around prismatic bluff obstacles is shown in Figure 2.3. The wind always seeks out the easiest path around a building (Cook, 1990). Hence, slenderness ratio of the building influences the path taken by the flow. When the building is tall, the wind finds it easier to flow around the sides than over the top, except for the zone very near the top. The characteristic size of the building 'seen' by the wind is the cross-wind breadth, B . The flow characteristics and the consequent loading both scale principally to this dimension. Conversely, when the

building is squat, the wind finds it easier to flow over the top than around the sides, except for the zones very near the ends. Now the characteristic size to which the flow characteristics and loading principally scale is the height, H . For intermediate cases where B and H have similar values, they may be equally important.

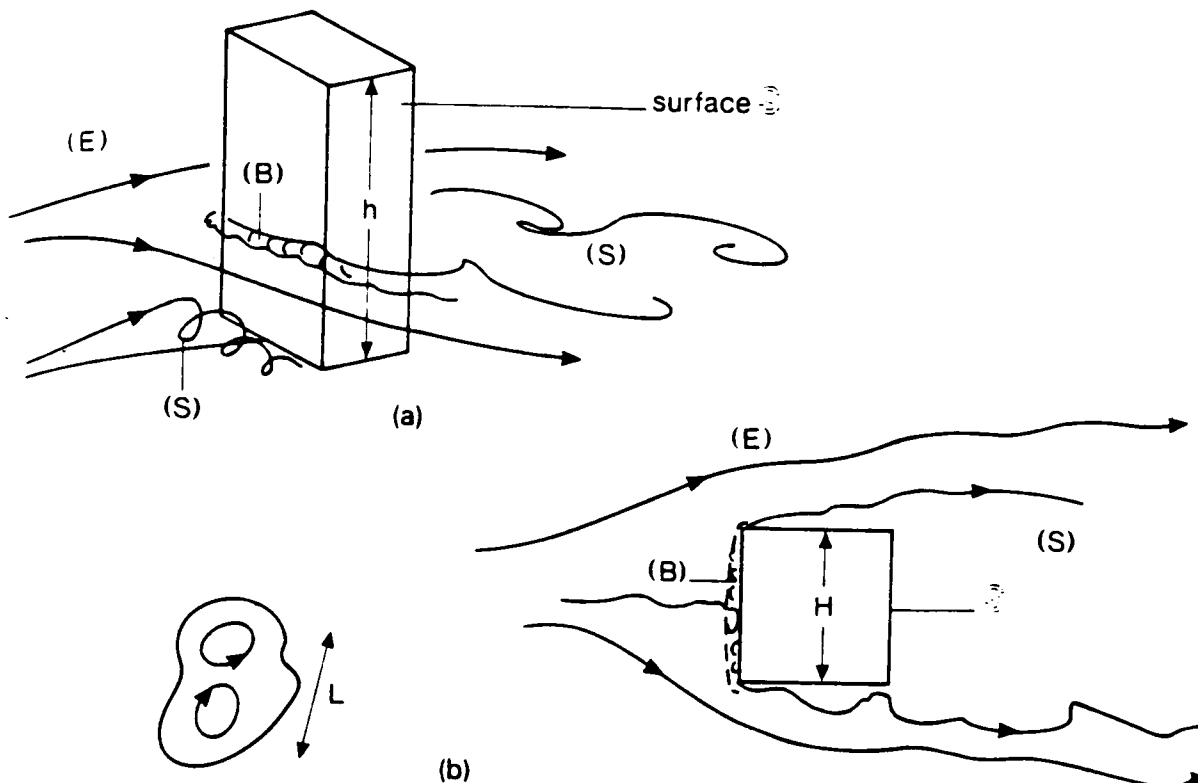


Figure 2.3. Schematic sketch of different regions of turbulent flow around bluff obstacles showing (E) external, (B) thin boundary layers, (S) separated flow regions. (a) 3-D view of a tall structure, (b) Sectional view through a 2-D flow (after Hunt et al., 1990).

Whenever the wind encounters a bluff structure, the flow diverges in both cross-wind directions, and hence is fully three-dimensional. As the wind encounters a structure, it exerts positive pressure on the windward face. The wind is then deflected around and over the structure and accelerated such that the velocity passing the upwind corners is greater than the velocity approaching the structure. The high-velocity fluid cannot negotiate the sharp corners and thus separates from the building, leaving a region of high negative pressure or suction. The separated flow forms a shear layer on each side and on the top and subsequent interactions between the layers result in their rolling up into discrete vortices that are shed alternatively. This region is generally known as the wake

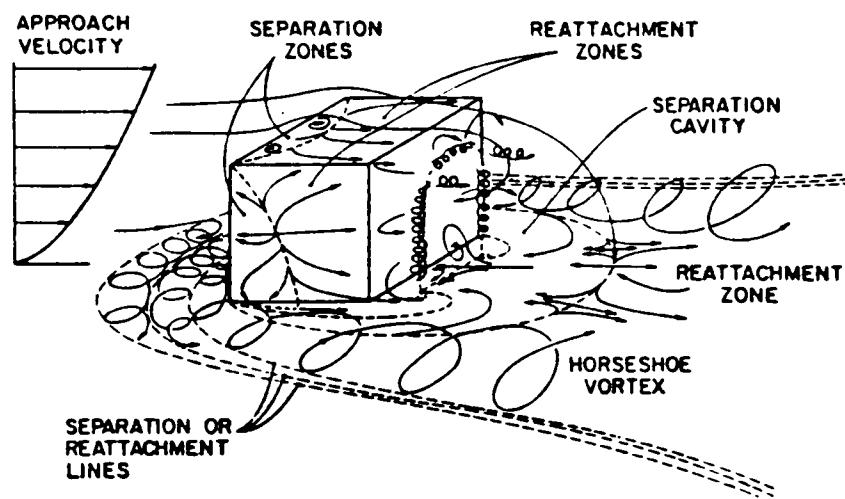
region. The separated flow will reattach only if the building is sufficiently long in the wind direction. Thus, we have negative pressures on all sides except the windward face. A model showing the complexity of the flow mechanisms and zones around a cuboidal building in a deep boundary layer is illustrated in Figure 2.4 (a).

The modification of the general wind flow determined by a large-scale pressure field creates a new local unsteady flow regime with the addition of small-scale turbulence. Small eddies are superimposed on larger ones with the result that wind speeds and pressures vary greatly in space and time. High suction appears along the edges of walls and the roof. With wind at 45° (diagonal, quartering) to the face of the building there will be a pair of strong conical or 'delta wing' vortices from the apex traveling along the concurrent edges. Very high suctions associated with these vortices develop along the eave and verge close to the roof corner.

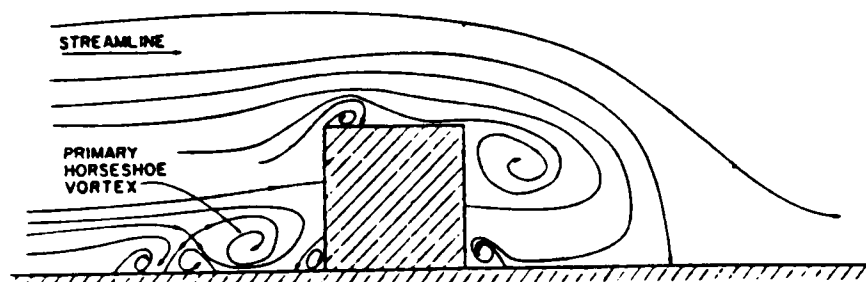
The main features of the flow normal to a cuboidal flat-roof building is shown in Figure 2.4. On the windward wall, the flow at about two-thirds of the building height comes to rest to form the front stagnation point. The maximum pressure on the windward wall is at the stagnation point. In the separated region on the roof, the effect of the upwind turbulence is to move the mean reattachment region of the shear layer closer to the leading edge and to reduce the bubble size. Flow visualization studies conducted by Wagaman (1993) on the Texas Tech test building showed that when the longer of the two walls was normal to the wind, the average separation bubble was 1.04 m (3.4 ft) tall and 4.42 m (14.5 ft) long. The separation bubble resulting from the shorter building face normal to the wind had an average height and length of 0.93 m (3.06 ft) and 4.24 m (13.9 ft), respectively. The interior flow structure of the separation bubble was reported to be similar for both the cases. The mechanism of the delta-wing vortices at the roof corner for a quartering wind is illustrated in Figure 2.5.

In the above manner, the pressure fluctuations on the surface of an isolated low-rise structure exposed to the atmospheric boundary layer result from the turbulence in the approach flow and building generated or signature turbulence. The building generated turbulence results from flow separation and reattachment, corner vortex, and from wake

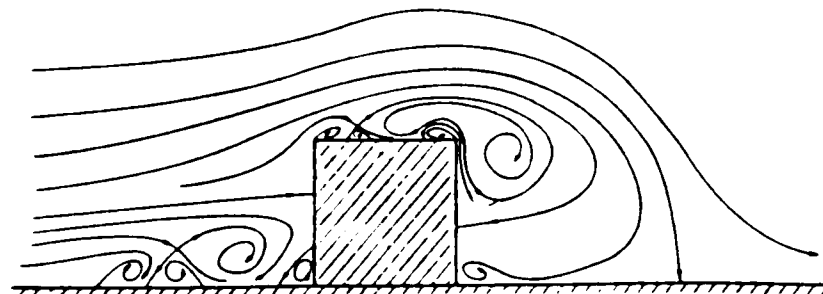
effects. These mechanisms do not take place in isolation. Rather more than one may collectively contribute to the pressure fluctuations and, hence, loads on a structure. Therefore, the aerodynamic loading may be categorized as due to the far-field which is the undisturbed flow pattern and the near-field that results from the fluid-structure interaction and the wake fluctuations. The scales associated with the far-field, near-field and wake fluctuations are quite different.



(a) Mean streamline patterns around whole building



(b) Centerline streamlines for flow reattaching to top



(c) Centerline streamlines for flow not reattaching to top

Figure 2.4. Flow around cuboidal buildings (after Peterka et al., 1985).

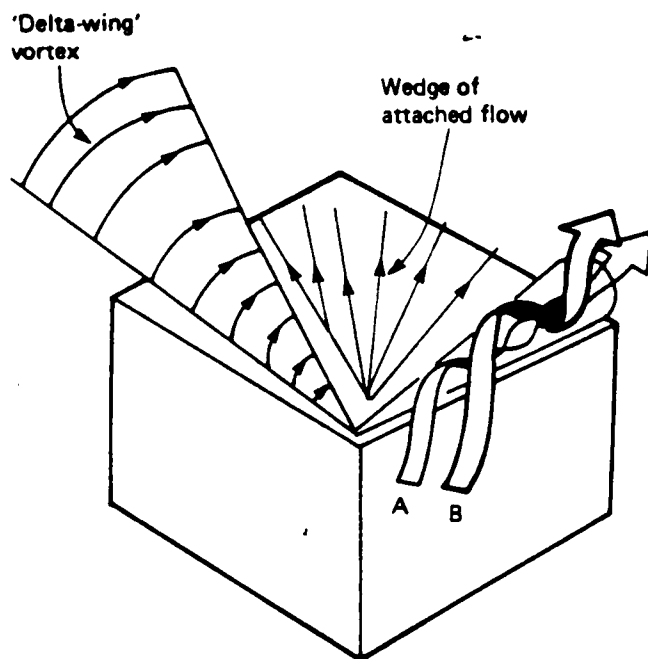


Figure 2.5. Flow structure of delta-wing vortices (after Cook, 1985).

2.2.2 Factors Affecting Wind Loads on Low-Buildings: Experimental Results

The major findings of experimental studies on low-rise buildings carried out so far either at full-scale or in wind-tunnel simulations of atmospheric flows are summarized in the following paragraphs.

2.2.2.1 Influence of Fluctuating Loads. The fluctuating part of the loading is usually significantly larger than its mean component. This is particularly true of local pressures, and is true to a lesser degree of distributed load effects. The rms fluctuating pressure coefficient is a measure of the general level of pressure fluctuations occurring at a particular point.

2.2.2.2 Influence of Terrain Roughness. In general, the rougher the terrain, the larger the magnitude of the pressure coefficients but trends are not always consistent. However, the peak pressures associated with a particular storm decrease somewhat as terrain roughness increases. This is so because the velocity pressure at eaves height is smaller over a rough terrain than over a smooth terrain for the same storm (gradient wind speed) conditions.

2.2.2.3 Influence of Wind Direction. The strong effect of wind angle of attack on the magnitude and distribution of wind loads has been shown in almost all studies of wind effects on low buildings. The critical angle of attack for pressures along the center-line of the building is normal to the face of the building and that for roof corner regions is approximately 30° to 40° to the face of the building.

2.2.2.4 Influence of Geometrical Parameters. The effect of length, height and roof slope of the building on wind loading are discussed below.

a. *Effect of Length.* For buildings with small height-to-width ratios and length-to-width ratios from 1.0 to 3.0 the wind loads do not depend significantly on the building length.

b. *Effect of Height.* Although wind loads increase with the height (h) of a building, it has been found by Davenport et al. (1977) that the dependence of peak, mean and rms pressure coefficients on height can be reduced considerably by referencing them to the velocity pressure at eaves height. Gerhardt and Kramer (1992) have observed that the roof pressure distribution is strongly affected by the relative building height for height-to-width ratios greater than or equal to 0.1. This information is yet to find a place in building codes and standards (Krishna, 1995).

c. *Effect of Roof Slope.* The roof slope strongly affects the magnitude and distribution of pressure coefficients since this is the main factor determining the wind flow pattern above the roof. In a study by Barnaud and Gandemer, referenced by Stathopoulos (1984) and ASCE Committee (1987), where pressure coefficients acting on low buildings were examined for three roof angles (0° , 22.5° and 45°), it was concluded that high suction appearing at edges and corners of flat roofs decrease for the 22.5° roof and disappear on the 45° roof. The windward wall pressures were found to be independent of roof slope. The above state-of-the art reviews have reported another study by Vickery (1976) where four low-rise buildings with roof angles of 0° , 6° , 12° and 22° were examined. It was found that for the 0° and 6° cases the pressure distribution is essentially continuous across the ridge; at 12° there is a marked change at the ridge and the pressure coefficient immediately behind the ridge is similar to that at the leading edge but falls away

rapidly towards the trailing edge; and at 22° , the leeward pressure coefficient is roughly constant. The observed distributions have been explained with reference to sketches of the shear layers which is reproduced in Figure 2.6. It was also suggested that for higher structures, the flow would not reattach.

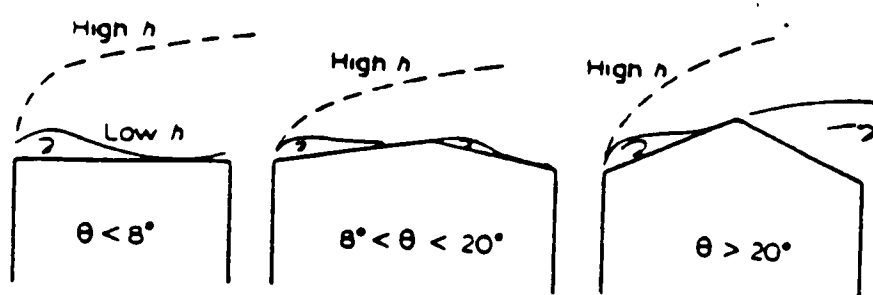


Figure 2.6. Wind flow patterns over roofs (after Barnaud and Gandemer referenced in Stathopoulos, 1984).

2.2.2.5 Influence of Tributary Area: Area Loads. The effective pressures acting on roof or wall panels can be considerably less than the very high instantaneous pressures encountered locally. This is particularly true near roof corners, ridges and wall edges.

2.2.2.6 Influence of Other Features. Architectural features such as mullions, overhangs, parapets, balconies and different edge profiles affect the wind flow in the building proximity and are able to modify the wind pressure coefficients of low buildings. Nearby structures generally tend to reduce the wind loads acting on low buildings but there are some cases of close proximity and/or large relative heights where loads are increased. Internal pressure can also be a significant proportion of the total loading. A more detailed treatment of these factors can be obtained in Stathopoulos (1984) and ASCE Committee (1987).

2.3 Assessment of Wind Loads

Any rational consideration of the way wind acts to produce loads on a structure requires an appreciation of the three fundamental aspects of the problem (Cook, 1985). These are:

1. the *wind climate*, comprising the weather systems that produce strong winds;

2. the *atmospheric boundary layer*, comprising the lower layers of the atmosphere in which the wind is modified by the rough surface terrain due to surface friction; and
3. the *structure*, which is immersed in the boundary layer and is itself a single element of the terrain.

Assessment of flow around a structure and the loads imposed on it by the wind should be made in a manner which accounts for the additional fluctuations introduced by the structure and also any interaction with the boundary layer. The typical wind climate has been shown by arguments of scale and frequency to be independent of the other two aspects and can be separated from them (Cook, 1985). However, there is significant interaction between the boundary layer and the structure and the two should ideally be assessed together as shown in Figure 2.7.

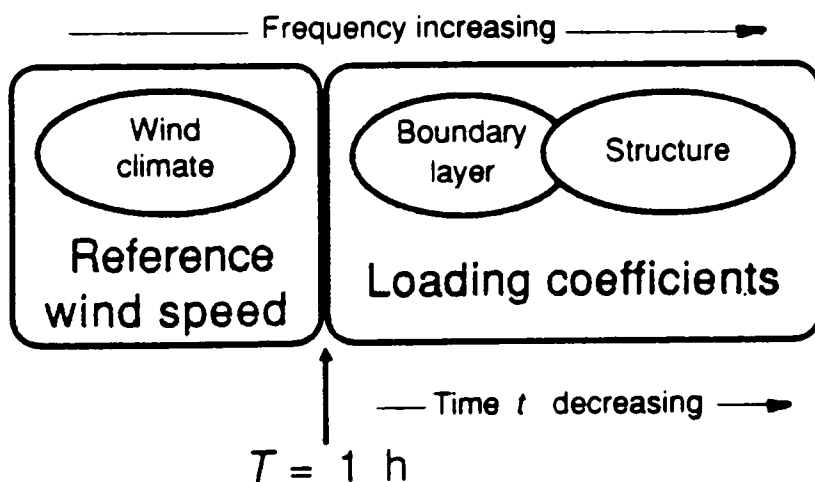


Figure 2.7. Ideal assessment of wind loading (after Cook, 1990).

The assessment of wind loading on buildings concerns the aerodynamic problem of predicting the forces (pressures) acting on the building from a knowledge of the mean and fluctuating components of the wind. The conversion from velocity to pressure is necessary in order to provide the input to the structural model and is very *sensitive* since the pressure is, generally, proportional to the square or even higher power of velocity. In general, this is a difficult problem and current efforts are only limited to cases which may be supported by experiments.

2.3.1 Concept of Aerodynamic Admittance

The relationship between wind speed and wind force or pressure acting on a structure can be expressed as a frequency dependent transfer function commonly referred to as *the aerodynamic admittance*, $\chi^2(f)$. Generally, this relation is based very much upon experimentally obtained coefficients since the flow around a structure in turbulent wind is too complex to be dealt with analytically. In the physical sense, the presence of a bluff structure in the flow regime essentially results in the distortion of the frequency characteristics of the upstream flow. Additionally, since the relation between force (or pressure) and wind velocity is not memoryless, i.e., it contains some aftereffects, a frequency domain representation as utilized in spectral analysis yields frequency dependent load (pressure) coefficients. This is so because the wind velocity can be approximated as a stationary Gaussian process. An important property of stationary Gaussian processes is that their Fourier transforms at different frequencies are uncorrelated and independent. The aerodynamic admittance is the Fourier transform of the linear impulse response function in structural dynamics. Physically, it accumulates the effects of all past fluctuations of wind speed.

In order to aid the prediction of buffeting loads, Davenport (1961) introduced the concept of an aerodynamic admittance function, relating fluctuating drag force to the longitudinal component of fluctuating velocity. Davenport also investigated extending the application of aerodynamic admittance from lattice plates and line-like strip models to bluff bodies. This was also investigated in detail in the United Kingdom at the National Physical Laboratory, first by Vickery (1966) and then by Bearman (1971). In a turbulent flow produced by a grid, the aerodynamic admittance has been measured by Vickery for a number of plates and prisms, and by Bearman for a series of thin square plates.

The form the admittance function takes depends on the geometric shape of the body and also on the nature of the velocity fluctuations (turbulence spectrum). For a square plate in a turbulent flow, the admittance is unity at zero frequency and decreases as the frequency of the velocity fluctuation increases. This results from the decreasing coherence of the turbulent eddies over the front surface of the plate as their scale decreases. Drabble

et al. (1990) presented measurements of the aerodynamic admittance of a square plate in a flow with a fully coherent fluctuation in the free-stream velocity. Drabble et al. (1990) found that, as the fluctuation frequency increases, the admittance increases from unity (its value by definition at zero frequency) in contrast to the decrease found in a turbulent flow because the velocity fluctuations are fully coherent over the front surface of the plate.

For a thin symmetrical aerofoil, the aerodynamic admittance functions associated with the vertical (lift) and longitudinal (drag) velocity fluctuations are well established on theoretical grounds and are given by the Sears' function (Jancauskas and Melbourne, 1986) and Horlock's function (Horlock, 1968), respectively. Jancauskas and Melbourne (1986) and Sankaran and Jancauskas (1992) have directly measured in the wind tunnel the aerodynamic admittance of two-dimensional rectangular cylinders in smooth and grid generated turbulent flows for sections with different chord-to-thickness ratio. These researchers concluded that the Sears' function can substantially underestimate the aerodynamic admittance of two-dimensional rectangular cylinders. The extent of this under-estimation increases with decreasing chord-to-thickness ratios. However, as the level of small-scale turbulence in the flow increases, the aerodynamic admittance converges to the Sears' function.

2.3.2 Modified Quasi-Steady Theory

In the case of flow around a building, the atmospheric turbulence is distorted by the divergence of the flow and additional fluctuations are introduced by the structure, whereas neither effect is accounted for by the quasi-steady theory. The quasi-steady theory makes the simple, but inaccurate assumption that the building structure responds to the atmospheric turbulence as if they were steady changes of mean wind speed and direction, so that the fluctuations of pressure correspond exactly with the variations of the incident wind. This implies that there is no interaction between the atmospheric boundary layer and the structure. Hence, a modified approach is necessary to predict fluctuating wind pressures on buildings, especially in separated flow regions where there is significant influence of the flow by the structure. Extensive literature related to the strip and quasi-

steady theories and their applicability can be obtained in Kawai (1983), Cook (1985, 1990), and Letchford et al. (1993).

Many codes of practice (e.g., AS:1170.2--1989; Holmes et al., 1990) use a modified quasi-steady approach for predicting fluctuating wind loads on low-rise buildings. A modified approach is required because the pressure fluctuations on a building are also influenced by building-generated or wake turbulence apart from fluctuations in the upstream velocities. The modified quasi-steady theory incorporating the second-order terms of velocity fluctuations, neglecting the vertical (w) velocity component, can be written in the frequency domain as follows (further to Letchford et al., 1993).

$$\begin{aligned}
 S_{C_p C_p}(f) = & \left\{ 4\bar{C}_p(\theta)^2 \frac{S_{uu}(f)}{U^2} + \bar{C}_p(\theta)^2 \frac{S_{u^2 u^2}(f)}{U^4} \right. \\
 & + (d\bar{C}_p(\theta)/d\theta_v)^2 \frac{S_{vv}(f)}{U^2} \\
 & \left. + \left[2(d\bar{C}_p(\theta)/d\theta_v)^2 + \bar{C}_p(\theta)^2 \right] \frac{S_{v^2 v^2}(f)}{U^4} \right\} \chi^2(f) \quad (2.3)
 \end{aligned}$$

where,

f is the frequency, U the mean longitudinal wind velocity, θ the mean wind direction;

- $S_{C_p C_p}(f)$ = spectrum of fluctuating pressure coefficients $C_p'(t)$,
- $C_p'(t)$ = $C_p(t) - \bar{C}_p(\theta)$,
- $S_{uu}(f), S_{vv}(f)$ = spectra of fluctuating longitudinal ($u(t)$) and lateral ($v(t)$) velocity components,
- $S_{u^2 u^2}(f), S_{v^2 v^2}(f)$ = spectra of $u^2(t)$ and $v^2(t)$,
- $p(t)$ = time history of wind pressure,
- $\theta(t)$ = $\theta + \theta_v$, the fluctuation in wind direction in the horizontal plane,
- θ_v = $\arctan[v/(U + u)]$,
- $\bar{C}_p(\theta)$ = $\overline{C_p(t, \theta(t))}$ = mean pressure coefficient, and
- $\chi^2(f)$ = aerodynamic admittance function.

Equation 2.3 was independently derived by the author and found to be different from Eq. 21 given in the paper by Letchford et al. (1993) with regard to the coefficients associated with the four terms. The terms inside the braces in Eq. 2.3 represent the prediction of the pressure-coefficient spectrum by the quasi-steady theory, which is then modified by a correction function $\chi^2(f)$ in order to account for the building-generated turbulence. The admittance function $\chi^2(f)$ is simply obtained by dividing the measured pressure-coefficient spectrum $S_{C_p C_p}$ by the terms inside the braces of Eq. 2.3, which includes the wind spectra and other constants. This approach treats the boundary layer and the structure separately. Also, this procedure does not account for any noise that is likely to be present in the measured spectra.

2.3.3 Non-linear Relation between Velocity and Pressure

The second-order terms in Eq. 2.3 are usually neglected for simplified analysis. Letchford et al. (1993) have presented a comprehensive analysis of the Texas Tech full-scale data viewed in the context of the quasi-steady theory. Typical admittance functions as shown in Figure 2.8 were obtained by Letchford et al. (1993) using the above modified quasi-steady approach for a few roof pressure taps of the Texas Tech WERFL test building. These functions showed that the worst cases of building-generated turbulence were associated with the shedding of conical vortices at the roof corner for quartering wind. The admittance functions were found to vary from 10 to as much as 800 times its ideal value of unity especially in the high frequency range. This deviation can be attributed in part to the fluid-structure interaction process and in part to the limited frequency response of the 3-cup anemometer used in the field measurement of wind velocity. It has been pointed out by Letchford et al. that the second-order velocity terms in the predicted pressure coefficient spectrum could be significant at high frequencies for high turbulence intensities. Their importance has been emphasized by Vaicaitis and Simiu (1977) for

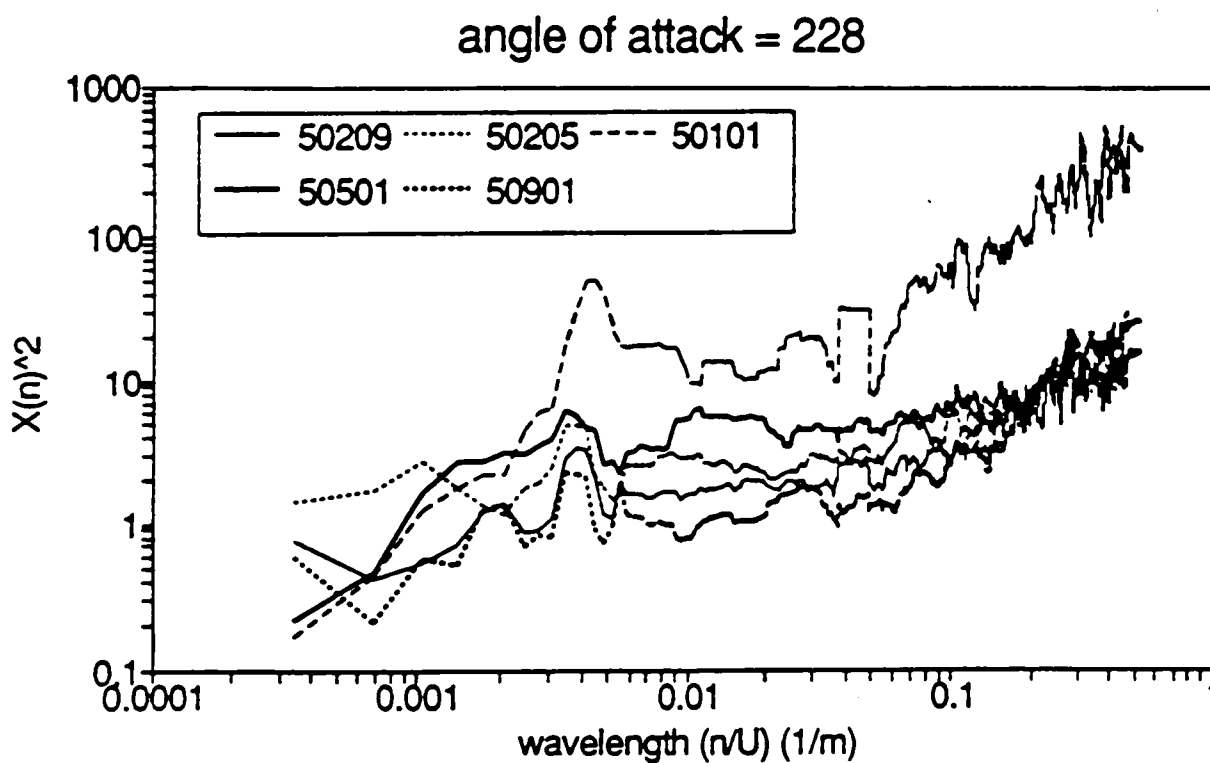
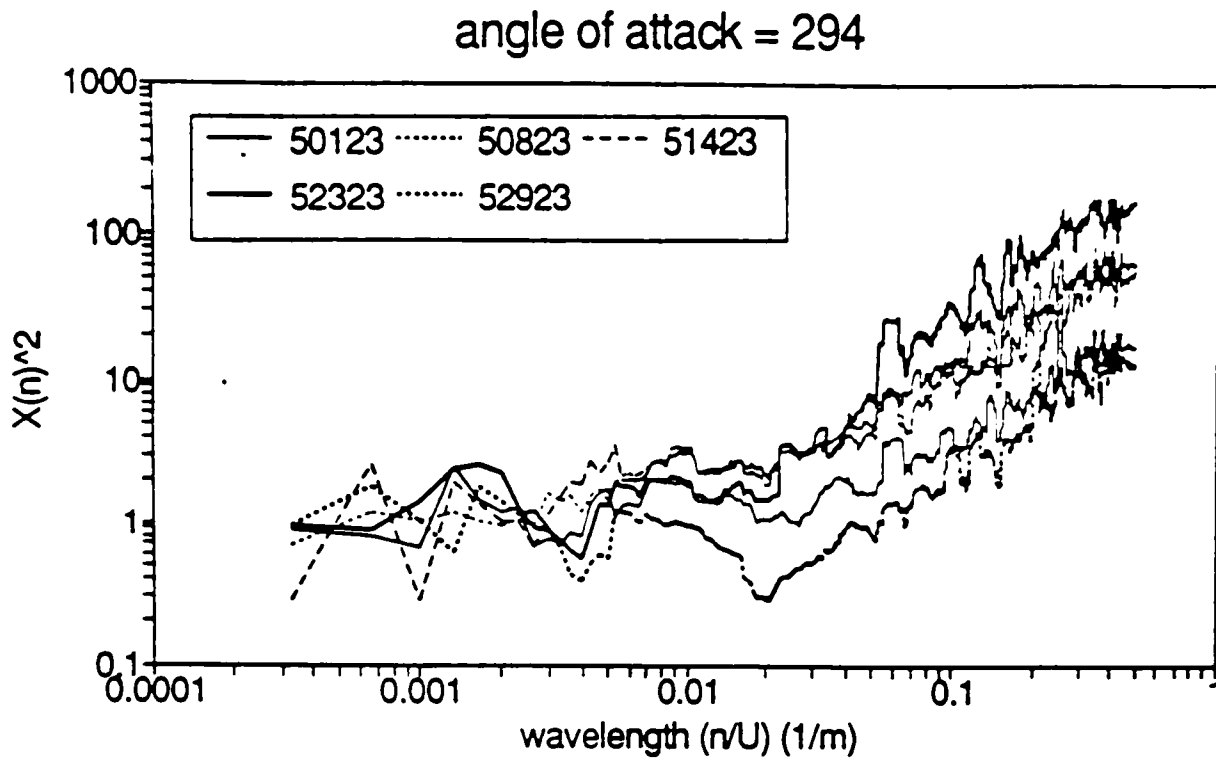


Figure 2.8. Typical admittance functions obtained from WERFL data (after Letchford et al., 1993).

buildings in urban exposure with heights less than 50 m. Tieleman (1993) presented evidence that the extreme pressures under corner vortices on roofs can only be explained with the interaction process for which the small-scale turbulence plays a key role. It should be stated that wind pressures, as opposed to wind velocity, do in fact exhibit non-Gaussian properties. The probabilistic analysis of pressure fields has demonstrated that for pressure regions where the mean pressure was below -0.25, the probability density functions (pdfs) are skewed (Peterka and Cermak, 1975). The measured pdfs of the pressure-coefficients for taps along the roof centerline and the roof corner of the Texas Tech test building were found by Letchford et al. (1993) to generally deviate from the Gaussian distribution especially at the tails of the distributions. Letchford et al. (1993) found the measured pdfs of the velocity components u and v to compare very well with the Gaussian distribution. Recent probabilistic studies by Yin (1996) using the Texas Tech full-scale data have again confirmed the non-Gaussian nature pdfs for pressures. The non-Gaussian probability distribution of wind pressures reiterates the non-linear relationship between wind velocity and pressures. Investigations by Holscher (1993, 1995) on finite cylinders under boundary layer flow in the wind tunnel have proved that a multivariate but linear model of admittance renders possible just an approximate explanation of the upstream turbulence effect. Further improvements can be achieved by at least incorporating the square relationship between velocity and pressure. Hence, it would be worthwhile to propose a non-linear transfer function model.

2.3.4 Concept of Multiple Transfer Functions

By defining just one admittance function (as in Eq. 2.3) to describe the effect of building-generated turbulence, it is assumed that both the u and v components of fluctuating wind velocity are modified in the same manner by the presence of the building. However, this may not be true physically and each of the u and v components might be modified independently due to interaction with the structure. Recently, Scanlan (1993) has discussed this issue in the context of bridge aerodynamics where two admittance functions, one associated with each of u and w components, have been defined. Sarkar

(1992) and Sarkar et al. (1994) have proposed a new buffeting-force model for lift, moment and drag buffeting forces on bridges based on two admittance functions (henceforth referred to as transfer functions), one each associated with the longitudinal (u) and vertical (w) velocity components. These researchers have emphasized that the single admittance function, unlike multiple transfer functions, cannot capture the relative importance of the separate horizontal and vertical turbulence components in producing the buffeting forces. It has been suggested that the use of the multiple aerodynamic transfer function approach is perhaps superior to the use of a single overall admittance function. Holscher and Niemann (1992a, 1992b) and Holscher (1993) have also applied a multiple aerodynamic admittance approach associated with longitudinal (u) and lateral (v) velocity components using linear system theory to boundary layer flow around a finite cylinder. Holscher has used a multivariate admittance for local surface pressures that considers the spatial and temporal structure of turbulence by means of a weighted superposition of the pressure-effects of different velocity components and parallel components at different upstream positions. This approach uses a multi-point wind field representation by taking the spatial partial velocity correlation into account. Holscher (1995) also has a study in progress which seeks to decompose the total surface pressure spectrum into uncorrelated linear, non-linear and residual contributions.

If the second-order terms are also included in a non-linear model, then two more transfer functions associated with u^2 and v^2 can be defined. This approach using the multiple transfer function concept groups the boundary layer and the structure together for assessment of wind pressures. It also enables a weighted assessment of the contribution of each of the linear and square terms of the wind velocity components to local and area-averaged pressures. This approach using multiple transfer functions enables physical insight into the mechanisms that produces pressures on building surfaces.

It may be noted that almost all of the work on admittance functions reviewed so far in this research have been based on wind tunnel experiments on prisms, plates and bridge-section models. Reed (1980) applied time-series analysis techniques to develop transfer function models for wind pressures on a hyperbolic cooling tower based on full-scale

measurements. However, the high quality comprehensive database of full-scale wind velocity and pressure data collected at the Texas Tech WERFL has provided this unique opportunity to the author for identification of transfer functions for wind-induced pressures on building surfaces based on full-scale measurements for the first time. The field facility and data have been described in Chapter 3. It is thus the aim of this work to investigate the influence of upstream turbulence on pressure fluctuations on building surfaces by applying system-theoretical principles.

2.4 System Identification in the Frequency Domain

System Identification is the process of developing a mathematical model of a physical system or process using experimental data to describe the input, output and noise relationships. A model can be defined as any mathematical representation approximating the relation between the input(s) and output of a system. These models can generally be classified as either parametric or non-parametric. In parametric models, a particular mathematical form such as a differential equation describing the essential features of the input-output relation is chosen and certain unknown parameters are designated as quantities to be identified. In non-parametric models, the relation between the input and output is represented mathematically using unknown functions called *transfer functions* rather than unknown parameters. These transfer functions are then evaluated using system identification techniques. Further, system identification methods may be classified into frequency and time domain methods. A comprehensive treatment on system identification can be obtained in Eykhoff (1974), Ljung (1987) and Imai et al. (1989). For reasons that will be evident from the discussion in this chapter a frequency domain approach is adopted in this research. A comprehensive treatment of non-linear analysis and identification from random data, in the frequency domain, is given in Bendat (1990).

For random data passing through either linear or non-linear systems, there are always three distinct parts to be considered, namely, input data properties, system properties, and output data properties. From knowledge of any two of these three parts, one could compute the third part so that one can solve the following three problems:

1. *System Identification Problem*: To identify system properties from knowledge of input data properties and output data properties.
2. *Spectral Decomposition and Output Prediction Problem*: To predict output data properties and contribution to it from different input components from knowledge of input data properties and system properties.
3. *Input Determination Problem*: To predict input data properties from knowledge of output data properties and system properties. This problem will not be dealt with in this research.

Bendat (1990) has described procedures for identifying, in the frequency domain, optimum non-linear system properties from simultaneous measurement of the input and output data properties. These procedures enable formulation of the problem of predicting wind pressures from wind velocity data as a non-parametric system identification problem in the frequency domain. The prediction of the pressure spectrum from the wind spectrum will be the output prediction problem. Bendat and Piersol (1982) and Bendat (1990) have presented practical methods as functions of frequency using basic and advanced spectral density functions with basic and advanced frequency response functions. These frequency domain results are much simpler to compute and interpret than associated time domain correlation formulas. A frequency domain approach enables characterization of a highly random phenomenon. It enables a better physical interpretation to the model by decomposition of the output to weighted contributions from different components of input using the multiple transfer function concept. Much of the theory presented here is taken from Bendat and Piersol (1982) and Bendat (1990).

2.4.1 Classification of Systems

Systems can be classified as constant-parameter or time varying. A linear system or a non-linear system is a *constant-parameter* system if the system response $y(t) = H[x(t)]$ due to an input $x(t)$ is independent of the time when $x(t)$ occurs. This means that $y(t + \tau) = H[x(t - \tau)]$, for any τ .

Systems may be classified as zero-memory, finite memory, or infinite memory. The idea of an *infinite memory* (infinite record lengths) is largely for mathematical convenience and gives negligible error if the system response due to all past inputs is known to be immeasurably small to inputs occurring in the far distant past and if long-time operation is involved. However, if these long-time effects do not die down, or if there is a starting switch in a system so that inputs are present only for a finite period after which the switch is closed, then a definite restriction of *finite memory* (finite record lengths) must be imposed to agree with the physical situation. Data obtained experimentally always last only for finite record lengths, leading to statistical errors in estimates of desired theoretical quantities based upon infinite record lengths. A *zero-memory* system acts instantaneously on the input data in some linear or non-linear fashion without any memory operations. It does not weight past inputs due to “memory” operations as in convolution integrals, where the present value of the output is a function of both the present and the past values of the input.

A zero-memory square-law system shown in Figure 2.9 is a non-linear system where the output $y(t) = x^2(t)$ when $x(t)$ is the input. The output spectral density function $S_{yy}(f)$ for Gaussian input through a zero-memory square law system is given by

$$S_{yy}(f) = \sigma_x^4 \delta(f) + 2 \int_{-\infty}^{\infty} S_{xx}(u) S_{xx}(f-u) du \quad (2.4)$$

where, σ_x^4 is the square of the variance and $\delta(f)$ is a delta function defined in Eq. 2.13.

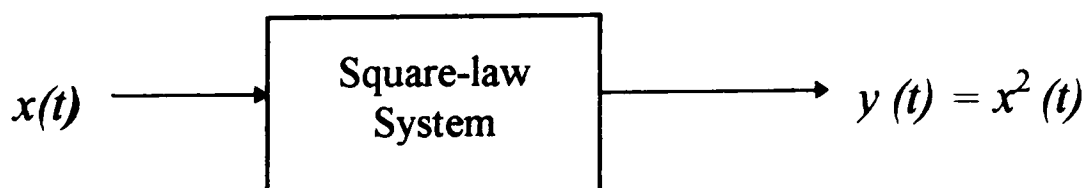


Figure 2.9. Zero memory square-law system.

Finite-memory non-linear systems are defined by inserting constant-parameter linear systems before or after the zero-memory non-linear systems. A finite memory square-law system can be defined as a zero memory square-law system that is either followed or preceded by a constant parameter linear system with memory as shown in Figures 2.10(a) and (b).

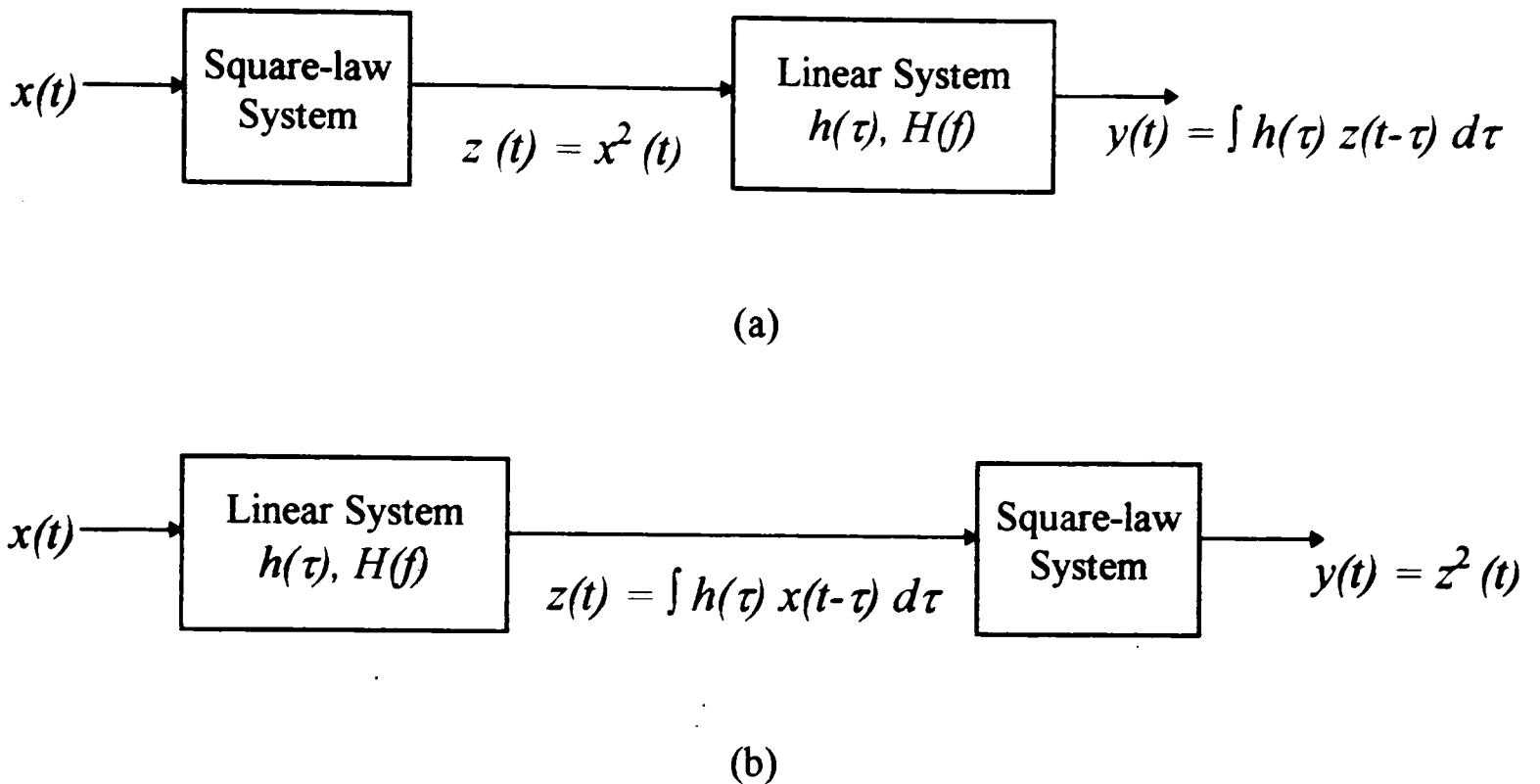


Figure 2.10. Finite-memory square-law system (a) followed by, and (b) preceded by a linear system.

2.4.2 Bispectrum Concept

As discussed earlier, there are regions over structures under separated flows that exhibit a strong non-Gaussian character with high skewness and kurtosis. The information contained in a power spectrum is essentially that which is present in second-order statistics (e.g., autocorrelation) of a signal. This would suffice for a complete statistical description of Gaussian processes only. Furthermore, second-order statistics are phase blind and only describe linear mechanisms governing the process. However, there are situations in practice where it may be necessary to go beyond the power spectrum and perform higher-order spectral (polyspectra) analysis in order to extract the phase and information due to deviations from linear and Gaussian character. In addition, cross-polyspectra may be used

for non-linear system identification from observations of input and output data. Exhaustive reviews on higher-order spectra are given by Mendel (1991), Bendat (1990) and Nikias and Petropulu (1993).

The simplest of the higher-order spectra is the third-order spectrum called the bispectrum. A detailed tutorial review on the bispectrum has been published by Nikias and Raghuvver (1987). The bispectrum, by definition, is the Fourier transform of the third-order cumulant sequence of a stationary random process. In other words, it is the double Fourier transform of the third-order statistical moment, and provides a measure of the multiplicative non-linear interaction of the frequency components in a signal. While the power spectrum $S_{xx}(f)$ represents the contribution to the mean product of two Fourier components whose frequencies are the same, the bispectrum $S_{xxx}(f_1, f_2)$ represents the contribution to the mean product of three Fourier components where one frequency equals the sum of the other two. The bispectrum $S_{xxx}(f_1, f_2)$ gives a decomposition of the skewness $E[x^3(t)]$ as a function of two frequency variables. An important property of all Gaussian processes is that their bispectra are identically zero.

The two-sided autospectrum $S_{xx}(f)$ of $x(t)$ is defined as

$$S_{xx}(f) = \frac{1}{T} E[X^*(f)X(f)]. \quad (2.5)$$

The two-sided cross-spectral density function $S_{xy}(f)$ between $x(t)$ and $y(t)$ is defined as

$$S_{xy}(f) = \frac{1}{T} E[X^*(f)Y(f)]. \quad (2.6)$$

The two-sided bispectrum $S_{xxx}(f_1, f_2)$ of a time-series $x(t)$ is defined as

$$S_{xxx}(f_1, f_2) = \frac{1}{T} E[X^*(f_1)X^*(f_2)X(f_1 + f_2)]. \quad (2.7)$$

The general two-sided cross-bispectral density function $S_{xy}(f_1, f_2)$ between $x(t)$ and $y(t)$, where f_1 and f_2 vary from $-\infty$ to ∞ , is defined as

$$S_{xy}(f_1, f_2) = \frac{1}{T} E[X^*(f_1)X^*(f_2)Y(f_1 + f_2)] \quad (2.8)$$

where,

f, f_1, f_2 are frequencies;

$X(f), Y(f)$ are Fourier transforms of $x(t)$ and $y(t)$, respectively, and $X^*(f)$ is the complex conjugate of $X(f)$;

T is the time length of the record and $E[]$ denotes an expected value ensemble average over the quantities inside the brackets.

It is the cross-bispectral density function that is of interest in the identification of quadratic transfer functions of non-linear systems. These quantities defined in Eq. 2.8 are functions of two frequency variables f_1 and f_2 . Consequently, they are very difficult to compute and to interpret. Along the line where $f_1 = f_2 = f$, one can define the special two-sided cross-bispectral density function $S_{xy}(f)$ as

$$S_{xy}(f) = S_{xy}(f, f) = \frac{1}{T} E[X^*(f)X^*(f)Y(2f)]. \quad (2.9)$$

This special result is a direct extension of the ordinary cross-spectral density function $S_{xy}(f)$ defined in Eq. 2.6. It is a function of only one variable that is relatively easy to compute and interpret. In particular, it is the key to detecting the presence and properties of the square-law system that will be discussed later. The physical importance of this result is that it facilitates simpler and practical ways to analyze and identify non-linear systems.

2.4.3 Modeling of Non-linear Non-Gaussian Processes

In the study of physical systems the relationship between the input and output is often sought to model the system response. Gurley and Kareem (1994) and Kareem et al. (1995) have examined advanced analysis and simulation tools for wind engineering with particular reference to analysis and simulation of non-Gaussian features of wind pressures. In many instances in wind engineering the input-output are not related by a linear transfer function due to non-linear characteristics. An example of such a situation is the turbulent fluctuations and the negative pressure fluctuations on building envelopes, which is the subject of this research. In such cases, the input-output relationship may be expressed in terms of a hierarchy of linear, quadratic and higher-order transfer functions or corresponding impulse response functions in the time domain (e.g., Kareem and Li, 1988). These transfer functions can be determined once information on the system input and output are available from experimental data or from theoretical considerations. Choi et al. (1985) have successfully applied a linear-quadratic transfer function system using cross-bispectral analysis to model the non-linear response of a moored vessel system in random seas. The treatment in this work will also be limited to second-order or quadratic nonlinearities in order to keep the formulation simple and computationally expedient, although applications to higher order non-linearities are immediate.

The output of a non-linear system can often be expressed as a “power series with memory” by using a Volterra functional representation (Schetzen, 1980). By this representation, the output $y(t)$ due to an input $x(t)$ is given in the time domain by

$$y(t) = \int_{-\infty}^{\infty} h(\tau)x(t-\tau) d\tau + \int_{-\infty}^{\infty} \int_{-\infty}^{\infty} h(\tau_1, \tau_2)x(t-\tau_1, t-\tau_2) d\tau_1 d\tau_2 + \dots \quad (2.10)$$

If only up to the quadratic terms are included, then $h_1(\tau)$ and $h_2(\tau_1, \tau_2)$ are the first- (linear) and second-order (quadratic or bilinear) impulse response functions (weighting functions), respectively. The Fourier transform of the Volterra series expansion in Eq. 2.10 gives the output or the response in the frequency domain as

$$Y(f) = H_1(f)X(f) + \int_{-\infty}^{\infty} \int_{-\infty}^{\infty} H_2(f_1, f_2) X(f_1) X(f_2) \delta(f_1 + f_2 - f) df_1 df_2 + \dots \quad (2.11)$$

where,

$$Y(f) = \int_{-\infty}^{\infty} y(t) e^{-j2\pi ft} dt = \text{Fourier transform of } y(t);$$

$$X(f) = \int_{-\infty}^{\infty} x(t) e^{-j2\pi ft} dt = \text{Fourier transform of } x(t); \quad (2.12)$$

$$j = \sqrt{-1} .$$

$H_1(f)$ and $H_2(f_1, f_2)$ are the linear and quadratic (bilinear) frequency response functions (or transfer functions), respectively; which are nothing but the Fourier transforms of the corresponding impulse response functions in the time domain, and

$$\delta(f_1 + f_2 - f) = \delta(g) \text{ is a } \textit{delta function} \text{ defined by } \delta(g) = 1, \text{ if } g = 0$$

$$= 0, \text{ otherwise.} \quad (2.13)$$

Theoretical background on the modeling and identification of non-linear systems as in Eq. 2.11 can also be found in Kim and Powers (1988), Nam and Powers (1994), Kanai et al. (1994) and Tseng and Linebarger (1995). The first term in Eq. 2.11 represents the linear contribution obtained through the linear transfer function. The second term describes the quadratic or bilinear term and includes the contribution of various pairs of frequencies in terms of their sums and differences that result from the quadratic interaction.

In general, the frequency response function $H(f)$ is a complex valued quantity which can be expressed in terms of a magnitude or gain factor $|H(f)|$ and an associated phase angle or phase factor $\phi(f)$ by the equation

$$H(f) = |H(f)|e^{-j\phi(f)}. \quad (2.14)$$

The complex-valued transfer function indicates a phase shift between the input (wind velocity) and the output (wind force/pressure). The frequency response function can also be expressed in terms of a real part $H_R(f)$ and an imaginary part $H_I(f)$ by the equation

$$\begin{aligned} H_R(f) &= |H(f)| \cos(\phi(f)) \\ H_I(f) &= |H(f)| \sin(\phi(f)). \end{aligned} \quad (2.15)$$

Also,

$$\begin{aligned} H(f) &= [H_R^2(f) + H_I^2(f)]^{1/2} \\ \phi(f) &= \tan^{-1}[H_I(f) / H_R(f)]. \end{aligned} \quad (2.16)$$

2.4.3.1 General Second-Order Model. Considering only up to second-order, the model in Eq. 2.11 can be represented as a general second-order non-linear model consisting of a linear system $H_1(f)$ in parallel with a bilinear system $H_2(f, g)$ as shown in Figure 2.11.

In the model,

$$y(t) = y_1(t) + y_2(t) + n(t) \quad (2.17)$$

where,

$y_1(t) = y_a(t)$ is the output due to the linear system,

$y_2(t) = y_b(t) + \bar{y}_2(t)$ is the output due to the bilinear system, and

$n(t)$ is the output residual or noise quantity that represents all uncorrelated deviations in the output $y(t)$ that are not due to the passage through the linear and bilinear systems.

To obtain closed-form answers, the input data are assumed to be a zero-mean Gaussian stationary random process with arbitrary spectral properties. For Gaussian input data, the outputs $y_1(t)$ and $y_2(t)$ will be uncorrelated. In the frequency domain,

$$Y(f) = Y_a(f) + Y_b(f) + N(f) \quad (2.18)$$

and in spectral form, the total output spectrum is given by

$$S_{yy}(f) = S_{y_a y_a}(f) + S_{y_b y_b}(f) + S_{nn}(f). \quad (2.19)$$

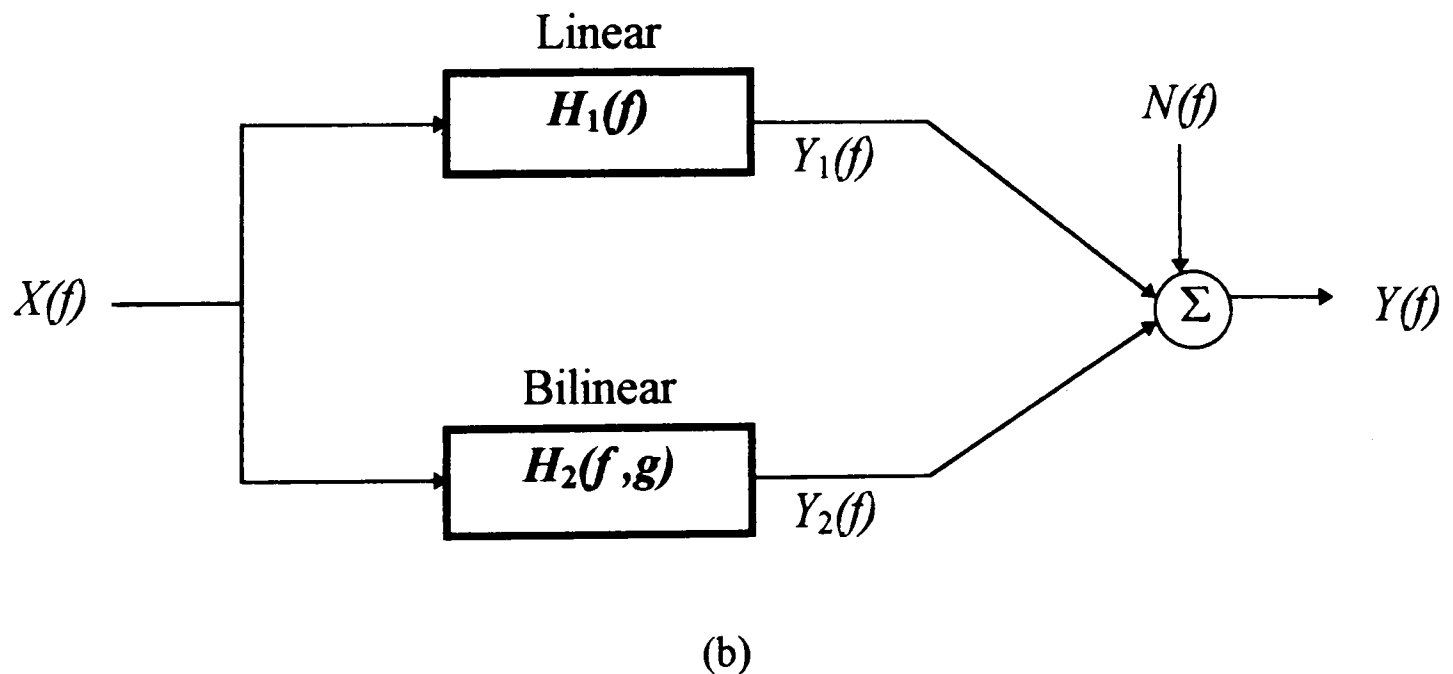
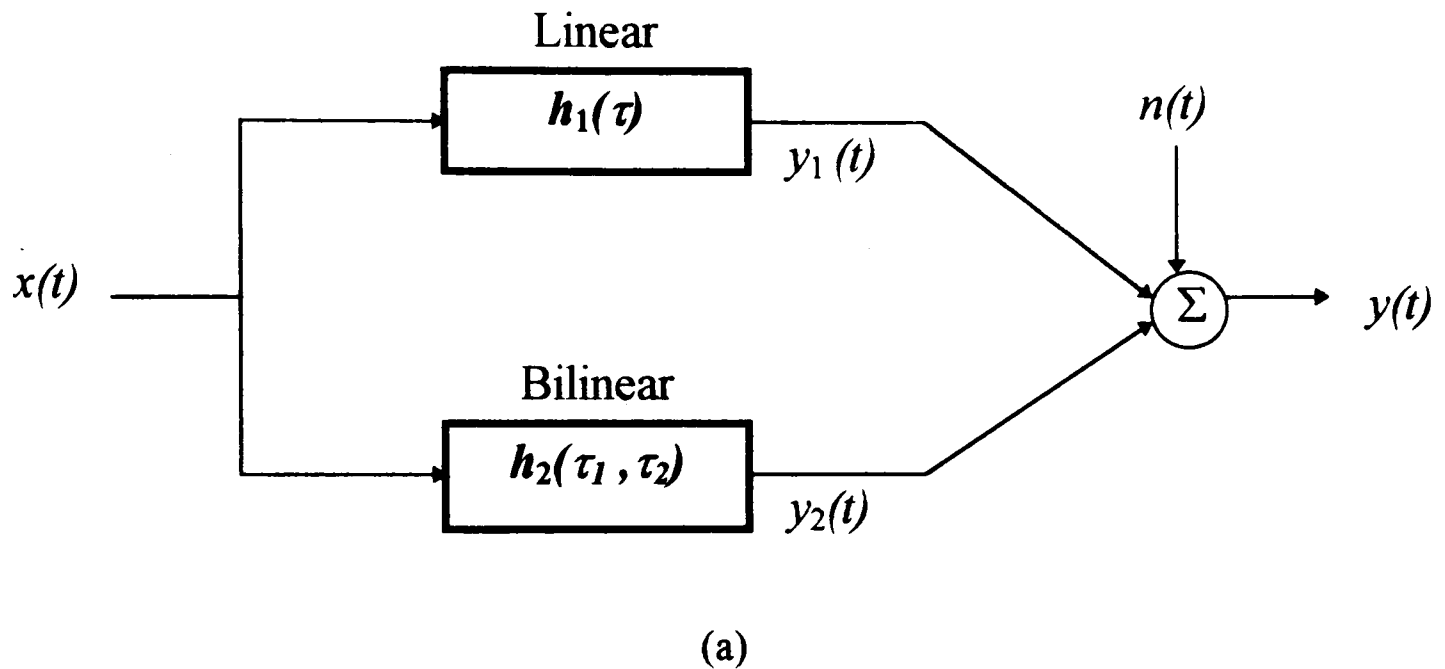


Figure 2.11. General bilinear model in (a) time domain and (b) frequency domain.

2.4.3.2 Identification of Optimum Systems. Formulas for identifying the optimum forms for the linear and bilinear systems $H_1(f)$ and $H_2(f, g)$ can be derived. These optimum forms are obtained by minimizing the output residual or noise spectrum $S_{nn}(f)$ in the linear-quadratic model with respect to all possible choices of H_1 and H_2 . When $S_{nn}(f)$ is minimized, it becomes automatically true that the residual $n(t)$ is uncorrelated with the outputs $y_a(t)$ and $y_b(t)$ (Bendat, 1990). For arbitrary choices of the systems H_1 and H_2 , the quantity $N(f)$, which is the Fourier transform of $n(t)$, is obtained by rearranging Eq. 2.18 as

$$N(f) = Y(f) - Y_a(f) - Y_b(f). \quad (2.20)$$

The autospectrum of the residual or noise is given by

$$S_{nn}(f) = \frac{1}{T} E[N^*(f)N(f)]. \quad (2.21)$$

From Eq. 2.20, omitting f to simplify notation,

$$\begin{aligned} E[N^*N] &= E[(Y^* - Y_a^* - Y_b^*)(Y - Y_a - Y_b)] \\ &= E[Y^*(Y - Y_a - Y_b) - Y_a^*(Y - Y_a - Y_b) - Y_b^*(Y - Y_a - Y_b)] \\ &= E[Y^*Y] - E[Y^*Y_a] - E[Y^*Y_b] - E[Y_a^*Y] + E[Y_a^*Y_a] - E[Y_b^*Y] + E[Y_b^*Y_b] \end{aligned} \quad (2.22)$$

plus other terms whose expected values are zero because $y_a(t)$ and $y_b(t)$ are mutually uncorrelated. Equation 2.22 can now be written in the spectral form as:

$$\begin{aligned} S_{nn}(f) &= S_{yy}(f) + [S_{y_a y_a}(f) - S_{yy_a}(f) - S_{y_a y}(f)] \\ &\quad + [S_{y_b y_b}(f) - S_{yy_b}(f) - S_{y_b y}(f)]. \end{aligned} \quad (2.23)$$

The system H_1 appears only within the first brackets and the system H_2 appears only within the second brackets of Eq. 2.23. Hence, the minimization of $S_{nn}(f)$ with respect to H_1 and H_2 will not involve any overlapping terms and can be carried out separately as shown below.

a. *Optimum Linear System:* Taking the Fourier transform of the first-order convolution integral, it has been derived in Bendat (1990) that

$$Y_a(f) = H_1(f)X(f). \quad (2.24)$$

It follows from Eq. 2.24 that the three spectral terms in the first brackets of Eq. 2.23 which involves $H_1(f)$, after omitting f for simplified notation, are given by

$$S_{y_a y_a} - S_{y y_a} - S_{y_a y} = H_1^* H_1 S_{xx} - H_1 S_{yx} - H_1^* S_{xy}. \quad (2.25)$$

The optimum linear system H_1 is defined as that particular H_1 over all possible H_1 that gives a minimum value for S_{nn} . This can be determined by setting the partial derivative of S_{nn} of Eq. 2.23 with respect to H_1^* equal to zero, holding H_1 fixed after substituting Eq. 2.25 in Eq. 2.23 giving the result

$$\frac{\partial S_{nn}}{\partial H_1^*} = H_1 S_{xx} - S_{xy} = 0. \quad (2.26)$$

Hence, the optimum linear system $H_1(f)$ must satisfy the equation

$$H_1(f) = \frac{S_{xy}(f)}{S_{xx}(f)}. \quad (2.27)$$

b. *Optimum Bilinear System*: Taking the Fourier transform of the second-order convolution integral, it has been derived in Bendat (1990) that

$$Y_b(f) = \int_{-\infty}^{\infty} H_2(u, f-u)X(u)X(f-u)du - \bar{y}_2\delta_1(f) . \quad (2.28)$$

where, $\delta_1(f)$ is a finite delta function defined as

$$\begin{aligned} \delta_1(f) &= \delta_1(-f) = T, \quad (-1/2T) < f < (1/2T) \\ &= 0, \quad \text{otherwise} \end{aligned} \quad (2.29)$$

in which T is the time period of the record.

It follows here that for Gaussian input data the three spectral terms in the second brackets of Eq. 2.23 involving $H_2(f, g)$ are given by

$$\begin{aligned} S_{y_b y_b}(f) &= 2 \int_{-\infty}^{\infty} H_2^*(u, f-u)H_2(u, f-u)S_{xx}(u)S_{xx}(f-u)du \\ S_{y y_b}(f) &= \int_{-\infty}^{\infty} H_2(u, f-u)S_{xy}^*(u, f-u)du \\ S_{y_b y}(f) &= \int_{-\infty}^{\infty} H_2^*(u, f-u)S_{xy}(u, f-u)du \end{aligned} \quad (2.30)$$

Now the partial derivative of S_{nn} of Eq. 2.23 with respect to H_2^* (holding H_2 fixed after substituting Eq. 2.30 in Eq. 2.23) when set equal to zero gives the result

$$\frac{\partial S_{nn}}{\partial H_2^*} = 2H_2(u, f-u)S_{xx}(u)S_{xx}(f-u) - S_{xy}(u, f-u) = 0 . \quad (2.31)$$

Hence, the optimum bilinear system $H_2(u, f-u)$ must satisfy the equation

$$H_2(u, f - u) = \frac{S_{xy}(u, f - u)}{2S_{xx}(u)S_{xx}(f - u)} \quad (2.32)$$

Equations 2.27 and 2.32 solve the *system identification problem* to determine all of the system properties from measurements only of the input data $x(t)$ and the total output data $y(t)$.

2.4.3.3 Output Prediction. The output autospectral density functions for the bilinear model with uncorrelated outputs have been derived from autocorrelation and direct methods in Bendat (1990) and are given as

$$S_{y_a y_a} = |H_1(f)|^2 S_{xx}(f) \quad (2.33)$$

$$S_{y_b y_b}(f) = 2 \int_{-\infty}^{\infty} |H_2(u, f - u)|^2 S_{xx}(u) S_{xx}(f - u) du, \quad f \neq 0. \quad (2.34)$$

Equations 2.33 and 2.34 solve the *output prediction problem* from the knowledge of input data properties and system properties.

2.4.3.4 A Special Case of the General Bilinear Model. A special case of the general bilinear model that is of physical interest and used in this research is one which consists of a linear system in parallel with a finite-memory non-linear square law system as shown in Figure 2.12. The non-linear square-law system consists of a zero-memory square-law system followed by a constant parameter linear system. This special case is referred to as Case 1 square-law model in Bendat and Piersol (1986) and Bendat (1990). The higher-order frequency response function (Eq. 2.32) and associated special bispectral density function (Eq. 2.9) become functions of only one frequency variable ($f = g$) that are much easier to compute than the functions of two variables required for general bilinear systems discussed earlier. The Case 1 Model can be represented in the time domain as

$$y(t) = \int_{-\infty}^{\infty} h_1(\tau) x(t - \tau) d\tau + \int_{-\infty}^{\infty} h_2(\tau) x^2(t - \tau) d\tau. \quad (2.35)$$

The Case 1 type of non-linear models occur when higher-order frequency response functions can be represented by additive of first-order frequency response functions such that the linear and bilinear systems discussed in the general model are given by

$$H_1(f) = A_1(f) \quad (2.35)$$

$$H_2(f_1, f_2) = A_2(f_1 + f_2) \quad (2.36)$$

$$H_2(f, f) = A_2(2f), \text{ for the case where } f_1 = f_2 = f. \quad (2.36a)$$

$$H_2(u, f - u) = A_2(f). \quad (2.36b)$$

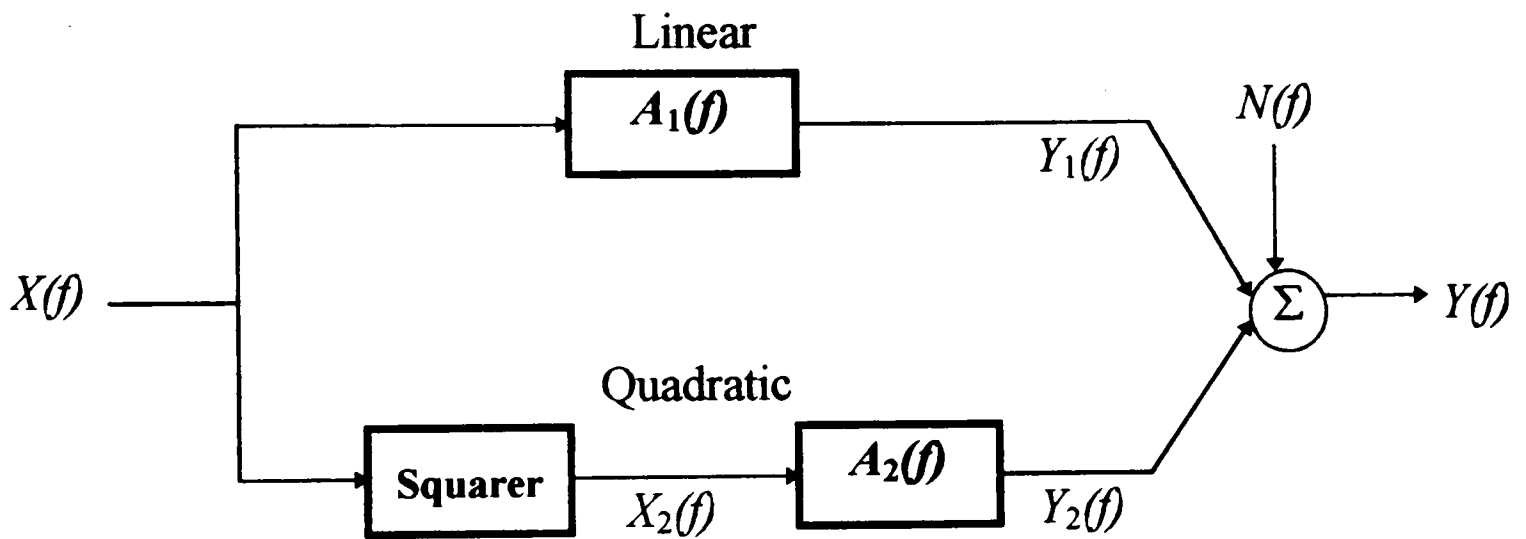


Figure 2.12. Parallel linear and square-law systems with squarer followed by linear system.

Substituting $f = g = f$ (i.e., $u = f/2$) and Equations 2.35 and 2.36b in Equations 2.27 and 2.32, respectively, for the general bilinear model gives the optimum linear and bilinear systems for the special case as

$$A_1(f) = \frac{S_{xy}(f)}{S_{xx}(f)} \quad (2.38)$$

$$A_2(f) = \frac{S_{xy}(f/2)}{2S_{xx}^2(f/2)}. \quad (2.39)$$

single-output bilinear model in Figure 2.12. Recognition of this equivalence makes system identification in Case 1 models a straight forward linear problem using conventional procedures. Since $x_2(t)$ and $x(t)$ are statistically independent for a zero mean Gaussian process it follows that

$$A_2(f) = \frac{S_{x_2y}(f)}{S_{x_2x_2}(f)} \quad (2.44)$$

where,

$$S_{x_2y}(f) = \frac{1}{T} E[X_2^*(f)Y(f)]; \quad (2.45)$$

$$S_{x_2x_2}(f) = \frac{1}{T} E[X_2^*(f)X_2(f)]. \quad (2.46)$$

The bilinear output spectral density function is now given by

$$S_{y_1y_1} = |A_2(f)|^2 S_{x_2x_2}(f) = S_{y_ay_a}. \quad (2.47)$$

The linear transfer function and output spectral density function are determined as before by equations 2.38 and 2.40, respectively.

The alternative linear analysis procedure is simpler because it does not require computation of special bispectral density functions. It offers certain practical advantages in terms of the necessary digital computations and estimation errors as compared with the bispectrum formulation (Bendat and Piersol, 1982; Rice and Fitzpatrick, 1988). Hence, it may be preferred for practical problems and has been adapted for the formulation used in this work.

CHAPTER 3

FIELD FACILITY AND DATA

3.1 Introduction

A permanent field research facility known as the Wind Engineering Research Field Laboratory (WERFL) has been constructed at Texas Tech University (TTU) to study full-scale wind effects on low-rise buildings. This experiment includes the study of wind loads and pressures on building surfaces. The field experiments conducted so far at the WERFL have made available a high-quality comprehensive database of full-scale wind velocity, pressure and other meteorological data for research.

The research presented here is primarily based on simultaneous measurements of full-scale wind-velocity and pressure-coefficient (C_p) time histories obtained at the WERFL. The field facility, instrumentation, data acquisition system, site characteristics, wind characteristics and terrain parameters at the WERFL have been described in detail by Levitan and Mehta (1992a,1992b). A description of the features of the facility relevant to this work and the full-scale data used is provided here. Much of the information presented here about the field facility have been taken from the papers by Levitan and Mehta(1992a,1992b). A very limited amount of wind-tunnel data obtained on the model of the WERFL test building at the Meteorological Wind Tunnel (MWT) at Colorado State University (CSU) that was used in this research is also described. Finally, a comparison of the velocity spectra obtained from different types of anemometers used in the field and the wind tunnel is presented.

3.2 The Field Facility: The WERFL

The WERFL has two main components: a 9.1 m x 13.7 m x 4.0 m (30 ft x 45 ft x 13 ft) metal test building on which the wind induced pressures are measured and a 48.8 m (160 ft) tall steel tower on which the meteorological instrumentation is mounted. A view of the test building and the tower is shown in Figure 3.1. The facility is located on TTU owned land in Lubbock, Texas.

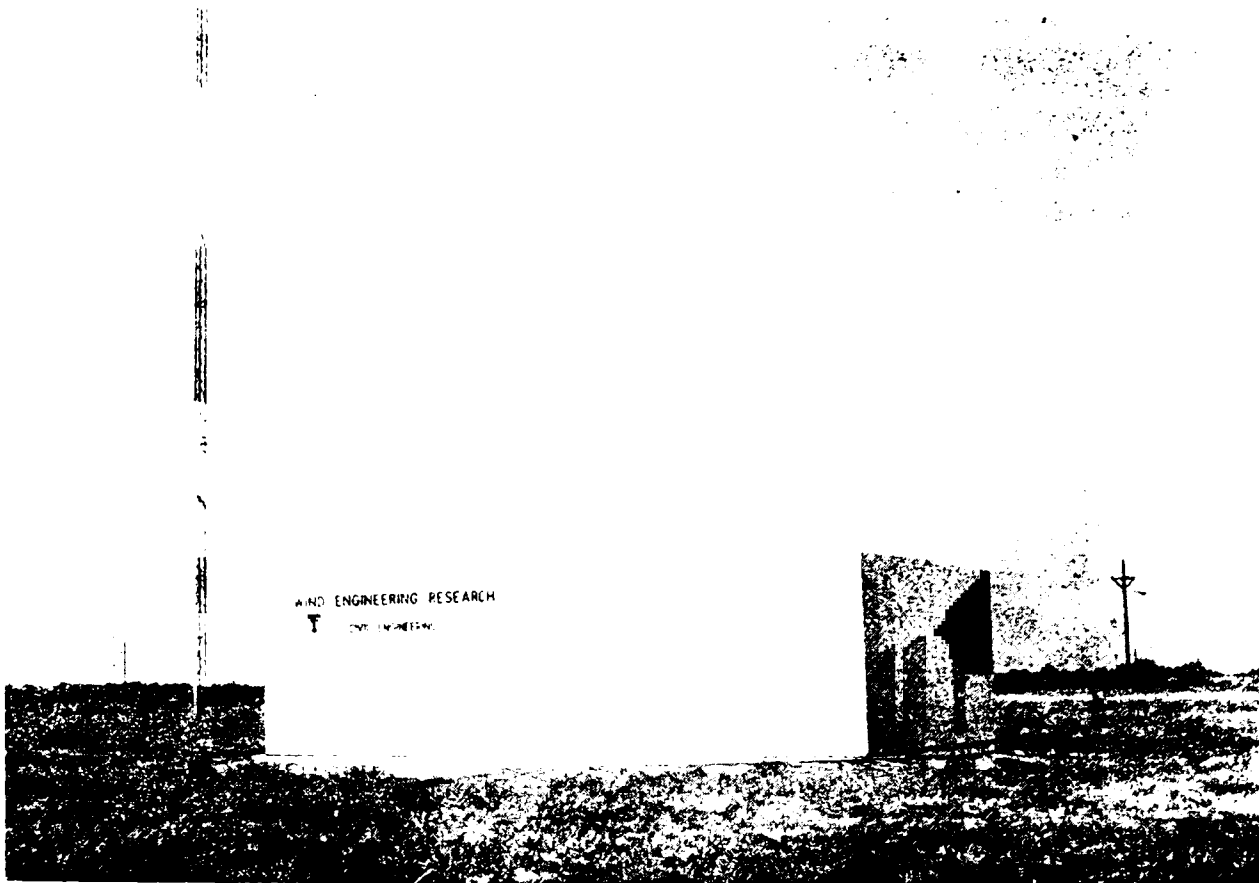


Figure 3.1. The WERFL: test building and meteorological tower.

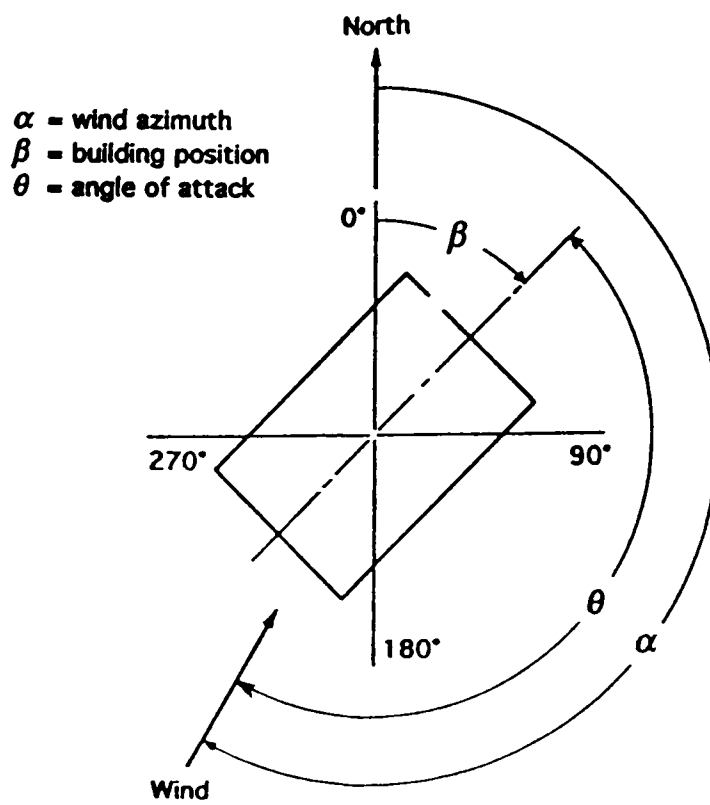


Figure 3.2. Wind azimuth, building position and angle of attack.

3.2.1 The Test Building

The test building is a prefabricated metal building with a flat roof constructed on a rectangular rigid undercarriage. A mechanism to rotate the building (at 15° intervals) provides positive control over wind angle of attack. The structure of the test building consists of three steel frames spanning 9.15 m (30 ft). Purlins and girts span between the frames. The building surface is smooth and has no architectural features. The building has a door and a window. Centrally located inside the test building stands a fixed concrete-block building housing the data acquisition system.

3.2.2 Some Definitions

Wind azimuth (α) is the angle measured clockwise from the true (geographic) north to the direction of the wind.

Building position (β) is the angle measured clockwise from the true north to the building north. The *building north* is defined as the longitudinal axis of the building directed from the center toward the *building north wall*, which is the short wall with the door.

Angle of attack (θ) is the angle measured clockwise from the building north to the wind direction. If α , β are measured in degrees, then θ can be computed in degrees by

$$\begin{aligned}\theta &= \alpha - \beta, & \text{if } \alpha > \beta \\ \theta &= 360^\circ + \alpha - \beta, & \text{if } \alpha < \beta\end{aligned}\tag{3.1}$$

The wind azimuth, building position and angle of attack defined above are pictorially illustrated in Figure 3.2.

3.2.3 Pressure Measuring System and Instrumentation

3.2.3.1 Pressure Taps. More than 100 pressure taps, each 9.5 mm (3/8 in.) inside diameter and 51 mm (2 in.) long, have been mounted flush with the outer skin of the building.

Tap numbering scheme: The pressure taps are uniquely numbered using a scheme based on tap coordinates. Each tap is assigned a 5-digit number, $sxxyy$. The s indicates

the building surface on which the tap is located: 1 for the building north wall, 2-4 for the other walls in a clockwise fashion, and 5 for the roof. The two pairs of digits xx and yy represent the nominal coordinates, in feet, of the tap on the given surface. The origin for each wall is its exterior lower left corner, while facing the respective wall from the outside. The origin for the roof is its southwest corner. For example, Tap 42206 indicates a tap on the building west wall (designated 4), nominally 22 ft from the left edge and 6 ft high on the wall. The location of all the pressure taps used in this study is shown in Figure 3.3. The exact coordinates of these taps are tabulated in Table 3.1.

3.2.3.2 Instrumentation and Measuring System. Wind induced pressures (external and internal) on the building surfaces are measured using differential pressure transducers of the Omega and Validyne types.

Seventeen Validyne Engineering Model DP103-22N-7-S-4-H differential pressure transducers are in use. Of these, thirteen have a full-scale (FS) range of ± 1.38 kPa (± 0.20 psi) and four of them have a range of ± 2.21 kPa (± 0.32 psi). The rated accuracy of these transducers, including effects of linearity, hysteresis and repeatability is $\pm 0.25\%$ FS. Diaphragm displacement causes a change in the magnetic field, which is converted to a voltage output linearly proportional to the applied differential pressure.

Thirty transducers of the Omega Engineering Inc. Model PX 163-005 BD 5V with a FS range of ± 1.24 kPa (± 0.18 psi) are in use. These Omega transducers have a rated linearity of $\pm 0.50\%$ FS max, and rated hysteresis and repeatability of $\pm 0.25\%$ FS. The diaphragm strain is converted to an analog output voltage proportional to the applied differential pressure. The Validyne transducers are more rugged, versatile and expensive than the Omega transducers. The pressure signals recorded using the Validyne and Omega transducers are analog low-pass filtered at 10 Hz and 8 Hz, respectively. Because of this lowpass filtering, it is not necessary to correct the data for potential distortion of the high frequency signals when the data is sampled at 30 or 40 Hz. The use of an analog lowpass filter eliminates the high frequencies present in the pressure waves. It also helps reject noise.

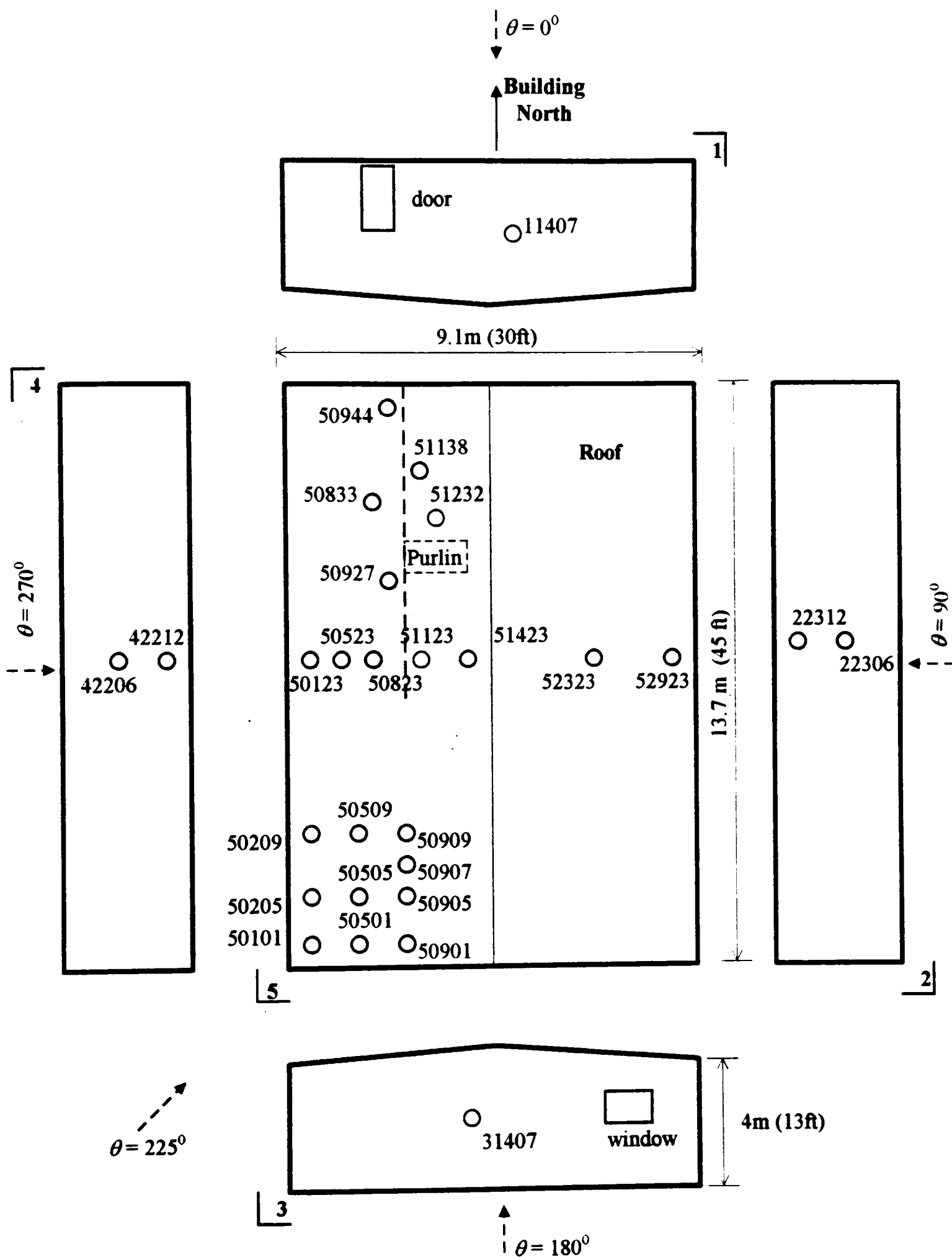


Figure 3.3. Location of pressure taps on the Texas Tech test building.

Table 3.1 Coordinates of Pressure Taps and Transducer Locations.

Tap #	Coordinates				Tap #	Coordinates			
	x		y			x		y	
	m	(ft)	m	(ft)		m	(ft)	m	(ft)
22306	7.03	(23.08)	1.96	(6.42)	50101	0.36	(1.17)	0.36	(1.17)
22312	7.03	(23.08)	3.61	(11.83)	50501	1.42	(4.67)	0.36	(1.17)
42206	6.76	(22.17)	1.96	(6.42)	50901	2.64	(8.67)	0.36	(1.17)
42212	6.76	(22.17)	3.61	(11.83)	50205	0.46	(1.50)	1.58	(5.17)
50123	0.30	(1.00)	7.06	(23.17)	50905	2.64	(8.67)	1.58	(5.17)
50523	1.42	(4.67)	7.06	(23.17)	50209	0.56	(1.83)	2.79	(9.17)
50823	2.31	(7.58)	7.06	(23.17)	50509	1.47	(4.83)	2.79	(9.17)
51423	4.29	(14.08)	7.06	(23.17)	50907	2.69	(8.83)	2.18	(7.17)
52323	6.88	(22.58)	7.06	(23.17)	50909	2.69	(8.83)	2.79	(9.17)
52923	8.91	(29.25)	7.06	(23.17)	51138	3.40	(11.17)	11.63	(38.17)
51123	3.40	(11.17)	7.06	(23.17)	50833	2.51	(8.25)	10.11	(33.17)
51232	3.73	(12.25)	9.80	(32.17)	50927	2.79	(9.17)	8.28	(27.17)
11407	4.32	(14.17)	2.06	(6.75)	50944	2.79	(9.17)	13.46	(44.17)
31407	4.32	(14.17)	2.06	(6.75)					

Note: See Fig. 3.3 and Section 3.2.3.1 for origin of coordinates and tap numbering scheme.

The transducers are mounted on boards, along with three-way electrical solenoid valves, on the inside surfaces of the test building close to the pressure taps. The building surface pressure at the pressure tap and the reference pressure are transmitted to the pressure transducers by a flexible plastic tubing system.

Ambient atmospheric pressure is used for the reference pressure. It is obtained from an underground box located 22.85 m (75 ft) to the west of the center of the building. This location is sufficiently away that the building has little effect on the static pressure at the reference pressure box. The ambient pressure is transmitted to the data acquisition building by means of a 203 mm (8 in.) diameter pipe. From there it is transmitted to each

transducer through a 4.76 mm (3/16 in.) internal diameter tubing. Zero drift of all transducers is automatically measured before and after each run by supplying reference pressure to both sides of the transducer.

The shortest duration gusts considered in wind loading assessments usually range from 1 to 3 seconds. This is partly due to the inability of commonly used field anemometers to respond to higher frequencies and partly due to the fact that many structural components may not themselves respond to the higher frequency excitations. However, it has been observed by Dalglish et al. (1979) that pressure fluctuations with frequencies greater than 1 Hz do occur and can be significant in determining localized loads. Indeed, it was noted in the discussions at the 1974 symposium on full-scale measurements of wind effects (1975) that "...an upper frequency limit of about 10 Hz is necessary for cladding design, although other problem areas place less stringent demands on the upper frequency limit." The peak pressures are associated with high frequency pressure fluctuations. Spectral analysis of full-scale pressure data seems to indicate that there is usually no significant energy in the pressure fluctuations above 5 Hz. Hence, a value of 5 Hz may be considered an appropriate upper limit of pressure fluctuations in moderate winds with mean speed of about 10 m/s.

The frequency response requirements of the pressure transmission and measuring system were investigated by Sandri (1992) and Letchford et al. (1992) and found to be more than adequate in the operating range of 5-10 Hz. These researchers have found that the roof and wall pressure measurement systems convey fluctuating pressures with frequencies up to 20 Hz with minimal distortion. Gains for both roof and wall tap setups were essentially unity up to 20 Hz. Phase lags were also small up to 20 Hz. The Omega transducers showed better frequency response characteristics than the Validyne transducers. Sandri (1992) has suggested that a sampling rate of 30 Hz for collection of pressure data would provide most of the information, including significant peaks, present in the fluctuating pressures. Even though the pressure signals are lowpass filtered at 8 Hz for Omega transducers and 10 Hz for Validyne transducers, this reduced frequency content does not prevent instantaneous peak pressure coefficients from being recorded

which have been found to be higher for records sampled at 40 Hz (M15 data) than those for records sampled at 10Hz (M04 data). For a sampling frequency of 30 to 40 Hz, the attenuation of peak and rms pressure coefficients were reported by Sandri (1992) to be in the range 0-8% and 0-3%, respectively, for mean wind speed of 20 mph. The corresponding attenuation were of the order 1-13% and 0-5%, respectively, for mean wind speed of 30 mph.

3.2.4 Meteorological Tower and Instrumentation

The meteorological instrumentation is mounted on a 48.8 m (160 ft) tall steel guyed tower. The tower is located 45.7 m (150 ft) to the west (280° azimuth) of the center of the test building. The tower is instrumented at 0.9, 2.4, 4, 10, 21.3 and 48.8 m (3, 8, 13, 33, 70 and 160 ft) levels with anemometers to measure wind speed/velocity. Temperature, barometric pressure and relative humidity sensors are mounted at the 4 m level with an additional temperature sensor at the tower top. In order to minimize tower interference of wind measurements, all the anemometers with the exception of the one at the 48.8 m level are mounted on 1.8 m (6 ft) booms oriented to the west-northwest (300°). However, tower interference is expected for winds from the azimuth range 70° - 160° .

Several different types of wind speed and direction anemometers provided by R.M. Young Company are used at the field site. Gill 3-cup anemometers (Model No. 12102) are in use to measure wind speed. The 3-cup anemometers have a rated maximum range of 50 m/s (112 mph) and a distance constant (63% recovery) of 2.7 m (8.9 ft). The 3-cup anemometer never overestimates the gust amplitude (see Figure 3.4). Gill microvanes (Model No. 12304) are used to measure wind direction. The microvane has a rated delay distance (50% recovery) of 1.1 m (3.6 ft) and a damped natural wavelength of 6.0 m (19.7 ft). The wind vane has a tendency to overshoot the actual wind direction when it is subjected to a sudden shift in direction. Figure 3.4 shows the dynamic response curve of the aluminum wind vane that overshoots the actual gust amplitude by as much as 30% at a gust wavelength (Uf) of about 7.5 m. The damping ratio of the vane helps to reduce the

overshoot. The wind vane used has a damping ratio in the range 0.42 which is high enough to damp out the second overshoot.

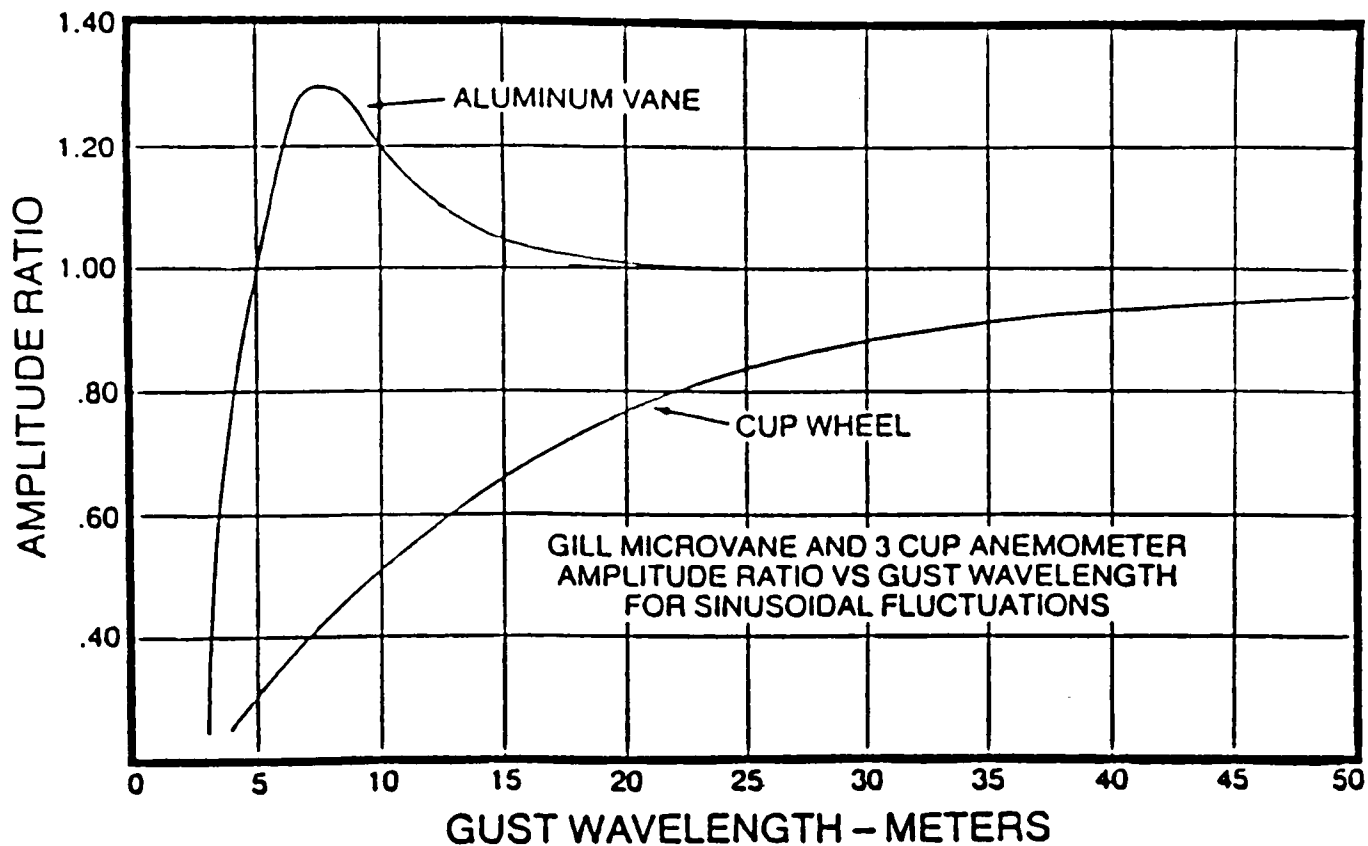


Figure 3.4. Response characteristics of 3-cup/microvane anemometer (R.M. Young Inc.: after Chok, 1988).

Three-component Gill UVW anemometers (Model No. 27005) are also used at the field site. The UVW anemometer measures directly three orthogonal vectors of the wind: along-wind component u , across-wind component v , and vertical component w . With the optional carbon fiber thermoplastic propellers (Model 08254), the UVW anemometer has a range of 0-40 m/s (110 mph) and a distance constant of 2.1 m (6.9 ft). The Gill microvane/3-cup and UVW anemometers have a threshold of 0.4 m/s (0.9 mph). All these anemometers produce an analog d.c voltage proportional to the wind component at each sensor.

The anemometer placement on the tower for the data acquisition mode M15 was as follows: 3-cup anemometers were mounted at the 0.9, 4.0, 21.3 and 48.8 m levels; wind direction vanes were placed at the 4 and 48.8 m levels; and UVW anemometers at 2.4 m

and 10 m levels. An additional 3-cup and vane anemometer is installed atop a 4 m pole located midway between the tower and the building for redundancy. The 3-cup anemometers at all levels on the tower, with the exception of that at 0.9 m, were then upgraded to UVW anemometers in the data acquisition mode M28; this remained the case for the current mode M38.

3.2.4.1 Frequency Response of Anemometers. The standard 3-cup anemometers can resolve gusts down to about 1 s duration, i.e., frequencies up to about 1 Hz. The Gill UVW propeller anemometers may resolve turbulence components at frequencies up to about 2 Hz at 10 m/s. The limited frequency response characteristics of these field anemometers is attributed to mechanical filtering because of inertia due to their mass and size. The frequency response improves with increasing wind speed, and so the vertical alignment is not the best because the vertical propeller sees a component which is zero on an average. Response is improved by tilting the array so that all three propellers point 45° to the mean wind vector. These observations were made by Cook (1990). Tieleman and Tavoularis (1977) have made a comparative study of the measurement of the turbulent velocity components in the atmospheric surface layer using a TSI three-dimensional split-film anemometer and a two-axis propeller-type Gill anemometer. The sampling rate used for data collection was 200 Hz for the split-film anemometer and 20 Hz for the Gill anemometer. These researchers have reported that the propeller-type Gill anemometer has the proper response capabilities up to 1 Hz. Due to the limited response characteristics of the Gill anemometers, the variances of the turbulence quantities were reported to be consistently lower (estimated about 11%) than those obtained from the TSI split-film anemometer. The mean measured by the Gill anemometer was higher by about 7%. The higher mean is attributed to the fact that the propeller anemometer accelerates faster as a result of sudden velocity increase and decelerates more slowly as a result of similar velocity decrease.

Higher frequencies up to about 50 Hz can be resolved using sonic anemometers. These measure the time delay in ultra sonic signals transmitted between two or three sets of detectors in an orthogonal array. The difference in time delay between both directions

along the same path is proportional to the wind speed. The average delay for both directions is a function of air temperature, so the sonic anemometer will also measure turbulent heat fluxes. The sonic anemometer is becoming more widely used for turbulence research because it offers high frequency response characteristics, while at the same time it has a sufficiently rugged construction for continuous operation. Sonic anemometers are typically an order of magnitude more expensive than cup or propeller anemometers and require more sophisticated data handling capabilities. The sampling rate can be as high as 100 Hz.

In light of the limited and varying frequency response characteristics of the cup-vane and UVW propeller anemometers used in the field, a limited number of 15-minute data records were collected using a sonic anemometer. The data runs taken using the sonic anemometer were approximately synchronized with the data acquisition mode M38. Thus, wind velocities on the tower with UVW anemometers and pressure coefficient data for pressure taps along the shorter center line of the building were also simultaneously measured for an angle of attack close to 270° . The instrument used was an ATI two-axis "K" probe sonic wind system anemometer (model SWS 503/2KZ, see Operator's Manual) manufactured by Applied Technologies Inc. The sonic anemometer was mounted vertically on top of a 4 m (roof level) high movable steel pole placed 3 m southwest of the tower. The instrument was oriented using a transit theodolite so that the array north axis (U axis) was along the true north. Hence the wind direction measurements are the azimuth values. The important specifications of the instrument relevant to wind velocity measurement are given in Table 3.2.

The wind system consists of a probe array, whose ultrasonic transducers are separated by 150 mm. The transducers comprised of piezoelectric crystals, 9.5 mm (3/8 in.) in diameter and 22.2 mm (7/8 in.) long, encased in aluminum housing and mounted at the end of each array arm. The system detects wind velocity components along mutually orthogonal acoustic paths and also computes the sonic virtual temperature corrected for velocity contamination. The transducers produce a sonic burst of about 200 KHz when subjected to a single high voltage pulse. The sonic anemometer measures the time of

flight of an ultrasonic pulse by counting a 12 MHz clock. The counters are started by a transmitter excitation pulse and stopped by a detected receiving pulse, which is controlled by a microprocessor. These counts are output as RS-232C compatible for direct interfacing to an external computer. These counts are mathematically manipulated as described in the manual to get meaningful wind speed and direction.

Table 3.2 Operating specifications of sonic anemometer (SWS 503/2KZ).

Characteristic	Magnitude
Path length of Kaimal (K) probe	150 mm
Horizontal Measurement Range	± 20 m/s
Accuracy:	
Wind speed	$\pm 1\%$ or ± 0.05 m/s
Wind direction	± 0.1 degree
Resolution:	
Wind speed	± 0.01 m/s
Wind direction	± 0.1 degree
Output:	
Data rate	up to 100 Hz
Digital	serial RS-232 compatible

The control box of the instrument was connected to the RS-232 serial port of a 80386-based laptop computer in the field. The instrument was calibrated inside the test building using a QuickBASIC calibration program before it was mounted on the pole in the field. The probe array is placed in a zero-air chamber (with no air movement) supplied with the instrument for calibration. A measurement of the ambient air temperature to an accuracy of $\pm 1^\circ$ C is input into the calibration program. The calibration program records counts for 10 minutes from which four calibration constants: U axis distance U_d , U axis velocity offset U_{off} , V axis distance V_d and V axis velocity offset V_{off} is known. These constants are fed into the interface program used for data acquisition. A QuickBASIC interface program was used to acquire the data and perform the necessary mathematical manipulations to get the wind speed in m/s and the direction in degrees. The analysis and results of the data collected using the sonic anemometer are presented in Chapter 5.

3.2.5 Terrain and Site Characteristics

The city of Lubbock is situated on the High Plains of Texas at an elevation of 1000 m (3300 ft) above sea level. The flat open plains extend for at least 100 kilometers in all directions. Most of the land is used for agriculture, the principal crops being cotton, sorghum and wheat. The flat terrain of the countryside minimizes possible changes in wind characteristics caused by terrain.

The terrain surrounding the field site is flat and open. Photographs of the surrounding terrain viewed in several directions and the land use map are given by Levitan and Mehta (1992b). The land to the north is open fields, with widely scattered small trees, extending several kilometers. Cotton fields lie immediately to the west and southwest, with suburban areas of one- and two-story houses beyond about a kilometer away. A small, shallow playa lake is located about 240 m (800 ft) south-southwest of the test building. To the south are residential areas about 1.5 km away and a few small research structures about 100 m south-southwest from the facility. To the northeast, low-rise residential areas begin about 800 m away. The TTU Health Sciences Center Building, approximately 30 m (100 ft) tall and 245 m (800 ft) long, located about 457 m (1500 ft) east-southeast, is the most significant feature of the local terrain. The main university campus is about 1.6 km away in the same direction. The closest structure to the facility is a 4.57 m (15 ft) tall dome-shaped observatory, which is about 30.5 m (100 ft) from the building in the same direction. A 13m (43 ft) tall power plant is located roughly 427 m (1400 ft) to the south-southeast. Winds from the azimuth range of 70-160 degrees are likely to be affected by these features and are not used for research.

3.2.6 Wind Climate

The location of the field facility is well suited for wind experiments since the terrain is flat open and strong winds frequent this region throughout the year. For example, the National Weather Service at Lubbock has recorded wind speeds greater than 8.95 m/s (20 mph) for 864 hours in 1981. Wind speeds higher than 20 mph are considered to have reasonable effects on structures.

The passage of weather fronts from the north and northwest in late fall and spring bring sustained wind of 9-16 m/s (20-35 mph). Prevailing winds during the summer months are from the south to southwest at speeds of 4.5-9.0 m/s (10-20 mph). Thunderstorms, common in late spring and summer, often bring strong winds of short duration. These thunderstorms can spawn tornadoes. Lubbock is located on the southwestern edge of the region known as "Tornado Alley."

3.2.7 Data Acquisition System

The instrumentation is hooked up, by appropriate cables, to the data acquisition system which is housed in a fixed small concrete block building centered inside the test building. The data is acquired through a dedicated personal computer (PC) with sufficient RAM and hard drive. A 20 MHz 80386 PC was in use for mode M15. The system was since then enhanced to a 33 MHz 80486 PC and currently to a 60 MHz Pentium processor PC. The incoming signals from the instruments are captured by a MetraByte DAS-8 analog-to-digital (A/D) conversion board installed in the computer. The DAS-8 is an 8 channel, medium speed 12 bit A/D board capable of recording analog input voltages in the range $\pm 5V$. Three compatible CIO-MUX32 multiplexor boards are used to expand input capacity to 96 channels.

LabTech Notebook (DOS version) software from Laboratory Technologies Corporation was used to drive the A/D board. A custom shell written in Microsoft QuickBASIC provides a simple interface for users working at the WERFL. The Notebook software has recently been upgraded to the Windows version. The software allows for different data acquisition modes to be created. Within the mode, it is possible to specify which instruments are to be sampled and at what frequency. The incoming data is written directly to the hard drive in binary integer form during the data acquisition run. With this system, sustained sampling rates up to 2000 Hz (total for all channels) can be achieved. The data acquisition system operates continuously, monitoring the wind speed and a data run is triggered automatically when the one-minute mean speed at the building roof height exceeds a preset threshold value (usually 20 or 25 mph). A typical 15 minute

data run generates about 5 MB of data in binary integer form. The data files are copied to an external 600 MB erasable optical cartridge drive after each run. The optical disk provides a reliable and convenient medium for transporting, processing and archiving such enormous amounts of data at the Wind Engineering Research Center (WERC).

3.2.7.1 Data record numbering scheme. Each data record is designated using a unique numbering scheme of the form MxxNyyy: xx is a pair of digits representing the data acquisition mode number (04, 15, 28, etc.) and yyy is a set of 3 digits representing the record number (006, 086, 545, etc.). For example, M15N086 designates a data record collected in mode M15 with record number 086.

3.2.7.2 Data analysis and validation system. The single most important task of researchers at the WERC is to ensure the data made available for research from the WERFL be of unquestionable quality. A systematic quality assurance program is implemented toward this end. The performance of all the instrumentation and data acquisition system at the WERFL are monitored on a daily basis in a systematic manner. Regular calibration and maintenance of all instrumentation is carried out. Timely analysis and validation of the acquired data also point to problems with the instrumentation and data acquisition system. Once the data is imported to the office computer, a processor program converts the raw data into engineering units. The summary statistics and time-history plots are printed for each run. Based on these, the data is validated by researchers through three stages. The validated data is then made available for research.

3.2.7.3 Stationarity check. One of the most important statistics generated by the processor program is the stationarity check of wind speed and direction data. Each 15-minute time history is divided into 18 equal time intervals and the mean and variance for each interval are computed. The sequences of interval means and variances are then tested for trends using both the run test and the reverse arrangements test as described by Bendat and Piersol (1986). These tests are performed at 0.05 level of significance. If any of the four tests indicate a trend, then the time history is labeled non-stationary. Mostly records with stationary wind speed and direction at roof height were used in this research.

3.3 Description of Field Data Used

This research is based on simultaneous measurements of wind velocity and pressure-coefficient time histories obtained at the WERFL. The wind velocity data used were obtained on the meteorological tower at the building roof height (4 m). Most of the data used in this research were collected in the data acquisition mode M15. Some data collected in the later mode M28 and current mode M38 were also used. The sonic anemometer data sets were synchronized with mode M38.

3.3.1 Data Sampling Rate

All the records used were of 15-minute duration. The pressure data were sampled at 40 Hz in mode M15, whereas they were sampled at 30 Hz in modes M28 and M38. These were appropriately decimated to 10 Hz for analysis. The velocity data were sampled at 10 Hz in all the three modes. The sonic anemometer data were sampled at 10 Hz or 20 Hz.

3.3.2 Data for Area-averaged Wind Loads on a Roof Purlin.

An experiment aimed at studying area-averaged effects of wind pressures on a roof purlin was conducted at the WERFL. The details of the experiment and results have been reported by Smith et al. (1994). The purlin is simply supported spanning 7.62 m. Pressures were measured at six pressure taps in the tributary area of a roof purlin on the test building (see Figure 5.26) along with wind velocities for different angles of attack. The data were collected in mode M15. The wind velocity and pressure data from this experiment were used in this research to identify transfer functions for area-averaged pressures on the purlin. The analysis and results of this data are presented in Chapter 5.

3.4 Wind Tunnel Data from CSU

The wind-tunnel study of the test building was conducted in the Meteorological Wind Tunnel (MWT) at Colorado State University (CSU) using model scales of 1:50 and 1:100. The low level of the building requires simulation of the atmospheric surface layer (ASL)

which is the lowest portion of the atmospheric boundary layer exhibiting some distinctly different flow characteristics from the upper layers. A detailed description of the MWT, its instrumentation, procedure for modeling the ASL properties of the TTU field site and comparative results with full-scale data are presented in detail by Cochran (1992).

The MWT at CSU has a cross-sectional test area of 3.34 m^2 (36 ft^2) and a long upstream fetch of 29.3 m (96.1 ft). The flow velocity can be varied from 0.6 m/s (2 ft/s) to 38 m/s (124.6 ft/s) in the free stream of a clear tunnel. A variety of flow modification devices such as spires, two-dimensional trips, angled vanes and floor mounted chains are used to achieve the desired profile and flow characteristics. A turbulent flow referred to as the RII flow simulates the environment at the TTU site. A cross-film anemometer (TSI probe type 1243-20) was used in the wind tunnel to measure wind velocity. A Honeywell Microswitch pressure transducer (160PC) was used to measure the fluctuating pressures on the building surface.

Three data sets of simultaneously acquired longitudinal wind velocity and pressure data for the roof pressure taps 50501 were obtained from CSU. These data were acquired on a 1:50 geometric scale model of the TTU test building for quartering wind (angle of attack 225°). Each data set contained 32767 data points sampled at 400 Hz. The longitudinal velocity measurements were made at roof height of the model at a distance of 1067 mm (42 in) upstream of the model. These data sets were used to identify transfer functions from wind-tunnel data for comparison with those obtained for the corresponding full-scale data. The analysis and results are presented in Chapter 6.

3.5 Comparison of Velocity Spectra from Different Anemometers

3.5.1 General

First, some information is presented on the frequency distribution of the field measured velocity data. Table 3.3 shows a comparison of the summary statistics of velocity data from the sonic data for sampling rates (f_s) of 20 Hz and 10 Hz for three field records. The data were sampled at 20 Hz. The records with sampling rates of 10 Hz

were obtained by decimating the ones sampled at 20 Hz by simply removing every alternate data point. It is seen from Table 3.3 that the mean and rms values of the records are almost exactly the same for both sampling rates. The only noticeable difference seen is in the peak velocities for some cases. It may thus be concluded from Table 3.3 that there is almost no energy content in the velocity spectrum beyond 5 Hz.

Table 3.3 Comparison of sonic anemometer velocity data for two sampling rates.

Record	Statistic [m/s]	<i>u</i> component		<i>v</i> component	
		$f_s=20$ Hz	$f_s=10$ Hz	$f_s=20$ Hz	$f_s=10$ Hz
SA071	mean	9.504	9.498	-0.177	-0.173
	rms	2.274	2.267	2.014	2.004
	max.	17.060	16.690	9.210	6.900
	min.	3.040	3.120	-11.120	-11.120
SA074	mean	10.066	10.061	-0.223	-0.226
	rms	2.160	2.161	1.810	1.812
	max.	18.170	18.170	7.000	7.000
	min.	3.190	3.280	-9.790	-8.610
SA075	mean	8.649	8.658	-0.133	-0.135
	rms	2.003	2.009	2.274	2.271
	max.	17.590	16.660	8.850	8.840
	min.	2.620	2.620	-13.38	-13.38

f_s is the sampling rate.

Table 3.4 shows the frequency distribution of the field velocity data sampled at 10 Hz using 3-cup and sonic anemometers. Comparison of the 3-cup and sonic distributions show that the 3-cup velocity data are deficient in energy above 0.5 Hz. It may, however, be concluded from Table 3.4 that more than 90 percent (for *u* component) and 85 percent (for *v* component) of the energy in the field velocity spectra is contained in frequencies below 1 Hz. It may be noted that there is more consistency in the frequency content of the longitudinal (*u*) spectrum, from one record to another, than for the lateral (*v*)

spectrum. Also, there is more of relatively higher frequency content in the lateral spectrum than in the longitudinal spectrum.

Table 3.4 Frequency distribution of field measured wind velocity.

Record / Anemo- meter	measured variance at $f_s=10$ Hz [m/s] ²	variance, as % of measured, from 0 Hz to					
		0.05 Hz	0.1 Hz	0.5 Hz	1 Hz	2 Hz	4 Hz
<u>3-Cup:</u>							
C539 - <i>u</i>	2.85	67.3	79.5	96.8	99.1	99.8	99.98
C544 - <i>u</i>	2.88	60.9	75.7	96.3	99.0	99.8	99.98
C539 - <i>v</i>	2.73	62.3	69.0	85.1	92.3	98.7	99.8
C544 - <i>v</i>	1.93	36.3	48.7	75.6	86.8	97.5	99.7
<u>Sonic:</u>							
CS070 - <i>u</i>	5.15	60.6	71.4	86.9	91.3	95.0	98.6
CS077 - <i>u</i>	4.56	59.3	71.3	88.1	92.9	96.3	99.0
CS070 - <i>v</i>	4.99	58.1	67.8	84.4	89.5	94.1	98.5
CS077 - <i>v</i>	3.88	45.8	56.6	77.7	85.6	92.5	98.1

Note: Area under spectrum from 0 to 5 Hz is the measured variance.

f_s is the sampling rate. For summary statistics of the above data, see Table 5.1.

A comparison is now made of the longitudinal (*u*) and lateral (*v*) velocity spectra at roof height ($z = 4$ m) obtained from data collected in the field at the WERFL using different types of anemometers and in the Meteorological Wind Tunnel (MWT) at CSU. The objective is to obtain a qualitative idea of the frequency characteristics of the different anemometers used in the measurement of wind velocity. These spectra are also compared with the universal velocity spectral model (Tieleman, 1995a) of the following generalized form.

$$\frac{f S_a(f)}{U_*^2} = \frac{A k^\gamma}{(C + B k^\alpha)^\beta}, \quad (3.2)$$

where,

$$k = fz/U,$$

f is frequency, z the height, U the mean longitudinal velocity at z ,

U_* the friction velocity,

$S_a(f)$ the power spectral density of the velocity component a ($= u, v, \text{ or } w$),

A, B and C are coefficients that influence the position of the spectrum function, and

α, β and γ are exponents that influence the shape of the spectrum function.

The terrain surrounding the WERFL can be classified as flat, smooth and uniform (FSU) with scattered roughness elements (slight perturbation). The universal spectral models recommended by Tieleman (1995a) for neutral air in the atmospheric surface layer over a FSU terrain with slight perturbation are defined for u and v velocity components, respectively, in equations 3.3 and 3.4. These equations make use values for the ratios of S_a/U_* of 2.5 and 2.0 for $a = u, v$, respectively, which are widely accepted for equilibrium turbulence in the surface layer (Tieleman, 1995a).

$$\frac{f S_u(f)}{S_u^2} = \frac{40.42 (fz/U)}{[1 + 60.62 (fz/U)]^{5/3}} \quad (3.3)$$

$$\frac{f S_v(f)}{S_v^2} = \frac{13.44 (fz/U)}{[1 + 20.16 (fz/U)]^{5/3}} \quad (3.4)$$

where,

f is frequency, z the height, U the mean longitudinal velocity at z ,

$S_u(f)$ and $S_v(f)$ are spectra of longitudinal and lateral velocity; and

S_u^2 and S_v^2 are variances of longitudinal and lateral velocity.

Longitudinal and lateral velocity spectra at roof height ($z = 4$ m) are compared for full-scale data obtained from sonic, UVW and 3-cup/vane anemometers; and wind tunnel data obtained using a cross-film anemometer. The following cases are presented.

- a. Field data using sonic anemometer,
- b. Field data using UVW anemometer,

- c. Field data using 3-Cup/Vane anemometer,
- d. Wind Tunnel data for 1:100 scale RII flow using cross-film anemometer, and
- e. Universal velocity spectra for FSU perturbed terrain defined in Eq. 3.3 and Eq. 3.4.

The field records used in the comparison of spectra from the Sonic, UVW and 3-cup/vane anemometers were not measured simultaneously. The spectra presented are the average spectra of six representative stationary 15-minute records from each anemometer. The spectra were computed for each record individually and ensemble averaged. The field records were sampled at 10 Hz. The wind tunnel spectra used are the same as that presented in the paper by Thomas et al. (1993). The wind tunnel data were collected on a 1:100 model scale (at $z = 40$ mm) in the RII flow. In order to get the large frequency range of velocity fluctuations in the wind tunnel, two sets of time series were collected with a cross-film anemometer. The high-frequency or fast time series were collected at 1000 Hz and filtered at 500 Hz and the low-frequency or slow time series were collected at 20 Hz and filtered at 10 Hz. Both time series contained 25000 points. The relevant summary statistics of the data used are given in Table 3.3 below.

Table 3.5 Summary of data used in spectral comparison at roof height ($z = 4$ m).

Data from	U m/s	u_rms m/s	v_rms m/s	z/U 1/Hz
Field Sonic	9.74	2.29	2.10	0.4107
Field UVW	9.38	1.88	1.63	0.4264
Field cup/vane	9.34	1.79	1.53	0.4282
Wind Tunnel	7.21 (for u)	1.97		0.5548 (FS)
1:100 cross film	7.12 (for v)		1.56	0.5618 (FS)

Note: The statistics of the field data are the average of 6 records.

3.5.2 Comparison of Longitudinal Velocity Spectra

The comparative spectra for longitudinal velocity are shown in non-dimensional form in Figure 3.6. Some of the important observations that can be made from the comparison are discussed below.

The wind tunnel and the universal spectral model compare well in the entire frequency range. However, all the field spectra do show deviations from these in the low and high frequency ranges. This means that the wind tunnel simulates ideal flow conditions very well, but does show some deviations from actual field flow conditions in terms of its energy content. In comparison to the field spectra from the sonic, UVW and 3-cup anemometers in the low frequency range, the wind tunnel spectra is slightly deficient for reduced frequency fz/U less than 0.0025 ($f \approx 0.005 \text{ Hz}$) and the universal spectral model is deficient for fz/U less than 0.006 ($f \approx 0.014 \text{ Hz}$). This may be due to deviations in field conditions from a truly neutral atmosphere (only mechanical turbulence) which is the condition assumed in the spectral model and actually developed in the wind tunnel flow. Except for the low frequencies mentioned above, all the spectra in Figure 3.6 compare reasonably well in the reduced frequency range 0.006 to 0.23.

In light of the superior technology (ultrasonic with no moving parts) and good frequency response characteristics (up to about 50 Hz) of the sonic anemometer, the sonic spectra may be considered to provide a more accurate description of actual field conditions than the 3-cup and UVW anemometers. The sonic and the wind tunnel spectra compare well even in the higher frequency range up to fz/U equal to about 1.0 ($f \approx 2.5 \text{ Hz}$) after which the wind tunnel is slightly deficient.

The field spectra from the UVW and 3-cup anemometers show very similar characteristics in the higher frequency range, although the UVW anemometer shows slightly higher energy. Both these spectra are deficient in comparison to the sonic and wind tunnel spectra for fz/U greater than 0.22, which corresponds to a frequency of about 0.5 Hz. This deficiency is due to insufficient frequency response of the 3-cup and UVW anemometers due to mechanical and electrical filtering. The energy of the 3-cup and UVW anemometers is about 1/14th that of the sonic spectra at fz/U equal to 1 (i.e., $f \approx 2.5 \text{ Hz}$) and about 1/32nd that of the sonic spectra at fz/U equal to 2.0 (i.e., $f \approx 5 \text{ Hz}$).

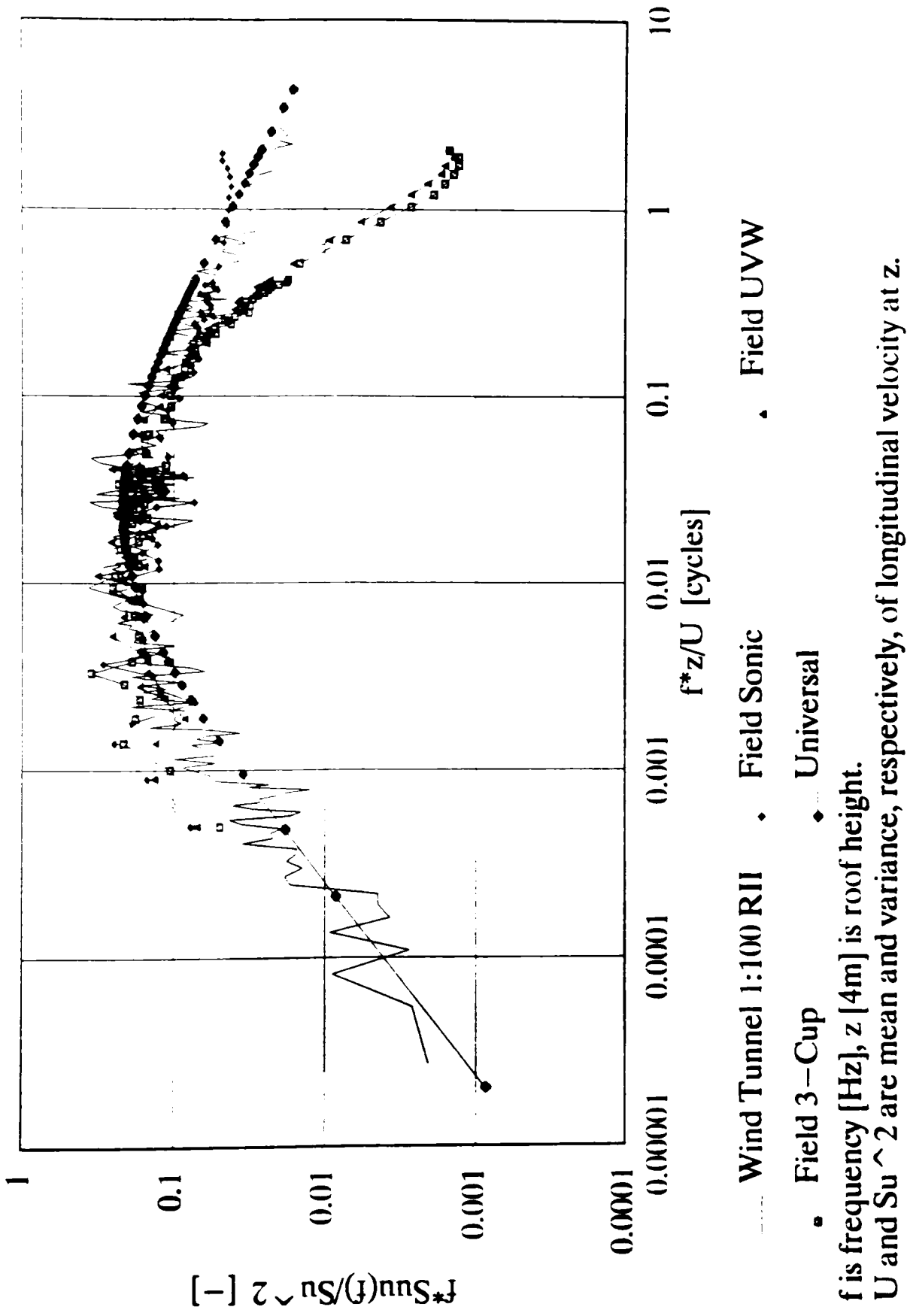


Figure 3.5. Comparison of longitudinal velocity spectra from different anemometers.

3.5.3 Comparison of Lateral Velocity Spectra

The comparative spectra for lateral velocity are shown in non-dimensional form in Figure 3.7. Some of the important observations that can be made from the comparison are discussed here.

The wind tunnel and the universal spectral model again compare well in the entire frequency range. The wind tunnel and universal spectral model are deficient in comparison with all the field spectra for fz/U less than 0.003 ($f \approx 0.007 \text{ Hz}$) and 0.015, respectively. The low-frequency energy content of the flow in the wind tunnel may be increased by use of random motion of vertical oscillating blades (Cochran, 1992; Thomas et al., 1993). However, it appears that the high energy at low frequencies seen in the field due to lateral turbulence is not adequately modeled in the wind tunnel. This may be the reason for deficiencies in the roof corner peak pressures in the wind tunnel.

All the field spectra match reasonably well up to fz/U equal to 0.2. Although the wind tunnel spectrum does match reasonably with the sonic, it shows slightly higher energy for fz/U range 0.04 to 0.6. The UVW spectrum falls off from the sonic spectra beyond fz/U of 0.2 ($f \approx 0.48 \text{ Hz}$) as was the case for the longitudinal spectrum. This deficiency can be again attributed to insufficient frequency response of the UVW anemometer due to mechanical and electrical filtering. The energy of the UVW lateral spectrum is about 1/50th of the sonic spectra at fz/U of 2.0 ($f \approx 5 \text{ Hz}$).

Unlike the longitudinal field spectrum, the 3-cup/vane lateral spectrum shows higher energy than the sonic spectrum in the fz/U range 0.05 to 0.8 and then falls off. A hump is noticed on the 3-cup lateral spectrum at fz/U around 0.5 in Figure 3.7. This corresponds to a frequency of approximately 1.2 Hz for a mean velocity U of 9.34 m/s. It can be seen from Figure 3.4 that the aluminum wind vane overshoots the actual gust amplitude by as much as 30% at a gust wavelength (U/f) of about 7.5 m. This wavelength corresponds to a frequency of $(9.34/7.5) \approx 1.245 \text{ Hz}$ at $U = 9.34 \text{ m/s}$, which is approximately the frequency at which the hump is seen on the lateral spectrum in Figure 3.7. This suggests that the wind vane has a natural frequency around 1.2 to 1.25 Hz at which a resonance effect causes high amplitude motions of the vane. This may be responsible for the peak

amplitude ratio at gust wavelength of 7.5 m in Figure 3.4 and the hump in the lateral spectrum at frequency of about 1.2 Hz. The higher energy noted above in the 3-cup lateral spectrum may thus be attributed to the tendency of the vane to overshoot the actual wind direction when it is subjected to a sudden shift in direction for gust wavelengths between 5 m ($f \approx 1.87 \text{ Hz}$) and 20 m as seen in Figure 3.4. This characteristic of the vane thus has a dominant effect over the insufficient frequency response of the anemometer that was seen for the longitudinal spectrum. The 3-cup spectrum falls off below the sonic spectrum at fz/U of 0.8 ($f \approx 1.87 \text{ Hz}$). The energy of the 3-cup lateral spectrum is about one-fourth that of the sonic spectrum at fz/U of 2.0 ($f \approx 5 \text{ Hz}$), which is much higher than that seen in the UVW spectrum.

3.5.4 Summary

The important observations derived from the study in Section 3.5 are as follows.

1. The 3-cup field anemometer was found to have sufficient response only up to about 0.5 Hz, but it has an improved response up to 1.25 Hz for the lateral component due to the overshoot phenomenon of the vane discussed in Section 3.5.3.
2. The analysis of the field velocity data from the sonic anemometer showed that there are practically no frequencies beyond 5 Hz in the upstream velocity field. It was also observed that more than 90 percent (for u component) and 85 percent (for v component) of the energy in the field velocity data is contained in frequencies below 1 Hz.
3. The longitudinal velocity spectrum was found to be much more consistent in frequency content from record to record than the lateral spectrum. This is indicative that local random changes in wind direction is instrumental in introducing variability in the velocity data. Also, there is more of relatively higher frequency content in the lateral spectrum than in the longitudinal spectrum. Hence, changes in wind direction play an important role in producing the higher frequencies in the upstream turbulence.
4. The wind-tunnel velocity spectra were found to be deficient, in comparison with the field spectra, in the low frequency end and especially so for the lateral component.

CHAPTER 4

PROPOSED MODEL AND METHODOLOGY

4.1 Introduction

A general linear-quadratic (bilinear) frequency domain model using the concept of multiple transfer functions is proposed to relate the longitudinal (u) and lateral (v) components of the upstream wind velocity to point or area-averaged wind pressures on building surfaces. Four transfer functions are defined: one each associated with u , v , u^2 and v^2 terms of wind velocity. The model is physically meaningful in that the measured output spectrum can be decomposed into components representing the linear operations, the quadratic or square-law operations, and the remaining uncorrelated residual/noise effects. The proposed model and the methodology used for optimal identification of the transfer functions are described in this chapter. The proposed model and methodology was chosen, by trial, from the different non-linear models for non-parametric system identification problems described in the book by Bendat (1990) and in the paper by Bendat and Piersol (1986). Some preliminary work on the model was presented in Thomas et al. (1995). The frequency domain formulation makes the model more physically significant and easy to compute and interpret than the associated time domain formulation.

4.2 The Proposed Model

Bendat (1990) has described procedures for identifying, in the frequency domain, optimum non-linear system properties from simultaneous measurement of the input and output data properties. These procedures enable formulation of the problem of predicting wind pressures from wind velocity data as a non-parametric system identification problem in the frequency domain. The time histories of velocity components u and v at *eave or roof height* (4 m) form the system input and the pressure-coefficient time history $C_p(t)$ forms the output. The proposed model is a two-input/single-output model. The schematic diagram of the model in the frequency domain describing the linear and quadratic dependence of the output Y on the two inputs X_1 and X_2 is shown in Figure 4.1.

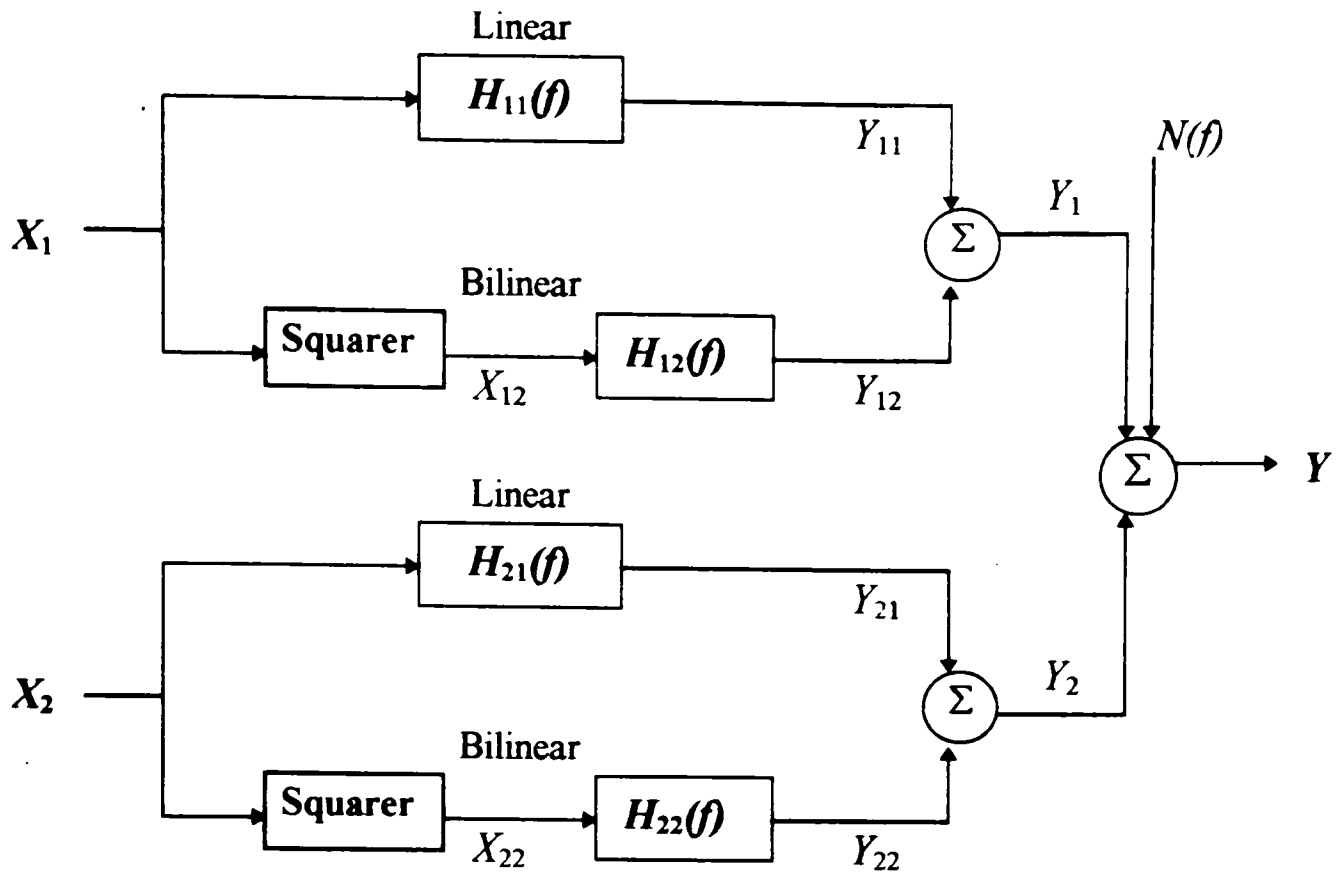


Figure 4.1. Schematic diagram of the proposed model.

4.2.1 Notation

The important notations used in the model are defined below.

t is time in seconds;

f is frequency in hertz;

U is mean longitudinal wind velocity at eave height (4 m);

$u(t)$ = time history of zero mean fluctuating longitudinal velocity component at 4 m;

$v(t)$ = time history of zero mean fluctuating lateral velocity component at 4 m;

$y(t)$ = time history of zero-mean fluctuating pressure coefficients $C_p(t)$;

$x_1(t) = u(t)/U$; $x_2(t) = v(t) \cdot U$;

$x_{12}(t) = x_1^2(t)$; $x_{22}(t) = x_2^2(t)$;

$Y = Y(f) =$ Fourier transform of $y(t)$;

$X_1 = X_{11}(f) =$ Fourier transform of $x_1(t)$;

$X_{12} = X_{12}(f) =$ Fourier transform of $x_{12}(t)$;

$X_2 = X_{21}(f) =$ Fourier transform of $x_2(t)$;

$X_{22} = X_{22}(f) =$ Fourier transform of $x_{22}(t)$;

$N(f)$ = Fourier transform of the residual or noise time history $n(t)$.

$H_{11}(f)$ = linear transfer function associated with $x_1(t)$ or u velocity component;

$H_{21}(f)$ = linear transfer function associated with $x_2(t)$ or v velocity component;

$H_{12}(f)$ = quadratic or bilinear transfer function associated with $x_1(t)$;

$H_{22}(f)$ = quadratic or bilinear transfer function associated with $x_2(t)$;

$S_{YY}(f) = \frac{1}{T} E[Y^*(f)Y(f)]$ = autospectral density function of the output Y ,

$S_{X_1X_1}(f) = \frac{1}{T} E[X_1^*(f)X_1(f)]$ = autospectral density function of the input X_1 ;

$S_{X_2X_2}(f) = \frac{1}{T} E[X_2^*(f)X_2(f)]$ = autospectral density function of the input X_2 ;

$S_{X_{12}X_{12}}(f) = \frac{1}{T} E[X_{12}^*(f)X_{12}(f)]$ = autospectral density function of X_{12} ;

$S_{X_{22}X_{22}}(f) = \frac{1}{T} E[X_{22}^*(f)X_{22}(f)]$ = autospectral density function of X_{22} ;

$S_{nn}(f)$ = autospectrum of the residual.

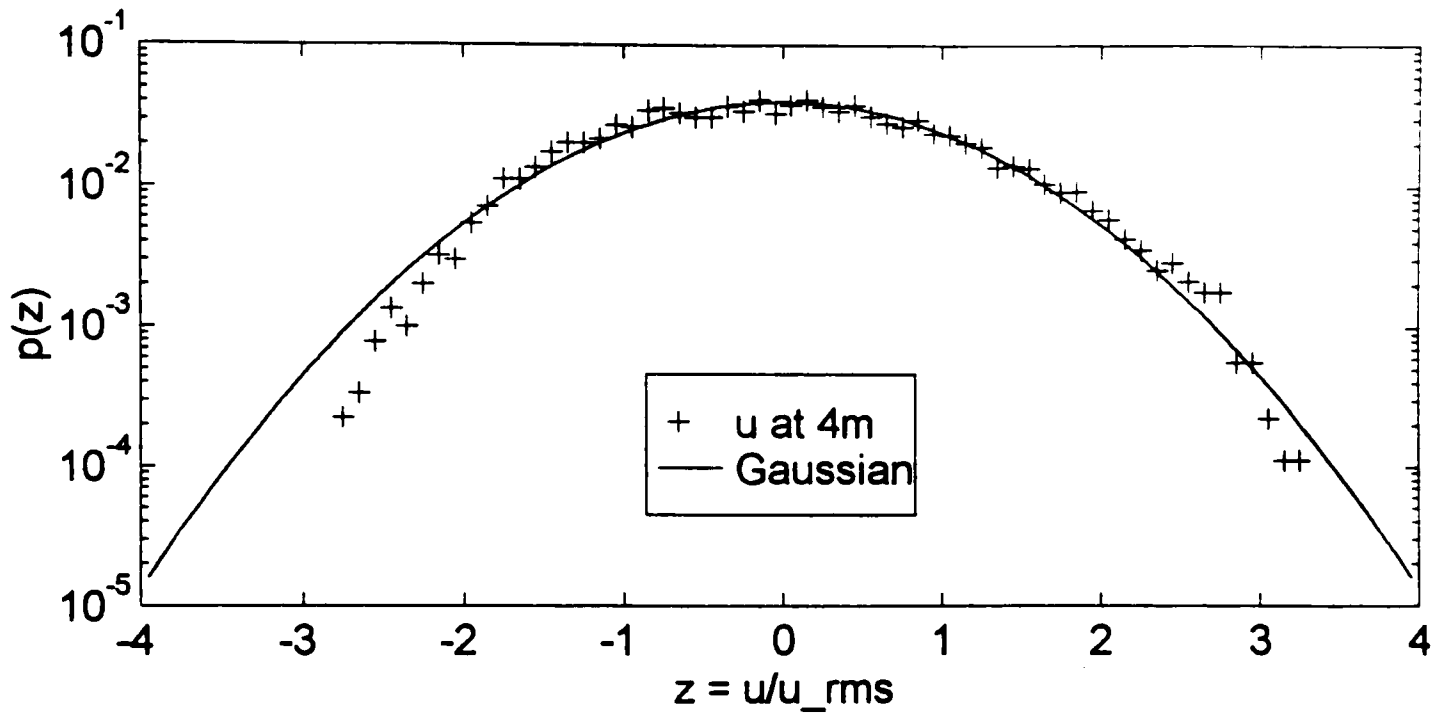
In the spectral expressions, Y^* , X_1^* , X_2^* , X_{12}^* , X_{22}^* are complex Fourier conjugates of Y , X_1 , X_2 , X_{12} and X_{22} , respectively, and T is the time length of sample records. In practice, $E[]$ denotes an expected value ensemble averaged over the quantities inside the braces.

4.2.2 Assumptions in the Model

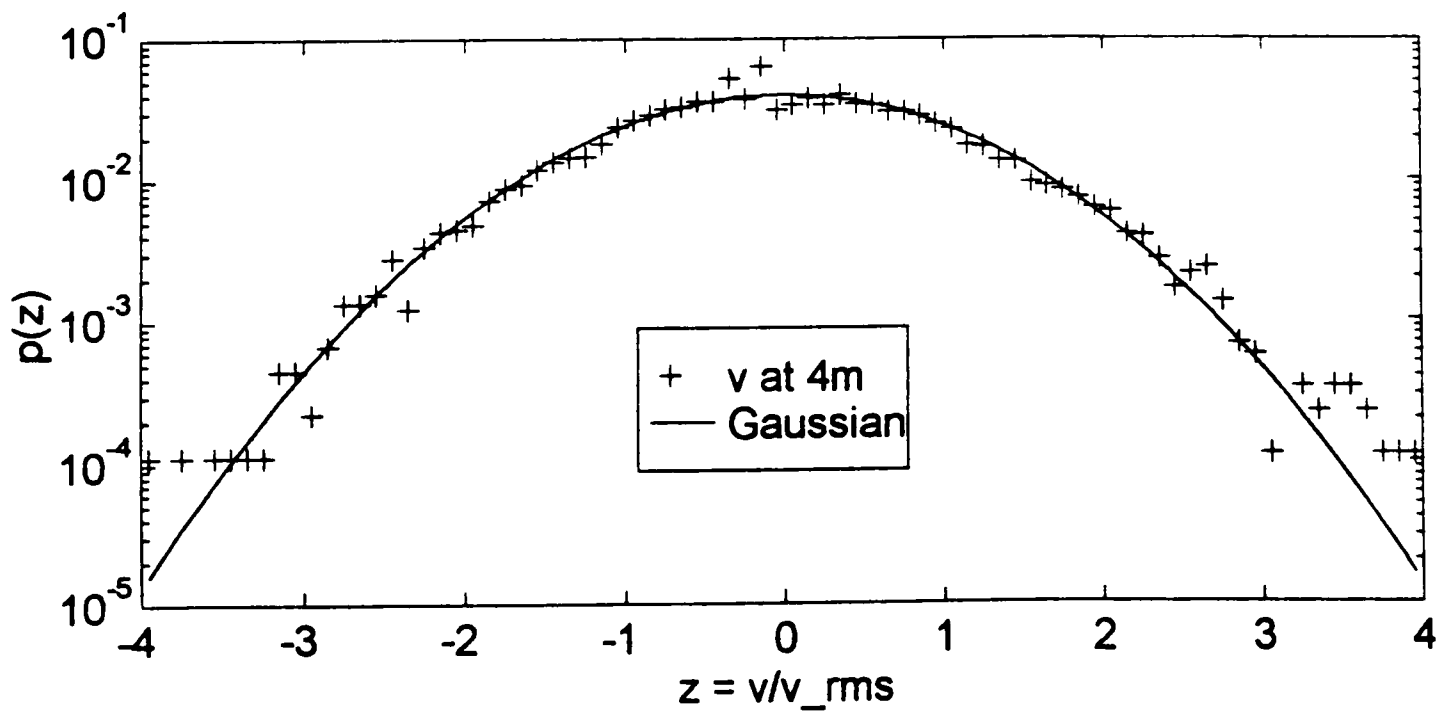
1. The input data are zero-mean Gaussian stationary random processes with arbitrary spectral properties.

This assumption is physically valid since the inputs are the fluctuating longitudinal ($u(t)$) and lateral velocity ($v(t)$) components with the mean removed. The data records used in this research were so chosen that the wind velocity time histories were stationary based on the routine stationarity check on the WERFL data discussed in Section 3.2.7.3. Further, the probability density functions of typical u and v velocity components measured

at the Texas Tech field site compare well with Gaussian distribution as evident from Figure 4.2.



(a) u component



(b) v component

Figure 4.2. Typical probability density functions for field wind velocity at 4 m.

In practical engineering situations, the input may not be an exact Gaussian fluctuation. There will usually be some deviations and this is expected in the case of wind velocity, which is the input in the present work. Even then, one may adopt the equations proposed in the model to get reasonable estimates of the transfer functions with only a little error if the assumptions are practically met to a reasonable degree.

2. The inputs are uncorrelated with each other.

Typical cross-correlation coefficient between u and v velocity components measured in the field were found to be in the range 0.06 to 0.20, which implies that they are very weakly correlated. This can be seen in the cross-correlation function between u and v velocity components for a typical field record shown in Figure 4.3.

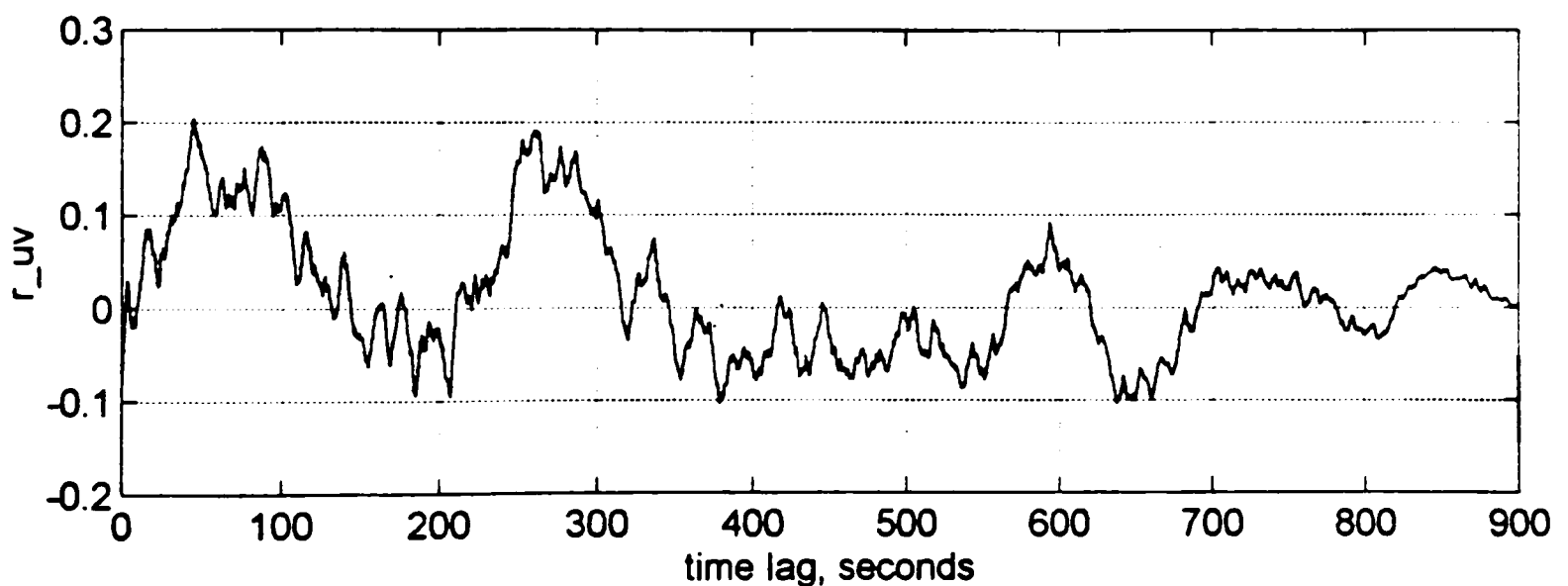


Figure 4.3. Typical cross-correlation function between u and v velocity components.

3. The model is based upon a single-point representation of the upstream wind velocity field.

This means that the upstream turbulence is considered to be homogeneous and completely represented in the model by the velocity recorded at the single point of measurement (i.e., the tower at the WERFL). At the WERFL, wind pressures have not yet been measured simultaneously with wind velocities at different points separated horizontally. Hence data for multi-point representation of the wind field is not available at

the present time. However, since the distance between the test building and the tower at the WERFL is 45.7 m (150 ft) and the average longitudinal integral scale at roof height is on the order of about 107 m (350 ft) (Levitan and Mehta, 1992a), it is reasonable to assume that the same gust hits the building and the single point representation is justifiable. Also, a multi-point representation will require a different and more complex model formulation.

Since perfect correlation is unlikely, it may be more precise to attempt to relate velocity fluctuations at one point to other points in the wind field. Holscher and Neimann (1992a, 1992b) and Holscher (1993) have proposed a linear multiple pressure admittance model, based on measurements on a cylinder in the wind tunnel, that relates the velocity fluctuations at various upstream positions to the pressure fluctuations at a point considered, taking the spatial velocity correlation into account. However, due to the non-availability of data and for simplicity of the model, a single point representation will only be used in this research based on the argument in the previous paragraph.

4. Any possible contribution to the pressures from the vertical (w) component of wind velocity has been omitted in the model.

The w component has been neglected in the present research for three reasons. First, most of the data used in this work were acquired in the data acquisition mode M15. In the M15 setup, the anemometer mounted on the tower at the roof level (4 m) was of the cup-vane type which cannot measure the vertical component of wind velocity. Second, the vertical turbulence can be considered negligibly small especially under neutrally stable atmospheric conditions. The vertical turbulence intensities (I_w) obtained at the WERFL from UVW anemometer measurements (Modes M28 and M38) at roof height (4 m) were found to be small (less than a third) compared to the longitudinal (I_u) and lateral (I_v) turbulence intensities. This can be seen in Table 4.1 where typical turbulence intensities at roof height (4 m) are shown for five random field records. Third, in the light of the above, the model is kept simple by neglecting the vertical component. However, if one wishes to consider the vertical component, it could be incorporated in the model. In such a case, two more transfer functions associated with the w component will have to be defined.

Table 4.1. Typical field turbulence intensities at 4 m level at WERFL.

Record	U, m/s	I_u	I_v	I_w
M28N362	8.7	0.185	0.173	0.047
M28N390	8.3	0.217	0.172	0.050
M28N392	8.4	0.227	0.251	0.053
M28N777	8.5	0.180	0.172	0.046
M38N072	10.6	0.211	0.168	0.049

5. The system is assumed to be a constant-parameter linear-quadratic system.

This means that the system properties are time-invariant and the relationship between velocity and pressure is non-linear to the second order. Also the proposed model is non-parametric. This means that there are no parameters defined for the system and no assumptions made regarding the form of the transfer functions. Since the transfer functions will be identified based on full-scale data, they will be reflective of reality and the mathematical principles used.

4.2.3 Mathematical Representation of the Model

The proposed formulation in Figure 4.1 is a two-input (X_1, X_2) / single-output (Y) model with parallel linear and non-linear (quadratic, in this case) systems. This is an extension of the single-input/single-output parallel linear and square-law system discussed in Section 2.4.3.4 to two uncorrelated inputs. The non-linear systems are modeled as finite-memory square-law systems which consist of a zero-memory square-law system followed by a constant parameter linear system. The output residual or noise quantity $n(t)$ represents all uncorrelated deviations in the output $y(t)$ that are not due to the passage through the linear systems and the finite memory square-law systems. The model of Figure 4.1 can be expressed mathematically in spectral form using equation 2.42 as follows.

$$S_{YY}(f) = S_{Y_1Y_1}(f) + S_{Y_2Y_2}(f) + S_{Y_1Y_2}(f) + S_{Y_2Y_1}(f) + S_{NN}(f)$$

$$\begin{aligned}
&= |H_{11}(f)|^2 S_{X_1 X_1}(f) + 2|H_{12}(f)|^2 \int_{-\infty}^{\infty} S_{X_1 X_1}(g) S_{X_1 X_1}(f-g) dg \\
&+ |H_{21}(f)|^2 S_{X_2 X_2}(f) + 2|H_{22}(f)|^2 \int_{-\infty}^{\infty} S_{X_2 X_2}(g) S_{X_2 X_2}(f-g) dg \\
&+ S_{nn}(f), \quad -\infty \leq f \leq \infty.
\end{aligned} \tag{4.2}$$

where,

$S_{Y_{11} Y_{11}}(f)$ and $S_{Y_{12} Y_{12}}(f)$ are contributions to the output from the linear and quadratic u terms, respectively, as shown in Figure 4.1; and

$S_{Y_{21} Y_{21}}(f)$ and $S_{Y_{22} Y_{22}}(f)$ are contributions to the output from the linear and quadratic v terms, respectively, as shown in Figure 4.1.

The equivalent of Eq. 4.2 using the practical linear analysis procedure (Eq. 2.47) discussed in Section 2.4.3.4 is given by

$$\begin{aligned}
S_{YY}(f) &= |H_{11}(f)|^2 S_{X_1 X_1}(f) + |H_{12}(f)|^2 S_{X_1^2 X_1^2}(f) \\
&+ |H_{21}(f)|^2 S_{X_2 X_2}(f) + |H_{22}(f)|^2 S_{X_2^2 X_2^2}(f) + S_{nn}(f) \\
&\quad -\infty \leq f \leq \infty.
\end{aligned} \tag{4.3}$$

The residual or noise spectrum $S_{nn}(f)$ may be due to any noise in the measuring system and/or any additional turbulence that is not explained by the proposed linear-quadratic model.

4.2.4 Identification of Optimal Transfer Functions

The four transfer functions indicated above are optimally identified by minimizing the output noise spectrum $S_{nn}(f)$ with respect to all possible choices of $H_{11}(f)$, $H_{12}(f)$, $H_{21}(f)$, and $H_{22}(f)$ as described in Section 2.4. This makes the method rational and significantly different from the identification method described in Section 2.2 for $\chi^2(f)$ appearing in the modified quasi-steady theory (Eq. 2.3).

The optimal linear transfer functions identified using Eq. 2.35 are given by

$$H_{11}(f) = \frac{S_{X_1Y}(f)}{S_{X_1X_1}(f)}; \quad H_{21}(f) = \frac{S_{X_2Y}(f)}{S_{X_2X_2}(f)}. \quad (4.4)$$

The optimal quadratic transfer functions identified using Eq. 2.36 are given by

$$H_{12}(f) = \frac{S_{X_1X_1Y}(f/2)}{2S_{X_1X_1}^2(f/2)}; \quad H_{22}(f) = \frac{S_{X_2X_2Y}(f/2)}{2S_{X_2X_2}^2(f/2)}. \quad (4.5)$$

The optimal quadratic transfer functions identified using the practical linear procedure discussed in Section 2.4.3.4 (Eq. 2.40) are given by

$$H_{12}(f) = \frac{S_{X_{12}Y}(f)}{S_{X_{12}X_{12}}(f)}; \quad H_{22}(f) = \frac{S_{X_{22}Y}(f)}{S_{X_{22}X_{22}}(f)}. \quad (4.6)$$

In equations 4.4, 4.5 and 4.6,

$$S_{X_1Y}(f) = \frac{1}{T}E[X_1^*(f)Y(f)] = \text{cross spectrum between } X_1 \text{ and } Y; \quad (4.6a)$$

$$S_{X_2Y}(f) = \frac{1}{T}E[X_2^*(f)Y(f)] = \text{cross spectrum between } X_2 \text{ and } Y; \quad (4.6b)$$

$$S_{X_{12}Y}(f) = \frac{1}{T}E[X_{12}^*(f)Y(f)] = \text{cross spectrum between } X_{12} \text{ and } Y; \quad (4.6c)$$

$$S_{X_{22}Y}(f) = \frac{1}{T}E[X_{22}^*(f)Y(f)] = \text{cross spectrum between } X_{22} \text{ and } Y; \text{ and} \quad (4.6d)$$

$S_{X_1X_1Y}(f)$, $S_{X_2X_2Y}(f)$ are special second-order cross-bispectral density functions defined as:

$$S_{X_1X_1Y}(f) = S_{X_1X_1Y}(f, f) = \frac{1}{T}E[X_1^*(f)X_1^*(f)Y(2f)]$$

$$S_{X_2X_2Y}(f) = S_{X_2X_2Y}(f, f) = \frac{1}{T} E[X_2^*(f)X_2^*(f)Y(2f)]. \quad (4.7)$$

The transfer functions in the present work are identified using equations 4.4 and 4.6. This alternative approach offers certain practical advantages in terms of the necessary digital computations and estimation errors as compared with the bispectrum formulation (Bendat and Piersol, 1982) in Eq. 4.5. Hence it has been adopted in this research.

4.2.5 Spectral Decomposition and Output Prediction

Once the four transfer functions are identified, the system properties are known. The spectrum of the output Y can be predicted or generated from the spectra of the inputs using Eq. 4.8, which is Eq. 4.2 or Eq. 4.3 without the noise term $S_{nn}(f)$. The spectrum S_{YY_P} so obtained will be henceforth referred to as the *predicted* or *generated* spectrum.

$$\begin{aligned} S_{YY_P}(f) &= |H_{11}(f)|^2 S_{X_1X_1}(f) + 2|H_{12}(f)|^2 \int_{-\infty}^{\infty} S_{X_1X_1}(g) S_{X_1X_1}(f-g) dg \\ &\quad + |H_{21}(f)|^2 S_{X_2X_2}(f) + 2|H_{22}(f)|^2 \int_{-\infty}^{\infty} S_{X_2X_2}(g) S_{X_2X_2}(f-g) dg \\ &= |H_{11}(f)|^2 S_{X_1X_1}(f) + |H_{12}(f)|^2 S_{X_1^2X_1^2}(f) \\ &\quad + |H_{21}(f)|^2 S_{X_2X_2}(f) + |H_{22}(f)|^2 S_{X_2^2X_2^2}(f) \end{aligned} \quad -\infty \leq f \leq \infty. \quad (4.8)$$

Equation 4.8 also gives a decomposition of the contribution to the output spectrum from the linear and quadratic components of each of the inputs.

4.2.6 Goodness-of-Fit of the Model

Linear and bilinear coherence functions will now be stated for the linear and quadratic terms of the model in Eq. 4.2 or Eq. 4.3. The linear coherence functions between inputs X_1, X_2 and output Y are defined for $f \neq 0$ as follows:

$$\gamma_{X_1Y}^2(f) = \frac{S_{Y_1X_1}(f)}{S_{YY}(f)} \quad \text{and} \quad \gamma_{X_2Y}^2(f) = \frac{S_{Y_2Y_2}(f)}{S_{YY}(f)}. \quad (4.9)$$

The bilinear coherence functions between inputs X_1 , X_2 and output Y are defined for $f \neq 0$ as follows:

$$q_{X_1Y}^2(f) = \frac{S_{Y_1Y_1}(f)}{S_{YY}(f)} \quad \text{and} \quad q_{X_2Y}^2(f) = \frac{S_{Y_2Y_2}(f)}{S_{YY}(f)}. \quad (4.10)$$

A goodness-of-fit measure of the model can be defined by seeing how close the total coherence function $C_{xy}^2(f) = [\gamma_{X_1Y}^2(f) + \gamma_{X_2Y}^2(f) + q_{X_1Y}^2(f) + q_{X_2Y}^2(f)]$ is to unity.

4.2.7 Effect of the frequency response of the anemometer used for measuring the input wind velocity

It is known from Chapter 3 that the pressure transducers at the WERFL have the necessary frequency response up to 10 Hz. But the 3-cup and UVW anemometers that have been used in the field for measurement have inadequate frequency response beyond about 0.5 Hz. It is velocity data from the 3-cup anemometer that were primarily used in the present research for the identification of transfer functions. The identification is carried out up to a frequency of 5 Hz. Thus we have data sets where the output measurements are good up to a frequency of 5 Hz, whereas the input data are deficient beyond about 0.5 Hz, except where sonic anemometer measurements are available. It may be noted that the identification method described in Eq. 4.3 through Eq. 4.5 overestimates the transfer function in the frequency range where the input is deficient. However, in the output prediction phase using Eq. 4.8, the overestimated transfer functions are multiplied by input spectra which are underestimated by the same order of magnitude as the transfer functions are overestimated. Hence, the error gets compensated and the predicted output is correct in the complete frequency range.

Thus the proposed methodology identifies transfer functions whose magnitude in the higher frequency range depend on the frequency response characteristics of the anemometer used in measuring the input velocities. However, these transfer functions give the correct output prediction when used with input data from the same type of anemometer as used for the identification work. It will also be seen from the results presented in Chapters 5 and 6 that even the measured pressure spectra do not have any significant energy beyond 1 Hz.

4.2.8 Implementation of the model

The identification and prediction procedures described above were coded and implemented using the high performance computation and visualization software MATLAB (1992). The spectral density functions were computed using the Spectrum and FFT routines in the Signal Processing Toolbox (Little and Shure, 1992) of MATLAB. These routines use the Welch algorithm for spectral analysis (Oppenheim and Schaffer, 1975). A Hanning window was used in the spectral estimation. A concise review of different data windows used in spectral analysis is given in Harris (1978).

It was seen from the Van der Hoven spectrum (Figure 2.1 in Chapter 2) that the wind spectrum obtained from a record of about 15 minutes duration contained most of the significant frequencies in the micrometeorological range. Hence, a segment length of 15 minute duration is used for the estimation of transfer functions in this work. However, it does not make any sense to obtain transfer function estimates from just a single 15 minute record. Therefore, three almost consecutive 15 minute field records were concatenated and divided into 15 minute subrecords with 33% overlap for the identification of transfer functions. This was done in order to have a reasonable number of sub-records for averaging to keep random and bias errors in the transfer function estimates to a minimum. The overlapped processing concept used here enables reduction in bias and variance errors in the transfer function estimates (Carter et al., 1973). It also helps in keeping the FFT bin width free from aliasing effects (DeFatta et al., 1988). It also takes into account bias errors due possible time delay between the input and output.

The time delay between the input and output is acceptable as long as the record length T is very long compared to the time displacement τ_1 between the input and output records (Bendat and Piersol, 1980). However, as $\tau_1 \rightarrow T$, the estimated coherence between the records will diminish due to a time delay bias error as

$$\hat{\gamma}_{xy}^2 \approx \left(1 - \frac{\tau_1}{T}\right)^2 \gamma_{xy}^2. \quad (4.11)$$

At the WERFL, any time delay between the input velocity, measured on the tower, and the output pressure, measured on the building, depends on the direction of the wind. The maximum time delay occurs when the wind blows from the west. For a mean wind speed of 9 m/s from the west, the time delay is about 5 seconds ($\approx 45\text{m} / 9\text{m/s}$) which is negligibly small compared to the record length $T = 900$ seconds (15 minutes) used in the present identification work.

Since the velocity data were sampled at 10 Hz, the pressure-coefficient data which were originally sampled at 40 Hz (M15) or 30 Hz (M38) were decimated to 10 Hz for autospectra and cross-spectra computation. This was done by simply removing the additional data points. Table 4.2 shows, for some typical taps, that there is practically no difference between the variance of the pressure data from the field records sampled at 40 Hz and those decimated to 10 Hz. This could be due to two reasons. First, the pressure data were analog low-pass filtered at 8 Hz and 10 Hz, respectively, for the Omega and Validyne transducers. Second, there may not be any significant frequency content in the pressures beyond 5 Hz. The latter will be verified in the analyses presented in Chapters 5 and 6.

Since the data records are of finite duration, the frequency range used in the system identification and output prediction equations was $-5 \text{ Hz} \leq f \leq 5 \text{ Hz}$. All computations were first made using two-sided spectra in the frequency range $-5 \text{ Hz} \leq f \leq 5 \text{ Hz}$, and were finally converted in the output prediction phase to one-sided spectra in the frequency

range 0 to 5 Hz by multiplying the two-sided spectra in the frequency range 0 to 5 Hz by 2. Thus, all the spectra presented in the results are one-sided.

Table 4.2 Comparison of pressure variance for two sampling rates.

Record	Pressure Tap	Cp_variance [-] for	
		$f_s = 40$ Hz	$f_s = 10$ Hz
M15N541	42206	0.1036	0.1038
M15N541	50123	0.2333	0.2331
M15N546	52323	0.0187	0.0188
M15N544	52923	0.0132	0.0134
M15N086	50101	0.1371	0.1374
M15N478	50101	0.1544	0.1548
M15N478	50501	1.0393	1.0372
M15N709	50501	1.2063	1.2093

If the power due to extraneous noise and/or higher order non-linearities is negligible, then the sum of the coherence functions in the model should be unity. In practical situations this seldom becomes unity, and usually it turns out to be greater than unity, because of random estimation errors due to measurement noise in the instrumentation, computational noise in digital calculations, and deviations from Gaussian behavior in the input: i.e., $[\gamma_{x_1Y}^2 \varnothing + \gamma_{x_2Y}^2 \varnothing + q_{x_1Y}^2 \varnothing + q_{x_2Y}^2 \varnothing] \geq 1$. This fact was observed and noted by Choi et al. (1985) and was also observed in this work. This implies that the estimated output power given by the quadratic model is greater than the actual power. The accuracy of a model like the one proposed depends essentially on a precise definition of the input signals (Holscher, 1995). In the present work, we are dealing with field data where the pressure data acquisition system is much superior relative to the velocity instrumentation, from the point of view of both technology and location. The very fact that the velocity instrumentation is physically located out in the open atmosphere makes the signals susceptible to noise contamination due to ravages of the weather, sudden changes in wind direction and hence a lack of control over the input under field conditions.

However, the results obtained are acceptable from a practical point of view as long as the mean coherence over the entire frequency range is close to unity and the residuals are small.

4.3 Physical Interpretation of the Model

In many physical systems the output to a given input is dictated by both linear and non-linear mechanisms. The non-linearities are of a higher order and at first sight may seem to play a secondary role in the problem at hand. They are accordingly often ignored. Neglecting the non-linear terms ensures that the predicted, or modeled, response or output of the system will occur only at the frequencies contained in the excitation input. In some problems, however, even weak non-linear terms can play an important role in the input-output relationship of a system. The role stems from the fact that in non-linear systems the input spectral components can interact with one another through sum and difference interactions to produce a rich abundance of new spectral components in the output which are not present in the input. The presence of these new frequencies, some of which can be quite low and others quite high relative to the input spectra, cannot be modeled by a linear frequency domain analysis.

Wind pressures or forces on building surfaces is a non-linear function of wind velocity. The non-linear function can consist of a combination of linear and higher order terms of the velocity components. Also the relation between velocity and pressure has 'memory' effects. This means that the pressure exerted by the wind on a building surface at a particular instant of time depends not only on the velocity input at that instant but also on the velocity inputs at previous instants of time. The proposed model attempts to account for the above factors up to second-order non-linearity.

The model in equations 4.2 or 4.3 aims at the spectral decomposition of wind-induced pressure fluctuations into linear and quadratic components associated with each of the longitudinal and lateral components of wind velocity by means of four transfer functions. This approach using the multiple transfer function concept groups the boundary layer and the structure together for assessment of wind pressures. It also enables a weighted

assessment of the contribution of each of the linear and square terms of the wind velocity components to local pressures.

In the physical sense, wind pressures on building surfaces are a result of two mechanisms: (1) the modification of the upstream flow, which results in change in momentum, due to interaction with the flow around the structure, and (2) the dissipation of some of the kinetic energy in the upstream turbulence when it encounters the structure. The linear terms in the model represent the contribution to the pressures due to the modification or change in momentum of the upstream flow. The linear u term represents the contribution to the pressures due to momentum in the upstream turbulence in the predominant direction of flow. The upstream along wind turbulence is influenced by the upstream terrain features along the mean flow direction. The effect of the longitudinal component is to strain the fluid elements and produce shear layers during the interaction process with the structure. Cross-correlation analysis between the lateral wind velocity and wind direction using the WERFL field data has consistently shown the correlation coefficient at zero time lag to be of the order 0.96 to 0.99. Hence the linear v term in the model represents effect on the local pressures due to local changes in wind direction. The effect of changes in wind direction during interaction is to rotate the fluid elements and produce vortices. The quadratic terms in the model aim at accounting for the non-linear relationship between velocity and pressure. The quadratic terms in the model represent the contribution to the pressures due to direct dissipation of the kinetic energy in the upstream wind flow when it encounters the structure. The quadratic v term represents the influence of local changes in wind direction in the dissipation process. The quadratic terms provide a measure of the multiplicative non-linear interaction of frequency components and provides physical insight into the nature and characteristics of non-linear fluctuations. The complex-valued nature of the transfer functions is indicative of a phase shift between wind velocity and wind force/pressure.

Wind pressures on a building surface depend on the wind direction, upstream terrain or turbulence characteristics, building geometry and location of the point of interest on the surface on the building. For a given building geometry, the formulation of the proposed

non-parametric model is such that the effect of upstream terrain or turbulence is taken care of by the input spectra and the location on the building and the angle of attack is taken care of by the output. Hence, the transfer functions are designed to capture the mechanism that transforms upstream wind velocity to pressure.

The model proposed in this chapter will now be applied to wind velocity and pressure-coefficient data to solve: (i) the system identification problem relating wind velocity to wind pressure, and (ii) the spectral decomposition and output prediction. The results are presented and discussed in the following chapters.

CHAPTER 5

TRANSFER FUNCTIONS FOR WIND NORMAL TO THE BUILDING

5.1 Introduction

In this chapter, transfer functions are identified and the spectral decomposition problem solved for pressure taps along the shorter axis of the building and on the side walls for wind normal to the long wall of the test building. The taps investigated are located on the windward wall, on the roof in separation and reattachment zones, on the leeward wall, and in the reattachment zone of the side walls. Results of field (Mehta et al., 1992) and wind-tunnel measurements (Cochran, 1992) on the Texas Tech test building show that the maximum rms pressures for many of these pressure taps, especially those on the windward wall and under the separation bubble, occur when the wind blows normal to the long walls. Hence, the study presented in this chapter is for the critical angle of attack of approximately 270° , which is normal to a long wall (see Figures 3.2 and 3.3).

The transfer functions are identified based on field wind velocity measurements made in the data acquisition mode M15 using a 3-cup/vane anemometer. Velocity data were obtained using the sonic anemometer for taps on the windward and side walls. Comparisons are made between the transfer functions identified from field velocity data obtained from 3-cup/vane (M15) and sonic (synchronized with mode M38) anemometers for a tap on the windward wall. Transfer functions are also identified for area-averaged pressures on the roof purlin for angles of attack of approximately 270° and 0° . The locations and coordinates of the pressure taps are detailed in Figure 3.3 and Table 3.1.

The summary statistics of velocity data of the concatenated records used in the study presented in this chapter are tabulated in Table 5.1. More of the summary statistics, including those for pressures, are tabulated in the appendix. It may be noted that records CS070, CS073 and CS077 are the ones where the wind velocities were measured using the sonic anemometer. For all the other records, the wind velocities were measured using a 3-cup/vane anemometer.

Table 5.1 Summary statistics of velocity data of concatenated records.

Concatenated Record No.	15-minute records used	Wind azimuth α°	Angle of attack θ°	U at 4 m m/s	I_u	I_v
C539	M15N539 + 540 + 541	353.1	263.1	9.11	0.194	0.194
C544	M15N544 + 545 + 546	357.7	267.7	9.36	0.189	0.144
CS070*	SA / M38N070 + 071 + 072	252.6	267.6	10.05	0.233	0.213
CS077*	SA / M38N077 + 078 + 079	270.3	270.3	9.27	0.247	0.219
CS073*	SA / M38N073 + 074 + 075	255.9	270.9	9.49	0.225	0.232
C325	M15N325 + 326 + 327	256.8	1.8	8.57	0.244	0.219
C728	M15N728 + 729 + 730	169.6	4.6	7.81	0.221	0.164

* Wind velocity was measured using the sonic anemometer.

The model proposed in Section 4.2 will now be applied to the above data to first solve the system identification problem for each set of simultaneously measured velocity and pressure-coefficient data using equations 4.4 and 4.6. The four transfer functions so identified will then be used on the same input spectra to predict the output pressure-coefficient spectrum using Eq. 4.8. This solves the spectral decomposition problem by determining the contributions to the predicted pressure-coefficient spectrum from the linear and quadratic velocity terms in the model. Physical interpretations can then be made about the mechanisms that produce turbulence-induced pressure fluctuations on building surfaces. The problem of simulation or output prediction of the pressure-coefficient spectrum using input spectra from a different record will be discussed later in Section 5.3 of this chapter.

5.2 Identification of Transfer Functions and Spectral Decomposition of Wind Pressures

5.2.1 Windward Wall

The windward wall experiences positive wind pressures. The pressure taps examined are 42206 and 42212. Tap 42206 is located near the middle of the windward wall a little

below the so-called 'stagnation point' (at about two-thirds the height of the building, i.e., 2.65 m in this case) where the maximum positive pressures occur. Tap 42212 is located near the top of the windward wall where divergence of the flow occurs before it separates from the top of the building. The transfer functions were identified from equations 4.4 and 4.6 for these taps using the input velocity data measured using two types of anemometers: the sonic and the 3-cup/vane. Two sets of concatenated data records (see Table 5.1) were used for each anemometer type (CS070 & CS077 for sonic, and C539 & C544 for 3-cup).

Representative linear and quadratic transfer functions for the windward wall for tap 42206 and their comparison for the 3-cup (C544) and sonic (CS070) case are shown in Figures 5.1(a) through 5.1(d). The comparison between sonic and 3-cup are shown separately on the same page, rather than on the same graph, for clarity. These transfer functions show variability over the entire frequency range, especially in the higher frequency range. It is observed that all the transfer functions from the 3-cup and sonic anemometers are similar in form up to a certain frequency. In fact all the transfer functions are quite flat up to about 0.5 Hz, indicating a direct relation between velocity and pressure. The magnitudes of these functions are close to one for the linear terms but higher for the quadratic terms. However, it is seen that the transfer functions for the 3-cup show an upward trend in relation to the corresponding ones for the sonic in the higher frequency end. This upward trend starts at about 0.5 Hz for the two transfer functions associated with the u component and around 1.2 Hz for the two associated with the v component. This overestimation of the transfer functions is due to the underestimation of the velocity spectra due to insufficient frequency response of the 3-cup in the frequency range mentioned as was observed in Section 3.5. The lateral component has an artificially improved response due to the overshoot phenomenon of the vane noted in Section 3.5.3. However, the total predicted spectrum obtained from the transfer functions is correct because the overestimated transfer functions in the higher frequency range are compensated to the same order by the underestimated input spectra in the output prediction process using Eq. 4.8. This issue was discussed in Section 4.2.7.

A comparison of the predicted total (S_{yyp}) and linear (S_{yypl}) pressure-coefficient spectra obtained from Eq. 4.8 using the above transfer functions, the measured pressure-coefficient spectrum (S_{yy}) and the residual spectrum (S_{nn}) is shown in Figure 5.2. The predicted spectrum is seen to match closely with the measured one. The spectral decomposition of the predicted spectrum into components due to the linear (S_{y11} and S_{y21}) and quadratic (S_{y12} and S_{y22}) are shown in Figure 5.3. The input velocity spectra (S_{x1x1} and S_{x2x2}) and the output pressure-coefficient spectrum (S_{yy}) used in this case are shown, as a typical illustration, in Figure 5.4. The transfer functions for different records with similar mean angles of attack of the wind were found to be quite similar with some variability. This variability in transfer functions will be discussed in Section 5.3.

The total coherence function as defined in Section 4.2.6 and computed using equations 4.9 and 4.10 is shown in Figure 5.5. The coherence function gives a measure of the goodness of fit of the model. The closer the coherence function is to unity, the better the goodness of the fit. The coherence function in Figure 5.5 has a mean of 1.02 over the frequency range 0 to 5 Hz. It is seen to randomly fluctuate about the mean with a standard deviation of 0.41. This is indicative of random errors in the transfer function estimates. Random errors in the estimates can be due to sources such as measurement noise in the instrumentation, deviations from Gaussian behavior of the input and computational noise in the digital calculations (Bendat and Piersol, 1980). The higher degree of variability in the transfer function estimates in the higher frequency (beyond 1 Hz) end is partly due to computational errors because of very small input/output spectral quantities involved. It was also observed by Choi et al. (1985) that in practical situations the coherence function seldom becomes unity due to random estimation errors as seen in this work. The accuracy of a model like the one proposed depends essentially on a precise definition of the input signals (Holscher, 1995). In the present work, we are dealing with field data where the pressure data acquisition system is much superior relative to the velocity instrumentation, from the point of view of both technology and location.

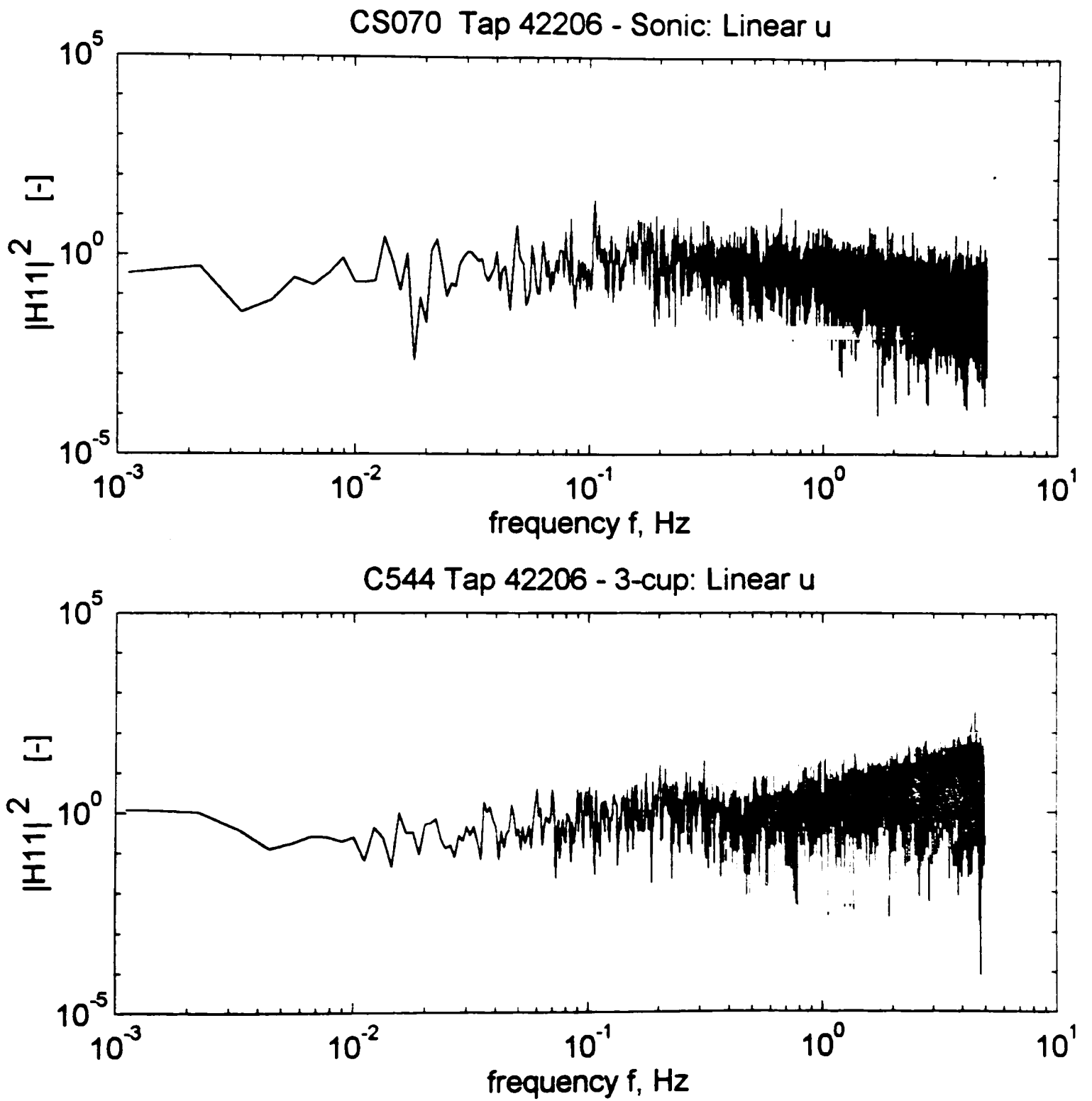


Figure 5.1. Transfer functions for windward wall tap 42206. (a) Linear u .

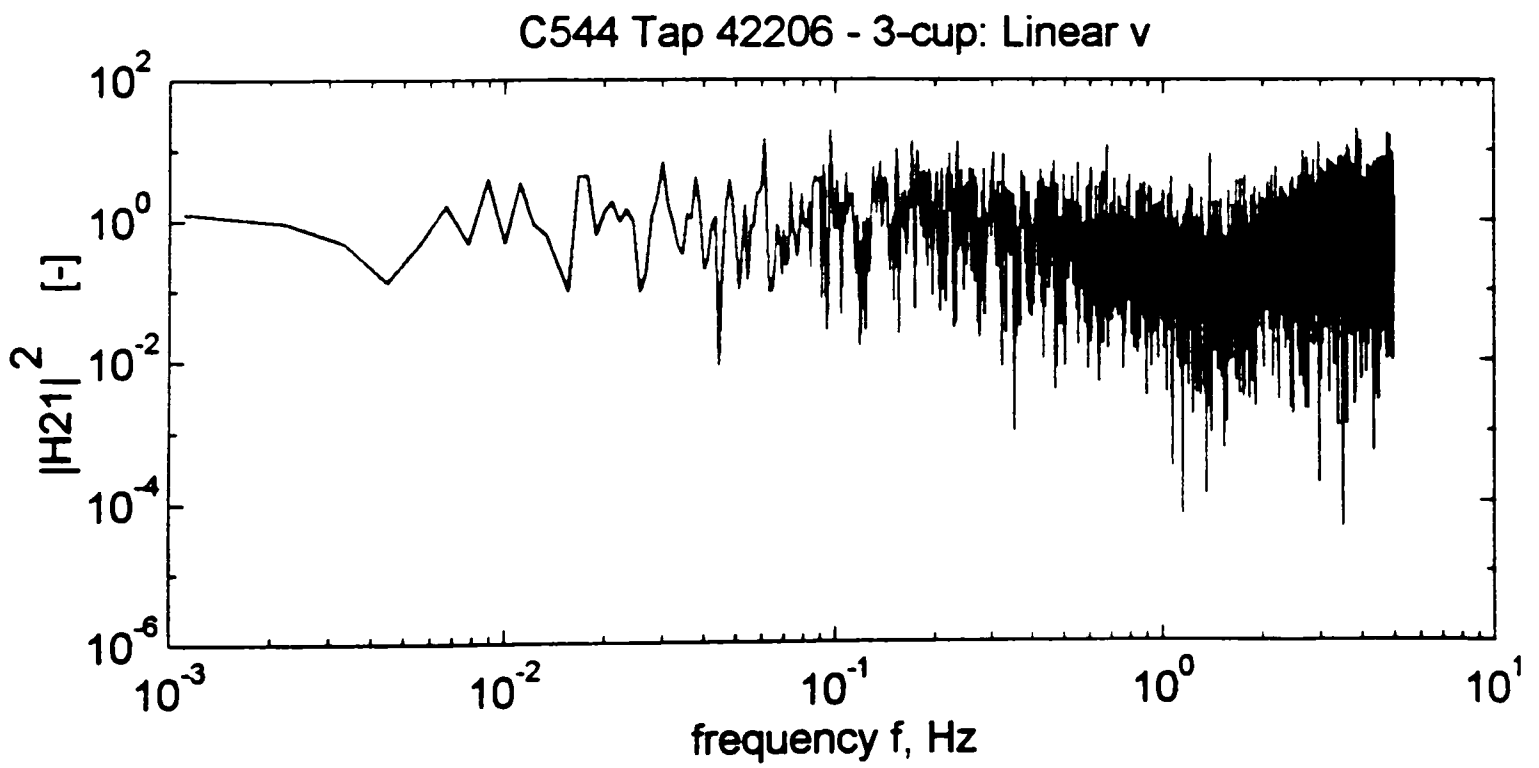
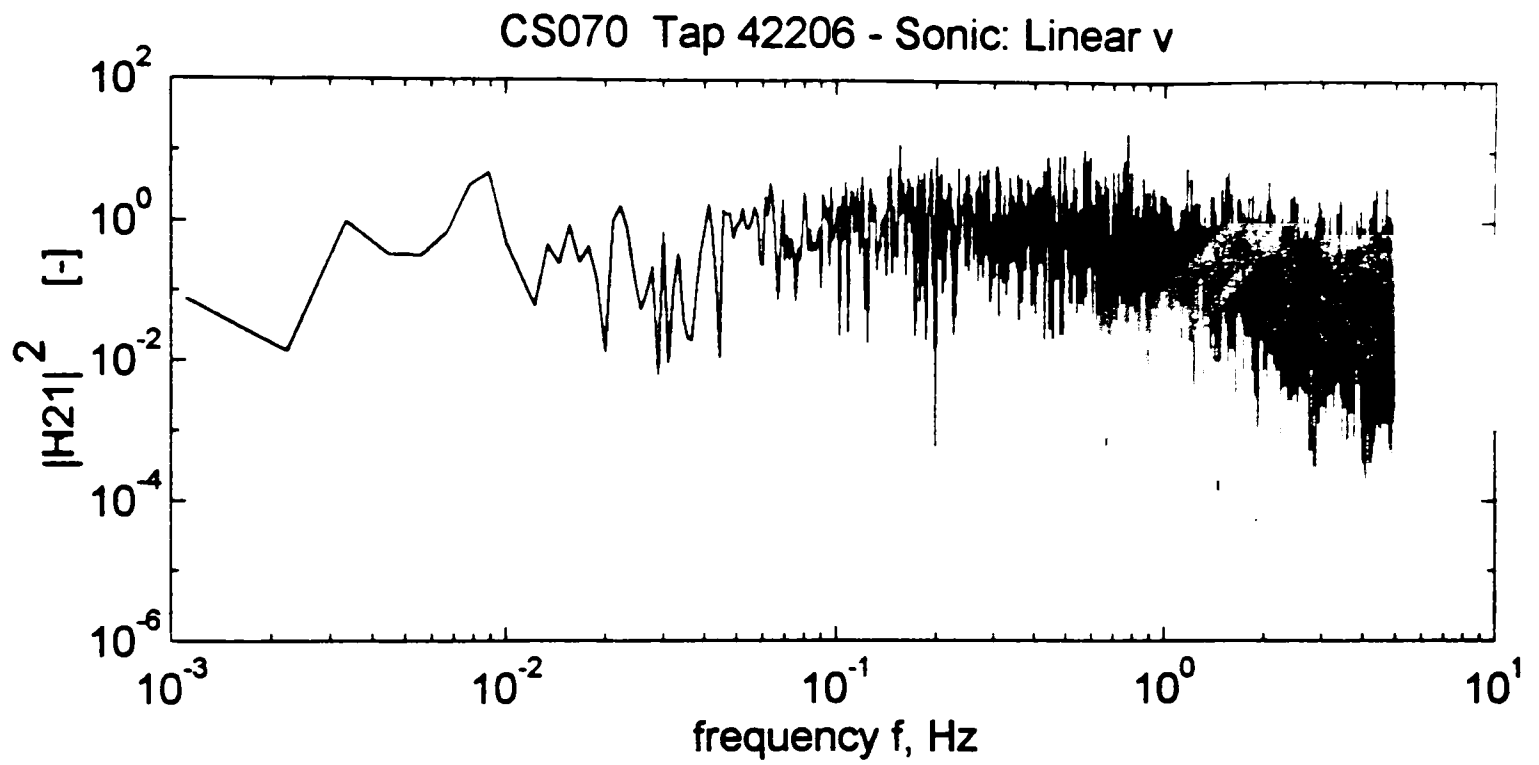


Figure 5.1. Continued. (b) Linear v .

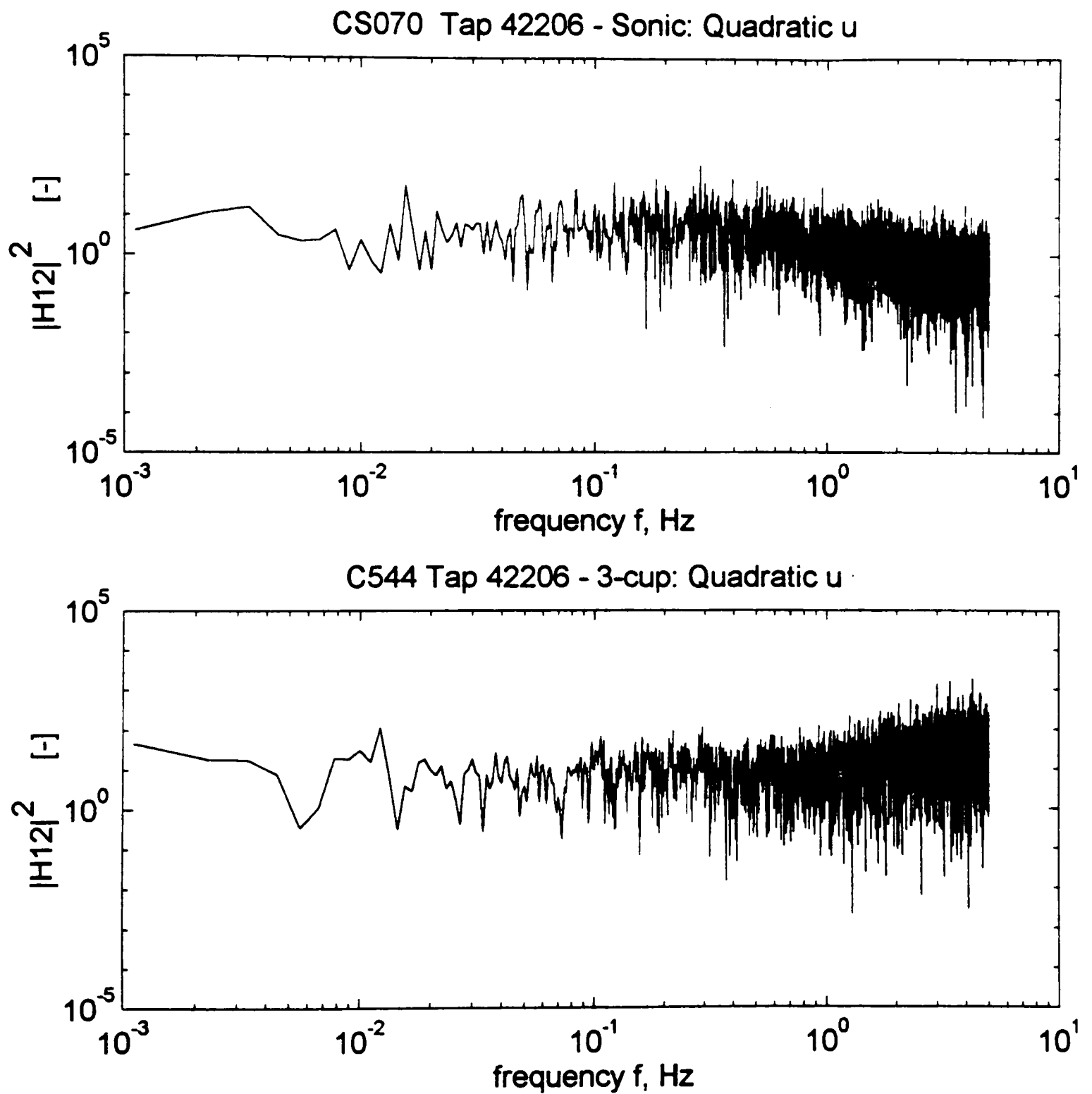


Figure 5.1. Continued. (c) Quadratic u .

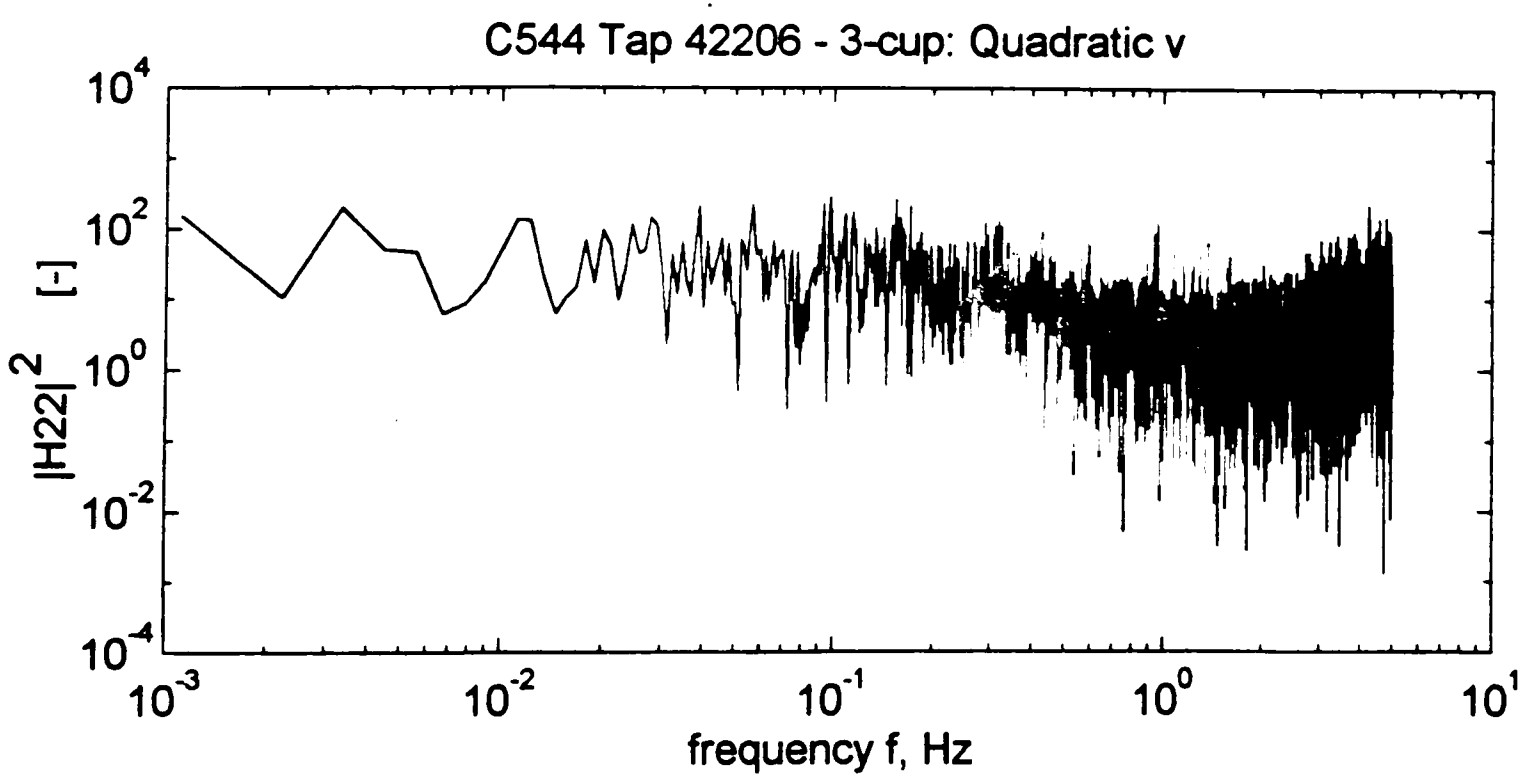
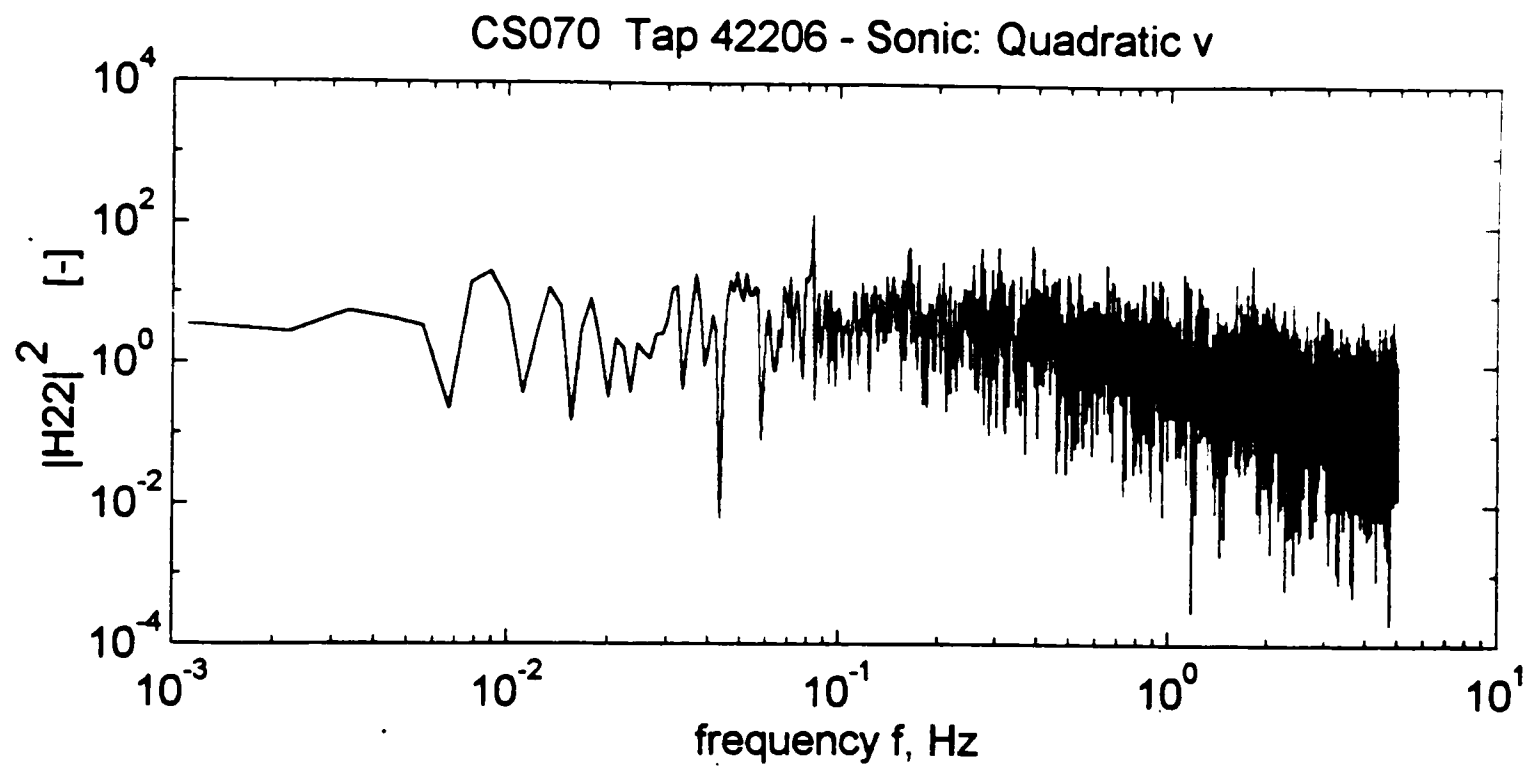


Figure 5.1. Continued. (d) Quadratic v.

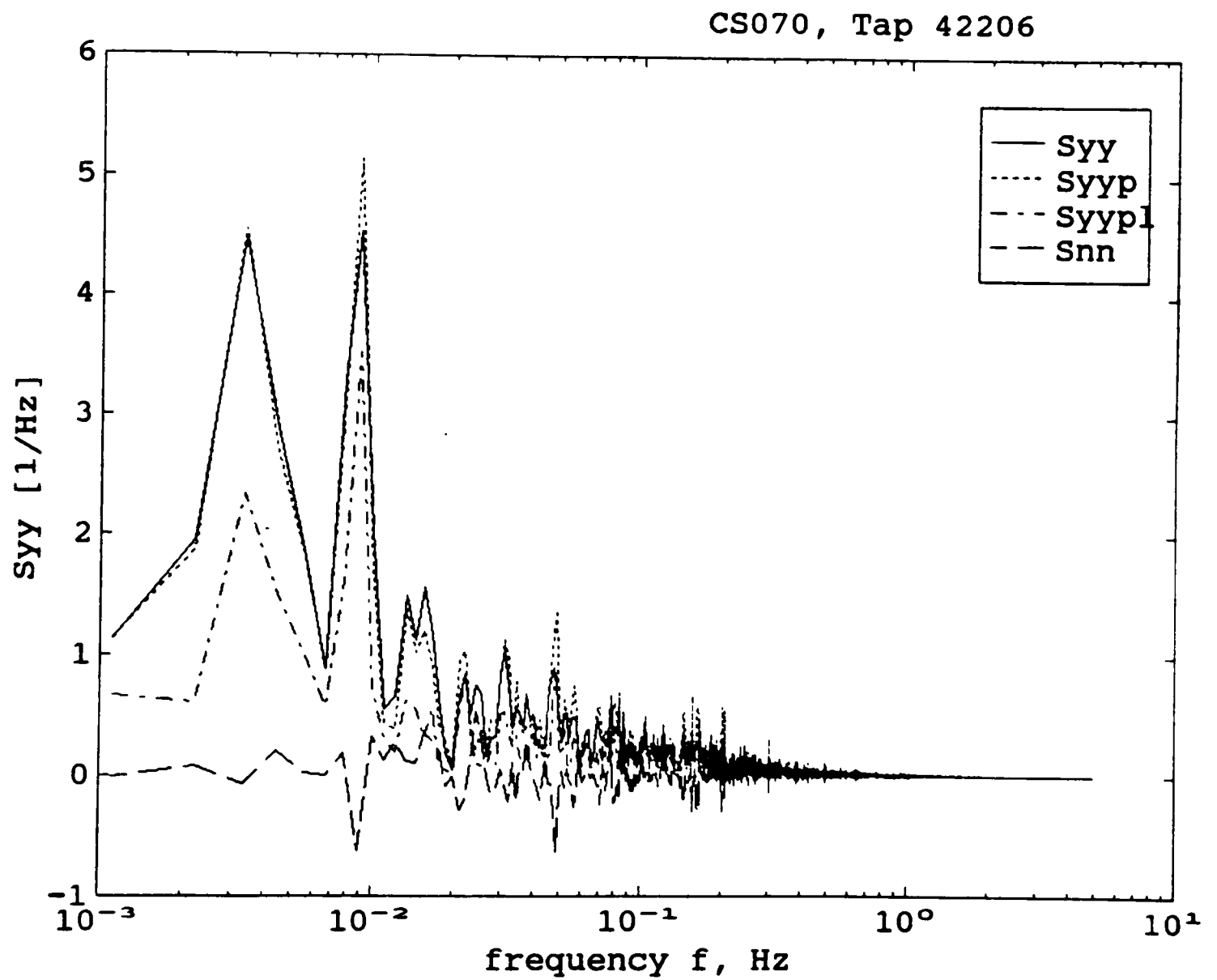


Figure 5.2. Output prediction for windward wall tap 42206 (CS070).

CS070: Tap 42206

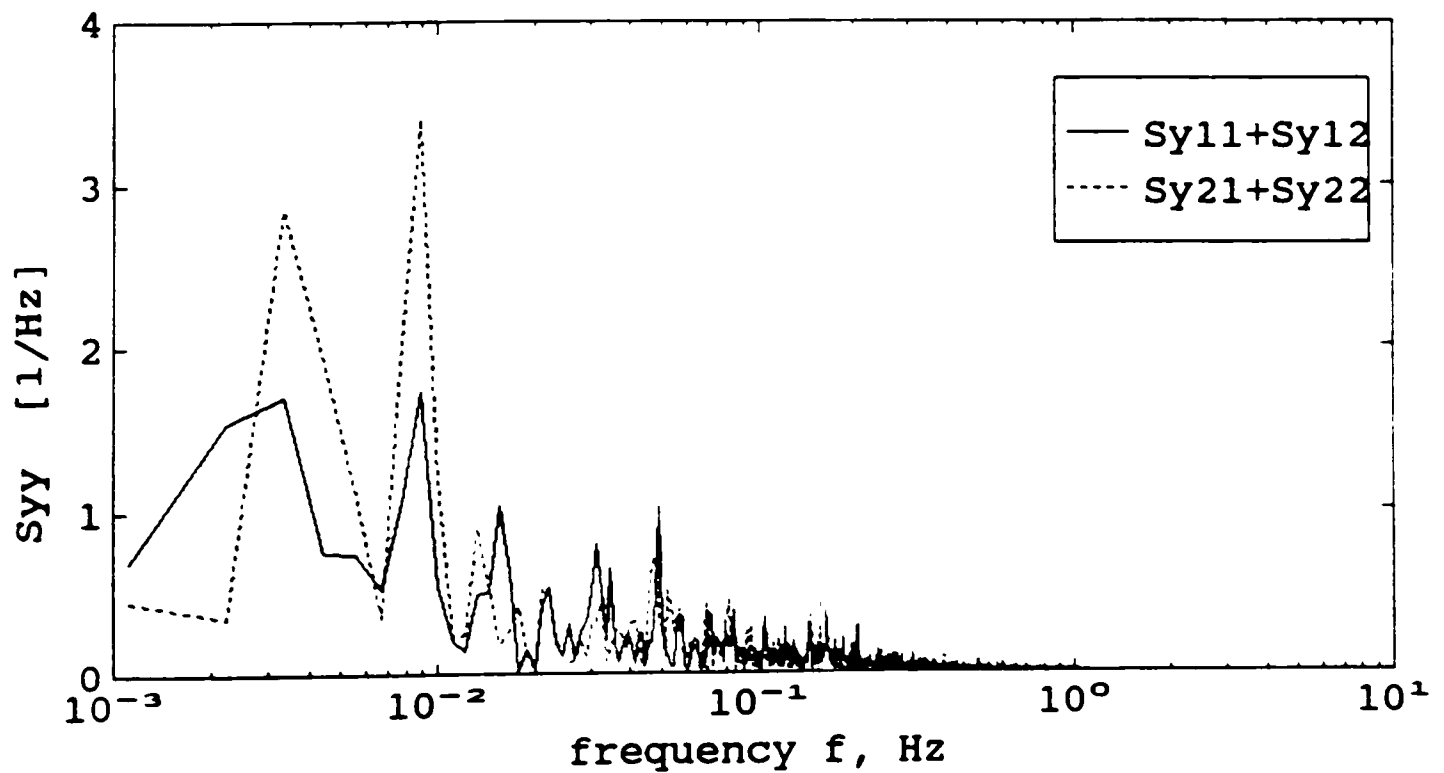
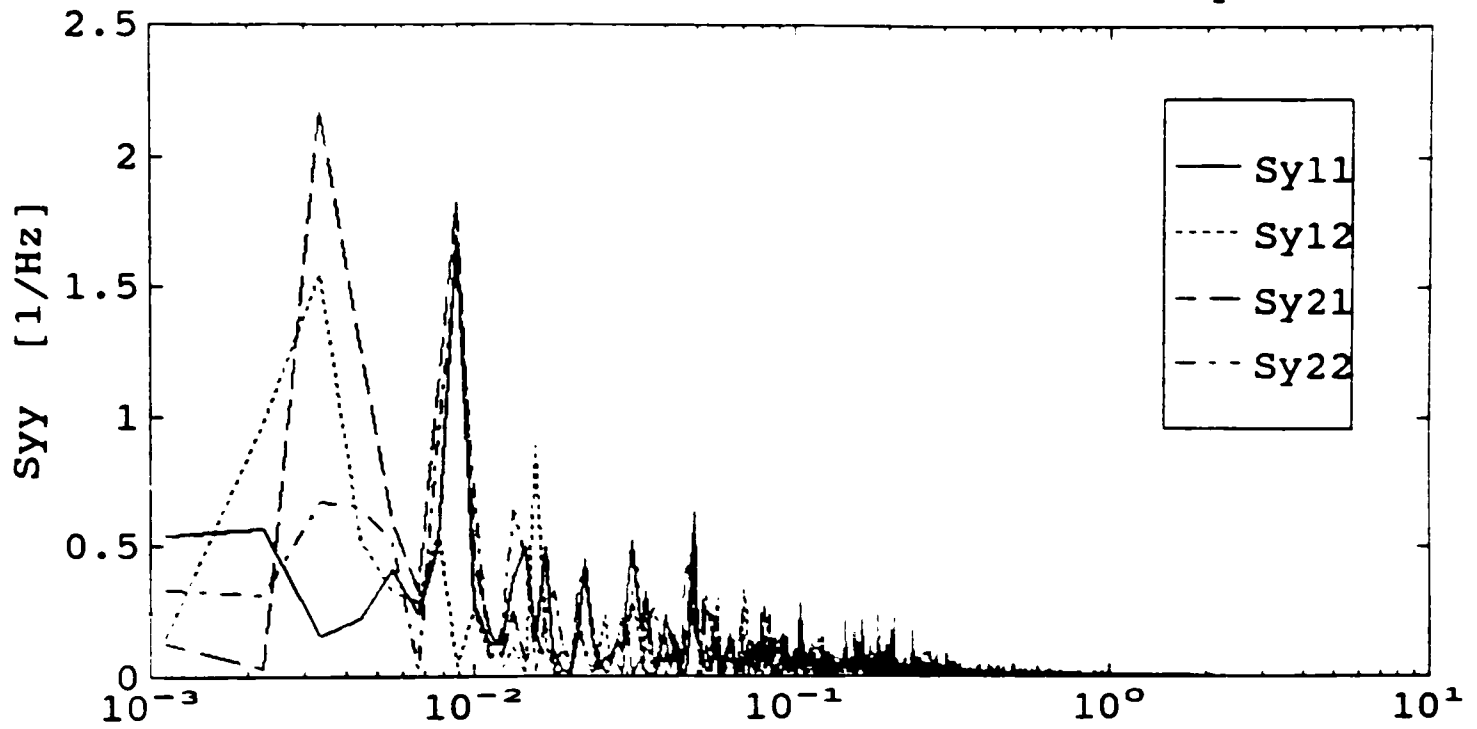


Figure 5.3. Decomposition of pressure-coefficient spectrum for windward wall tap 42206 (CS070).

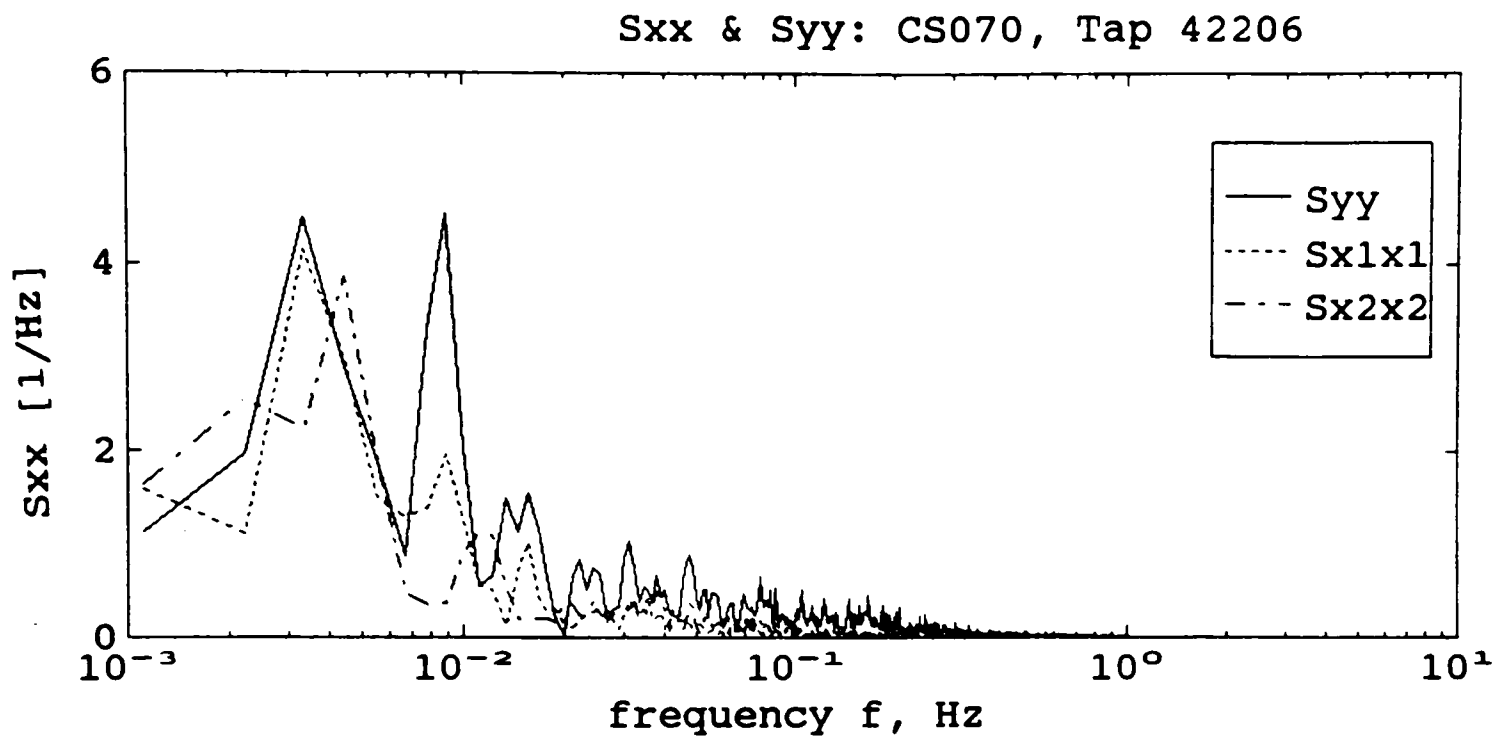


Figure 5.4. Input and output spectra for tap 42206 (CS070).

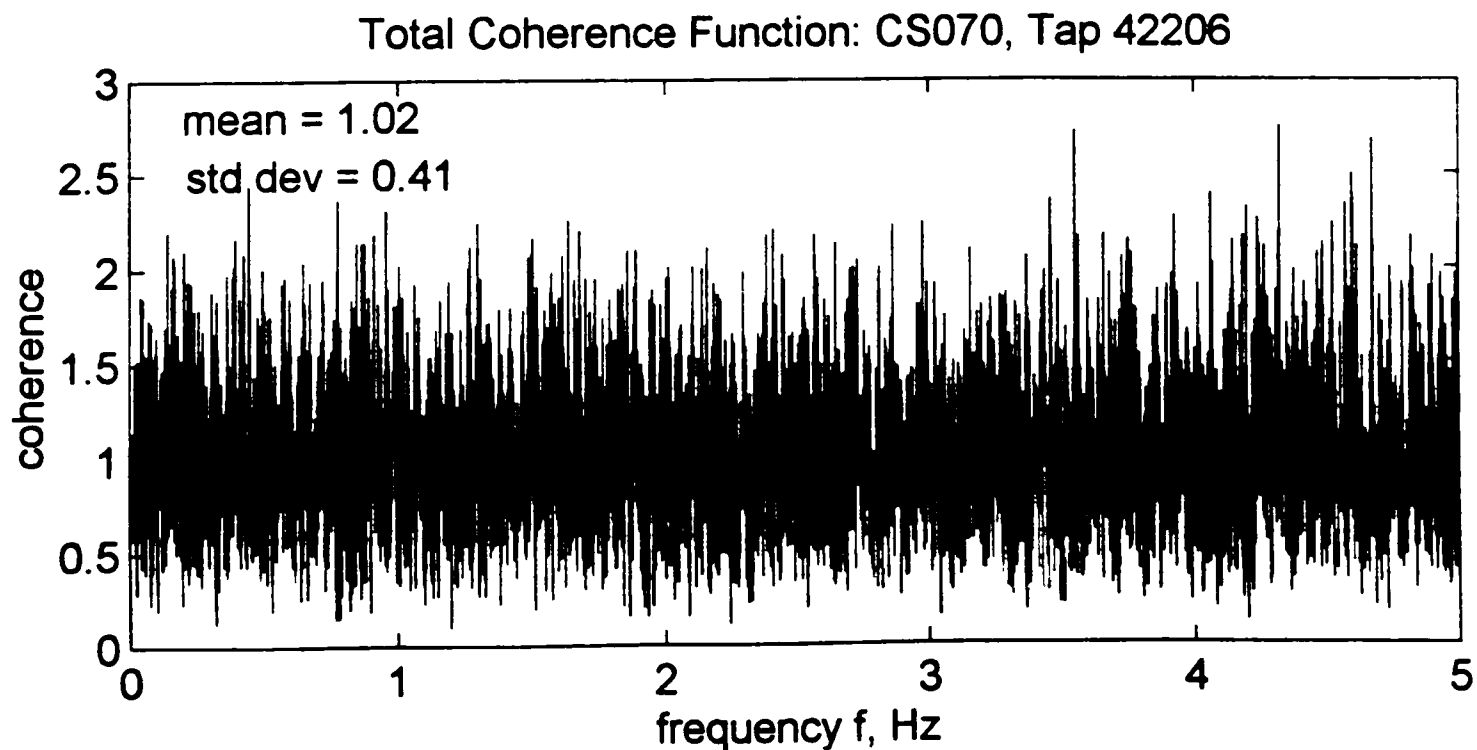


Figure 5.5. Total coherence function for tap 42206 (CS070).

The very fact that the velocity instrumentation is physically located out in the open atmosphere makes the signals susceptible to noise contamination due to ravages of the weather, sudden changes in wind direction and hence a lack of control over the input under field conditions. However, the results obtained are acceptable from a practical point of view since the mean coherence over the frequency range is close to unity and the residuals are small as seen from Figure 5.2.

The bispectrum of the pressure-coefficient time history for the windward wall tap 42206 is shown in Figure 5.6 for a typical field record. As discussed in Section 2.4.2, the bispectrum gives a decomposition of the skewness or non-Gaussian character of a process as a function of two frequency variables. The non-Gaussian character of the wind pressure process can be mainly attributed to the non-linear relationship between wind velocity and pressures. It is seen from Figure 5.6 that the bispectrum exhibits a sharp peak at low frequencies. This goes to indicate that the nonlinear relationship is more significant at lower frequencies. This observation can also be made from Figure 5.3 where contributions from the quadratic terms in the model show peaks at low frequencies (0.003 Hz). Schueller (1991) has shown a qualitative similarity between the bispectrum from field measurements and an analytical bispectrum derived based on a square-law relationship between velocity and pressure. This further justifies the selection of a square-law model in this study.

The transfer functions obtained for tap 42212 for a typical field record, CS070, are shown in Figures 5.7(a) and 5.7(b). The velocities for this record were measured using the sonic anemometer. The coherence function for this tap was also similar to that for tap 42206 with a mean of 1.01 and standard deviation of 0.4. The predicted spectrum also closely matched the measured one as was the case for tap 42206. It can be seen from Figures 5.1 and 5.7 that all the four transfer functions for tap 42212 (CS070) are flatter than the corresponding ones for tap 42206 for higher frequencies beyond 0.5 Hz. This indicates a more direct relationship between the velocity and pressure at that point since it is located closer to the roof height (4 m) at which the velocity measurements were made.

The decomposition of the pressure-coefficient spectra into contributions from the linear and quadratic terms in the model and the total coherence are tabulated in Table 5.2 for taps 42206 and 42212 on the windward wall for several sets of records.

Table 5.2 Contribution from different components of the model to pressures on the windward wall.

Record	Cp_variance		Contribution, as % of measured spectrum, from					Total Coherence	
	meas- ured	pred- icted	u	v	u^2	v^2	Resi- dual, S_{nn}	mean	std. dev.
<u>Tap 42206</u>									
C539	0.0952	0.0940	26.7	22.6	26.2	23.3	1.2	1.02	0.42
C544	0.0885	0.0886	24.8	23.9	26.1	25.3	-0.1	1.02	0.41
CS070	0.1139	0.1161	24.7	26.5	23.4	27.4	-2.0	1.02	0.41
CS077	0.0852	0.0873	28.7	21.9	25.2	26.6	-2.4	1.03	0.41
<u>Tap 42212</u>									
C539	0.1199	0.1187	25.9	23.6	24.8	24.7	1.0	1.02	0.41
C544	0.1148	0.1170	24.3	25.1	26.6	25.9	-1.9	1.02	0.41
CS070	0.1288	0.1328	25.5	27.4	23.1	27.0	-3.0	1.01	0.40
CS077	0.1126	0.1143	27.2	22.2	26.4	25.8	-1.6	1.04	0.42
CS073	0.1586	0.1630	28.7	24.5	24.8	24.8	-2.8	1.00	0.40

It is observed from Table 5.2 that the linear and quadratic components of the model associated with both u and v have a comparable contribution to the pressure variance on the windward wall. This indicates that about 50% of the turbulence-induced pressure is caused by a change in momentum in the flow as it maneuvers around the building. The other 50% is produced by dissipation of kinetic energy in the upstream turbulence as it encounters the structure. The significant contribution from the linear and quadratic v terms suggest that local changes in wind direction play an equally vital role as the longitudinal velocity fluctuations in producing fluctuating surface pressures.

Bispectrum of $y=C_p$: Tap 42206, M15N545, $\theta=268$, dyn. pr.=5.93 kg/m²

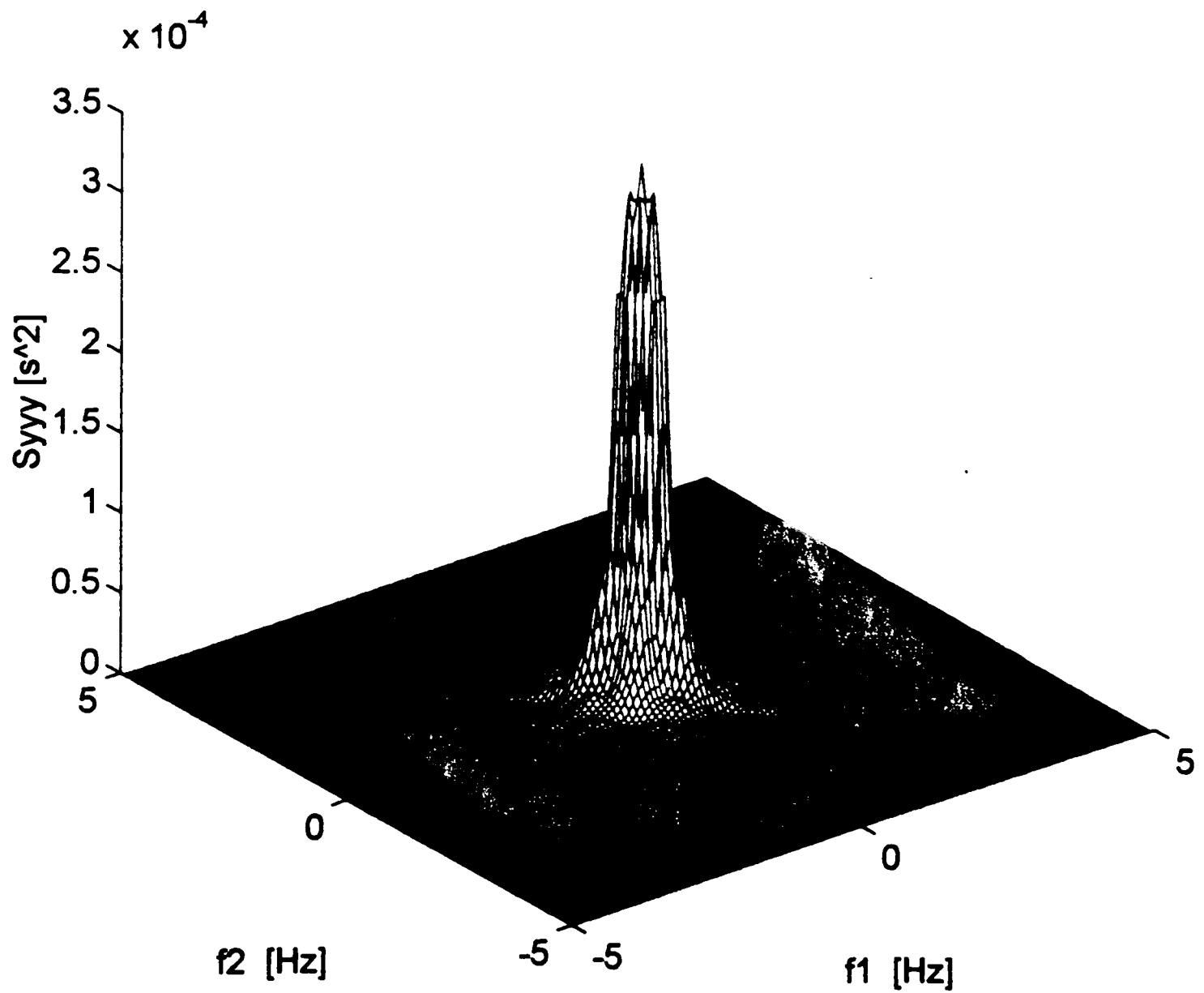


Figure 5.6. Bispectrum of wind pressure for windward wall tap 42206 (M15N545).

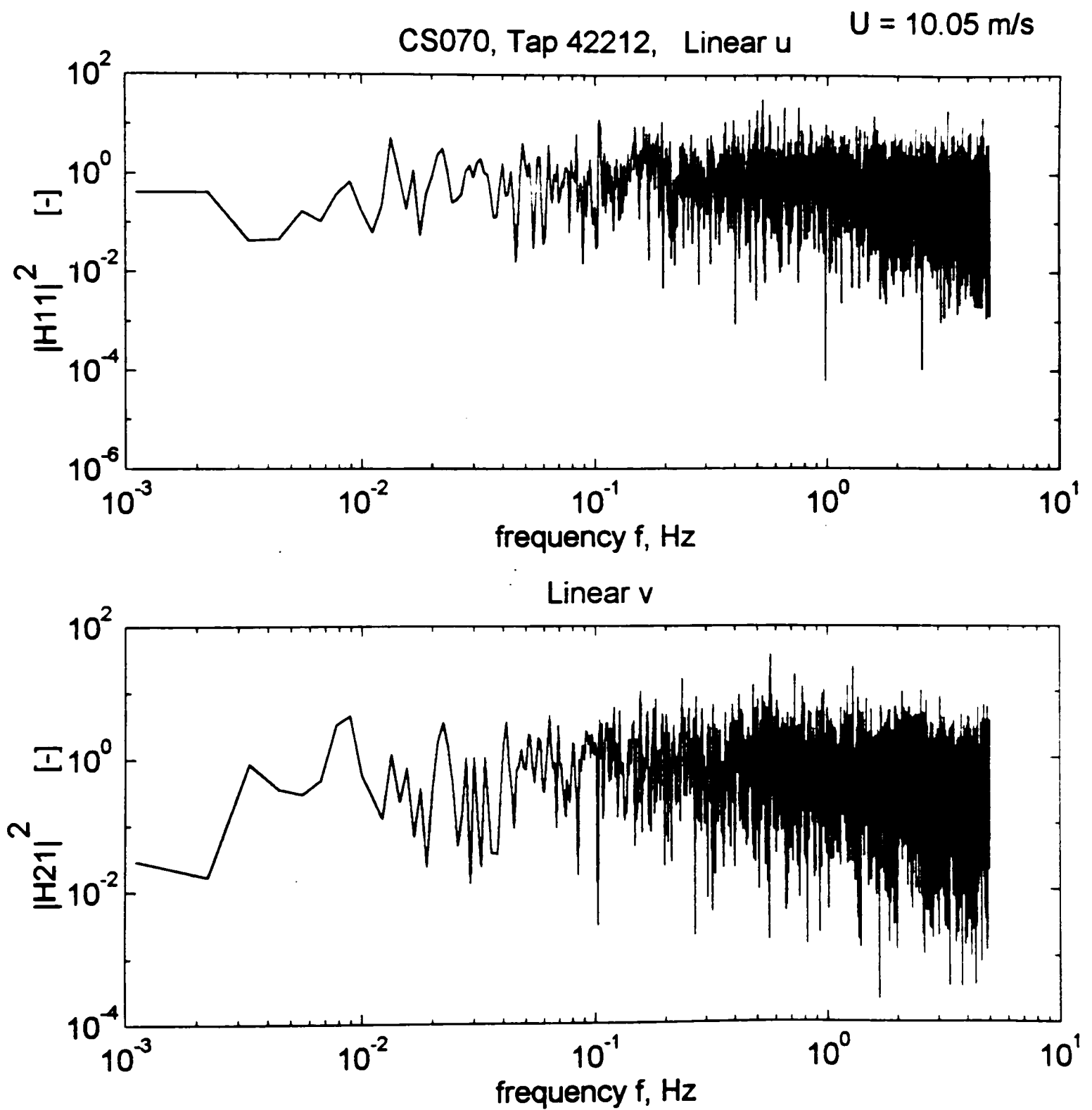


Figure 5.7. Transfer functions for windward wall tap 42212 (CS070). (a) Linear.

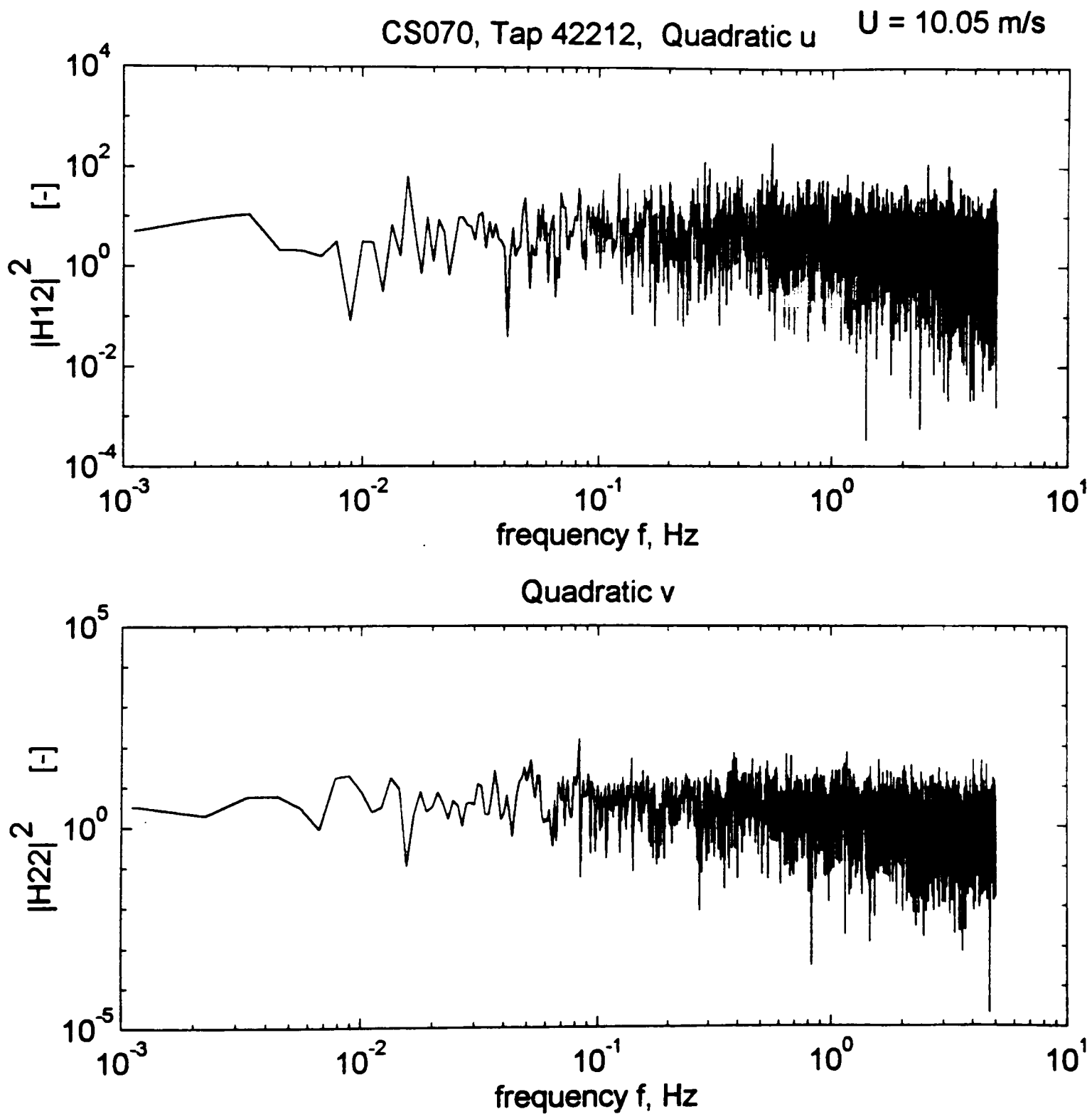


Figure 5.7. Continued. (b) Quadratic.

5.2.2 Separation Region on the Roof

With flat roofs, the flow separates at the upwind edge and may reattach at some distance downwind, if the building is long enough in the wind direction, to form a separation bubble. The external flow is separated from the bubble by a thin but growing shear layer: a region of high suction, high velocity gradients and high local turbulence and vorticity (Holmes, 1982). The velocity profile and the downwards momentum of Reynolds stress both assist the reattachment to occur sooner. For pitched roofs, the position of reattachment and whether separation occurs at all depend on the angle of the roof pitch.

Flow visualization studies conducted by Wagaman (1993) on the Texas Tech test building found the average separation bubble to be 4.42 m (14.5 ft) long for wind normal to the long wall. The range of the bubble length was 3.2 m to 5 m (10.5 ft to 16.6 ft). Letchford and Mehta (1993) and Letchford (1995) have observed from studies on the test building that the mean length of the separation bubble is approximately equal to the height (H) of the building; i.e., $x/H = 1$, x being the distance measured from the upwind edge of the roof, which is the reattachment point in this case. Based on this, data were available for three taps under the separation bubble: 50123 ($x/H = 0.08$), 50523 ($x/H = 0.36$) and 50823 ($x/H = 0.58$).

Transfer functions identified from record C544 (3-cup) for a typical tap, 50523, under the separation bubble are shown in Figures 5.8(a) and 5.8(b). The linear transfer functions are again flat with a magnitude around unity up to about 0.5 Hz. and the quadratic ones have a higher magnitude and show a slight downward inclination. The transfer functions for the other two taps were also similar in form. However, some degree of variability was observed in the field measured input lateral velocity spectra, the output pressure-coefficient spectra and the transfer functions for different records with similar mean angles of attack of the wind. The comparison of the predicted total (S_{yyp}) and linear ($S_{yyp/l}$) pressure-coefficient spectra, the measured pressure-coefficient spectrum (S_{yy}) and the residual spectrum (S_{nn}) is shown in Figure 5.9. The predicted spectrum is again seen to match closely with the measured one. The spectral decomposition of the predicted

spectrum into components due to the linear ($Sy11$ and $Sy21$) and quadratic ($Sy12$ and $Sy22$) is shown in Figure 5.10. The input velocity spectra ($Sx1x1$ and $Sx2x2$) and the output pressure-coefficient spectrum (Syy) used in this case are shown in Figure 5.11. The total coherence function is shown in Figure 5.12. The coherence function has a mean of 0.99 and a standard deviation of 0.41. The fluctuation is indicative of random errors in the transfer function estimates due to reasons discussed in Section 5.2.1. However, the results are acceptable from a practical viewpoint since the mean coherence over the frequency range is close to unity and the residuals are small as seen from Figure 5.9.

The bispectrum of the pressure-coefficient time history for tap 50523 under the separation bubble is shown in Figure 5.13 for a typical field record. Again it is seen from Figure 5.13 that the bispectrum exhibits higher peaks at low frequencies. However, a higher degree of skewness is indicated in the separation case when compared to the windward wall since the bispectrum in this case has a higher peak and a broader frequency spread.

The decomposition of pressure-coefficient spectrum into contributions from the linear and quadratic terms in the model and the total coherence are tabulated in Table 5.3 for the three taps under the separation bubble for two sets of records (C539 and C544). It is observed from Table 5.3 that the linear and quadratic components of the model have a comparable contribution to the pressure variance under the separation bubble also. This is also pointing to the importance of the quadratic terms in producing surface pressures on buildings. It is also seen from Figure 5.10 that the linear and quadratic u terms have a significantly higher contribution at very low frequencies.

Table 5.3 Contribution from different components of the model to pressures in the roof separation zone.

Record	Cp_variance		Contribution, as % of measured spectrum, from					Total Coherence	
	meas- ured	pred- icted	<i>u</i>	<i>v</i>	<i>u</i> ²	<i>v</i> ²	Resi- dual, <i>S_{nn}</i>	mean	std. dev.
<u>Tap 50123</u>									
C539	0.2024	0.2010	29.6	22.8	22.2	24.7	0.7	1.01	0.41
C544	0.1822	0.1755	24.4	23.3	23.6	25.1	3.6	0.99	0.41
<u>Tap 50523</u>									
C539	0.1951	0.1941	28.6	22.6	23.6	24.7	0.5	1.01	0.41
C544	0.1818	0.1783	24.8	23.2	25.3	24.8	1.9	0.99	0.41
<u>Tap 50823</u>									
C539	0.1583	0.1582	27.3	22.7	24.7	25.2	0.1	1.02	0.41
C544	0.1578	0.1564	24.0	24.0	26.3	24.9	0.8	0.99	0.40

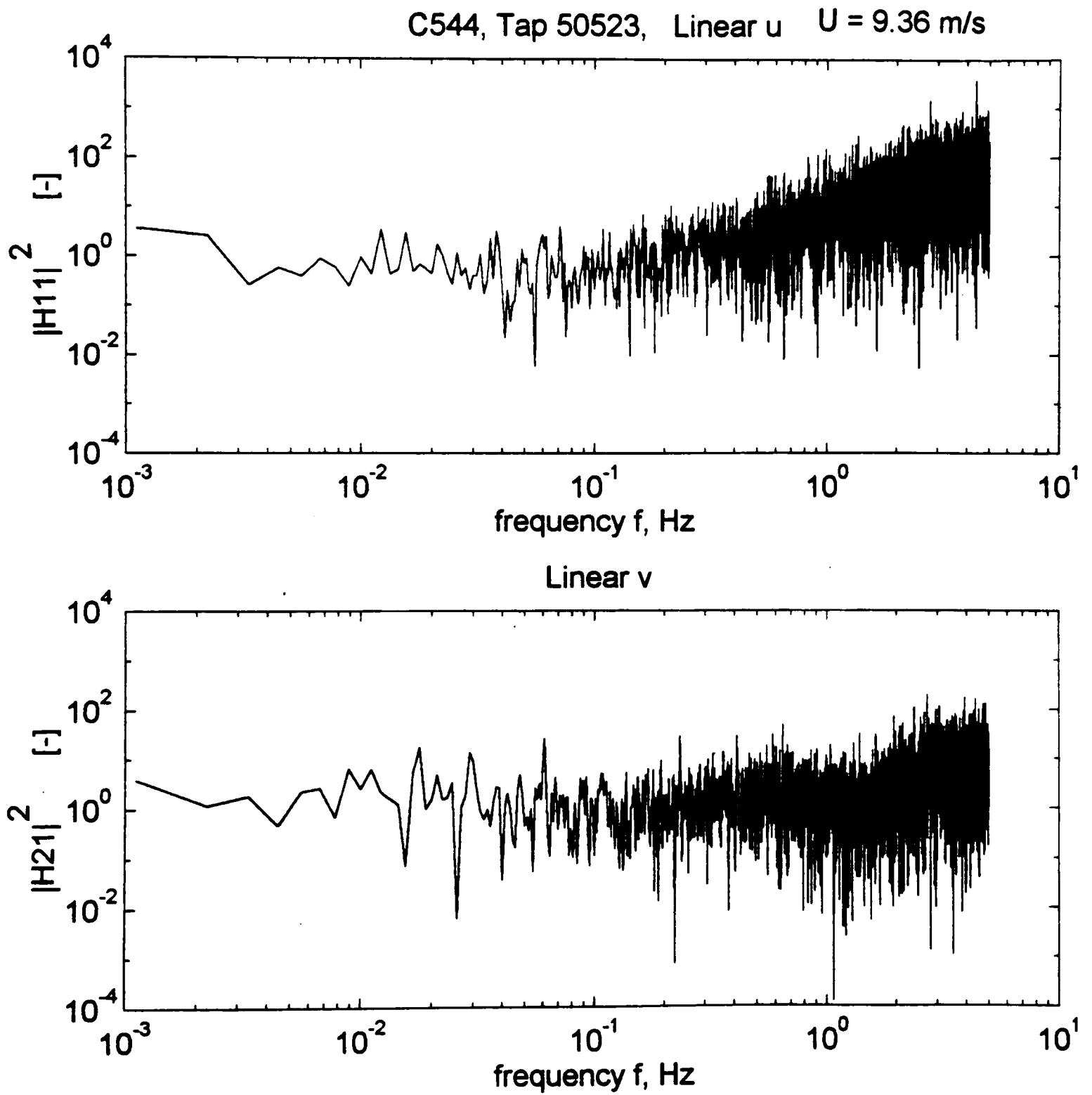


Figure 5.8. Transfer functions for tap 50523 under the separation bubble (C544).
 (a) Linear.

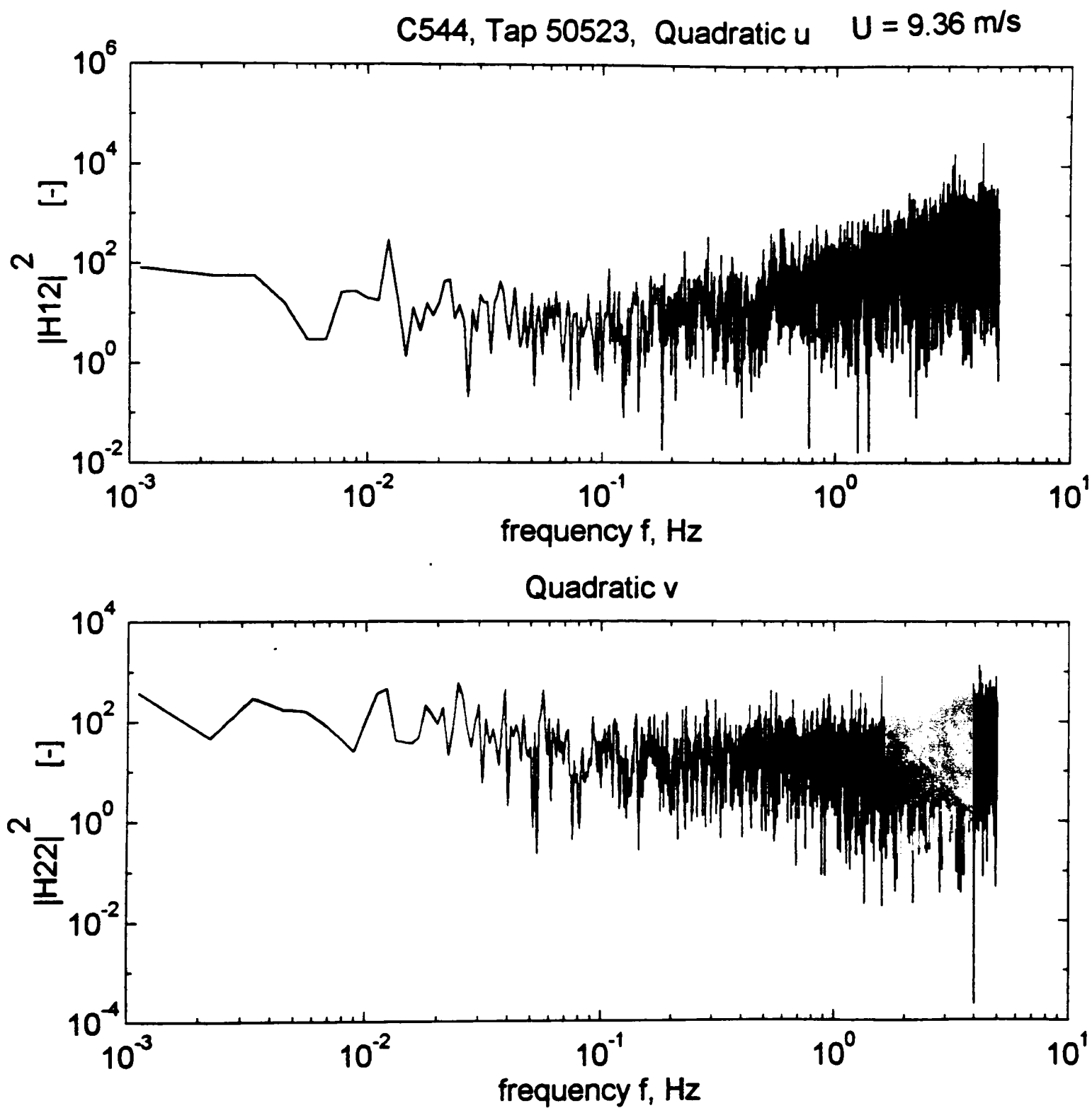


Figure 5.8. Continued. (b) Quadratic.

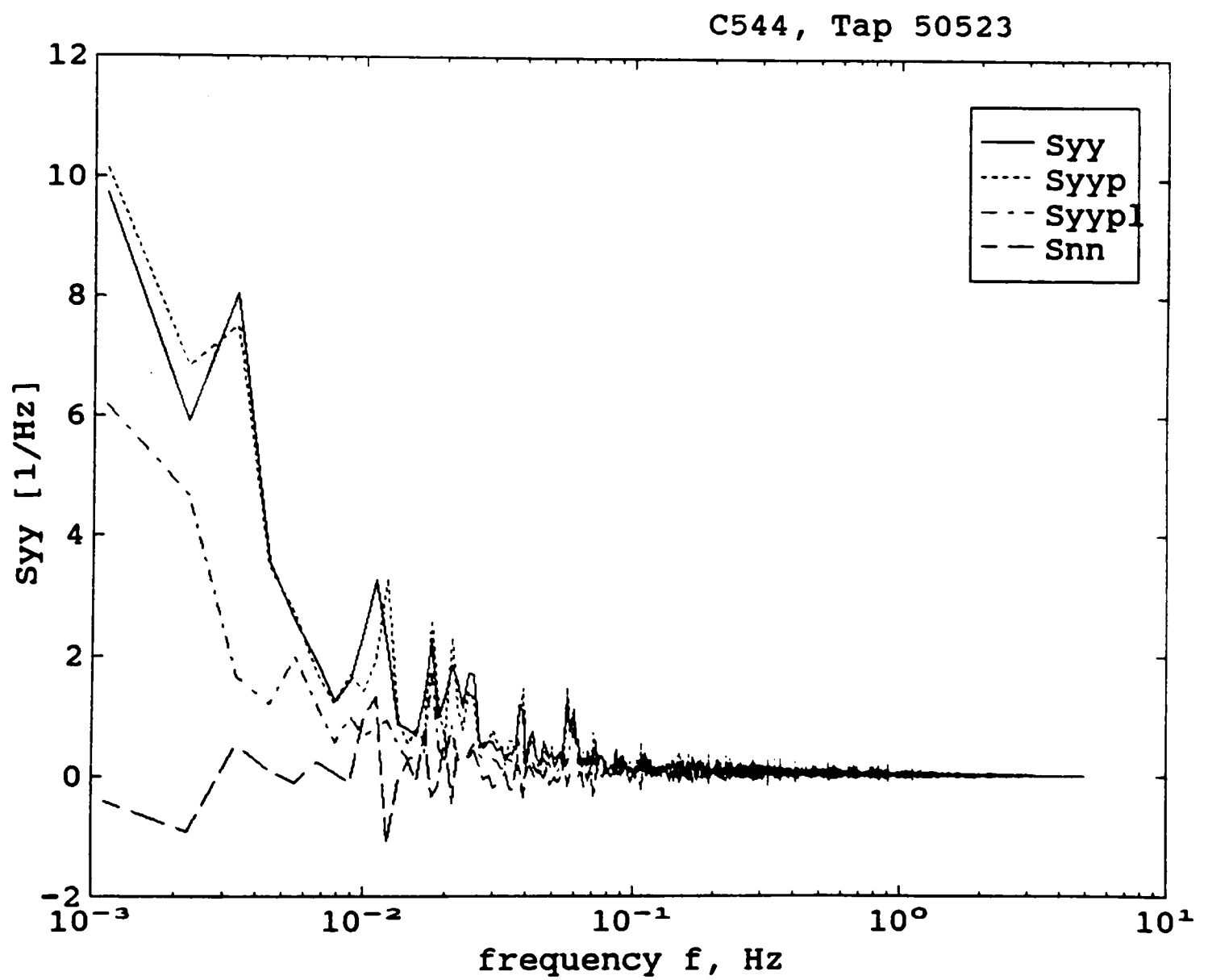


Figure 5.9. Output prediction for tap 50523 under the separation bubble (C544).

C544: Tap 50523

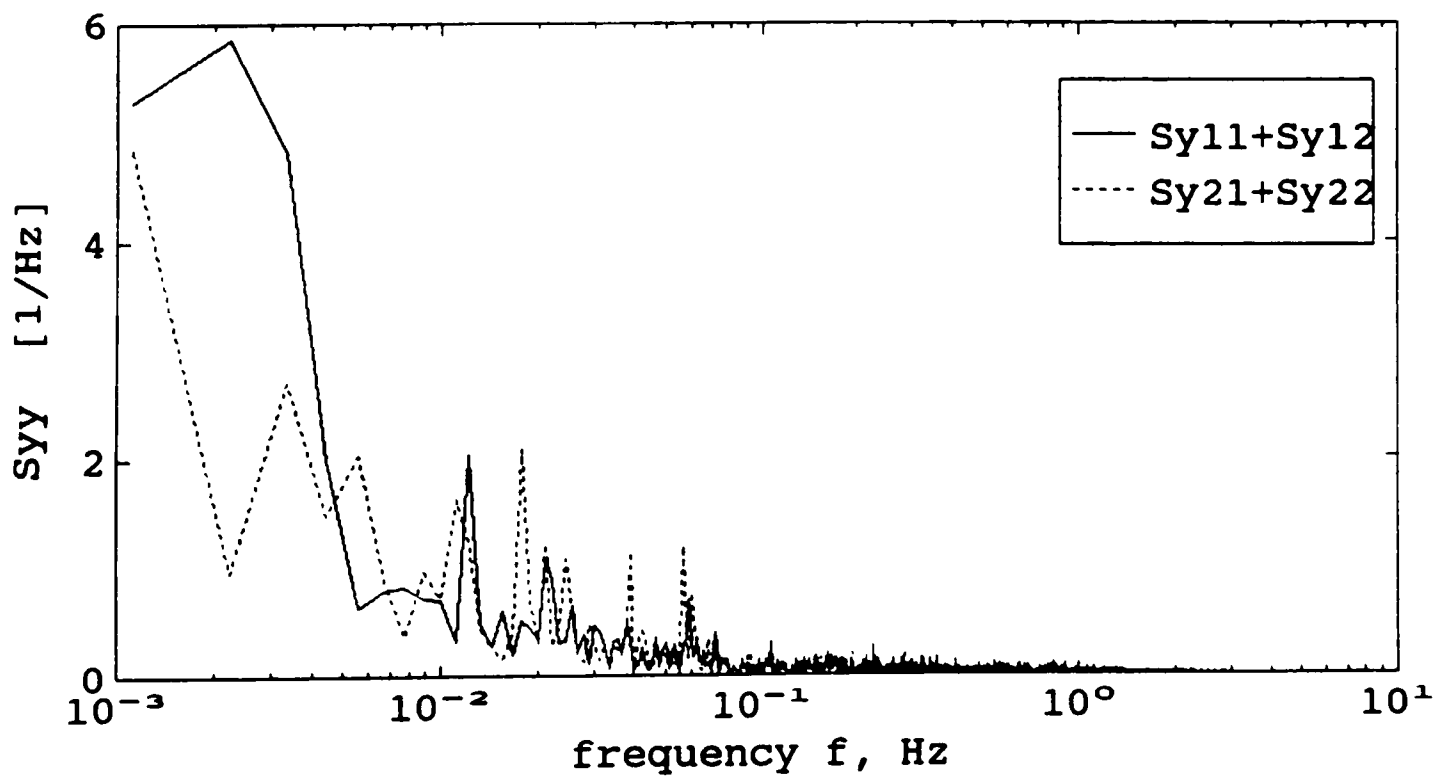
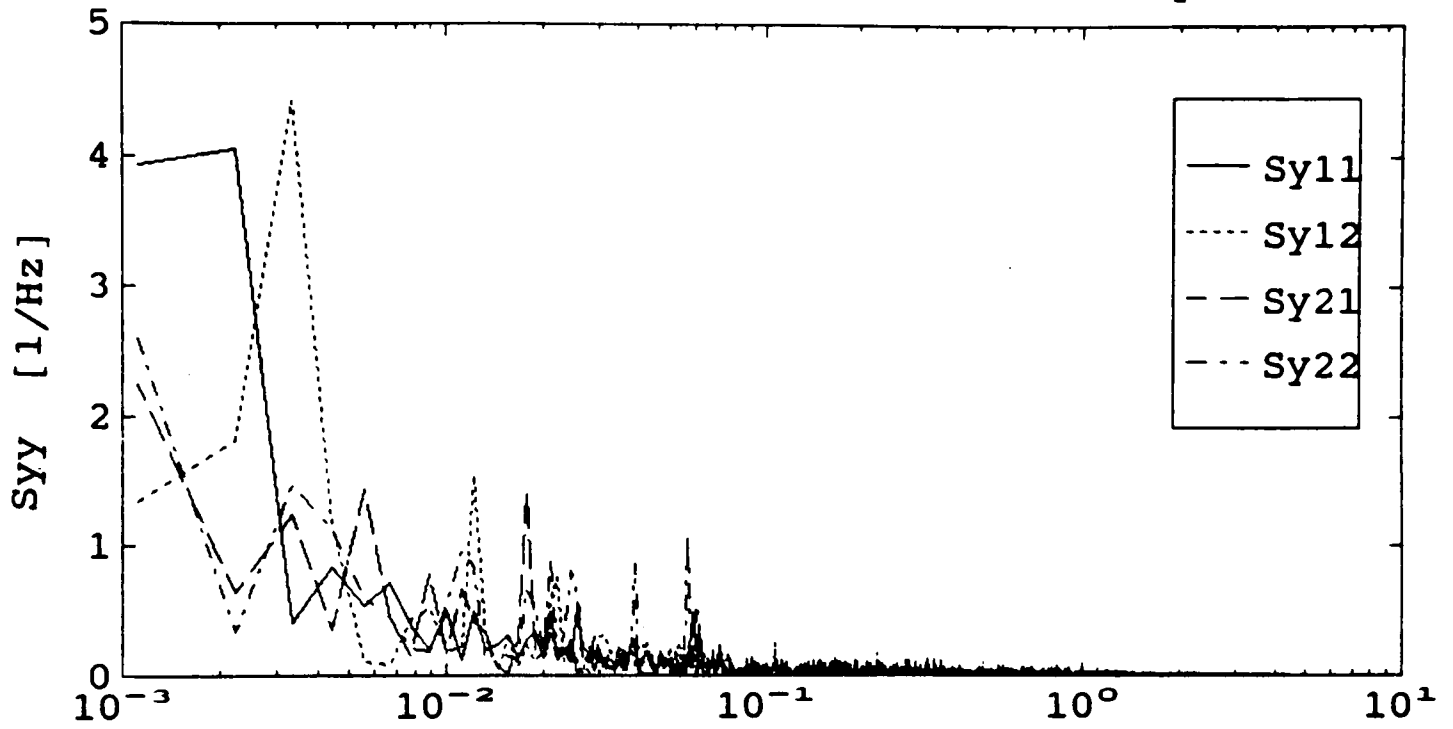


Figure 5.10. Decomposition of pressure-coefficient spectrum for tap 50523 (C544).

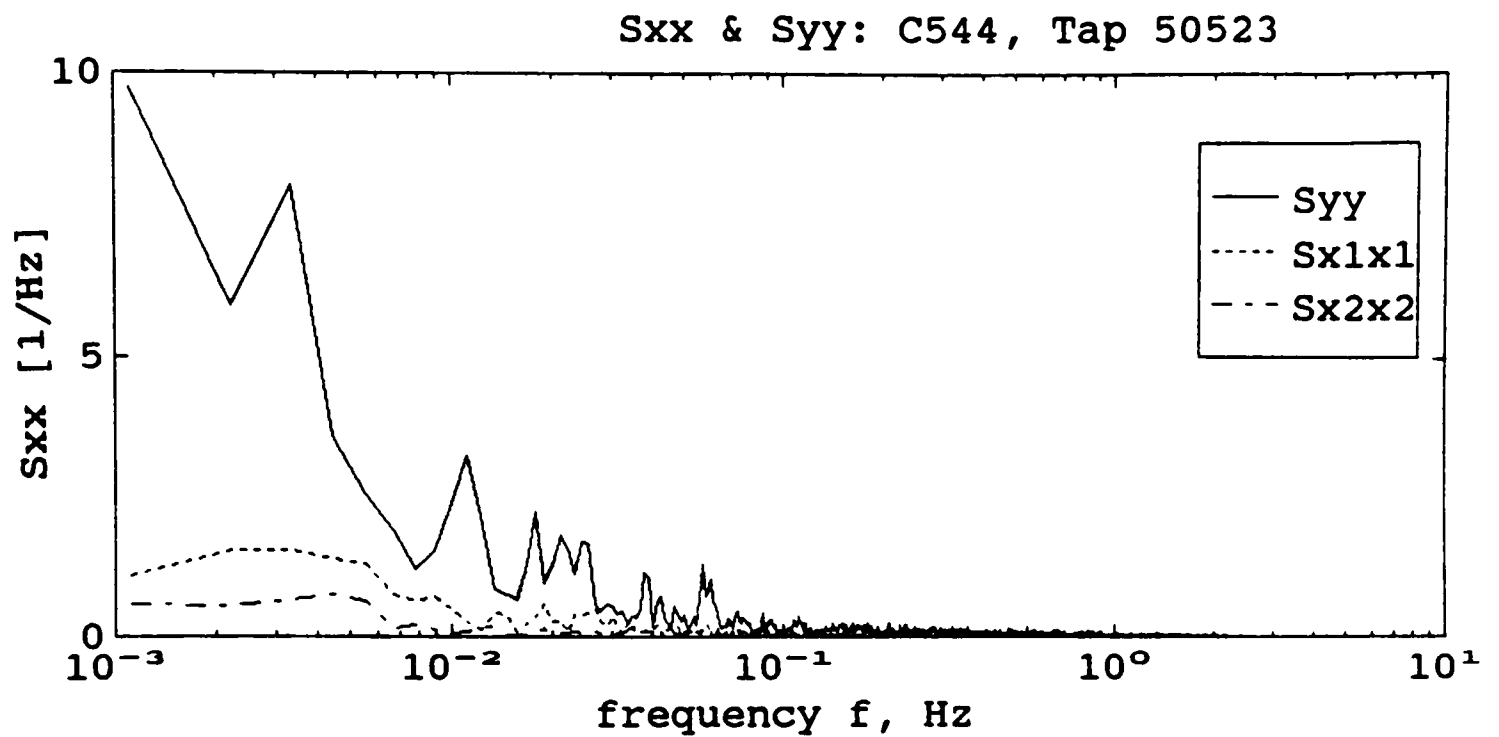


Figure 5.11. Input and output spectra for tap 50523 (C544).

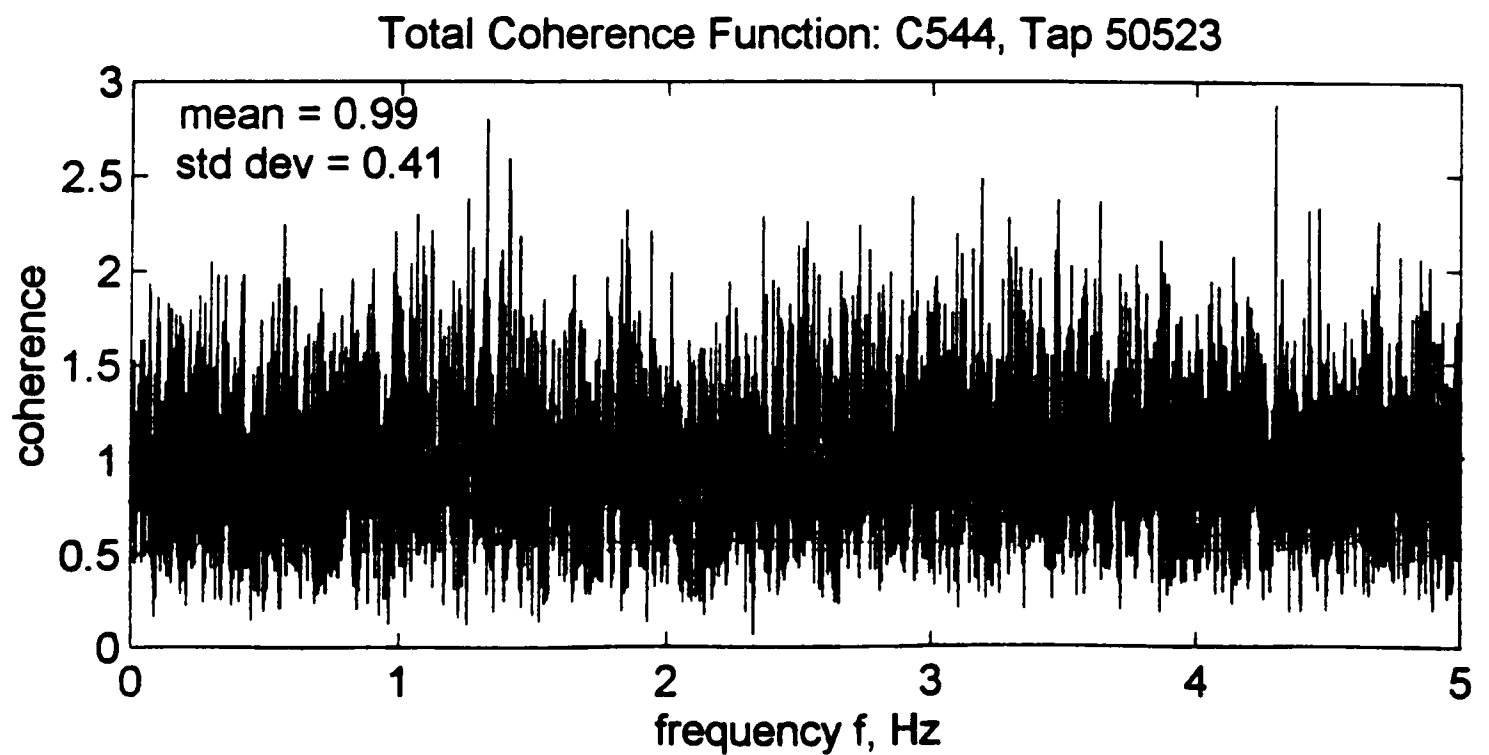


Figure 5.12. Total coherence function for tap 50523 (C544).

Bispectrum of $y=C_p$: Tap 50523, M15N545, $\theta=268$, dyn. pr. = 5.93 kg/m^2

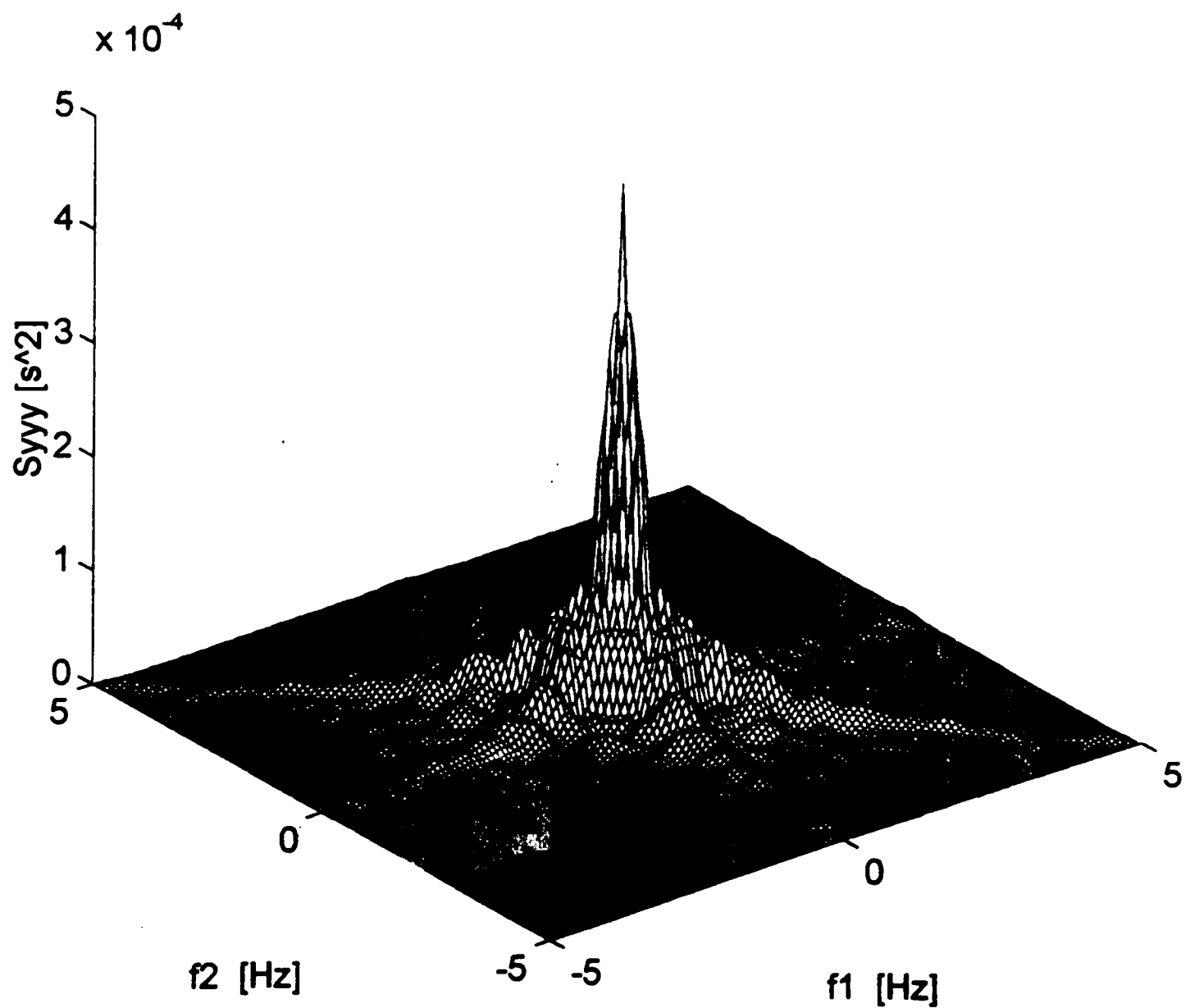


Figure 5.13. Bispectrum of wind pressure for tap 50523 under the separation bubble (M15N545).

5.2.3 Reattachment Region on the Roof

If the building is sufficiently long in the direction of the wind, the flow will reattach to the roof with rapid pressure recovery resulting in reduced suctions. Data were available for three pressure taps in the reattachment region: 51423, 52323 and 52923.

Transfer functions identified from record C544 for a typical tap, 52323, in the reattachment region are shown in Figures 5.14(a) and 5.14(b). Unlike the windward wall and separation region, the linear transfer functions have magnitudes less than one up to about 0.5 Hz, whereas the quadratic transfer functions have a magnitude close to one in that frequency range. This indicates a direct dissipation of the energy in the wind when the flow reattaches. The transfer functions for the other tap 52923 were also similar in form, but those for 51423 were more similar to the separation case. This is because tap 51423 is located in the border region between separation and reattachment. The transfer functions for different records with similar mean angles of attack of the wind are similar with some variations in the quantitative sense. The comparison of the predicted total (S_{yyp}) and linear ($S_{yyp/l}$) pressure-coefficient spectra, the measured pressure-coefficient spectrum (S_{yy}) and the residual spectrum (S_{rm}) is shown in Figure 5.15. The predicted spectrum is seen to match closely with the measured one. It is seen that there is noticeable energy in the high frequency range above 0.5 Hz, unlike the previous flow regions. The spectral decomposition of the predicted spectrum is shown in Figure 5.16. The total coherence function has a similar form as for the previous cases with a mean of 1.01 and a standard deviation of 0.41.

The bispectrum of the pressure-coefficient time history for tap 52323 in the reattachment zone is shown in Figure 5.17 for a typical field record. The bispectrum in this case shows a significant scatter even at frequencies above 2 Hz. There seems to be considerable dissipation of energy from the high frequency components in the flow.

The decomposition of pressure-coefficient spectrum into contributions from the linear and quadratic terms in the model and the total coherence are tabulated in Table 5.4 for the three taps in the reattachment region for two sets of records (C539 and C544). It is observed from Table 5.4 that the linear and quadratic components of the model again have

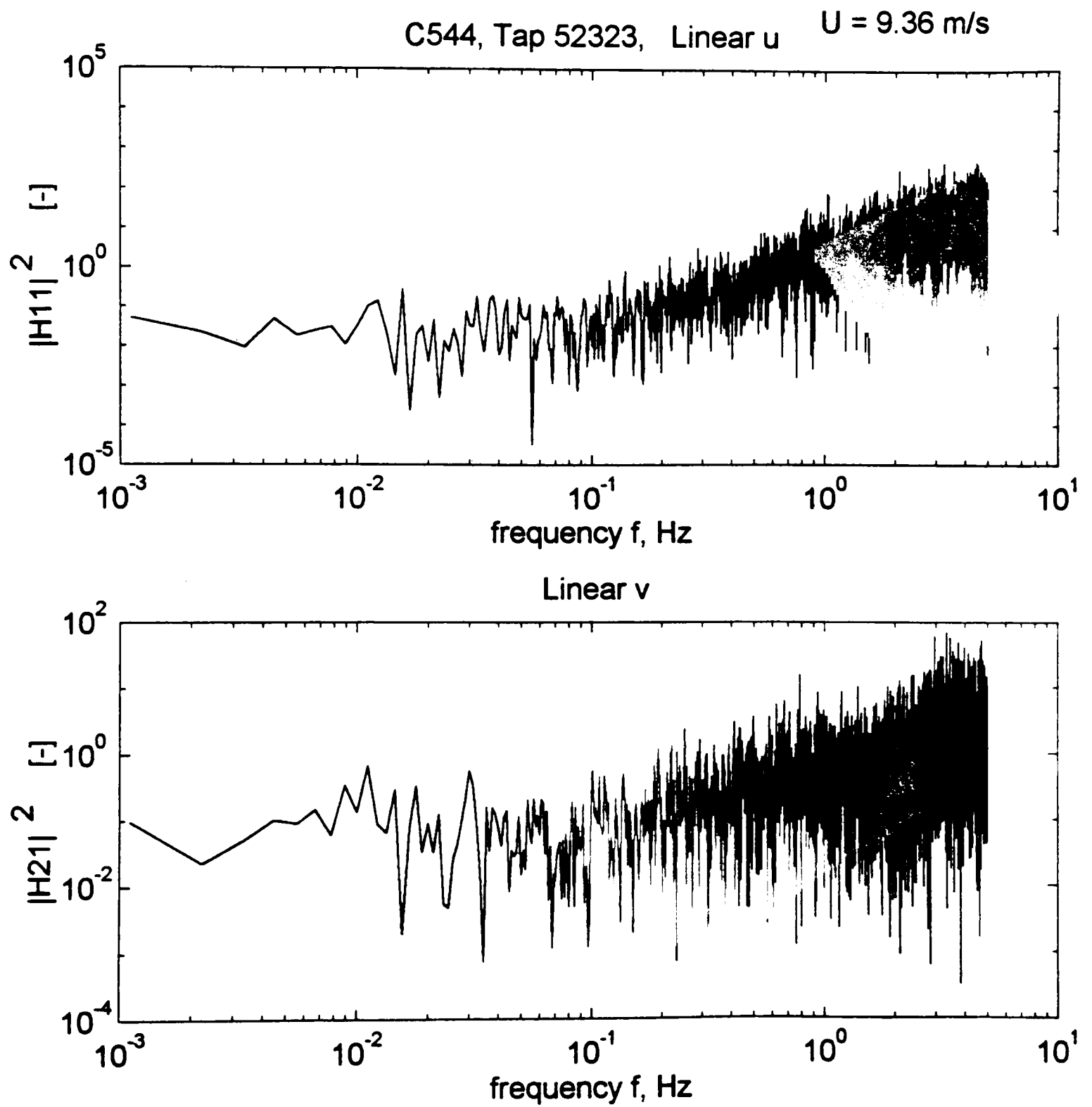


Figure 5.14. Transfer functions for tap 52323 in the reattachment zone (C544).
 (a) Linear.

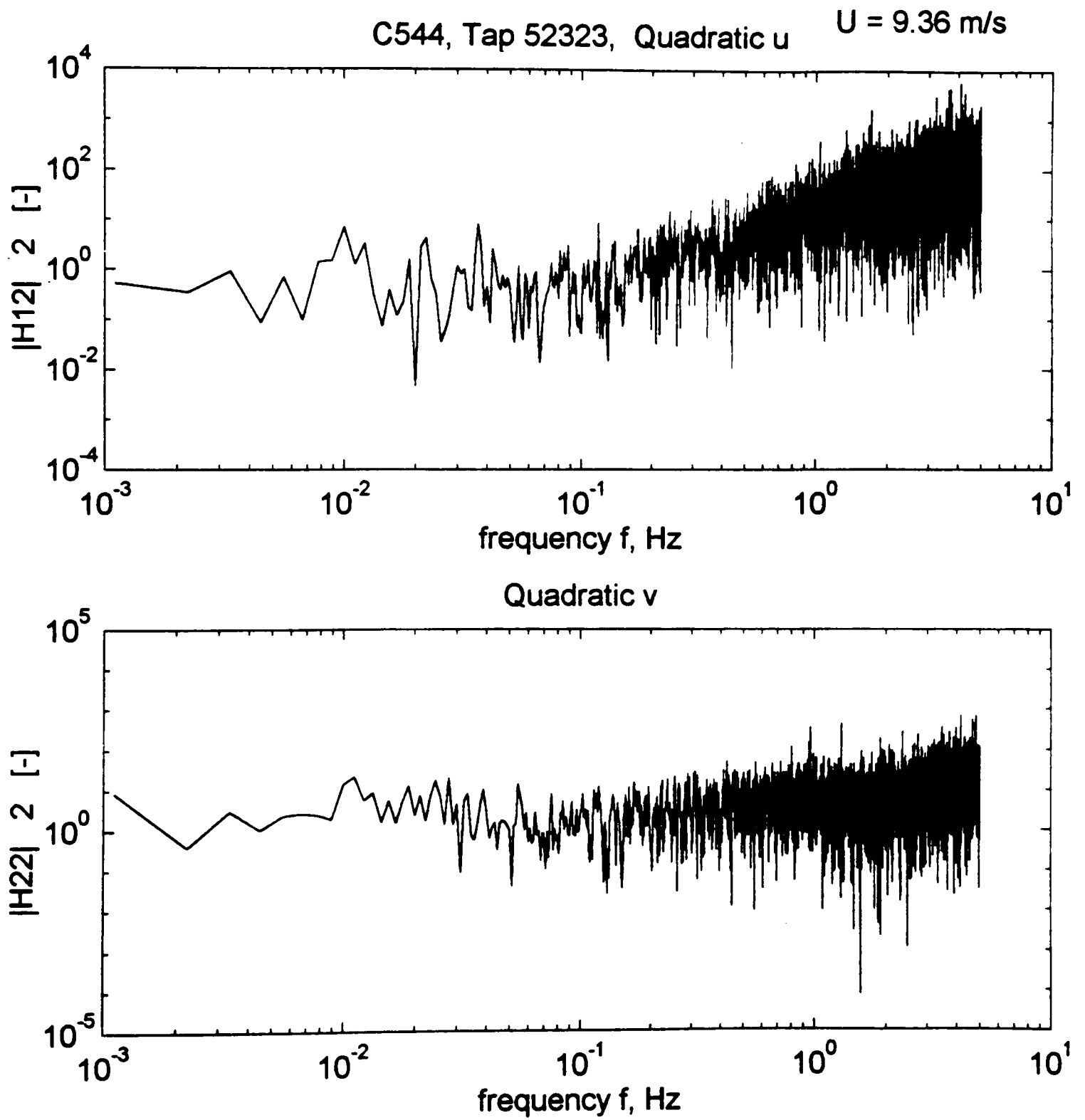


Figure 5.14. Continued. (b) Quadratic.

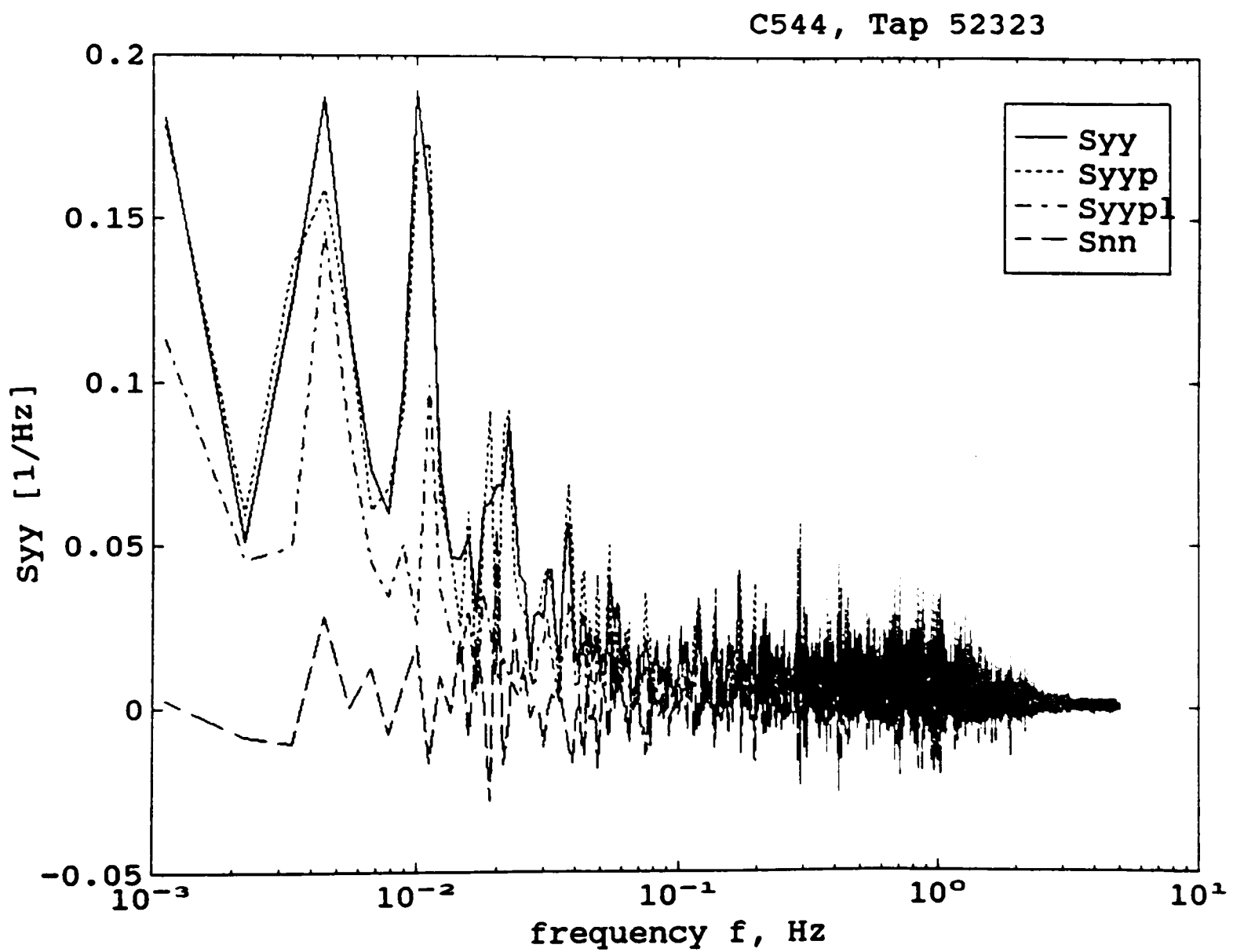


Figure 5.15. Output prediction for tap 52323 in the reattachment zone (C544).

C544: Tap 52323

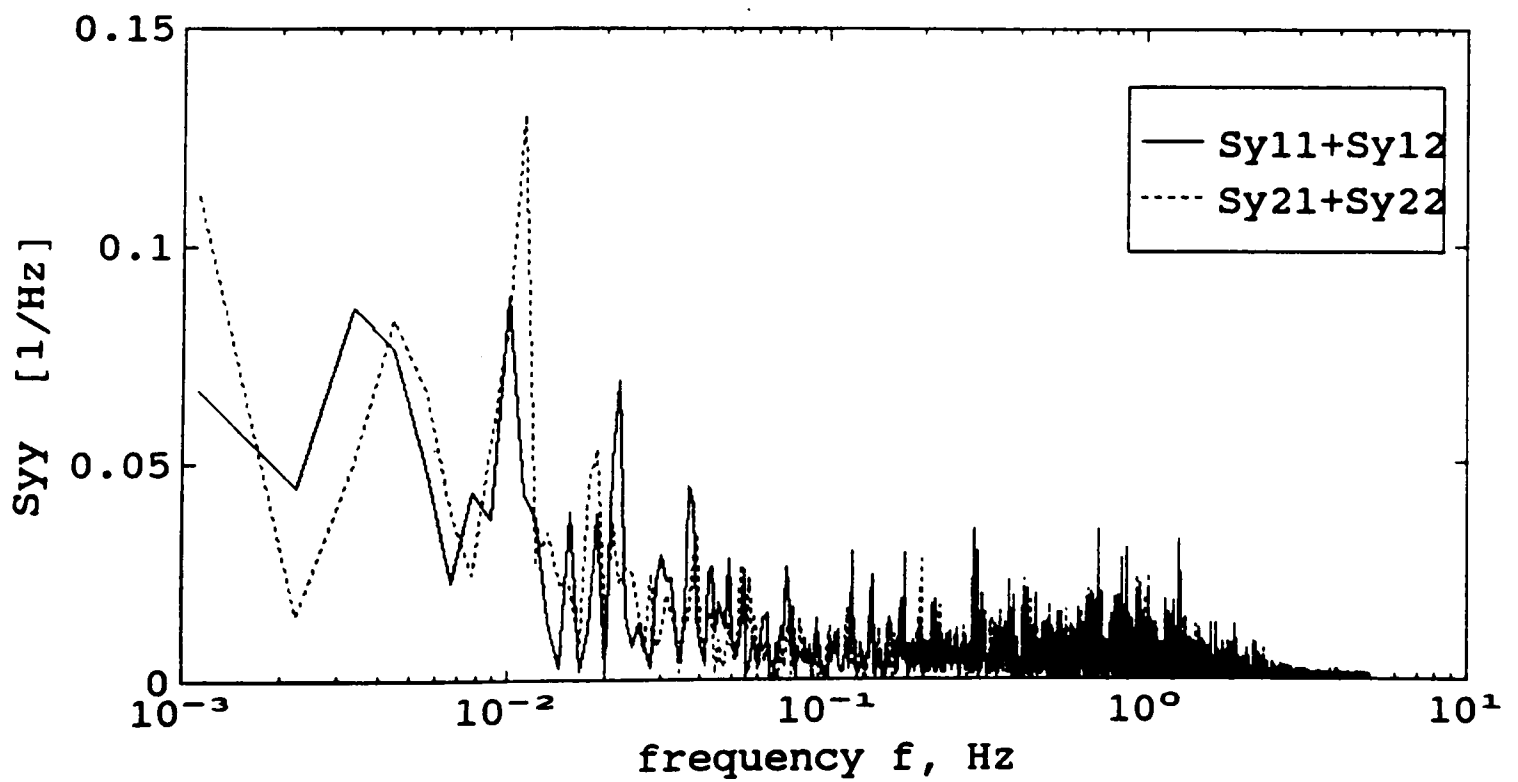
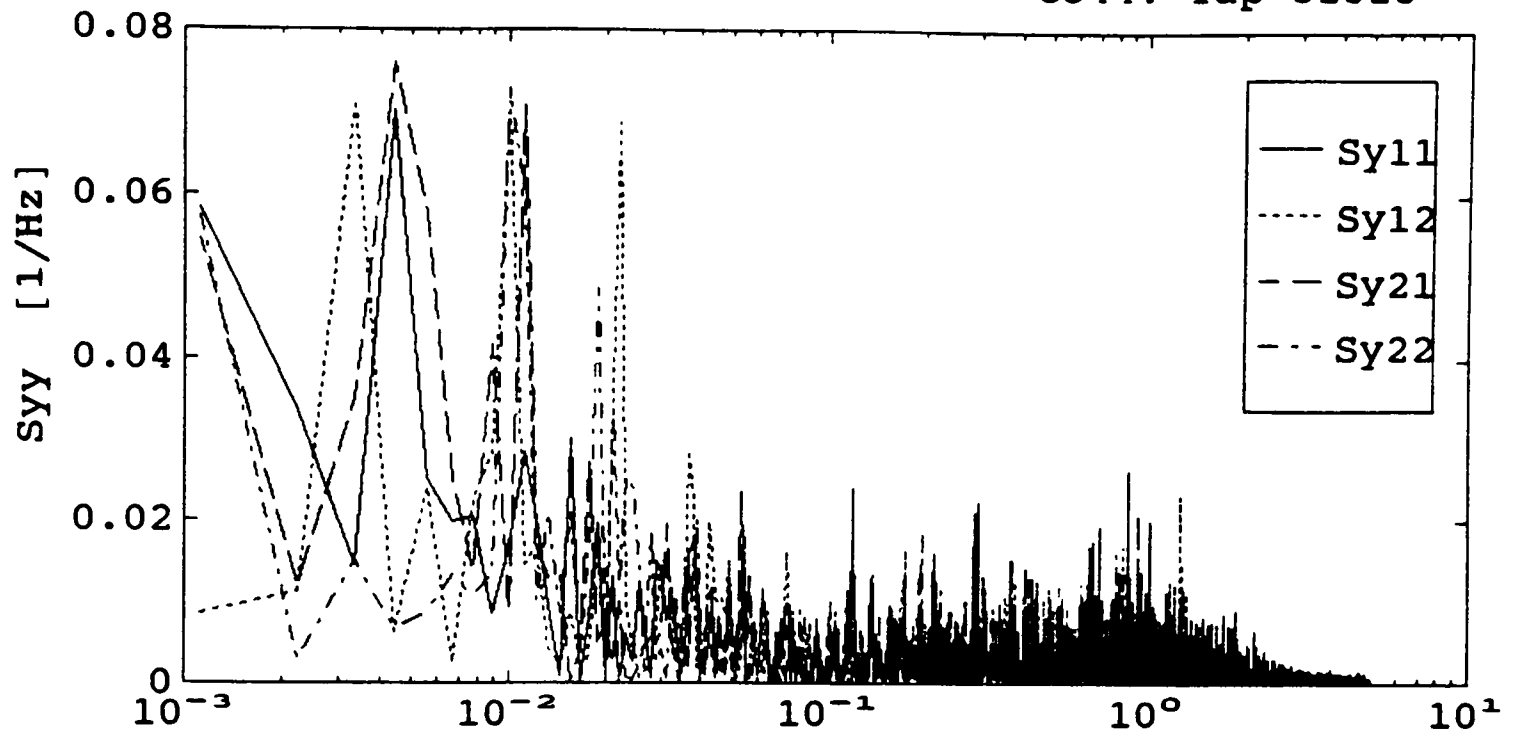


Figure 5.16. Decomposition of pressure-coefficient spectrum for tap 52323 (C544).

Bispectrum of $y=C_p$: Tap 52323, M15N545, $\theta=268$, dyn. pr. = 5.93 kg/m^2

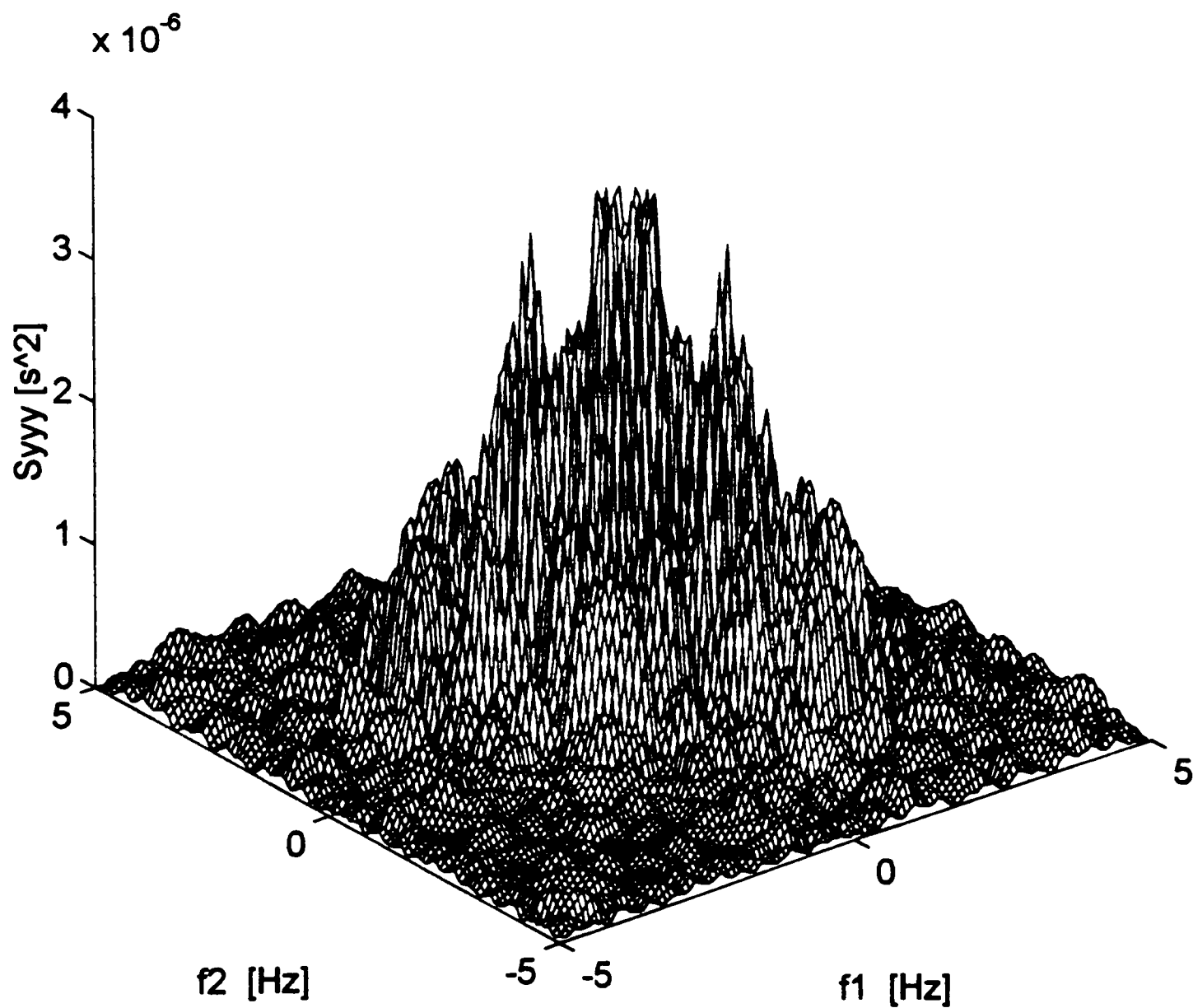


Figure 5.17. Bispectrum of wind pressure for tap 52323 in the roof reattachment zone (M15N545).

a comparable contribution to the pressure variance. It is seen from Figure 5.15 that the reattachment zone has the highest contribution to the variance from high frequencies.

Table 5.4 Contribution from different components of the model to pressures in the roof reattachment zone.

Record	Cp_variance		Contribution, as % of measured spectrum, from					Total Coherence	
	meas- ured	pred- icted	<i>u</i>	<i>v</i>	<i>u</i> ²	<i>v</i> ²	Resid- ual, <i>S_{mn}</i>	mean	std. dev.
<u>Tap 51423</u>									
C539	0.0692	0.0694	26.5	23.7	24.8	25.3	-0.4	1.02	0.41
C544	0.0700	0.0704	23.5	24.8	25.8	26.5	-0.1	1.01	0.41
<u>Tap 52323</u>									
C539	0.0222	0.0216	24.0	24.1	24.5	24.8	2.6	1.00	0.41
C544	0.0242	0.0243	25.0	23.8	26.1	25.1	-0.1	1.00	0.41
<u>Tap 52923</u>									
C539	0.0114	0.0113	24.3	26.6	22.0	26.9	0.2	1.00	0.42
C544	0.0106	0.0106	25.0	24.8	25.4	24.7	0.1	1.00	0.40

5.2.4 Leeward Wall or Wake Region

The wake is the name given to the turbulent flow behind a bluff body from which momentum has been lost as drag on the body. Only the near wake, which is the region of recirculating flow immediately behind the building, will be considered here. Data from two pressure taps, 22306 and 22312, were available. Tap 22306 is located near the middle of the leeward wall and Tap 22312 near the top of the leeward wall where the flow again separates from roof reattachment, but with much less strength than separation from the roof.

Transfer functions identified from record C544 for tap 22306 on the leeward wall are shown in Figures 5.18(a) and 5.18(b). The transfer functions are quite similar to those for the reattachment region. The transfer functions for tap 22312 were also similar in form. The comparison of the predicted total (*S_{yyp}*) and linear (*S_{yyp/l}*) pressure-coefficient

spectra, the measured pressure-coefficient spectrum (S_{yy}) and the residual spectrum (S_{nn}) is shown in Figure 5.19. The spectral decomposition of the predicted spectrum is shown in Figure 5.20. The total coherence function has a similar form as for the previous cases with mean of 1.0 and standard deviation of 0.42. The bispectrum of the pressure-coefficient time history for tap 22306 is shown in Figure 5.21 for a typical field record. The bispectrum shows only a sharp low frequency peak.

The decomposition of pressure-coefficient spectrum into contributions from the linear and quadratic terms in the model and the the total coherence are tabulated in Table 5.5 for the two taps on the leeward wall. It is observed from Table 5.5 that the quadratic v component has a higher contribution compared to the others. This is indicative of changes in wind direction being instrumental in dissipating energy by aiding in inducing vortices in the flow in the near wake region. It is also seen that the quadratic u term has the lowest contribution. This means that the pressure in this region is least influenced by direct dissipation of energy from the along-wind flow. This is expected as this region has the least direct contact with the undisturbed upstream flow.

Table 5.5 Contribution from different components of the model to pressures on the leeward wall.

Record	Cp_variance		Contribution, as % of measured spectrum, from					Total Coherence	
	meas- ured	pred- icted	u	v	u^2	v^2	Resid- ual, S_{nn}	mean	std. dev.
<u>Tap 22306</u>									
C539	0.0096	0.0099	22.6	29.1	17.9	33.8	-3.4	1.02	0.41
C544	0.0053	0.0052	25.1	23.5	23.8	24.5	3.1	1.00	0.42
CS070	0.0076	0.0077	23.4	24.2	21.2	33.0	-1.8	1.00	0.40
CS077	0.0054	0.0053	32.4	17.7	17.5	32.0	0.4	1.02	0.40
<u>Tap 22312</u>									
C539	0.0105	0.0109	23.1	29.2	19.0	31.9	-3.2	1.01	0.42
C544	0.0066	0.0065	25.2	25.0	24.2	24.4	-1.2	1.01	0.41

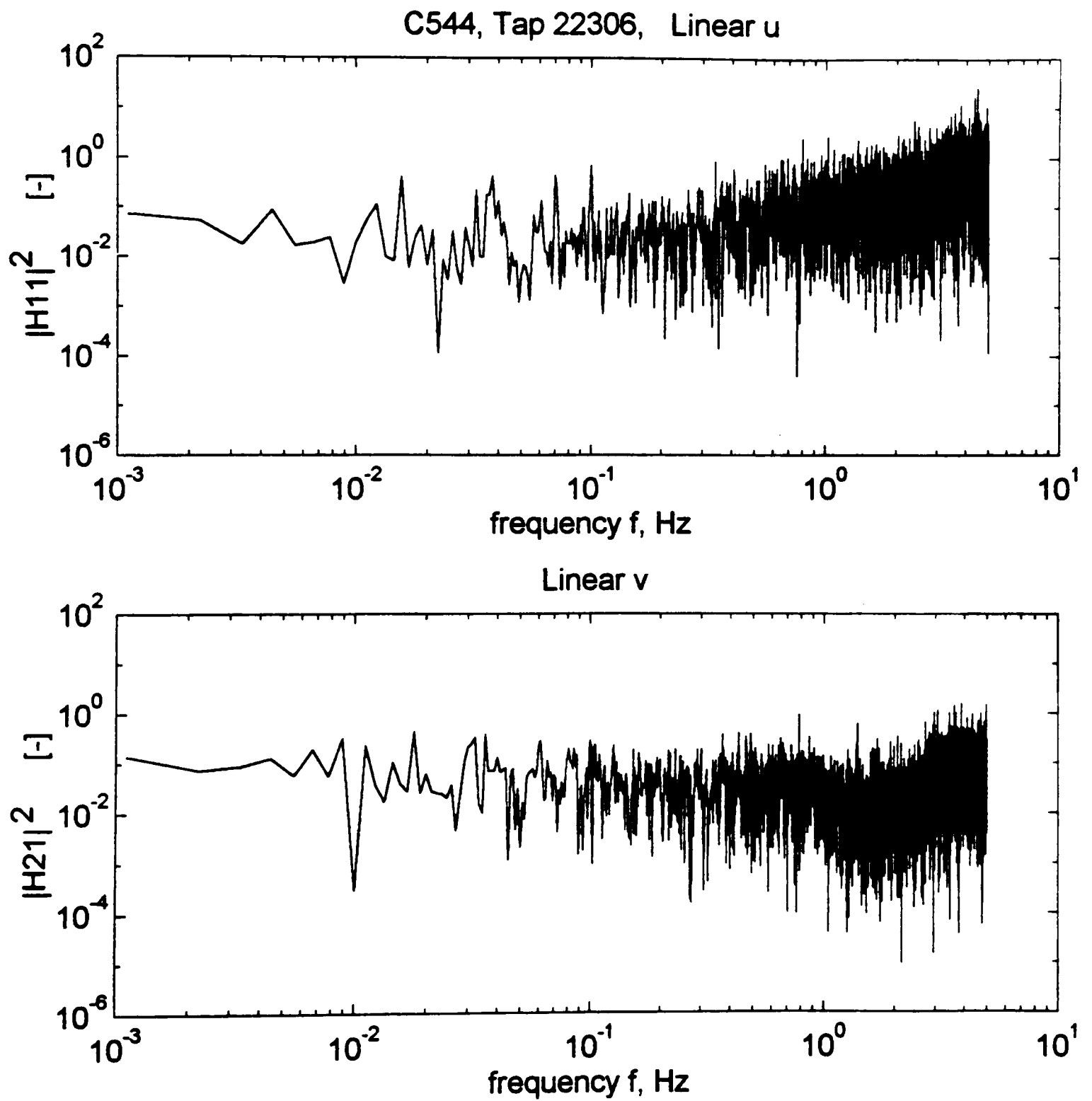
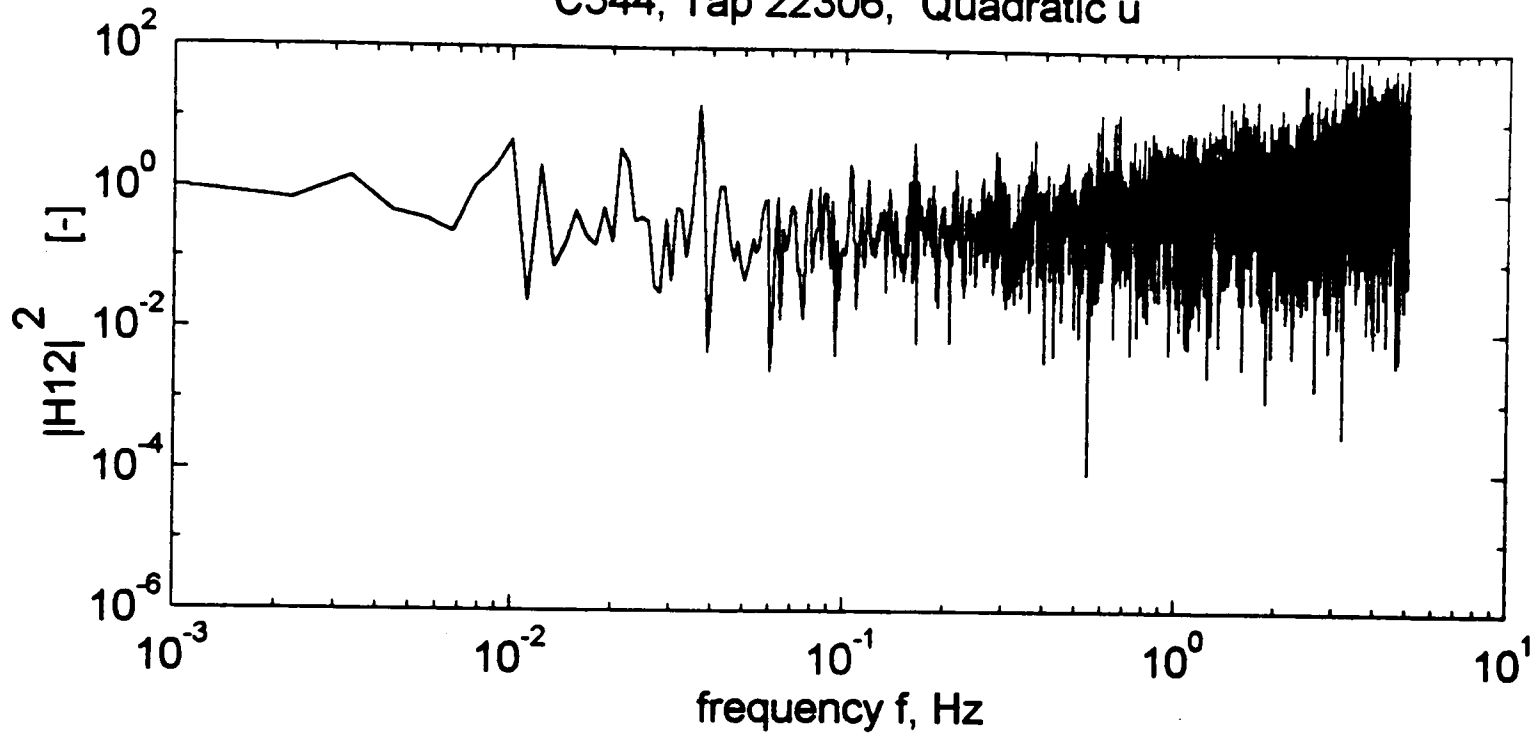


Figure 5.18. Transfer functions for tap 22306 on the leeward wall (C544). (a) Linear.

C544, Tap 22306, Quadratic u



Quadratic v

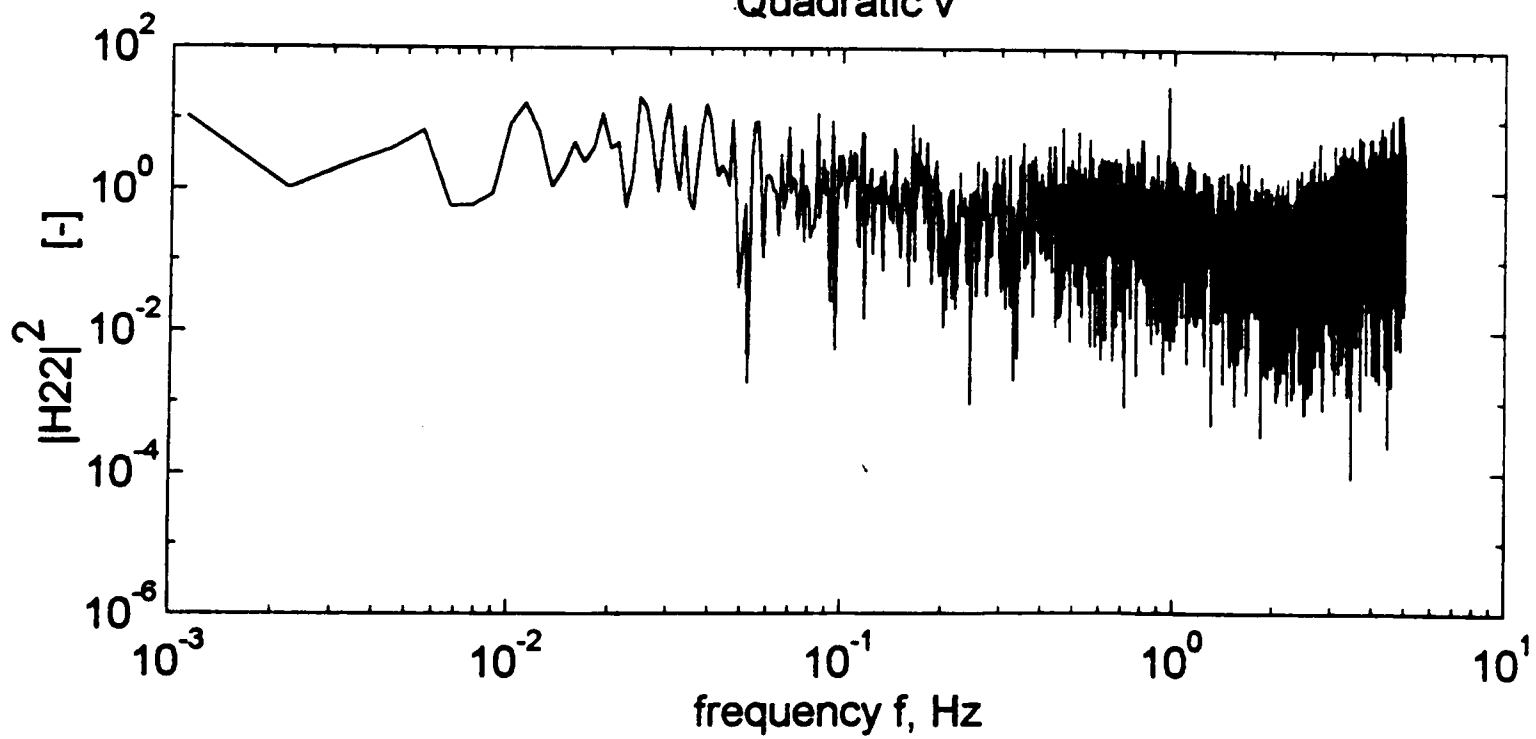


Figure 5.18. Continued. (b) Quadratic

C544, Tap 22306

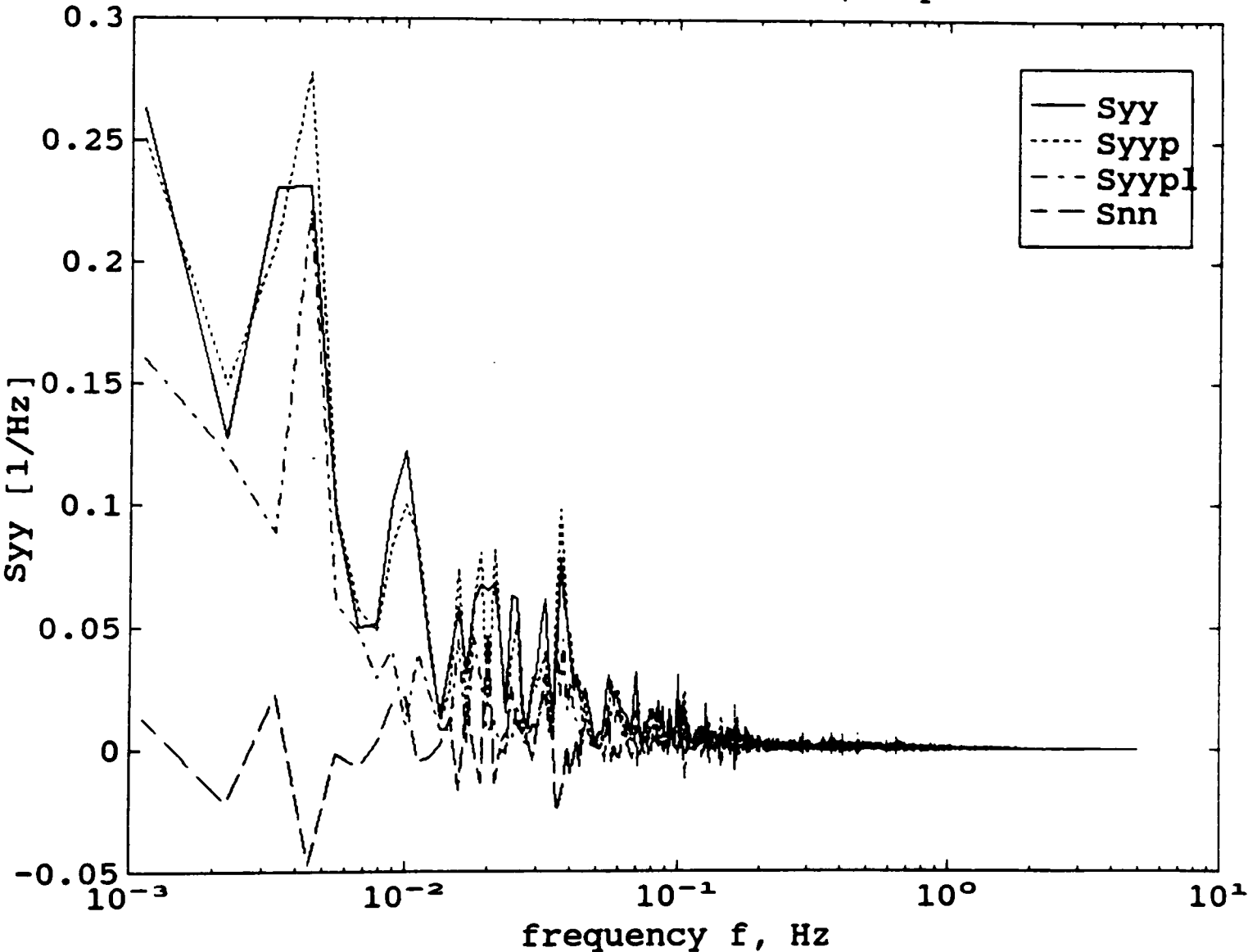


Figure 5.19. Output prediction for tap 22306 on the leeward wall (C544).

C544: Tap 22306

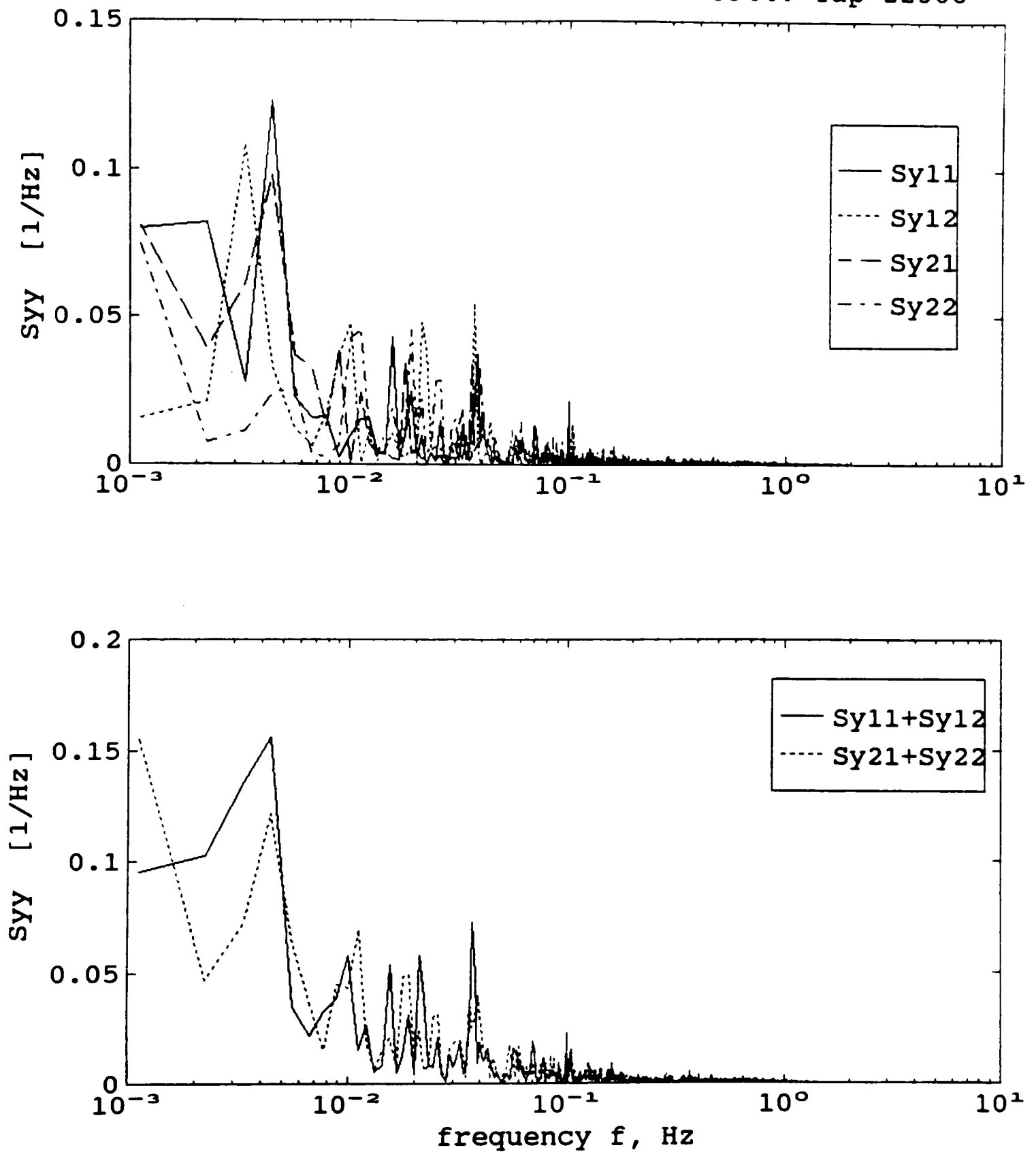


Figure 5.20. Decomposition of pressure-coefficient spectrum for tap 22306 on the leeward wall (C544).

Bispectrum of $y=C_p$: Tap 22306, M15N545, $\theta=268$, dyn. pr.=5.93 kg/m²

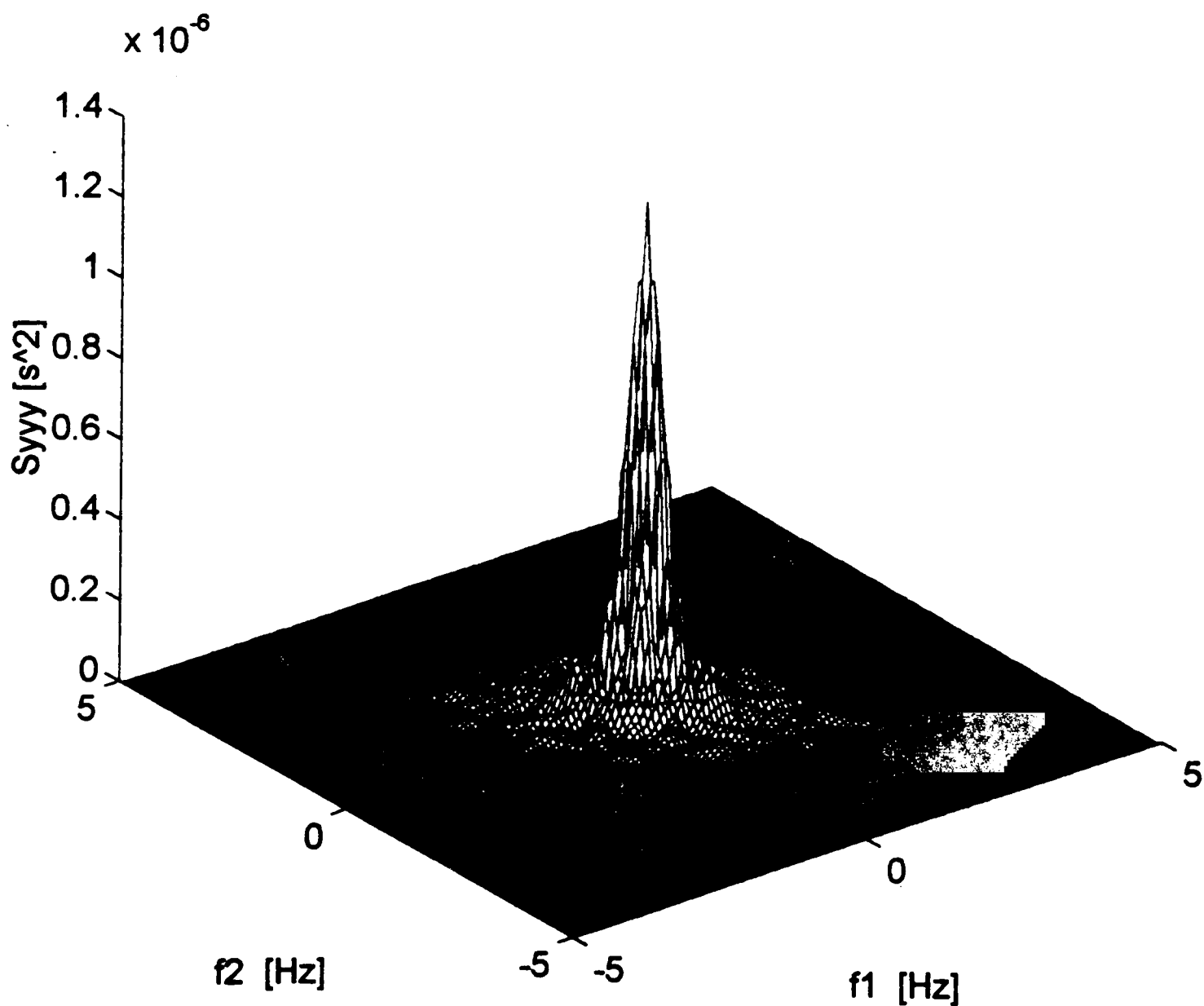


Figure 5.21. Bispectrum of wind pressure for tap 22306 on the leeward wall (M15N545).

5.2.5 Side Walls

The flow over the windward face separates from the building surface along the upstream edge of the side wall leaving each face in a bubble of separated flow. The separated flow will reattach as for the roof, if the wall is long enough. The pressure distribution on the side walls is thought to be similar to that on the roof. One difference on roofs is that the velocity profile and downwards momentum of the Reynolds stress both assist the reattachment to occur sooner. Data was available for taps 11407 and 31407, one each near the middle of the shorter side walls. These taps are located near the location where the flow is expected to reattach with the side walls.

Transfer functions identified from record C544 for tap 31407 on the south side wall are shown in Figures 5.22(a) and 5.22(b). The transfer functions are similar to those on the windward wall and separation zones, except that they have a magnitude of slightly over one for the linear v term at the very low frequency end. The transfer functions for tap 11407 were also similar in form. The comparison of the predicted total (S_{yyp}) and linear ($S_{yyp/l}$) pressure-coefficient spectra, the measured pressure-coefficient spectrum (S_{yy}) and the residual spectrum (S_{rm}) is shown in Figure 5.23. The spectral decomposition of the predicted spectrum is shown in Figure 5.24. The total coherence function has a similar form as for the previous cases with a mean of 1.02 a standard deviation of 0.41. The bispectrum of the pressure-coefficient time history for tap 31407 is shown in Figure 5.25 for a typical field record. The bispectrum shows a low frequency peak slightly broader than that for the windward wall.

The decomposition of pressure-coefficient spectrum into contributions from the linear and quadratic terms in the model and the total coherence are tabulated in Table 5.6 for the two taps on the side walls. It is observed from Table 5.6 that, for majority of the records, the linear v component has the highest contribution compared to the others. This is indicative of changes in wind direction being instrumental in modifying the flow resulting in producing pressures on the side walls. It is also seen that the contribution from the two linear terms is higher than the two quadratic terms for most of the cases shown. This shows that the pressures on the side walls are more influenced by modification of the flow.

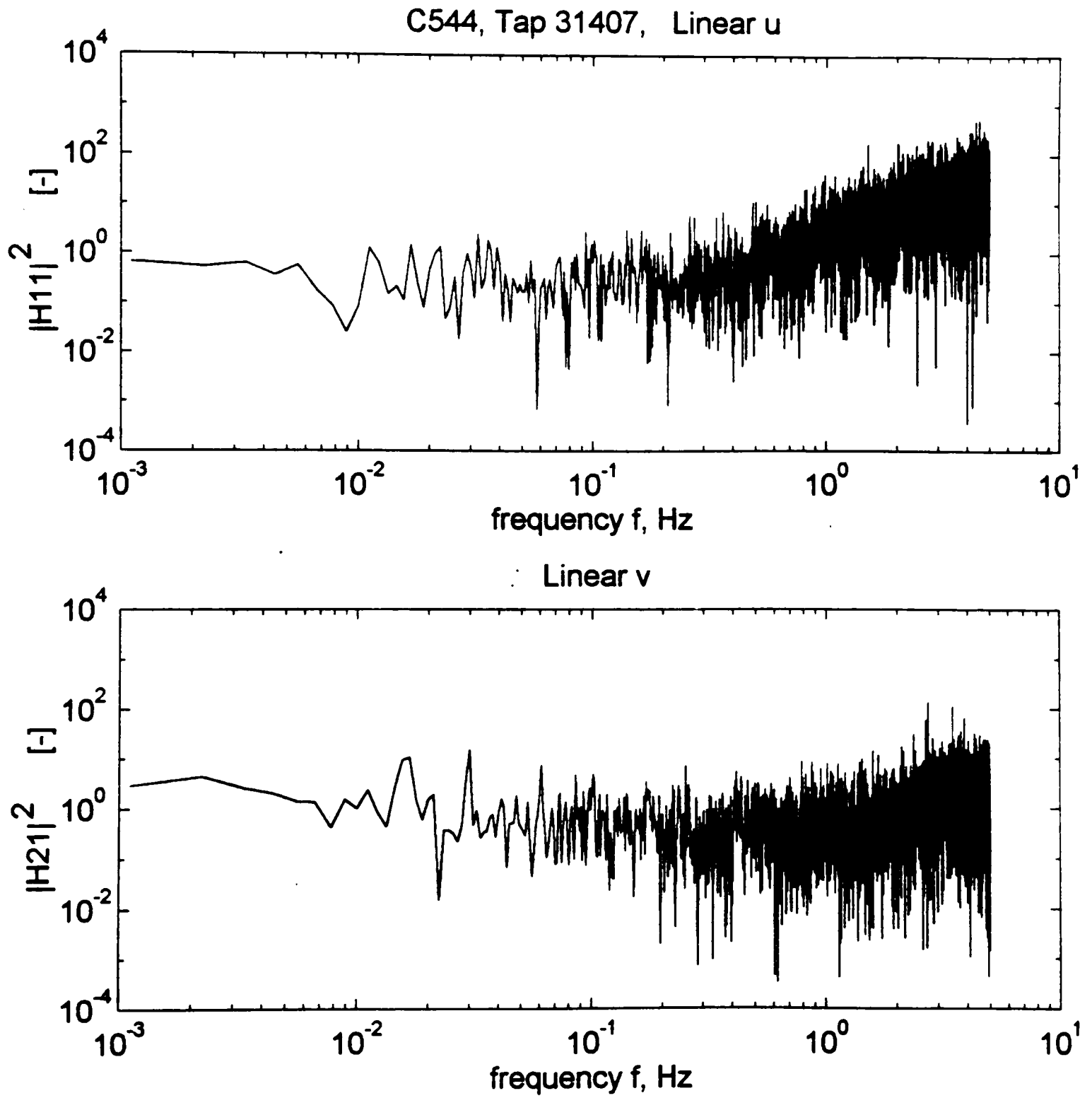


Figure 5.22. Transfer functions for tap 31407 on the side wall (C544). (a) Linear.

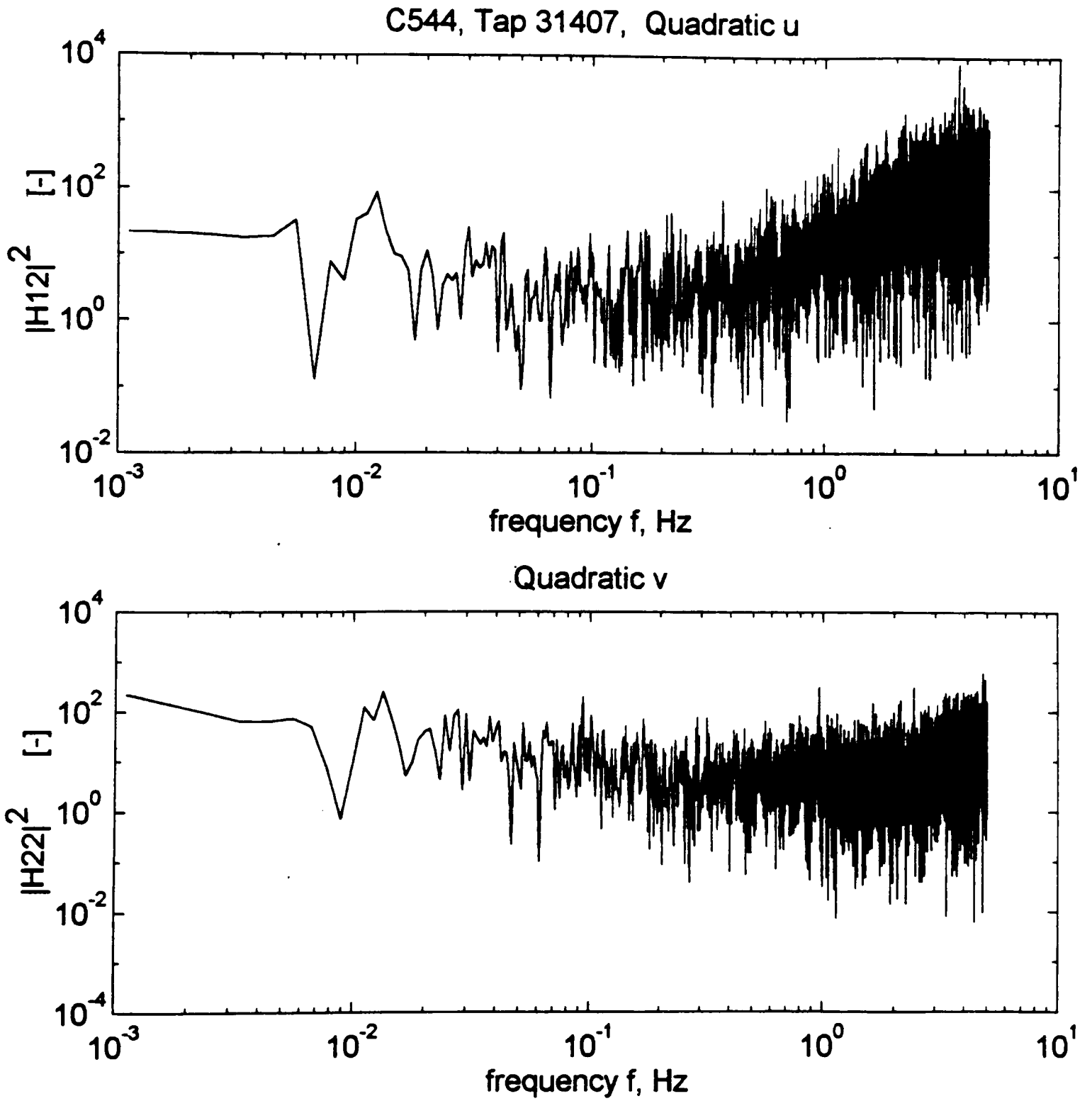


Figure 5.22. Continued. (b) Quadratic.

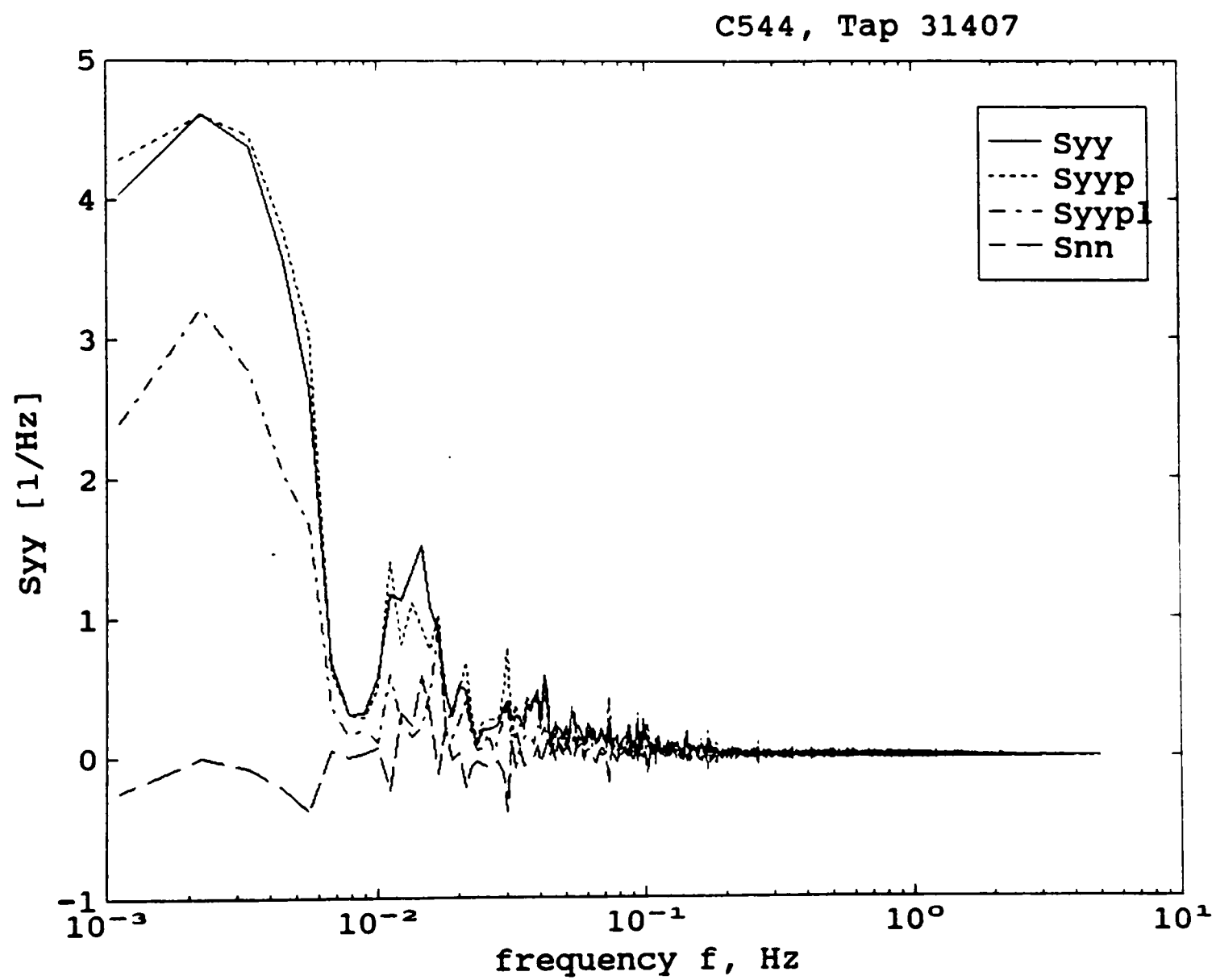


Figure 5.23. Output prediction for tap 31407 on the side wall (C544).

C544: Tap 31407

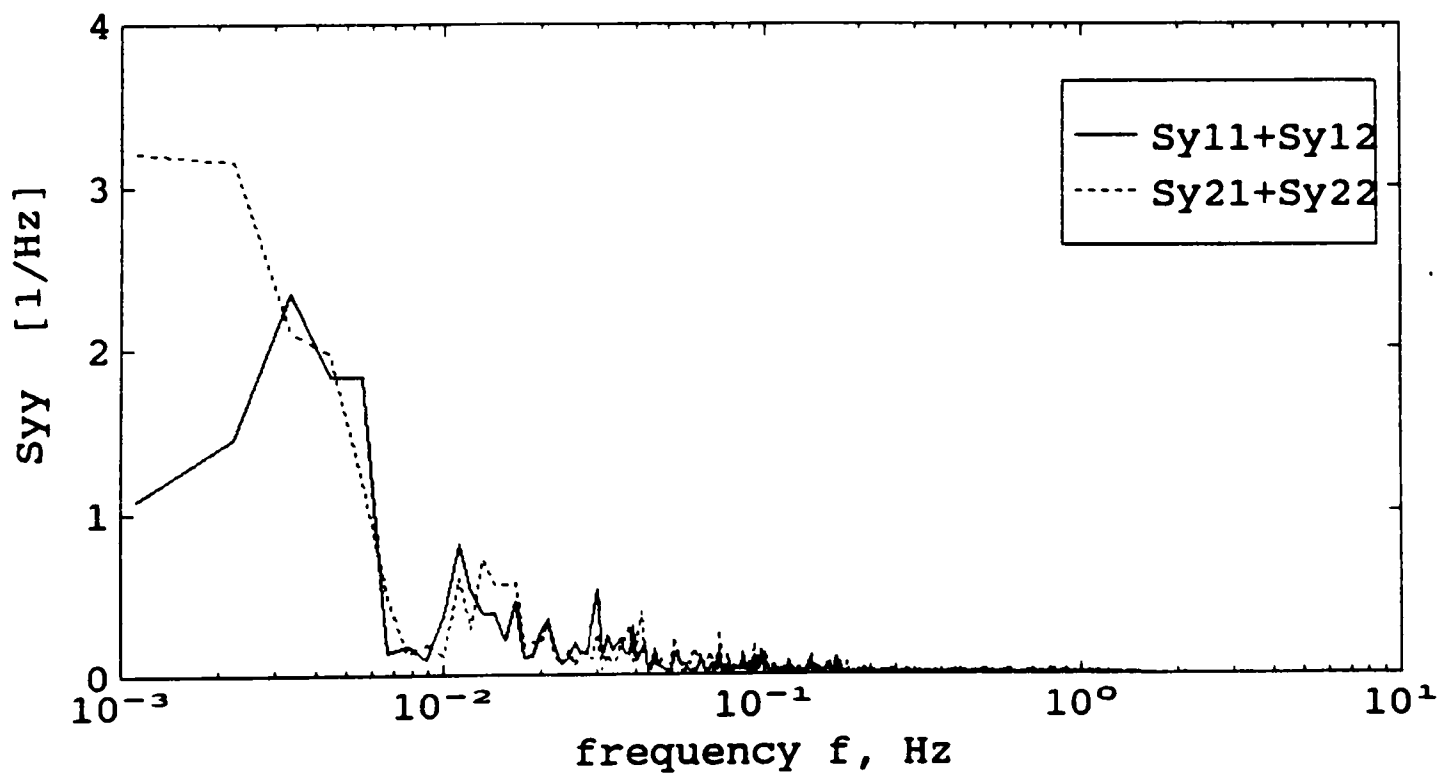
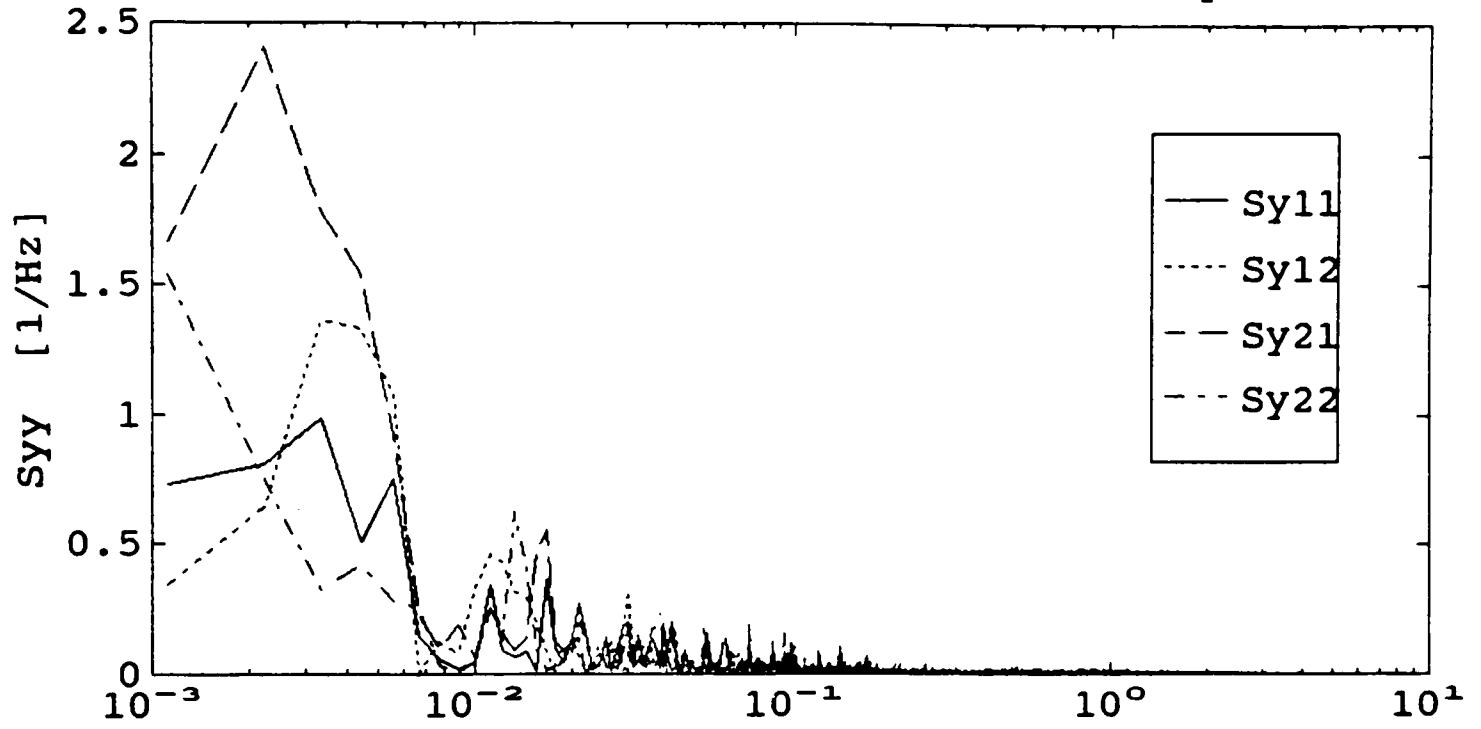


Figure 5.24. Decomposition of pressure-coefficient spectrum for tap 31407 (C544).

Bispectrum of $y=C_p$: Tap 31407, M15N545, $\theta=268$, dyn. pr.=5.93 kg/m²

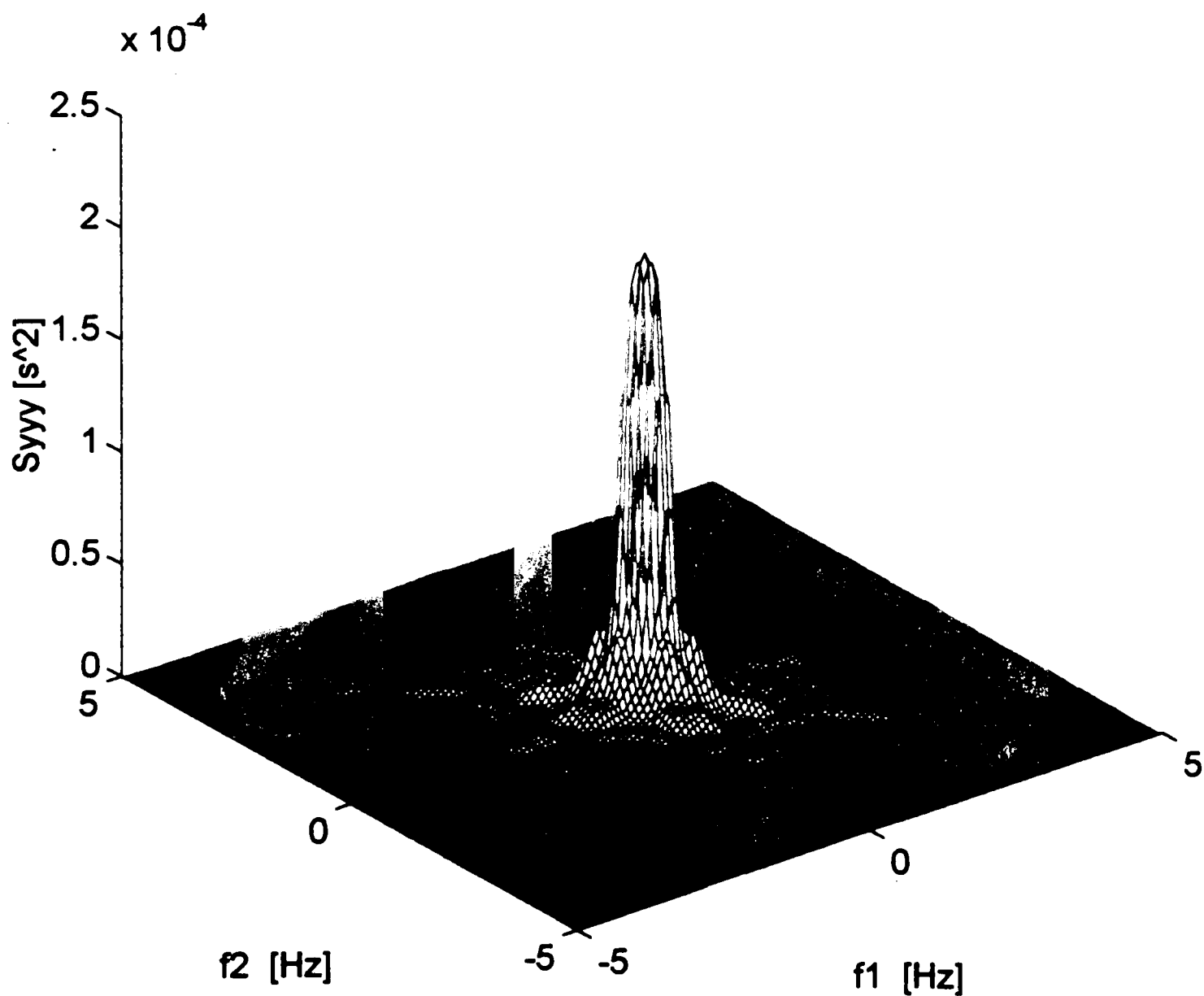


Figure 5.25. Bispectrum of wind pressure for tap 31407 on the side wall (M15N545).

Table 5.6 Contribution from different components of the model to pressures on the side walls.

Record	Cp_variance		Contribution, as % of measured spectrum, from					Total Coherence	
	meas- ured	pred- icted	<i>u</i>	<i>v</i>	<i>u</i> ²	<i>v</i> ²	Resid- ual, <i>S_{nn}</i>	mean	std. dev.
<u>Tap 11407</u>									
C539	0.0763	0.0787	33.2	27.6	20.1	22.1	-3.0	1.02	0.42
C544	0.0871	0.0850	22.8	32.0	21.8	21.1	2.4	1.00	0.41
CS070	0.0588	0.0583	21.9	28.7	20.5	28.0	0.9	1.02	0.40
CS077	0.0541	0.0535	24.9	22.4	24.1	27.4	1.2	1.02	0.39
<u>Tap 31407</u>									
C539	0.0806	0.0826	21.7	34.3	21.9	24.7	-2.5	0.99	0.41
C544	0.0751	0.0750	22.0	30.4	24.8	22.7	0.1	1.02	0.41
CS070	0.1179	0.1190	23.2	29.7	19.3	28.8	-0.9	0.99	0.39
CS077	0.1004	0.1022	27.6	25.0	25.7	23.5	-1.8	1.03	0.40

5.2.6 Area-averaged Pressures on Roof Purlin

The overall wind load on a structural component or cladding is the integral effect of the point pressure characteristics over the tributary area of the component, hence, the importance of area-averaged pressures. A 7.62 m (25 ft) span roof purlin on the test building was instrumented with six pressures transducers along its tributary area. The location of the purlin and that of the transducers are shown in Figure 5.26. The tributary area and the weight associated with each transducer is tabulated in Table 5.7.

Two critical cases are considered: (i) Wind normal to the long wall ($\theta \approx 270^\circ$) and, (ii) Wind normal to the short wall ($\theta \approx 0^\circ$). In the former case, the purlin is located near the downstream end of the separation bubble where moderate suction act over the entire effective area of the purlin. In the latter case, about one-half of the purlin is located under the separation bubble with high suction and the other half is located in the reattachment region with much lower suction.

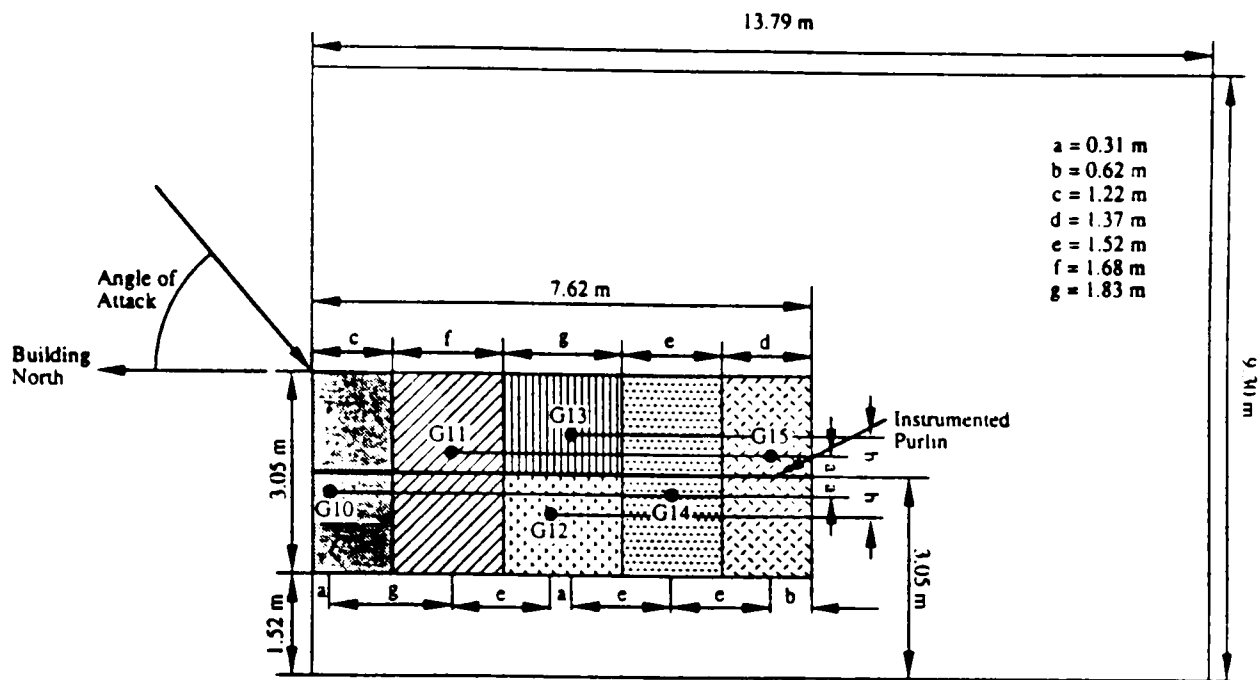


Figure 5.26 Location of purlin , instrumented pressure taps and tributary areas (after Smith et al., 1994).

Table 5.7 Tributary area associated with each pressure tap on roof purlin.

Pressure Tap	Transducer number	Tributary area a_i (m ²)	Weight $W_{ai} = a_i / \sum a_i$
50944	G10	3.72	0.16
51138	G11	5.11	0.22
50833	G12	2.79	0.12
51232	G13	2.79	0.12
50927	G14	4.64	0.20
51122	G15	4.18	0.18
	Σ	23.23	1.00

The transfer functions for the roof purlin for $\theta \approx 270^\circ$ case are shown in Figures 5.27(a) and 5.27(b) for a typical record (C544). The corresponding comparison of measured, predicted and residual spectra are shown in Figure 5.28. Analogous transfer functions and output prediction for $\theta \approx 0^\circ$ case are shown in Figures 5.29(a & b) and 5.30. The mean and standard deviation of the coherence function were 1.01 and 0.42 for the former case and 1.08 and 0.47 for the latter case. There are more errors in the estimates for the latter case because of the mixed separated and reattached flow conditions experienced in that case. It is also observed from Figures 5.27 and 5.29 that the individual transfer functions for the area-averaged cases show a lower degree of variability than those for point pressures.

The decomposition of pressure-coefficient spectrum into contributions from the linear and quadratic terms in the model and the total coherence are tabulated in Table 5.8 for the two area-averaged cases for the roof purlin. Table 5.8 seems to indicate that the linear u component has a higher contribution compared to the others. This means that the modification of the upstream along-wind flow, resulting in the formation of a cylindrical vortex during separation, has a slightly more dominant effect in producing wind load on the purlin. Contributions from other terms are also comparable.

Table 5.8 Contribution from different components of the model to area-averaged pressures on the purlin.

Record	Cp_variance		Contribution, as % of measured spectrum, from					Total Coherence	
	meas- ured	pred- icted	u	v	u^2	v^2	Resid- ual, S_{nn}	mean	std. dev.
<u>$\sim 270^\circ$</u>									
C539	0.0588	0.0612	31.5	22.9	25.4	24.5	-4.2	1.02	0.41
C544	0.0549	0.0544	24.4	24.3	26.5	23.8	1.0	1.01	0.42
<u>$\sim 0^\circ$</u>									
C325	0.0574	0.0601	33.7	28.9	19.8	22.4	-4.8	1.08	0.47
C728	0.0477	0.0521	29.7	22.9	29.9	26.7	-9.2	1.09	0.46

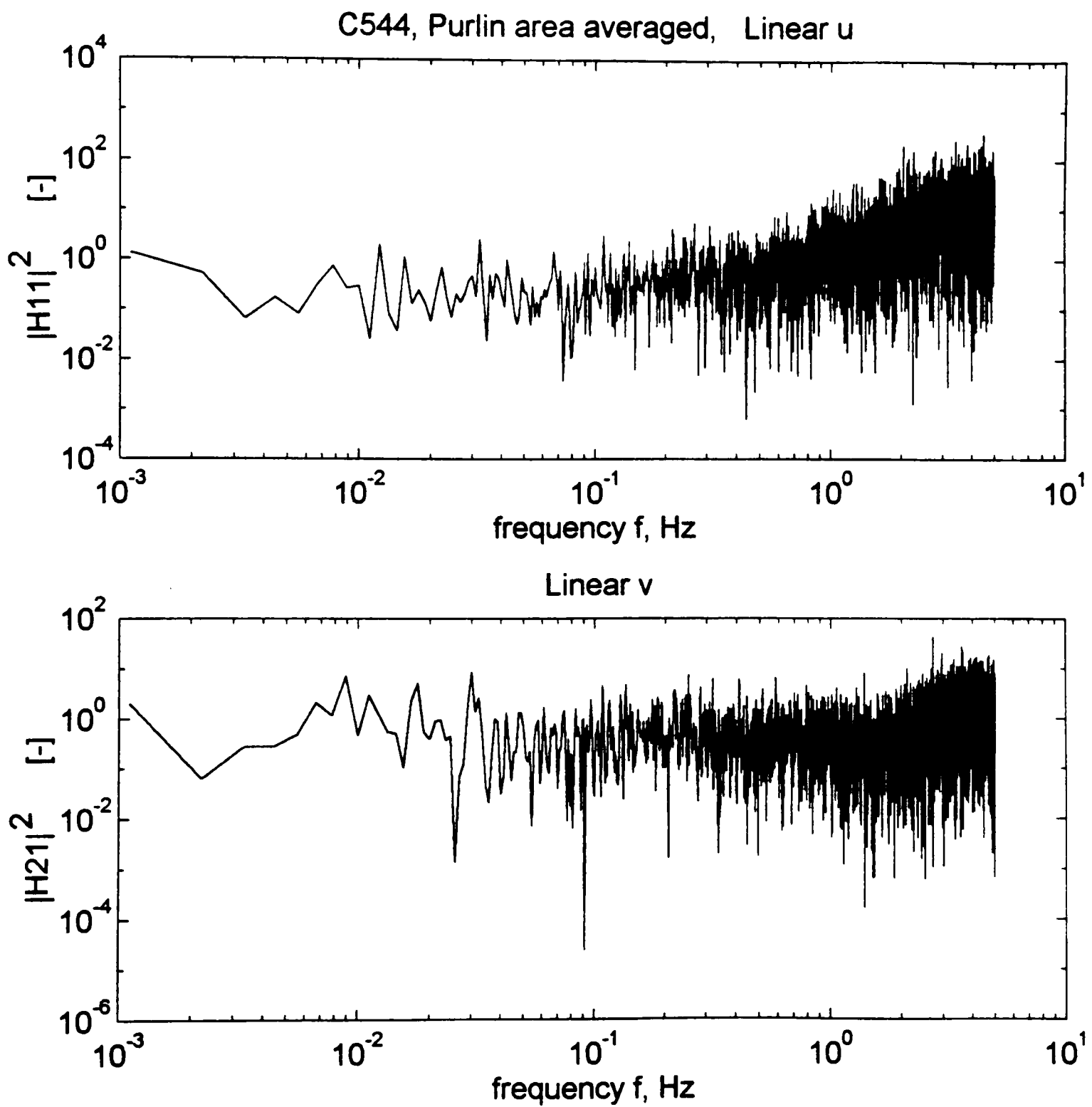


Figure 5.27. Transfer functions for roof purlin with $\theta \approx 270^\circ$ (C544). (a) Linear.

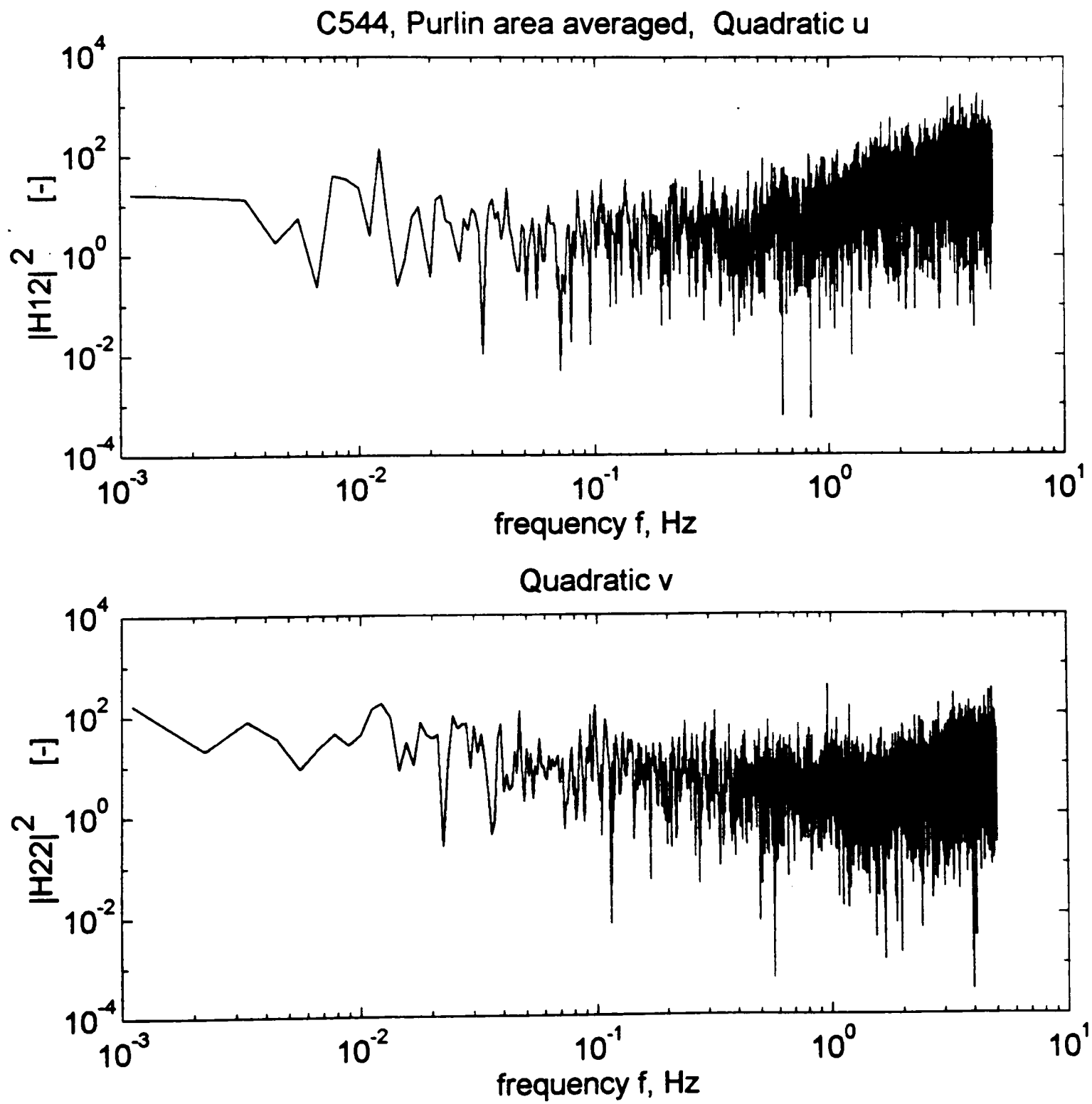


Figure 5.27. Continued. (b) Quadratic.

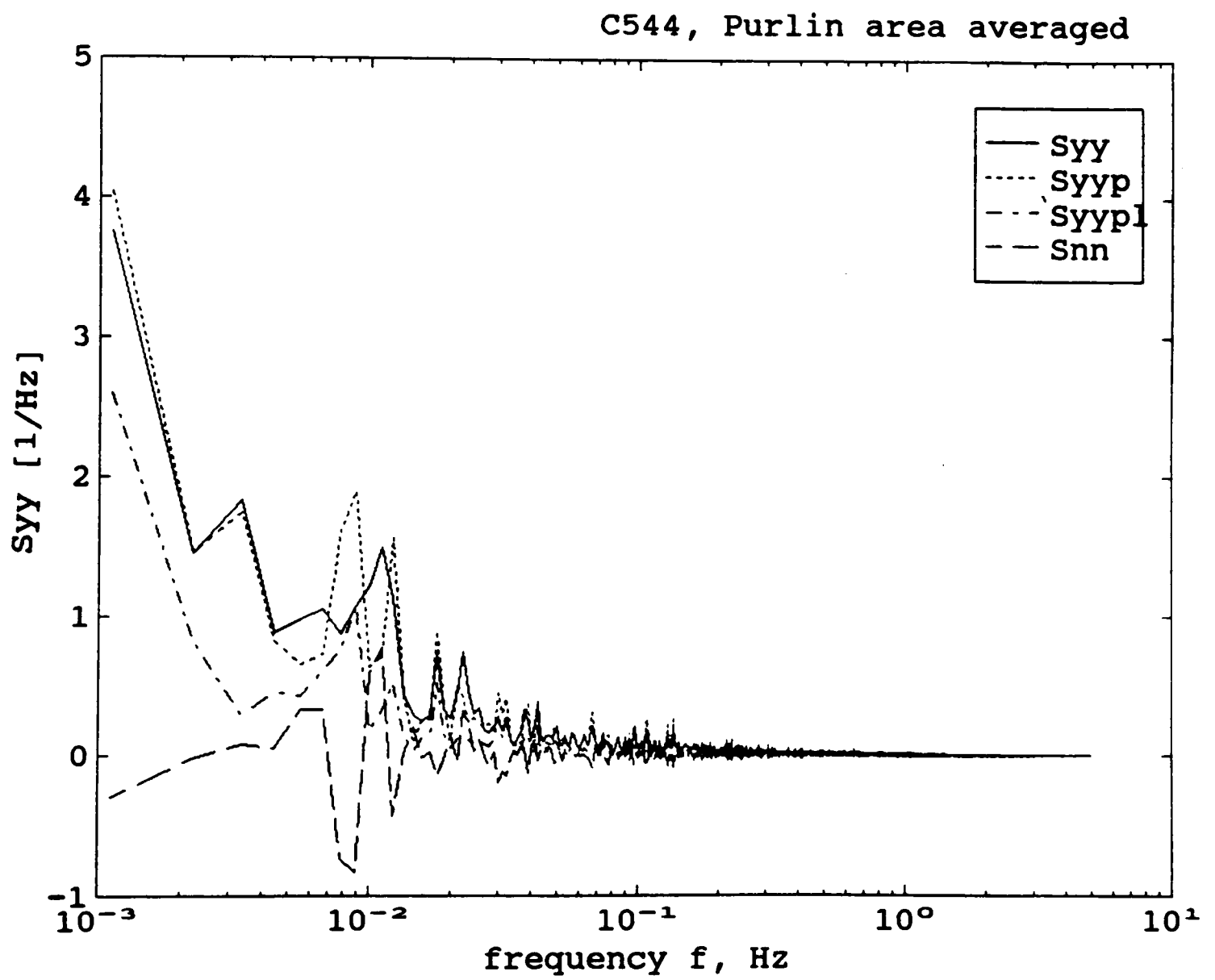


Figure 5.28. Output prediction for roof purlin with $\theta \approx 270^\circ$ (C544).

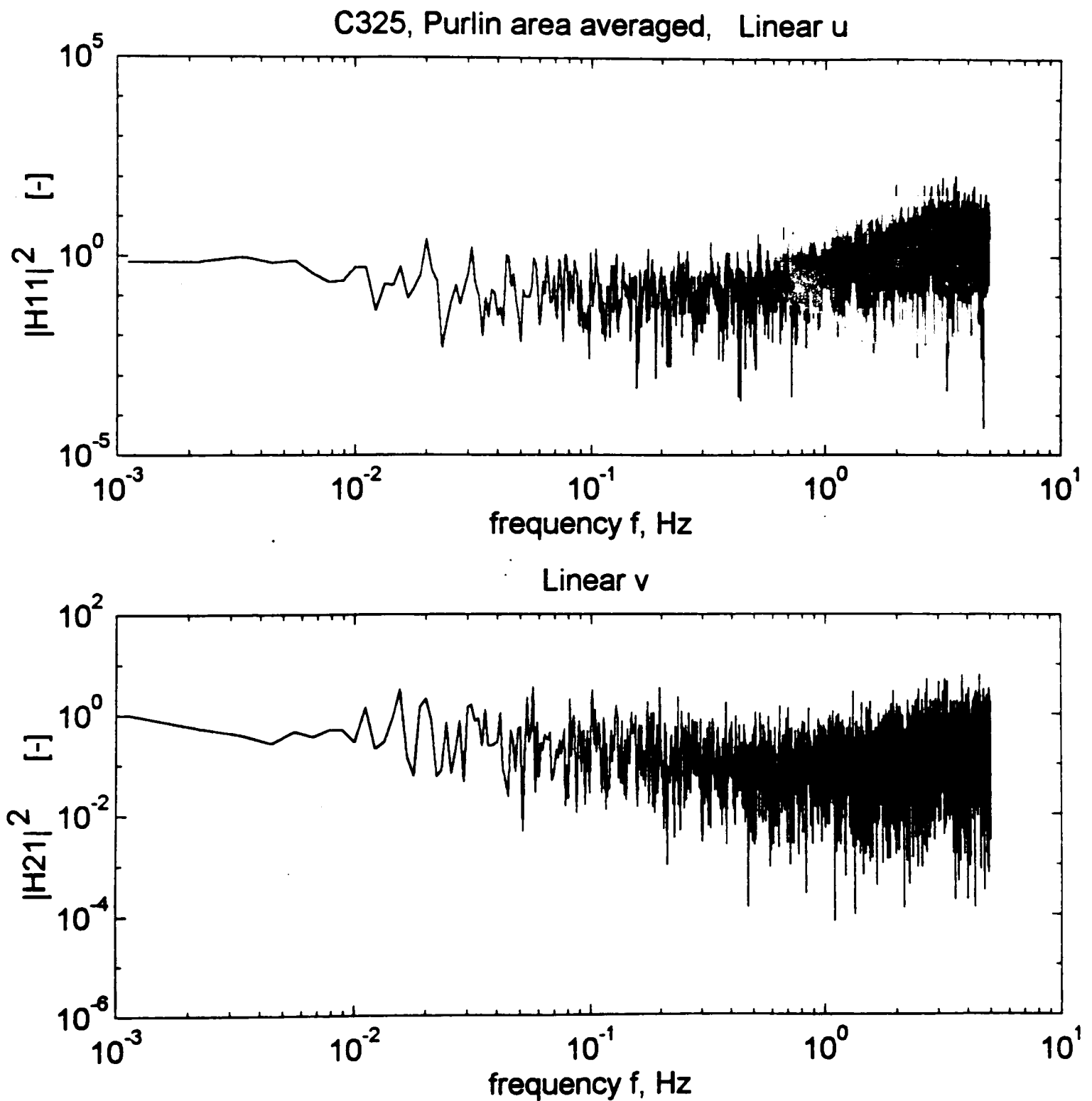


Figure 5.29. Transfer functions for roof purlin with $\theta \approx 0^\circ$ (C325). (a) Linear.

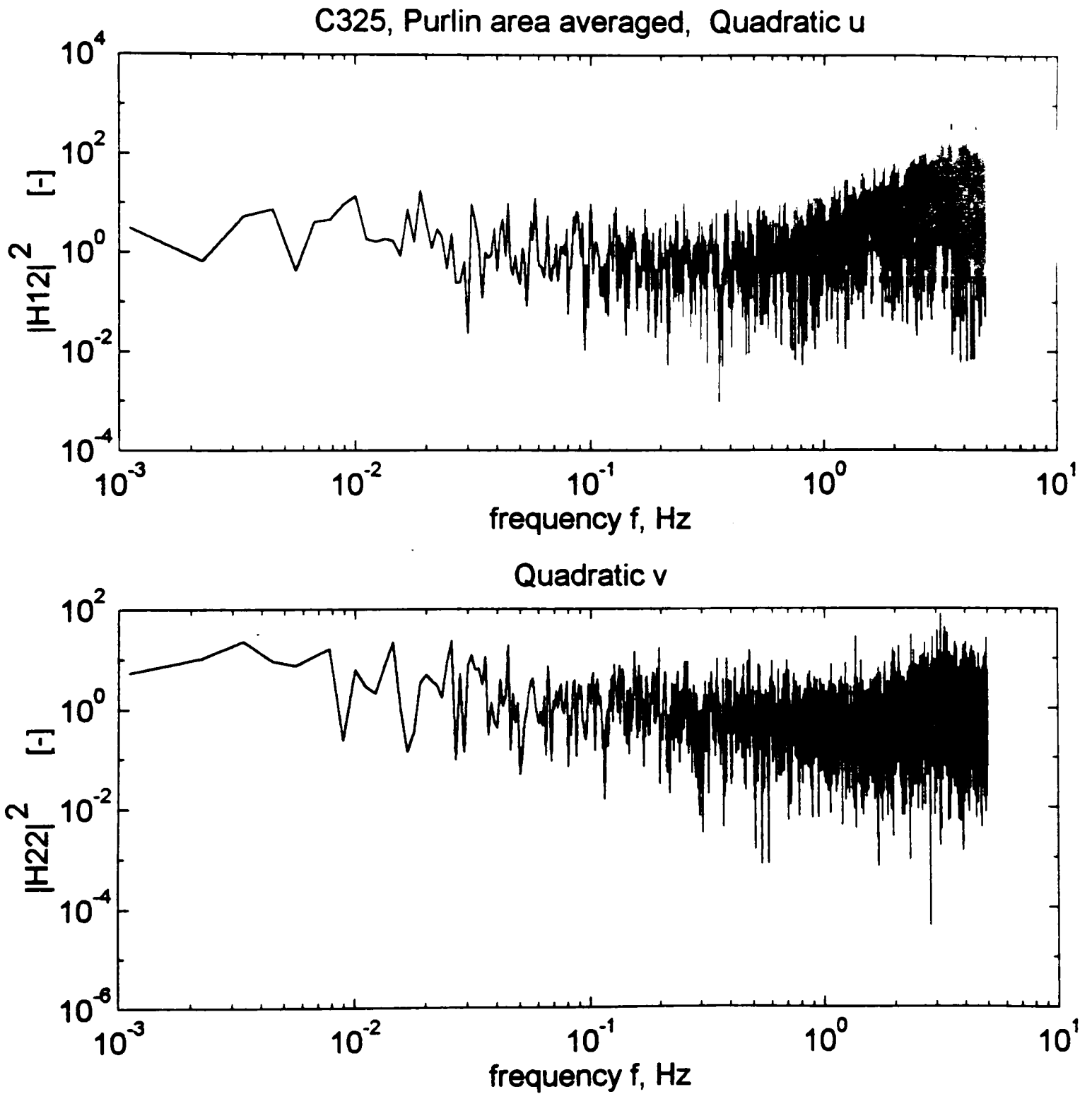


Figure 5.29. Continued. (b) Quadratic.

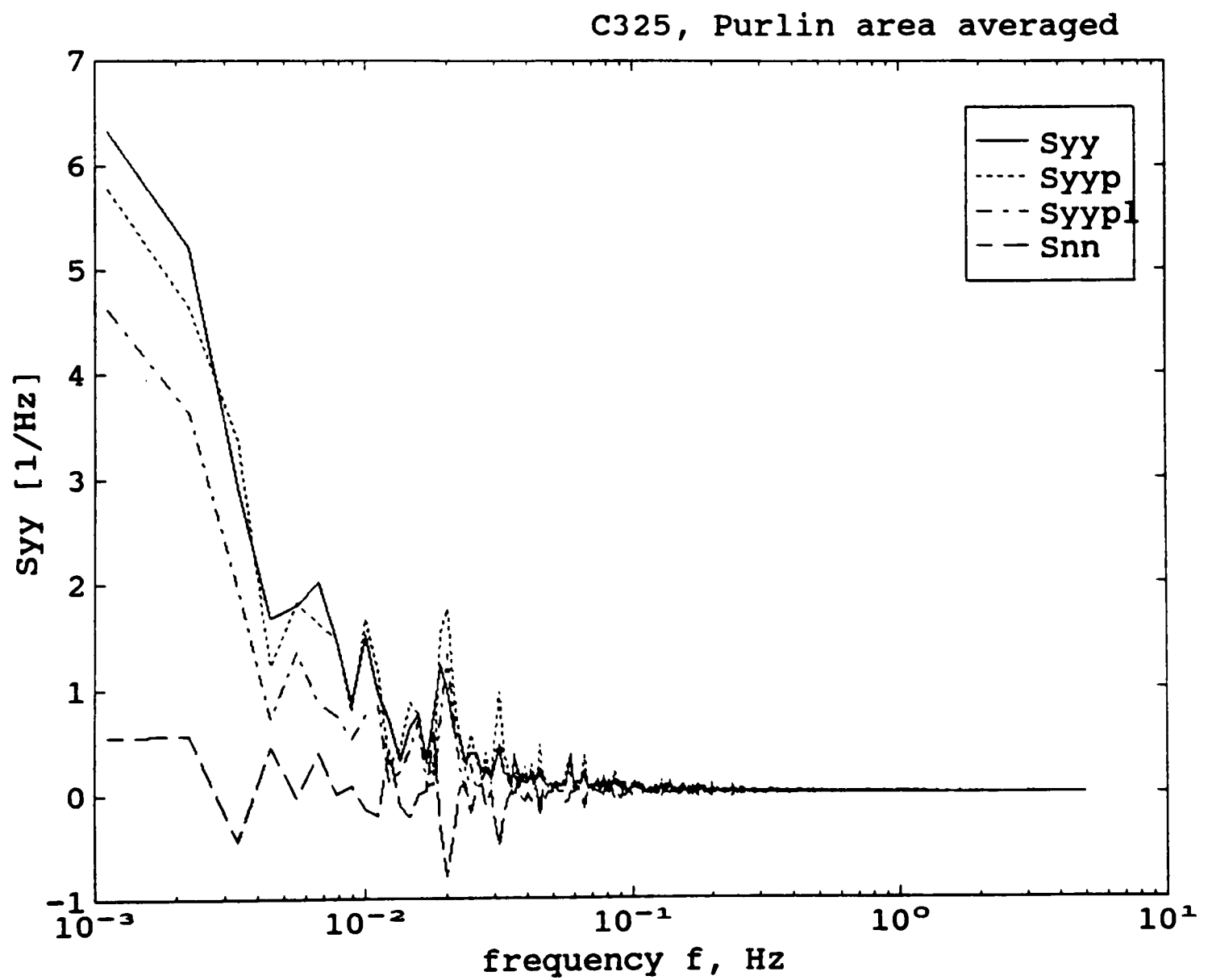


Figure 5.30. Output prediction for roof purlin with $\theta \approx 0^\circ$ (C325).

5.2.7 Frequency Distribution of the Variance of Measured Pressures

It was observed in Section 4.2.8 that there may not be any significant frequencies above 5 Hz in the pressure time histories. This was generally found to be true for the measured spectra for different pressure taps presented earlier in this chapter. The averaged frequency distribution of the variance between 0 and 5 Hz for these taps are tabulated in Table 5.9 for an angle of attack of approximately 270° .

Table 5.9 Average frequency distribution of measured pressures ($\theta \sim 270^\circ$).

Flow Region	Pressure Tap	variance, as % of measured, from 0 Hz to					
		0.05 Hz	0.1 Hz	0.5 Hz	1 Hz	2 Hz	4 Hz
Windward wall	42206	42.8	56.8	90.7	96.0	98.6	99.8
	42212	40.0	53.0	82.2	90.8	96.3	99.2
Roof Separation	50123	54.4	63.0	83.2	90.3	95.4	99.0
	50523	47.9	55.6	74.8	86.0	94.5	99.0
	50823	39.9	47.5	70.3	82.6	93.0	98.8
Roof Reattachment	51423	22.7	29.4	53.4	70.6	88.5	97.9
	52323	12.9	16.1	37.7	61.7	84.6	97.0
	52923	24.4	28.7	43.0	60.6	81.8	96.2
Leeward wall	22306	63.5	74.1	90.4	96.2	98.7	99.7
	22312	53.7	62.3	85.6	88.0	96.0	99.4
Side walls	11407	62.2	70.8	85.9	92.5	97.2	99.5
	31407	59.8	69.1	84.4	90.8	96.4	99.3
<u>Area-averaged</u>							
	Purlin ($\sim 270^\circ$)	52.6	62.0	84.1	91.2	96.6	99.3
	Purlin ($\sim 0^\circ$)	71.5	79.2	90.1	93.4	96.6	99.3

Note: Area under spectrum from 0 to 5 Hz is the measured variance.

It is seen from Table 5.9 that more than 95 percent of the pressure variance is contained in frequencies below 2 Hz for all the taps except those in the reattachment region. In the reattachment region, more than 80 percent of the pressure variance is

contained in frequencies below 2 Hz. It is also seen that more than 99 percent of the pressure variance is contained in frequencies below 4 Hz except for the reattachment region for which it is 95 percent. Hence it is reasonable to conclude that there are no significant frequencies beyond 5 Hz for the point pressures treated in this chapter. It is also observed that the reattachment zone has the most predominant higher frequency content. The windward, leeward and side walls along with the area-averaged cases show less high frequency content with about 85 to 90 percent of the pressure variance being contained in frequencies below 0.5 Hz.

5.2.8 Phase of Transfer Functions and Pressure Spectra

The transfer functions obtained from the proposed model are complex quantities indicating a phase shift between wind velocity and pressure. So far only the magnitude-squared of the transfer functions were presented because only the magnitude was of consequence in the output prediction process. However, for the sake of completeness, typical phase angles associated with the transfer functions will be presented. The phase functions for tap 42206 on the windward wall and tap 50523 in roof separation are shown in Figures 5.31 and 5.32, respectively, for a typical field record. These functions are shown only for the frequency range 0-1 Hz for clarity. It is seen from these figures that the phase angles associated for all the transfer functions were uniformly distributed between $-\pi$ and $+\pi$ radians with a mean and standard deviation of approximately 0 and 1.8, respectively.

The phase part of the discrete Fourier transform (DFT) of a time history is normally discarded during computation of the spectrum. The digital synthesis of the non-Gaussian distribution property and the sharp spike events observed in wind pressure time histories is strongly dependent on the organization of the phase part of the Fourier representation of the signal and its active control (Seong, 1993). Thus the study of the phase part of the Fourier transform can be a useful means for uncovering hidden information within time series. The phase of the pressure spectrum for taps 42206 and 50123 are shown in Figure 5.33 for typical records. Their corresponding probability density functions (pdf) are shown

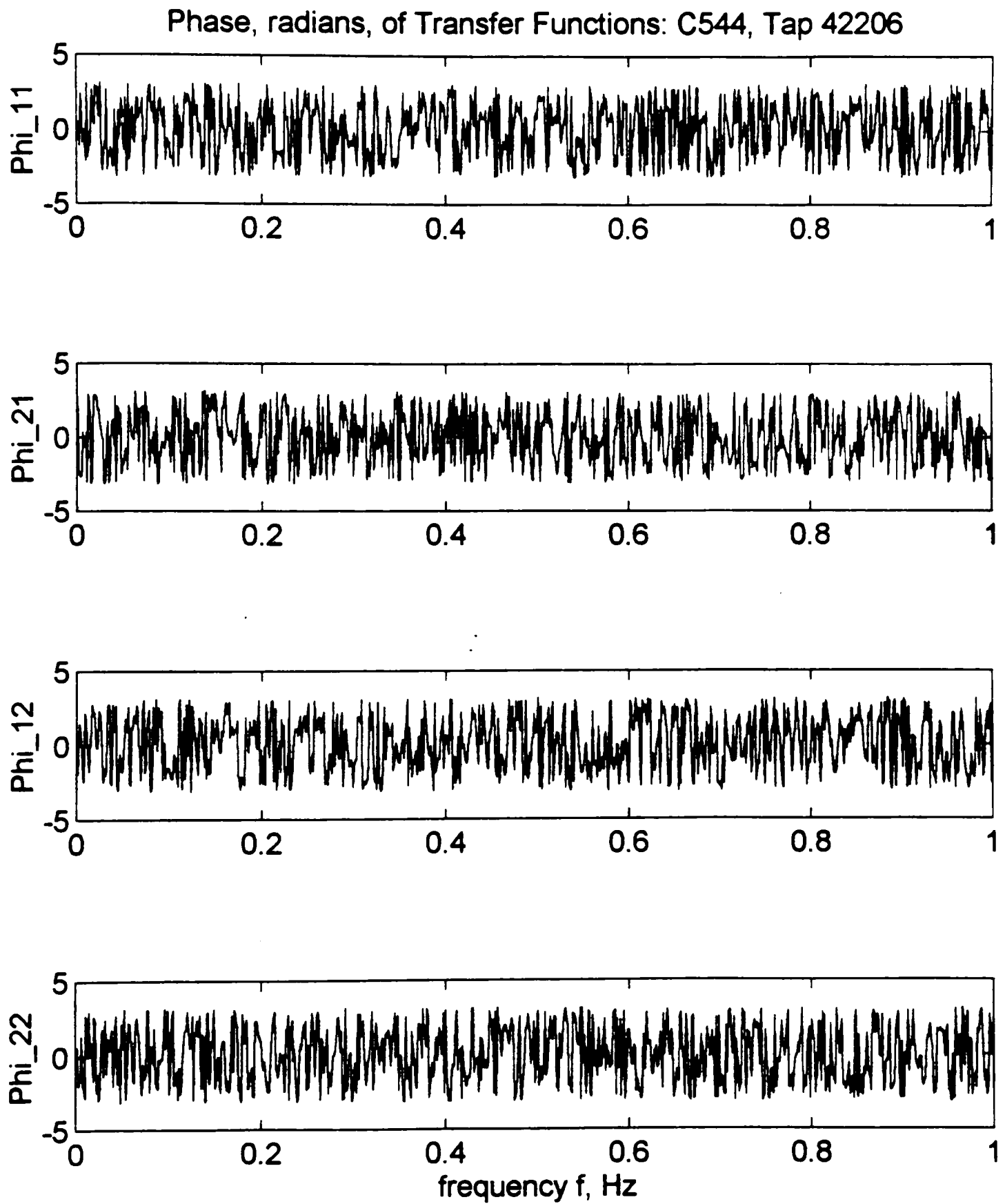


Figure 5.31. Phase of transfer functions for tap 42206 on the windward wall (C544).

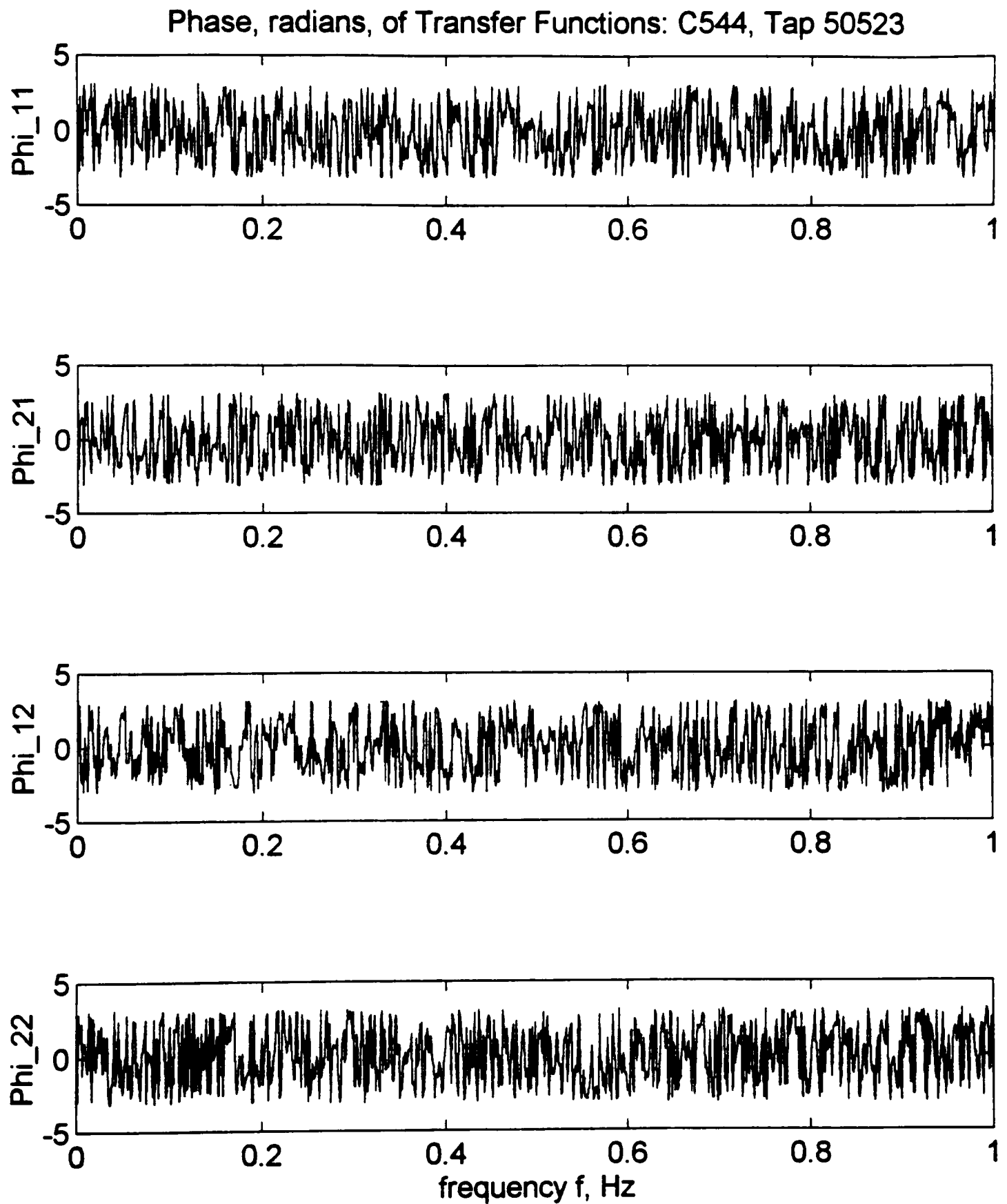
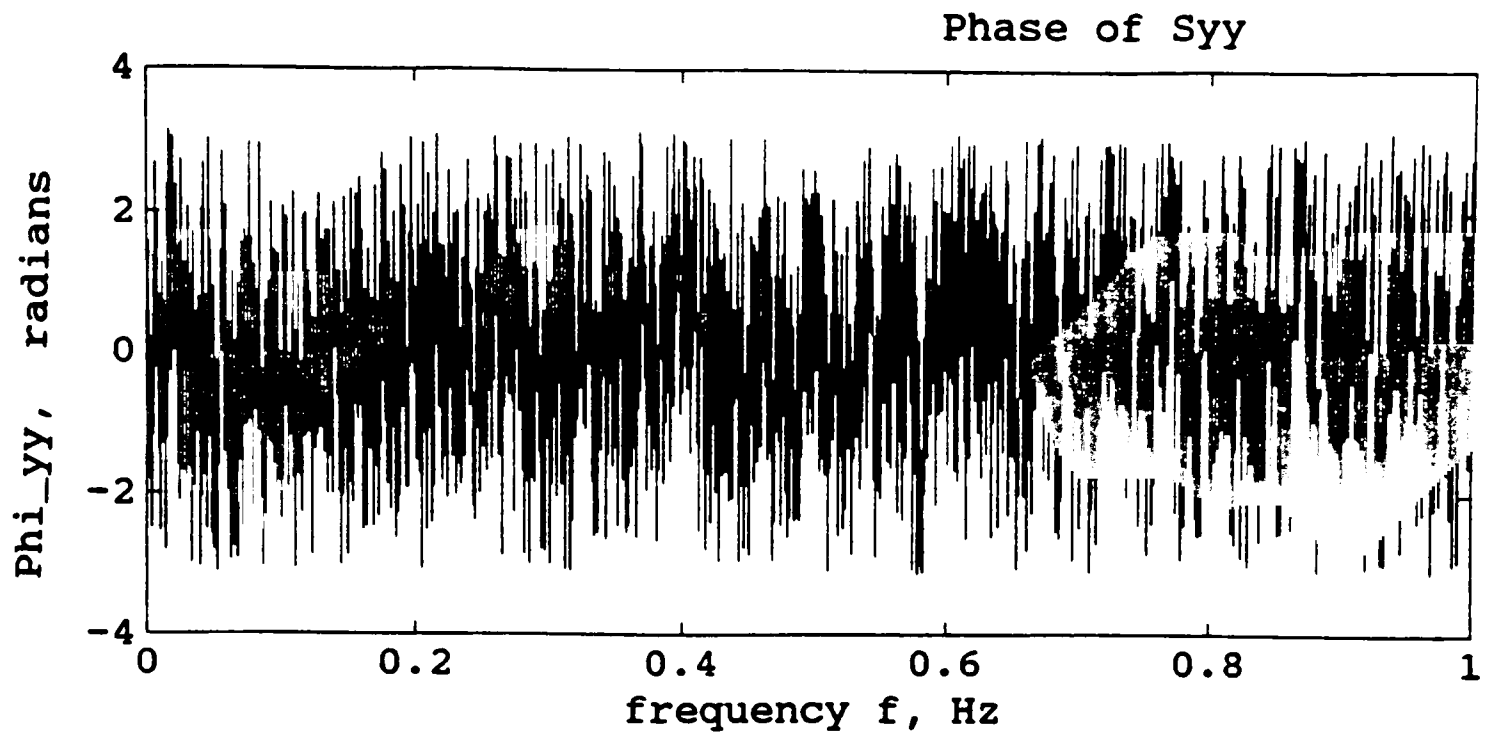
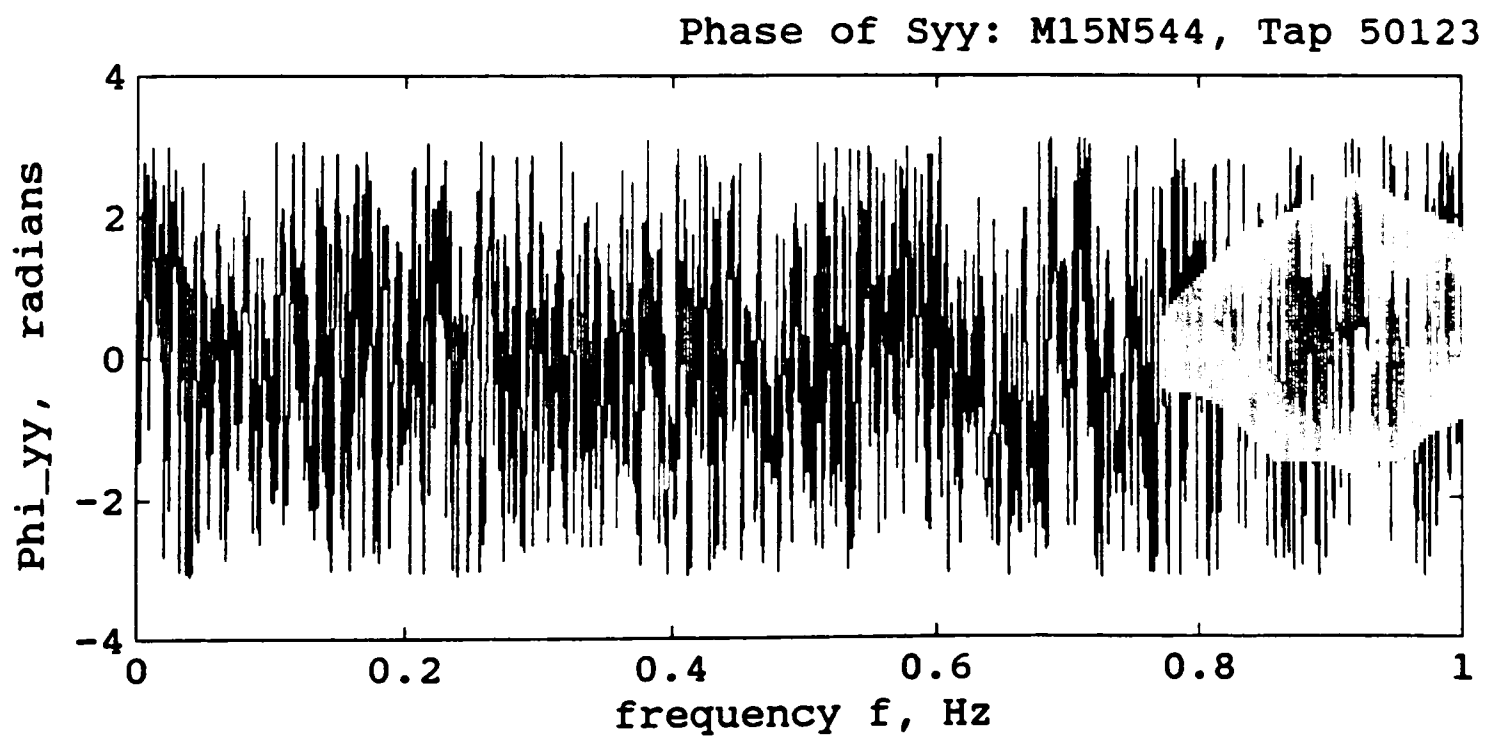


Figure 5.32. Phase of transfer functions for tap 50523 under the separation bubble (C544).

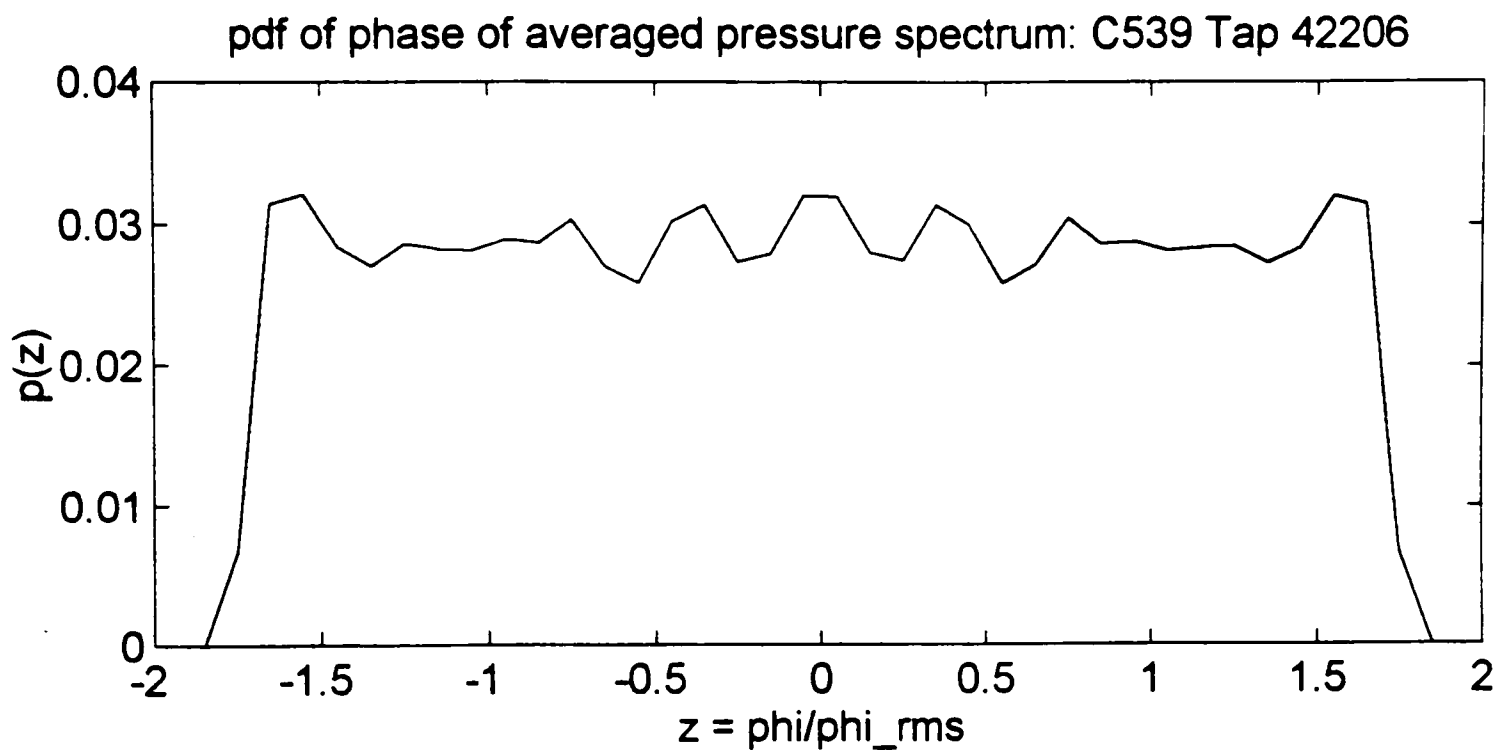


(a) Tap 42206 on the windward wall.

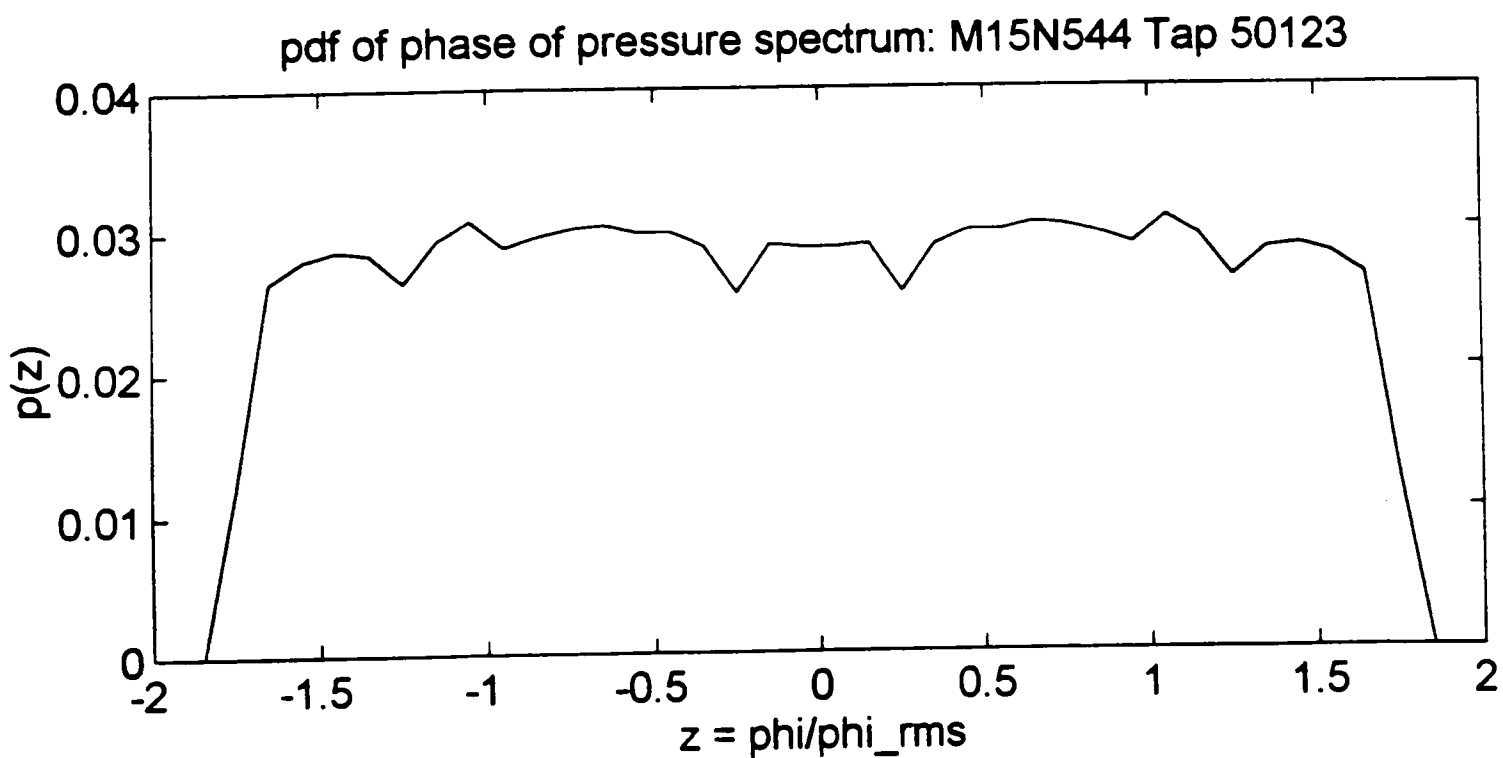


(b) Tap 50123 in the roof separation zone.

Figure 5.33. Phase of pressure spectra (M15N544).



(a) Tap 42206 on the windward wall



(b) Tap 50123 in the roof separation zone

Figure 5.34. Pdf of phase of pressure spectra.

in Figure 5.34. It can be observed from these figures that the phase angles are uniformly distributed between $-\pi$ and $+\pi$ radians. The mean of the phase angles were found to be zero for both taps. Their standard deviations were found to be 1.9 and 1.8 for taps 42206 and 50123, respectively.

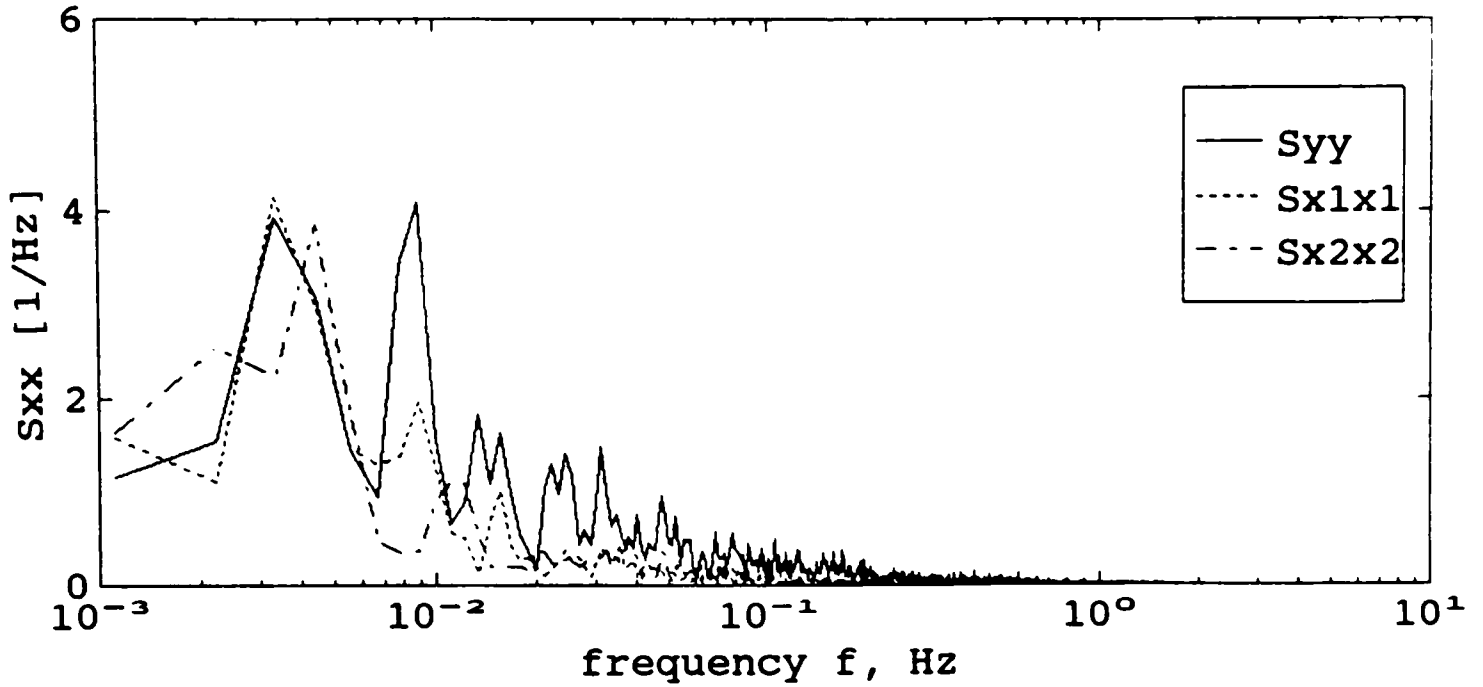
5.3 Simulation of Pressure-coefficient Spectra

In Section 5.2, the same input data were used for the identification of transfer functions (system identification) as well as for the output prediction or spectral decomposition for each record. In this section, a comparison will be made between the transfer functions for a particular tap obtained from two different records with approximately same mean angles of attack. The input spectra from one record will then be applied to the transfer functions identified from the second record to simulate the output pressure-coefficient spectrum of the first record.

Consider the pressure tap 42212 located near the top of the windward wall. Records CS070, CS077 and CS073 with mean angles of attack of 267.6° , 270.3° and 270.9° , respectively, will be used. The wind velocities for these records were measured using the sonic anemometer. These records were collected on the same day about 30 minutes apart with the wind blowing from approximately the same direction. The input velocity spectra and the output pressure-coefficient spectra for records CS070 and CS077 are shown in Figure 5.35. From Figure 5.35, it is seen that there exists a noticeable variability only in the lateral velocity spectra (S_{x2x2}) between the two records. This variability exists both in the qualitative and quantitative sense. This points to the fact that the random changes in wind direction observed in the field is a significant factor responsible for variability between the spectra even for very similar mean direction of the wind.

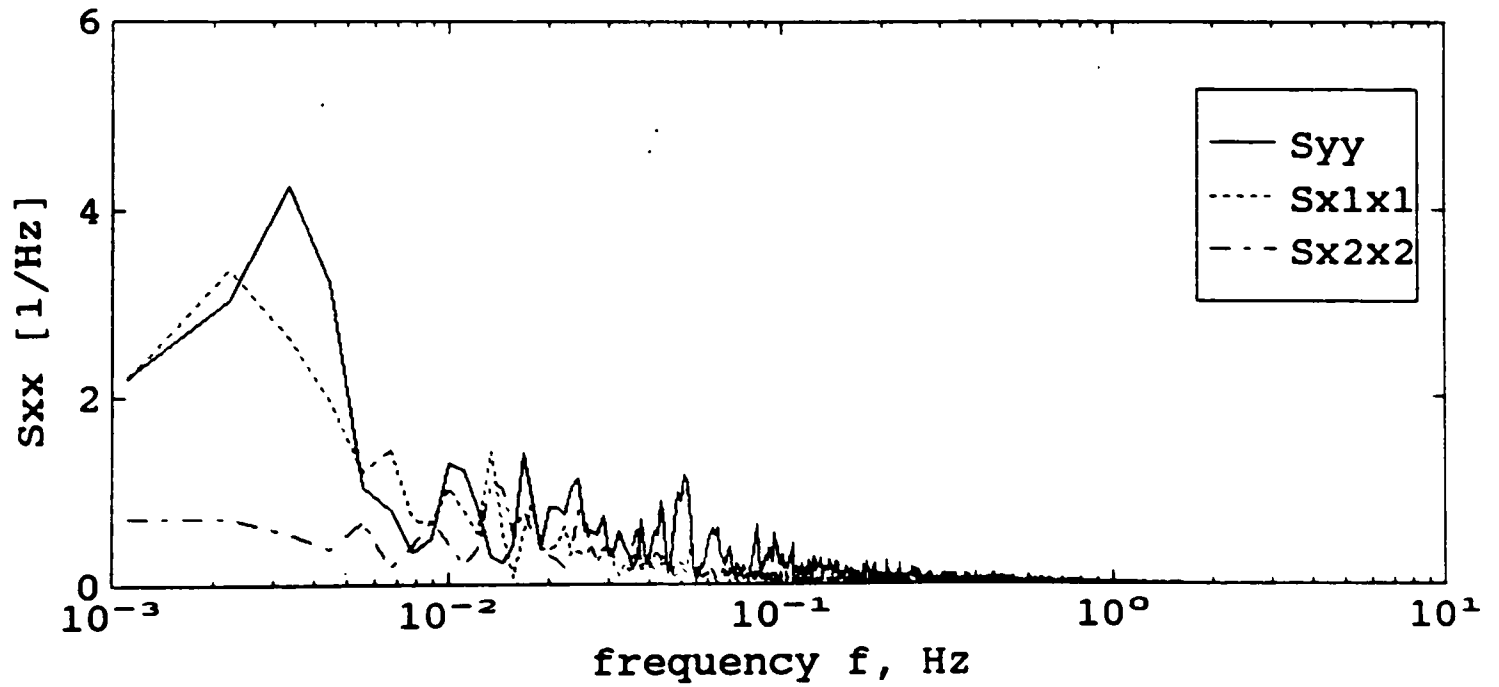
The comparison of the transfer functions for these records is shown in Figure 5.36. Although the transfer functions are very similar in form, they are seen to exhibit some quantitative variation. This variability could be attributed to the variation in wind direction characteristics discussed in the previous paragraph, possible noise in the input

Sxx & Syy: CS070, Tap 42212



(a) Record CS070.

Sxx & Syy: CS077, Tap 42212



(b) Record CS077.

Figure 5.35. Input velocity spectra and output pressure-coefficient spectra for tap 42212 on the windward wall.

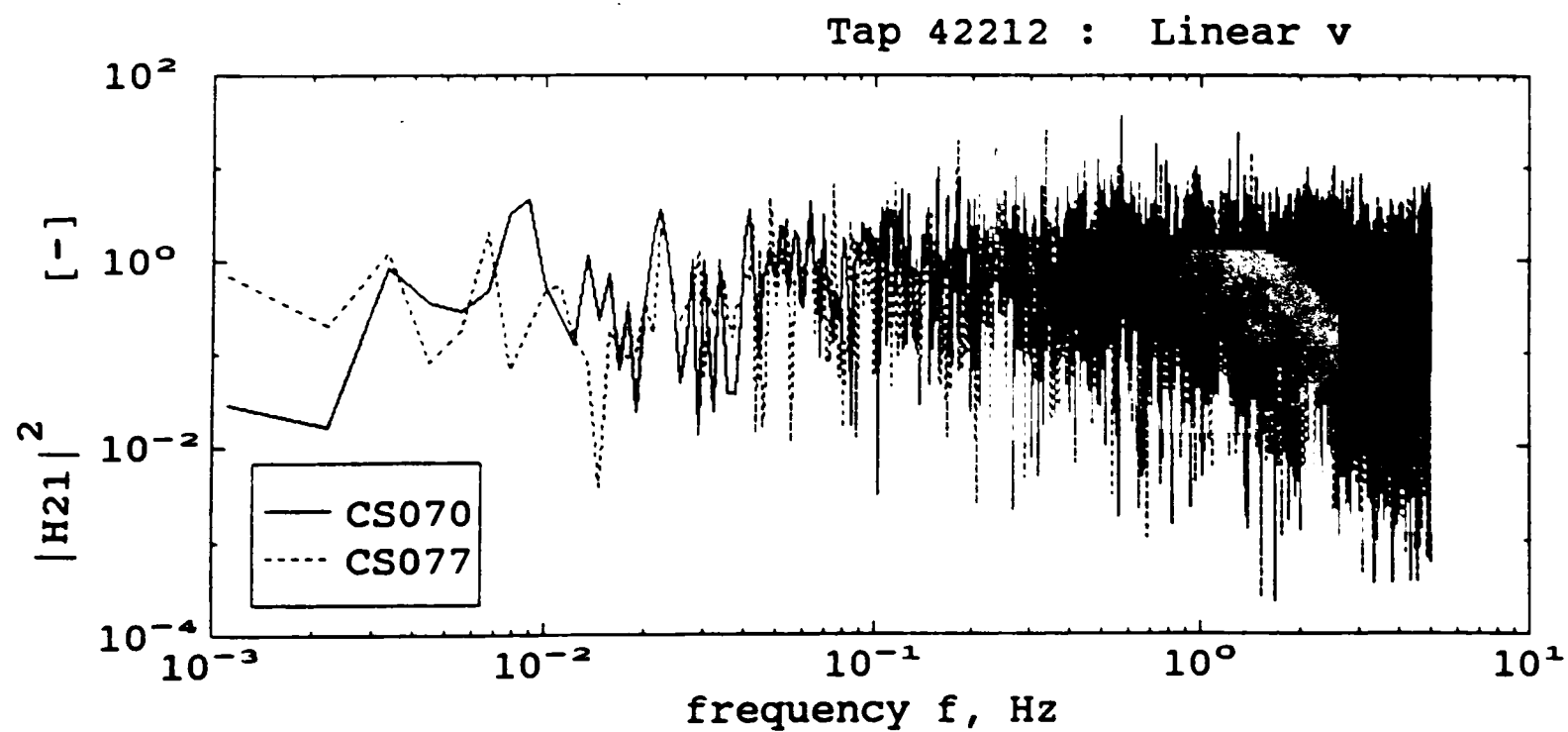
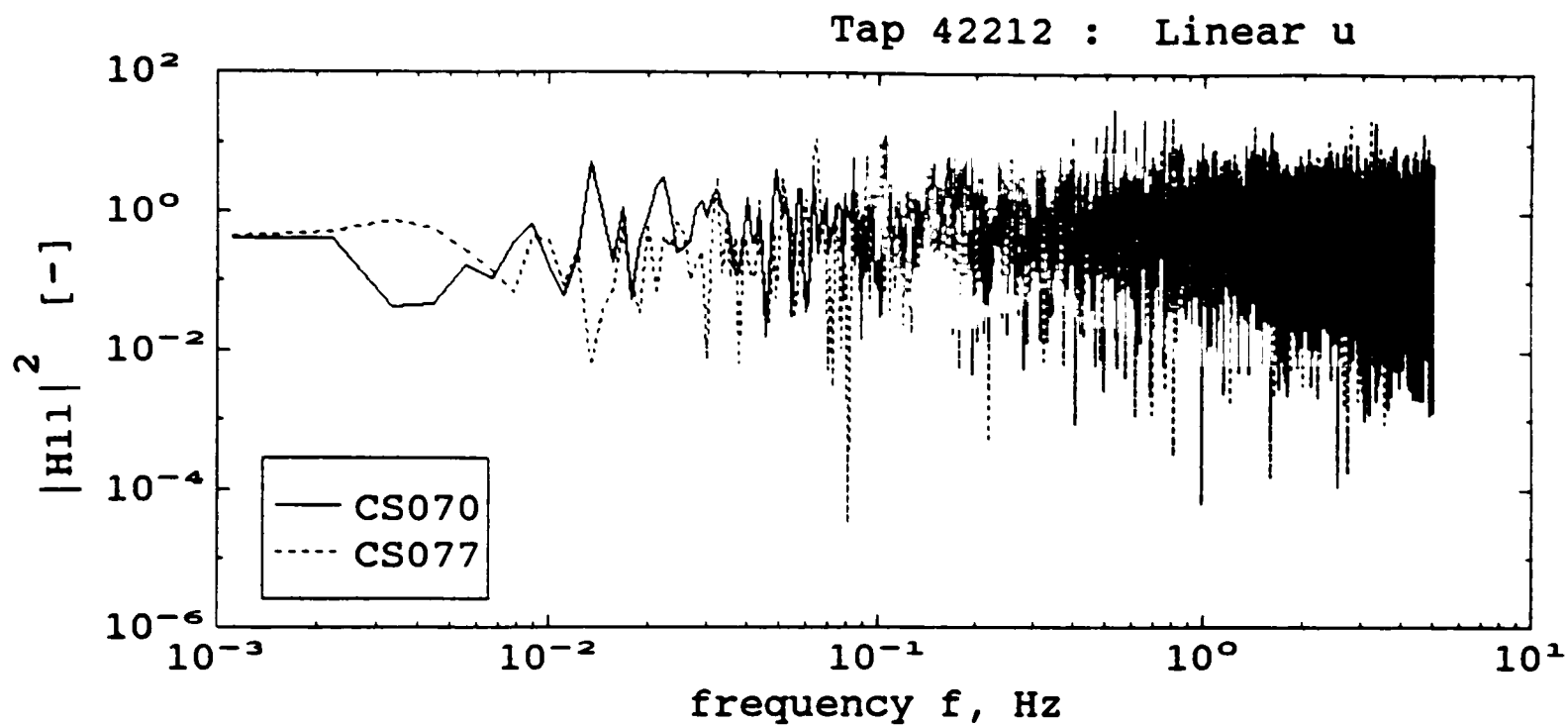


Figure 5.36. Comparison of transfer functions for tap 42212 on the windward wall.
 (a) Linear.

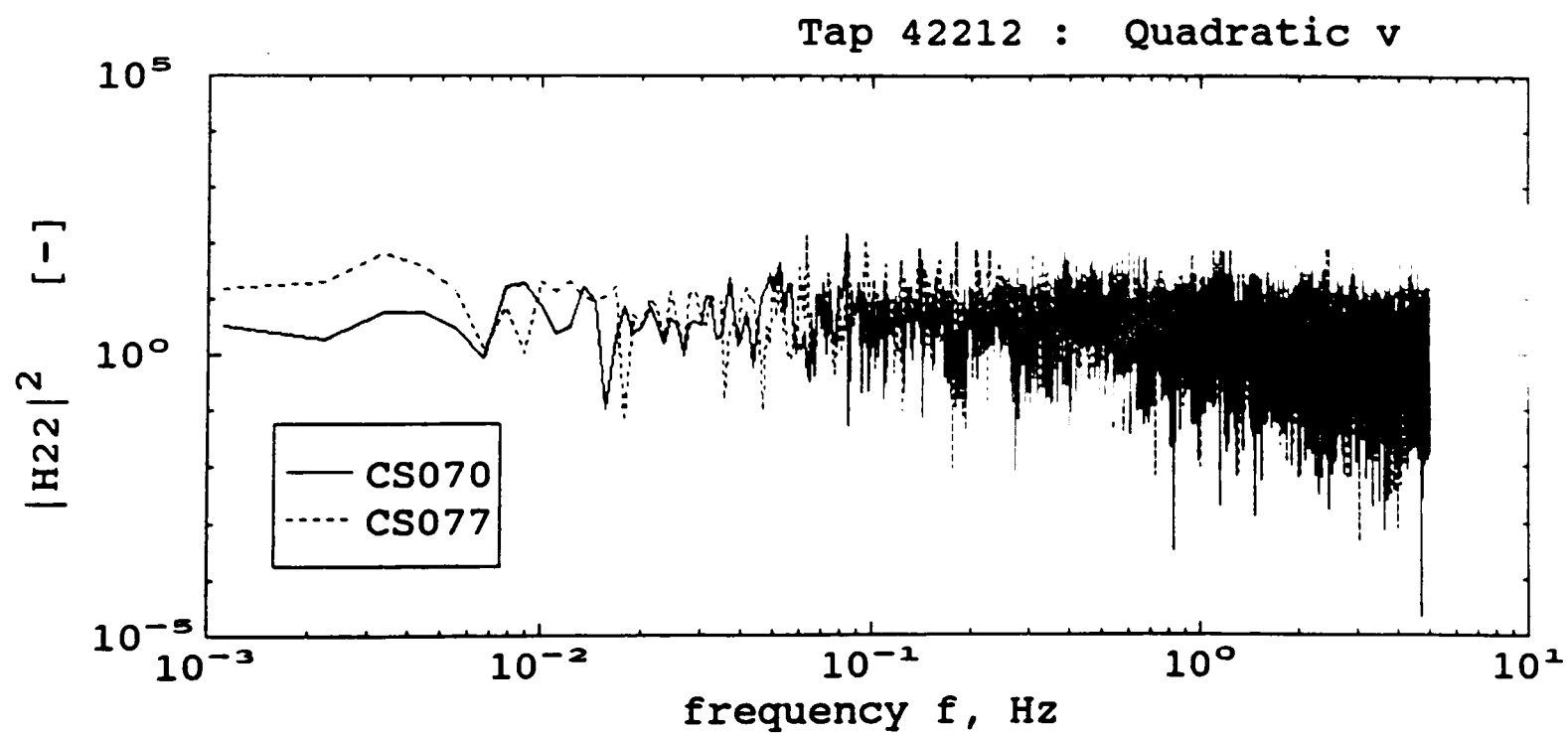
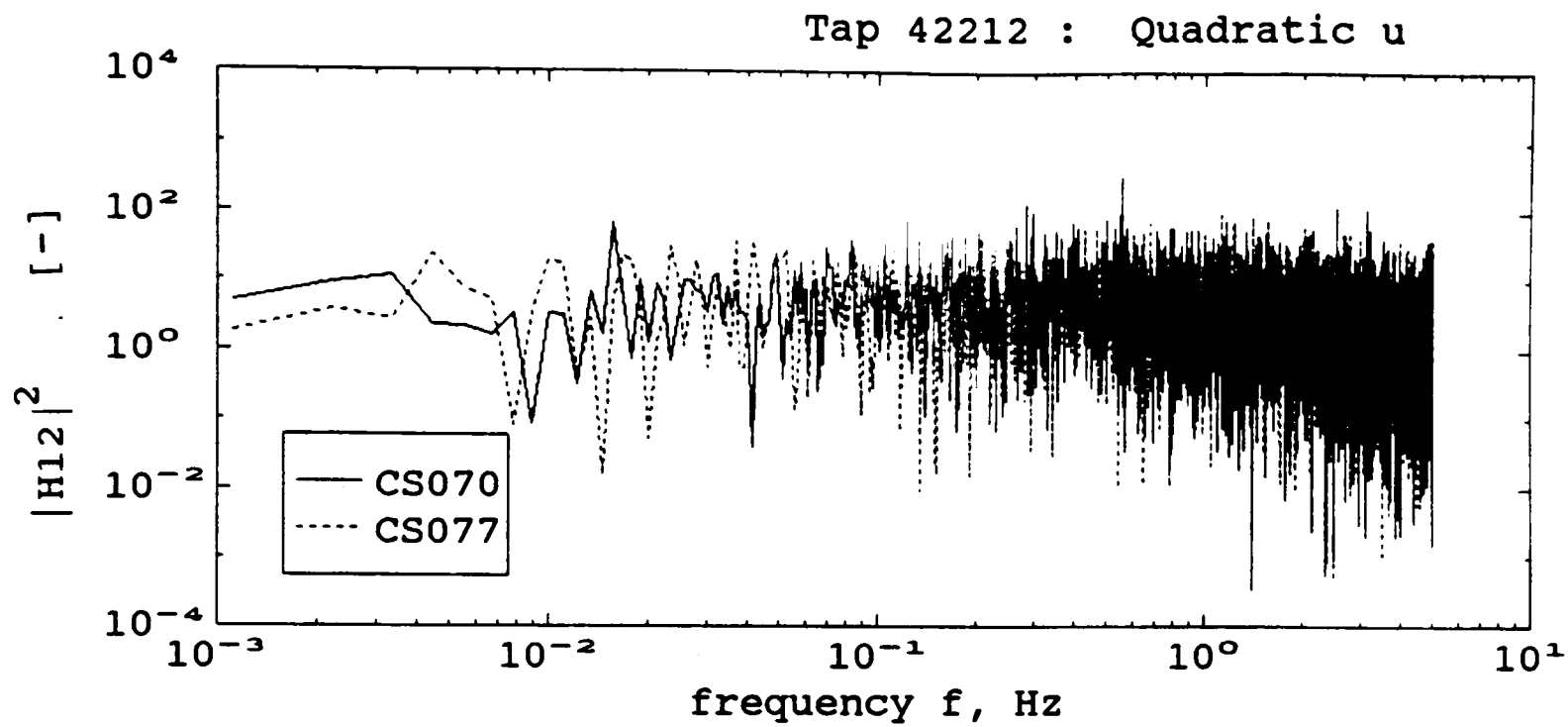


Figure 5.36. Continued. (b) Quadratic.

that is correlated to the wind and hence passing through the system, and computational noise.

Now the transfer functions of CS070 and CS077 will be used with the input velocity spectra of CS073 in order to simulate the pressure-coefficient spectrum for CS073. Two cases were examined: (i) the transfer functions of only CS077 were used, and (ii) the averaged transfer functions of CS070 and CS077 were used. The input spectra (S_{x1x1} and S_{x2x2}) and the measured output spectrum (S_{yy}) for CS073 for tap 42212 are shown in Figure 5.37. The comparison of the simulated pressure spectrum (S_{yyp}) and the measured one (S_{yy}) for record CS073 for tap 42212 for the two cases is shown in Figure 5.38. The simulated and measured pressure variances are also indicated therein. It is seen from Figure 5.38 that the simulated or predicted pressure variances were about 1.06 times the measured one for both cases, which is an excellent match. It is also seen that the frequency content of the simulated spectrum matches reasonably well with the measured spectrum, considering the degree of variability observed in the field.

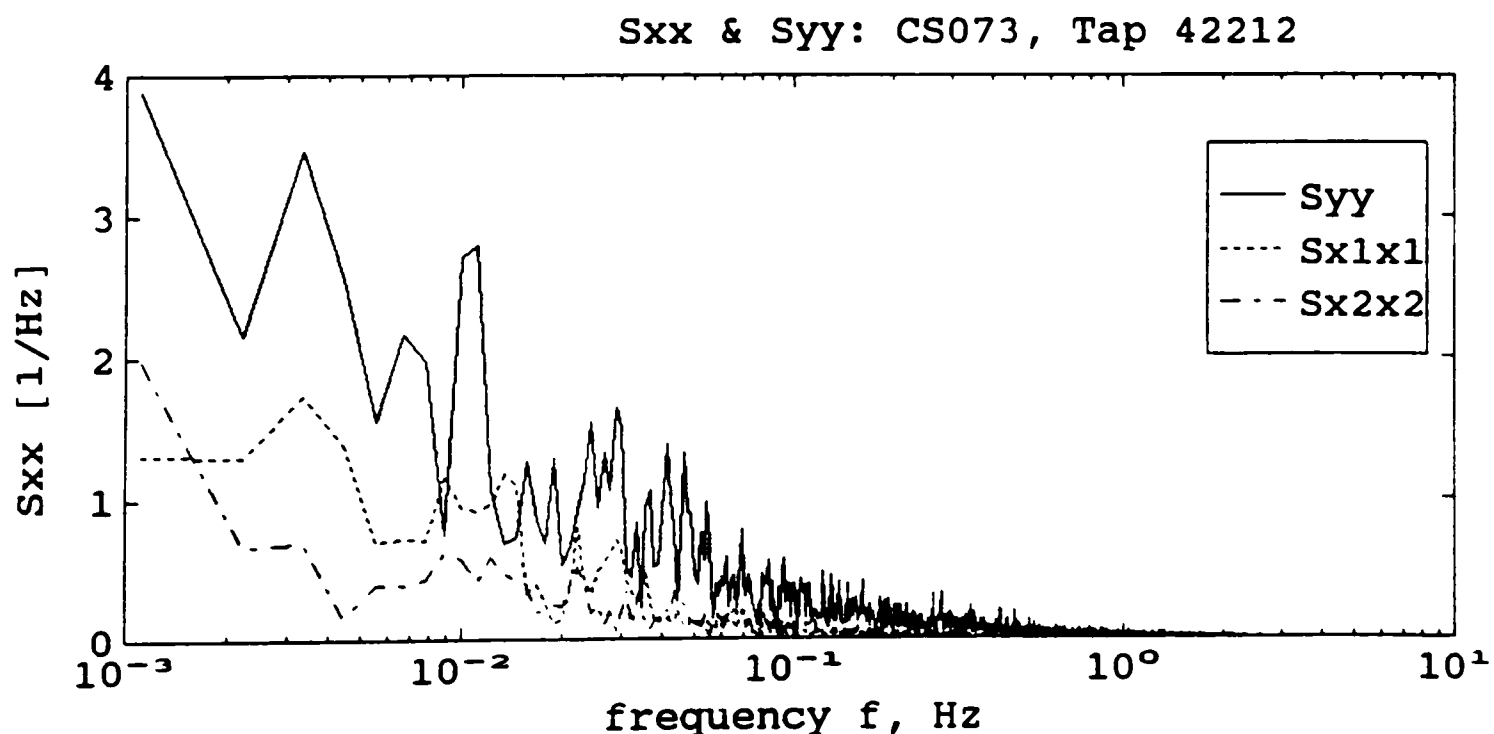
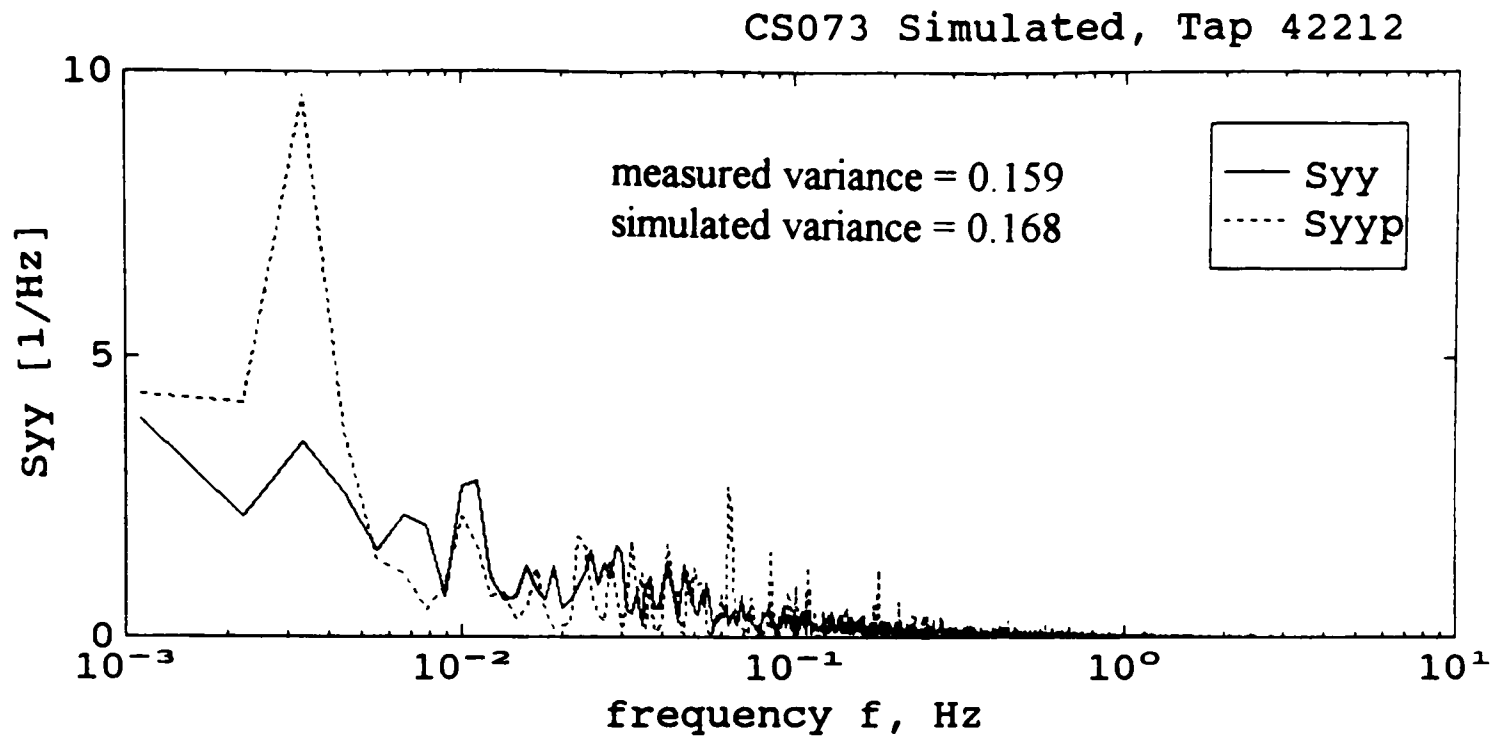
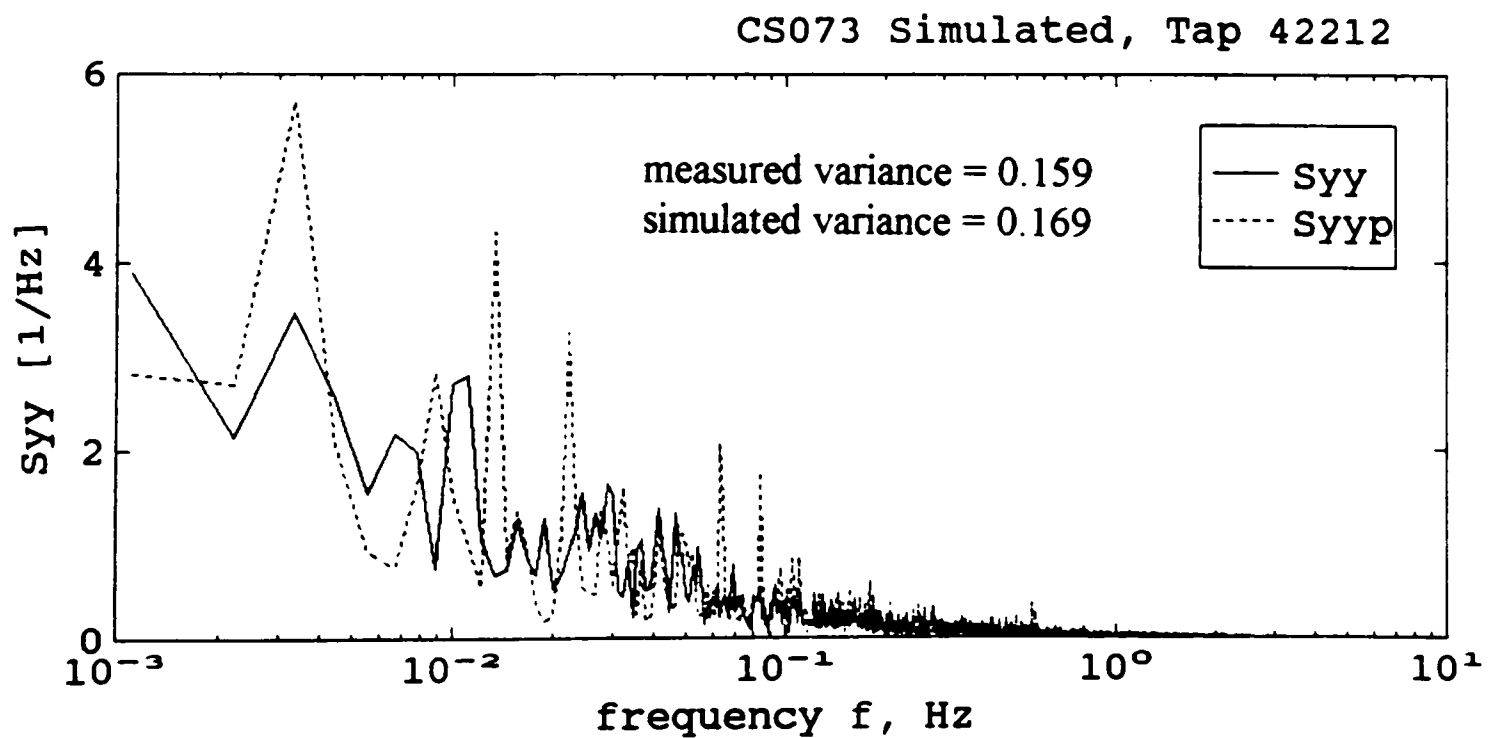


Figure 5.37. Input velocity spectra and output pressure-coefficient spectrum for tap 42212 (CS073).

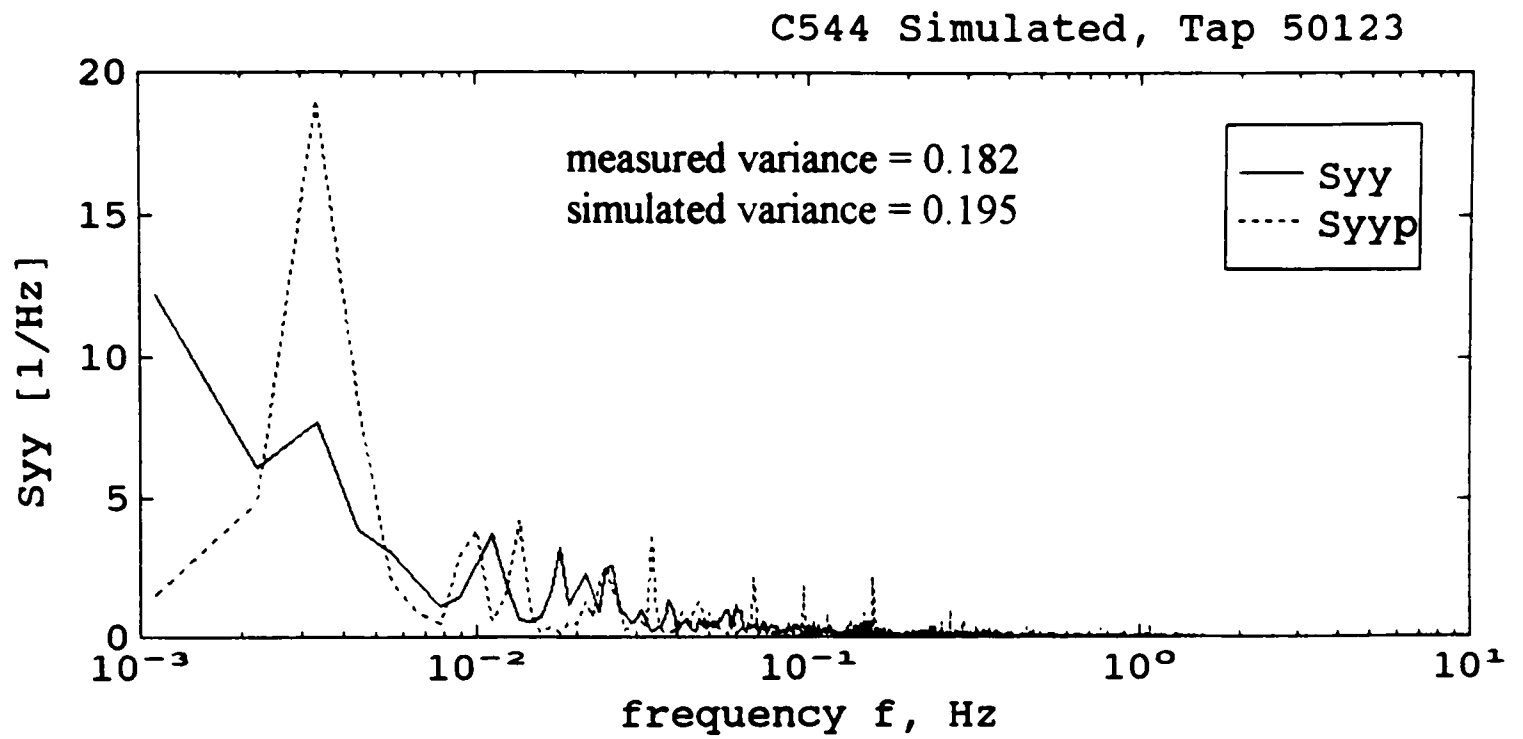


(a) Using transfer functions of CS077 only.

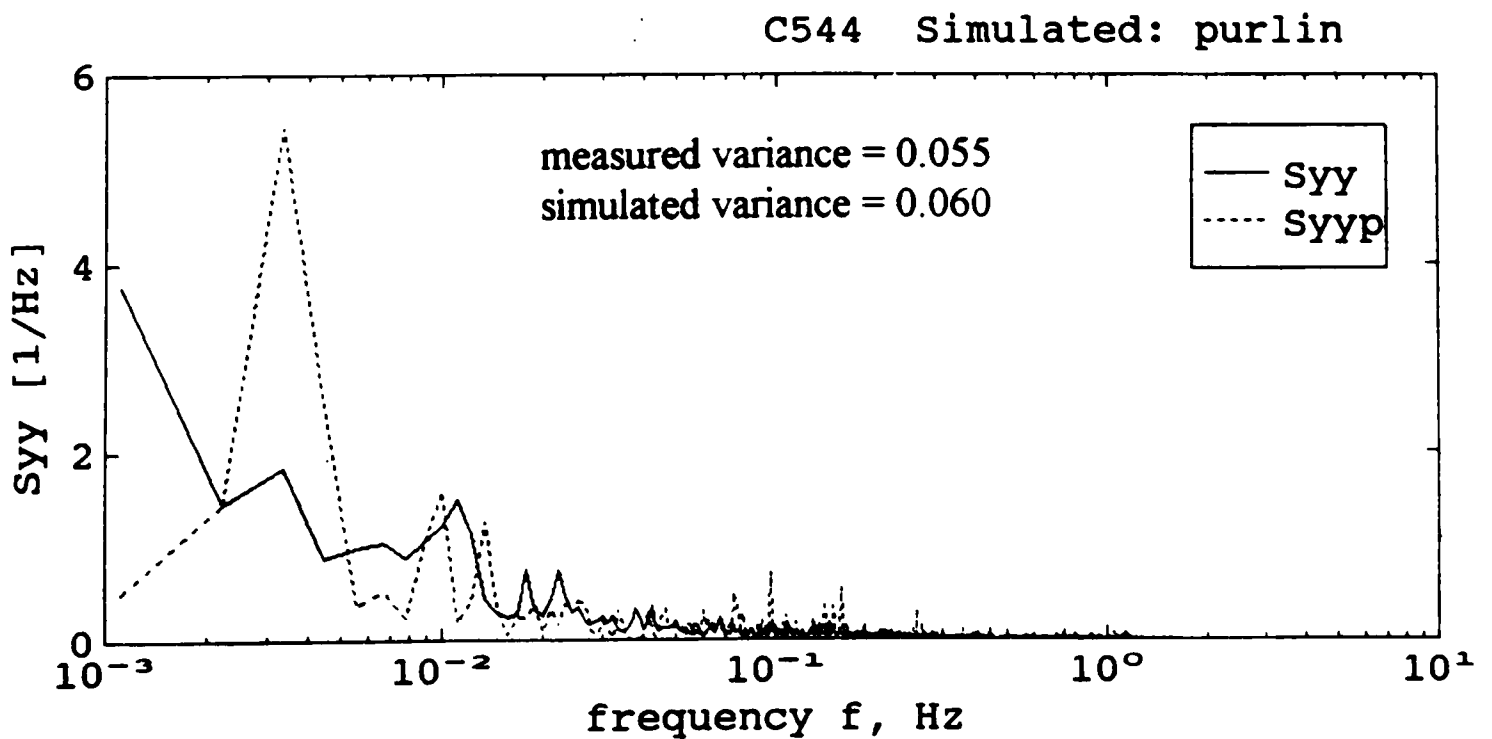


(b) Using averaged transfer functions of CS070 and CS077.

Figure 5.38. Simulated pressure-coefficient spectrum for tap 42212 for record CS073.



(a) Tap 50123 under the separation bubble.



(b) Roof purlin area-averaged ($\theta \approx 270^\circ$) case.

Figure 5.39. Simulation of pressure-coefficient spectra for record C544 using transfer functions from record C539.

Further simulations of the pressure-coefficient spectra for record C544 using the transfer functions of record C539 for tap 50123, in the roof separation zone, and for the roof purlin area-averaged ($\theta \approx 270^\circ$) case are illustrated in Figure 5.39. The simulated and measured pressure-coefficient variances are also indicated therein. It is seen from Figure 5.39 that the simulated variances were 1.07 and 1.10 times the measured ones for tap 50123 and roof purlin, respectively. This is again an excellent prediction falling well within the range of pressure variances observed in the field for the particular cases. The frequency content is also matched reasonably well for field conditions.

It was seen that the transfer functions for different records with similar mean angles of attack did exhibit small variations due to the reality of field conditions and the very limited number of similar field records that were available for averaging. However, they can be considered very similar, both qualitatively and quantitatively, from a practical point of view and the success achieved in simulation justifies this. It is thus seen that the transfer functions essentially capture the mechanism that transforms wind velocity to pressures on building surfaces. The successful simulation of the pressure-coefficient spectrum using transfer functions identified based on the proposed model, as illustrated by the above cases, suggests that practical applications of the model for the prediction of the pressure spectrum on building surfaces and the digital synthesis of pressure time histories (Seong, 1993) seem promising. This aspect will be further discussed, qualitatively, in Chapter 6 after simulation exercises are carried out for the roof corner cases.

5.4 Summary

In this chapter, transfer functions, spectral decomposition, and simulation results obtained from full-scale data were presented for the windward wall, roof separation and reattachment zones, leeward wall, side walls and a roof purlin for wind normal to the building. The important observations are summarized herein. The proposed model was found to predict and simulate the pressure spectrum from the upstream velocity spectra reasonably well. The residuals were small and the predictions were seen to fall well within the range of variability observed in the field data.

The transfer functions for different flow regions were found to be quite similar in form, but exhibited quantitative variation. The transfer function for a tap for a particular velocity component was found to exhibit variability over the entire frequency range. The transfer functions from two different records with similar mean angles of attack were found to be very similar with some quantitative variation. These variations may be attributed to deviation from Gaussian behavior of the input, instrumentation noise, computational noise, non-stationary effects in the data, and the limited number of similar records that were available for averaging in the identification process. The transfer functions obtained from the 3-cup/vane data showed an upward trend in the higher frequency end (beyond 0.5 Hz) in comparison to the ones obtained from the sonic data because of insufficient frequency response. The phase angles of the pressure spectra and transfer functions were found to be uniformly distributed between $-\pi$ and $+\pi$ radians.

The spectral decomposition results show that the linear and quadratic terms of both the u and v components have a comparable contribution to the pressure variance for most of the cases. The lateral and quadratic terms are important. The v terms, signifying the effect of local changes in wind direction, are more dominant for the side and leeward walls. The linear v term is most significant for the side walls, whereas the quadratic v term is most significant for the leeward wall. The linear u term is more dominant for the area-averaged cases on the purlin. There is also an indication that the mechanisms producing pressures in the reattachment regions of the roof and side walls may be different.

The bispectra of pressure-coefficients indicate that the non-Gaussian and hence the non-linear character of wind pressures are associated with low frequencies (less than 0.2 Hz for most cases). The reattachment zone is the only exception where frequencies above 1 Hz are also conspicuous. On the roof, the higher frequencies become more significant as the distance from the upstream edge increases and more so well into the reattachment region. More than 95 percent of the pressure variance is contained in frequencies below 2 Hz for all taps except those in the reattachment region for which the figure is 80 percent. For the windward, leeward and side walls and purlin area-averaged cases about 85 to 90 percent of the pressure variance is contained in frequencies below 0.5 Hz.

CHAPTER 6

TRANSFER FUNCTIONS AT THE ROOF CORNER FOR QUARTERING WIND

6.1 Introduction

The roof corner is the most critical region on a building where the majority of the wind-induced failures on low buildings are initiated due to high suction pressures experienced in that region. In this chapter, transfer functions are identified and the spectral decomposition problem solved for pressure taps 50101, 50501, 50505, 50901, 50905, 50907 and area-averaged cases using some or all of the nine pressure taps at the southwest corner of the roof. Results of field (Mehta et al., 1992) and wind-tunnel measurements (Cochran, 1992) on the Texas Tech test building show that the critical rms pressures for the roof corner pressure taps occur for near quartering winds. Hence, the study presented in this chapter for the roof corner is for the critical angle of attack of approximately 225° , unless mentioned otherwise. The transfer functions identified herein are based on wind velocity measurements in the field using a 3-cup/vane anemometer. Transfer functions, associated with linear and quadratic u velocity only, are identified for tap 50501 using the limited wind-tunnel data obtained from CSU on a 1:50 model and compared with the corresponding ones identified from full-scale data.

The locations and coordinates of the pressure taps are given in Chapter 3 in Figure 3.3 and Table 3.1. The summary statistics of velocity data of the concatenated records used in the results presented in this chapter are tabulated in Table 6.1. More of the summary statistics, including those for pressures, are tabulated in the appendix.

The model proposed in Section 4.2 will now be applied to the data summarized in Table 6.1 to first solve the system identification problem for representative roof corner taps. The four transfer functions so identified will then be used on the same input spectra to predict the output pressure-coefficient spectrum using Eq. 4.8. This solves the spectral decomposition problem by determining the contributions to the predicted pressure-coefficient spectrum from the linear and quadratic velocity terms in the model. Physical

interpretations can then be made about the mechanisms that produce high suction at the corner. The problem of simulation or output prediction of the pressure-coefficient spectrum using input spectra from a different record will be discussed later in Section 6.3 of this chapter.

Table 6.1. Summary statistics of velocity data of concatenated records.

Concatenated Record No.	15-minute records used	Wind azimuth α°	Angle of attack θ°	U at 4 m m/s	I_u	I_v
C081	M15N081 + 082 + 086	272.6	227.6	8.79	0.234	0.259
C478	M15N478 + 479 + 482	304.0	214.0	11.56	0.201	0.170
C709	M15N709 + 710 + 711	27.1	222.1	9.88	0.196	0.203
WT1*	CSU Wind Tunnel	-	225.0	10.32	0.192	-
WT2*	CSU Wind Tunnel	-	225.0	10.19	0.201	-
WT3*	CSU Wind Tunnel	-	225.0	10.11	0.203	-
C539	M15 N539 + 540 + 541	353.1	263.1	9.11	0.194	0.194
C544	M15N544 + 545 + 546	357.7	267.7	9.36	0.189	0.144

* Only u velocity time history data was available from the wind tunnel.

6.2 Identification of Transfer Functions and Spectral Decomposition for the Roof Corner

When the wind is skewed from the normal, the flow separating from the upwind edge of the roof will have a component of velocity along the line of separation. As shown in Figure 2.4, the flow marked A separating near the upwind corner will tend to be displaced under the flow B separating immediately downwind. The vorticity of the shear layer from A adds to that of B and this process continues along the roof edge, increasing the circulation and resulting in a strong conical vortex called the *delta-wing* vortex. These vortices generally occur in pairs, one along each windward edge as shown in Figure 2.4. The strength of each vortex depends on the wind angle and is strongest at about 30° (Cook, 1985) from normal to the respective edge. The pressure along the eave and verge

under these vortices is strongly negative, becoming even more negative towards the corners. These vortices, acting directly and interacting with the incident turbulence, are the principal cause of high peripheral uplift on roofs resulting in much of the damage experienced by buildings. The rotation of both vortices pulls the flow down behind them to form a V-shaped wedge of attached flow as illustrated in Figure 2.4. In the apex of this 'V', the flow speed is higher than the approach flow and the pressure is still negative, but recovers downwind towards zero as the flow diverges out of the 'V'. The center-line of the 'V', which is the dividing line from the effect of either vortex on the roof surface, remains approximately in the incident wind direction (Cook, 1985). An experimental study of the distribution of pressure near roof corners of flat roof low buildings has been recently published by Lin et al. (1995).

6.2.1 Individual Taps

The results of system identification and spectral decomposition for pressure taps 50101, 50501, 50505, 50901, 50905 and 50907 at the roof corner for near quartering winds are now presented and discussed

The transfer functions for tap 50101, which is the tap located closest to the corner along the line inclined 45° to the roof eave, are shown in Figure 6.1 for a typical record C081 ($\theta = 227.6^\circ$). A comparison of the predicted total (S_{yyp}) and linear (S_{yypl}) pressure-coefficient spectra, the measured pressure-coefficient spectrum (S_{yy}) and the residual spectrum (S_{nn}) are shown in Figure 6.2. The predicted spectrum is seen to match closely with the measured one. The spectral decomposition of the predicted spectrum into components due to the linear (S_{y11} and S_{y21}) and quadratic (S_{y12} and S_{y22}) is shown in Figure 6.3. The transfer functions for the other records with similar mean angles of attack (C709 and C478 with $\theta = 222.1^\circ$ & 214° , respectively) of the wind were found to be very similar in form but do exhibit small variations in the quantitative sense. This variability in transfer functions will be discussed in Section 6.3

The total coherence function is shown in Figure 6.4. The coherence function in Figure 6.4 has a mean of 0.95 over the frequency range 0 to 5 Hz. It is seen to randomly

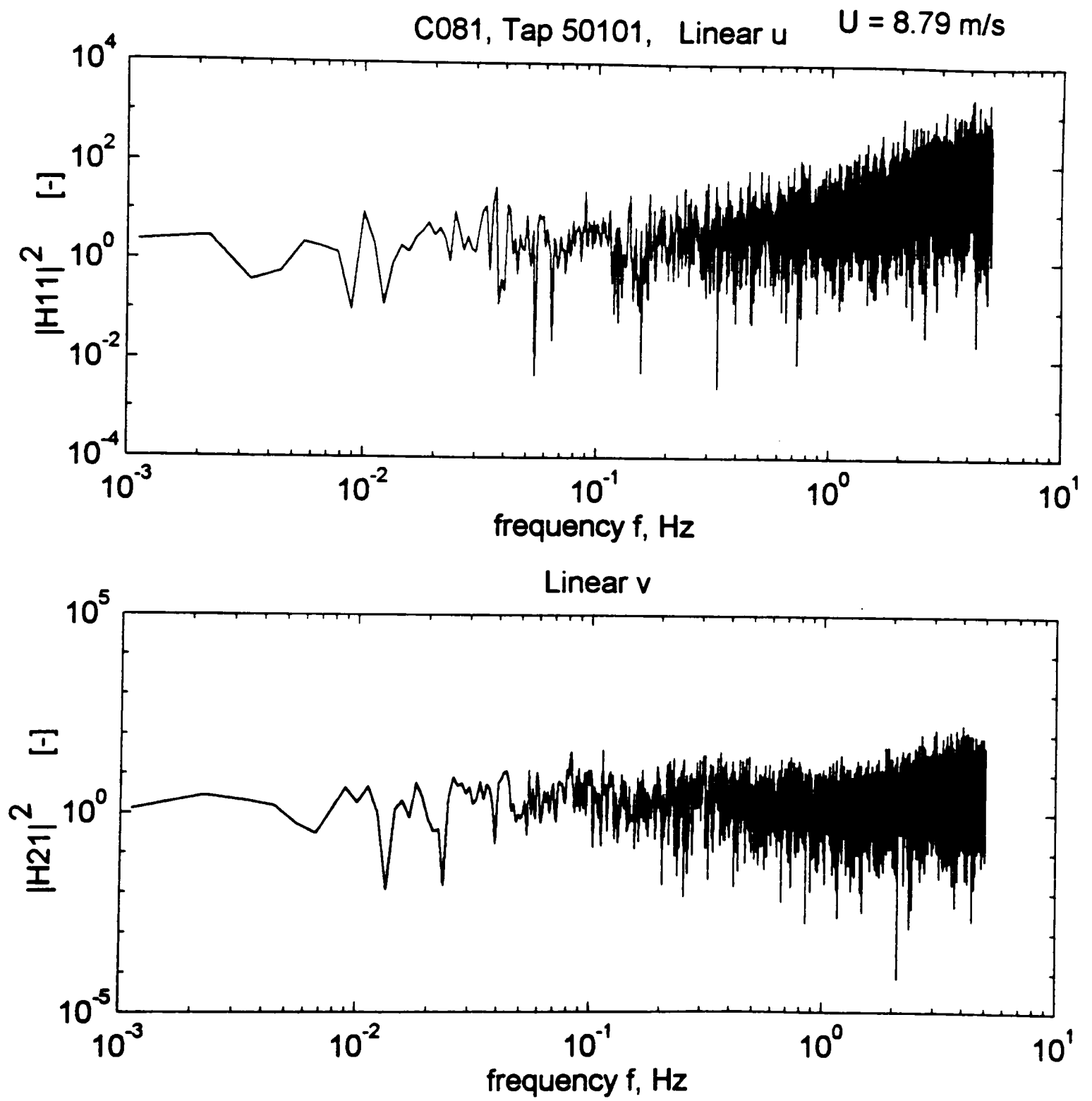


Figure 6.1. Transfer functions for tap 50101 (C081). (a) Linear.

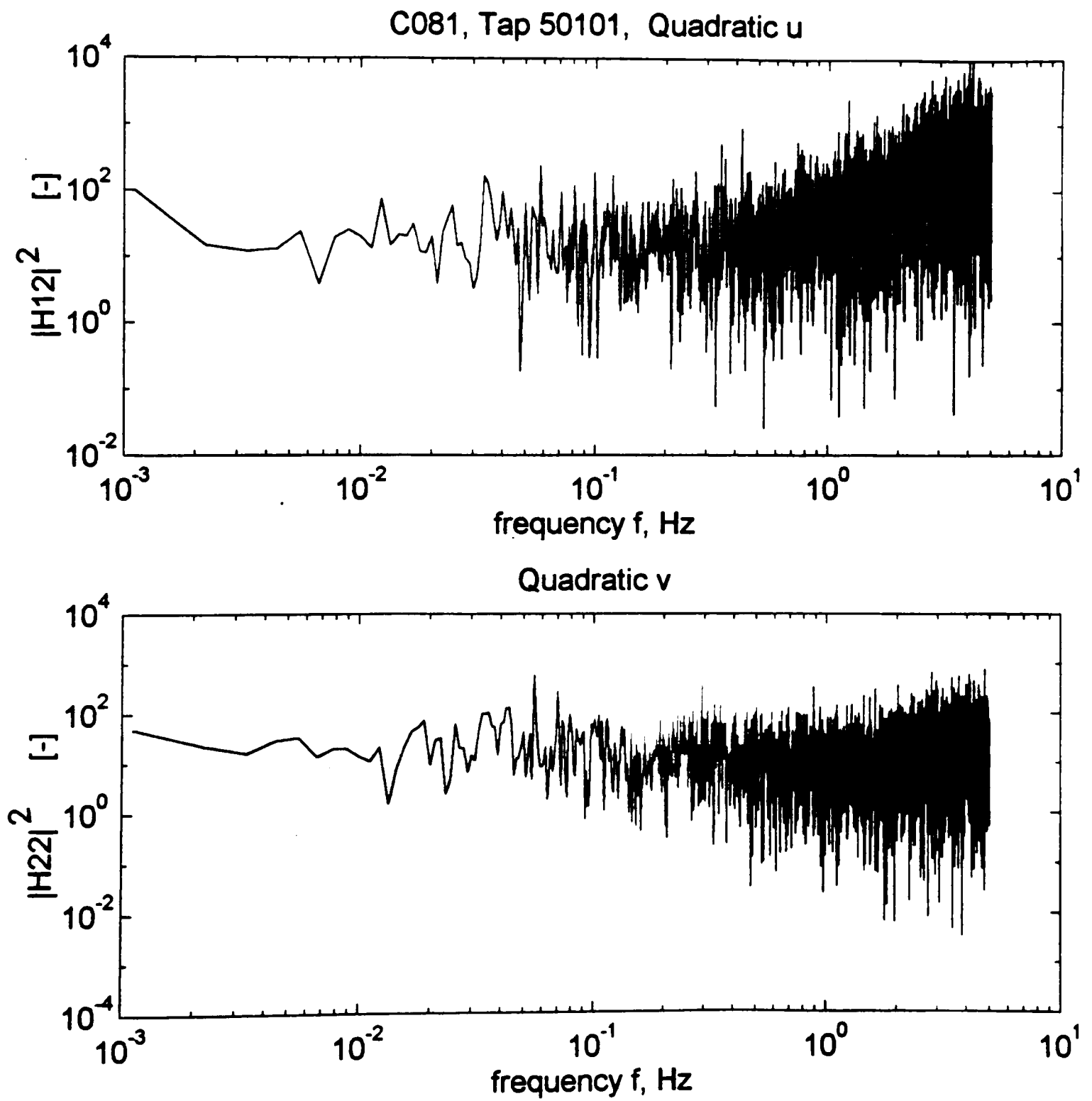


Figure 6.1. Continued. (b) Quadratic.

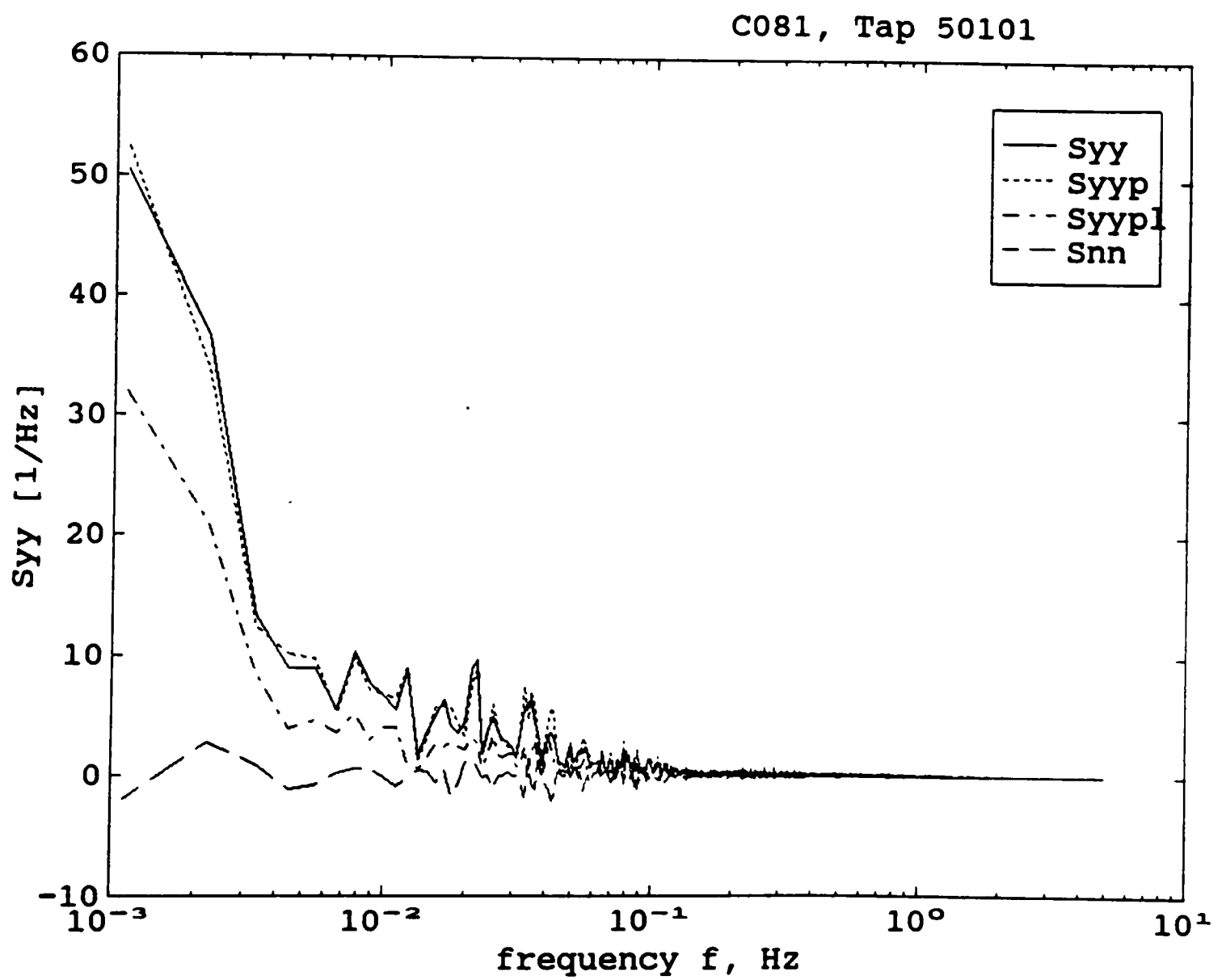


Figure 6.2. Output prediction for tap 50101 (C081).

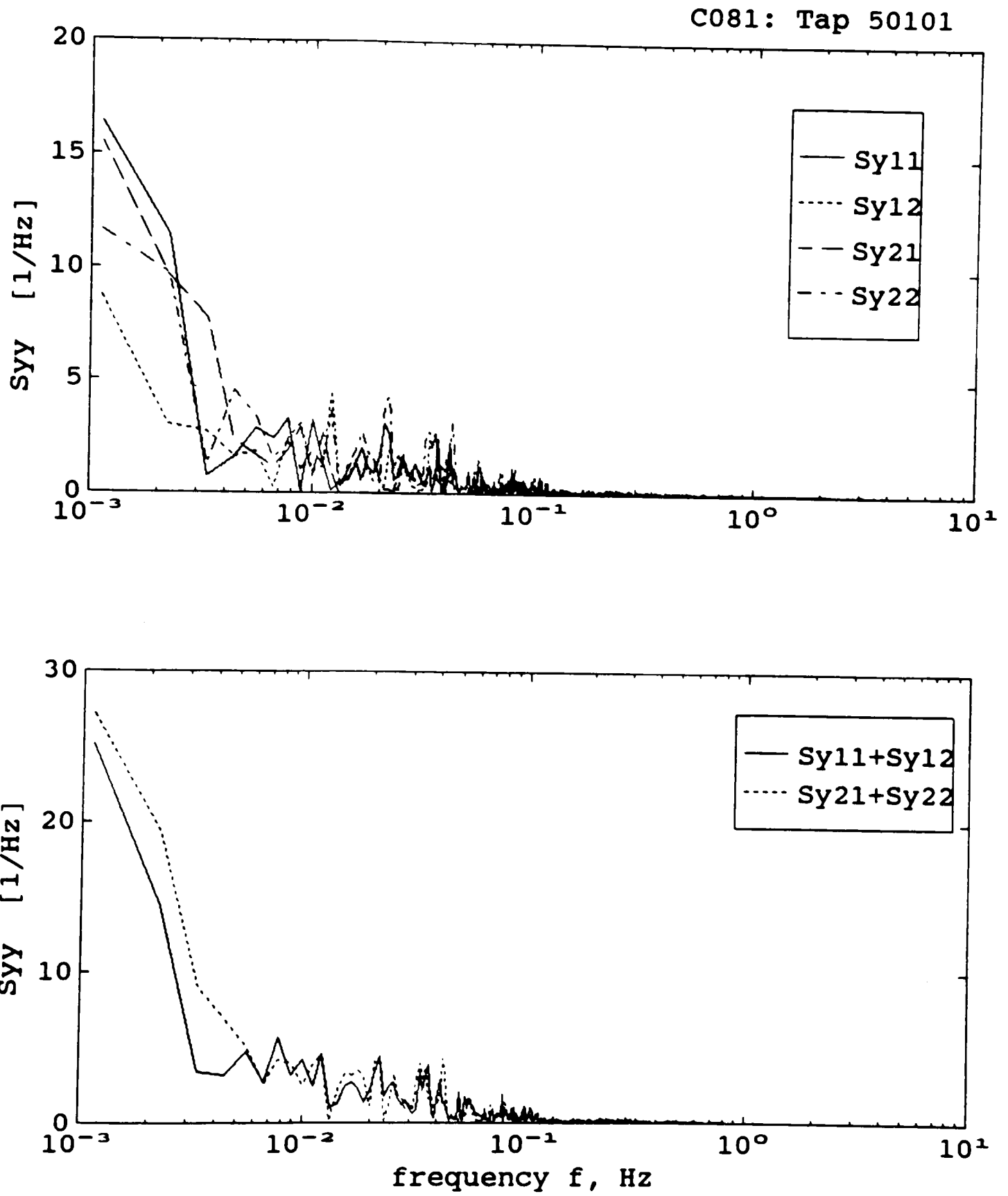


Figure 6.3. Decomposition of pressure-coefficient spectrum for tap 50101 (C081).

fluctuate about the mean with a standard deviation of 0.45. This is indicative of random errors in the transfer function estimates for the same reasons as for the results presented in Chapter 5. However, the results obtained are acceptable from a practical point of view since the mean coherence over the frequency range is close to unity and the residuals are reasonably small as seen from Figure 6.2.

The relative contributions of the linear and quadratic terms in the model to the pressure variance and the total coherence are tabulated in Table 6.2 for the different data records summarized in Table 6.1. It is seen from Table 6.2 that all the terms have almost comparable contributions to the pressure variance. This means that at the location of tap 50101, the fluctuating pressures are equally influenced by modification of the upstream flow and dissipation. A typical bispectrum of the pressure-coefficients for tap 50101 is shown in Figure 6.5. The bispectrum shows a slightly broadened peak at low frequencies, indicating that the non-linear and non-Gaussian character are mainly due to the low frequency content in the pressure fluctuations.

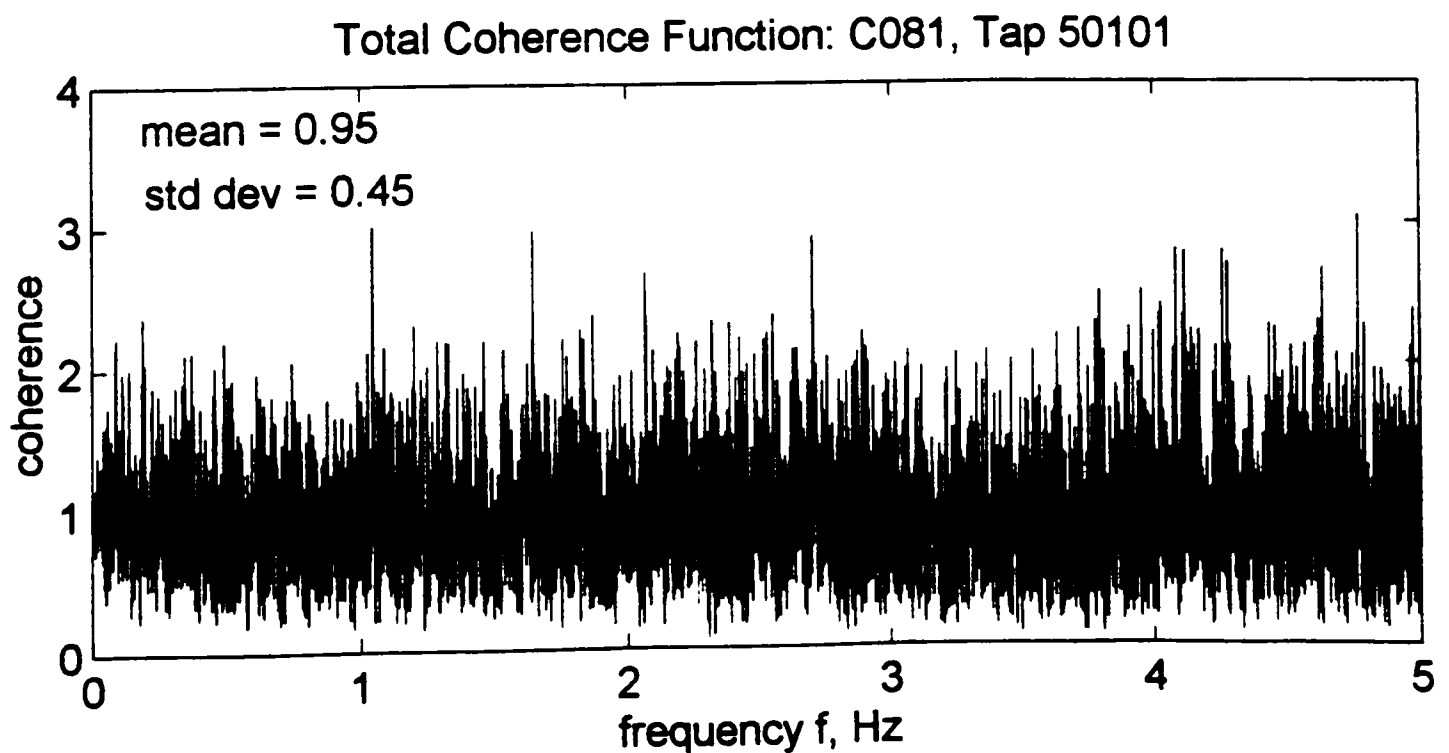


Figure 6.4. Total coherence function for tap 50101 (C081).

Bispectrum of $y=C_p$: Tap 50101, M15N086, $\theta=228.1$, dyn. pr.=5.1 kg/m²

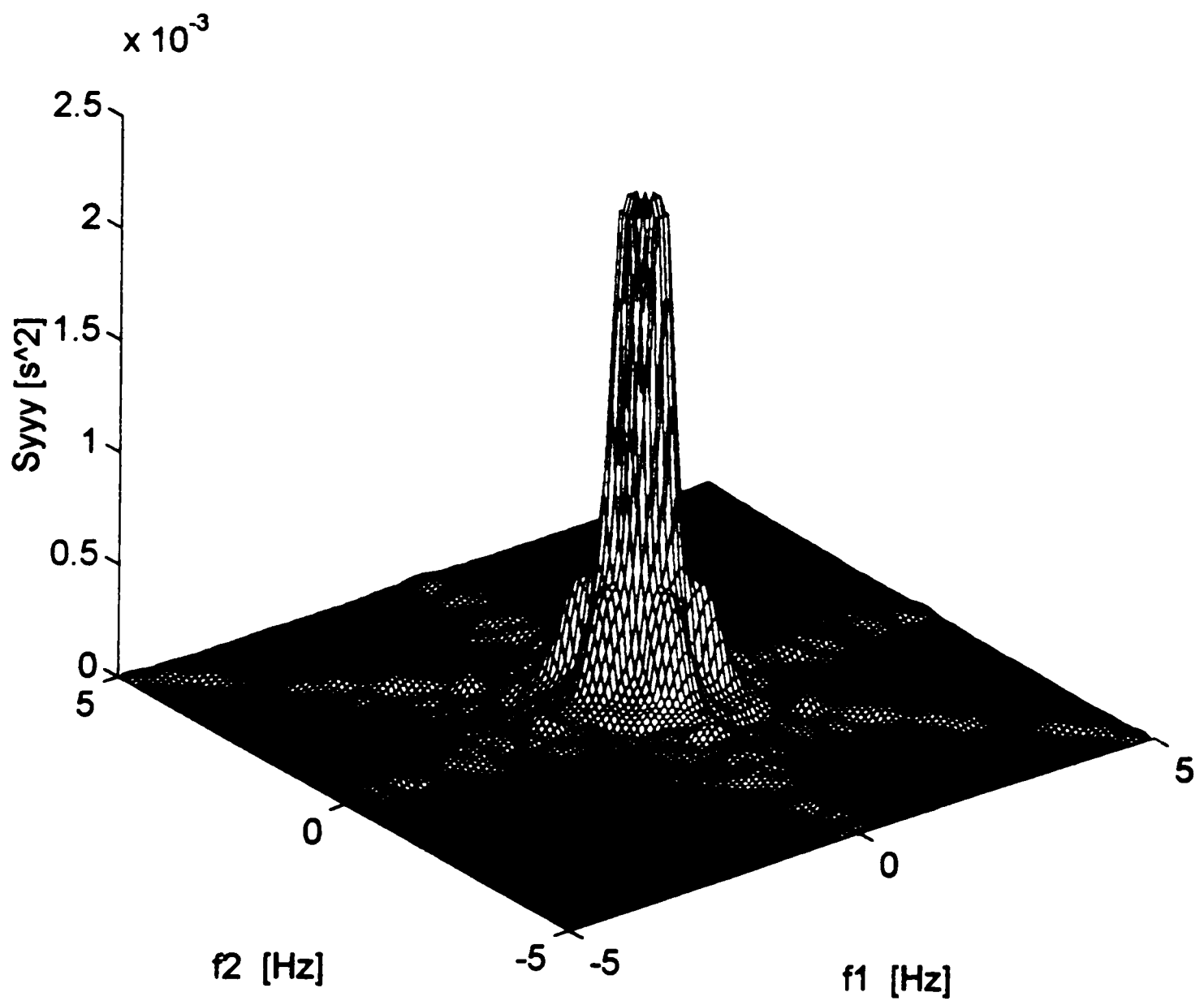


Figure 6.5. Bispectrum of pressure-coefficients for tap 50101 (M15N086).

Table 6.2. Contribution from different components of the model to pressures for the roof corner taps.

Record	Cp_variance		Contribution, as % of measured spectrum, from					Total Coherence	
	meas- ured	pred- icted	<i>u</i>	<i>v</i>	<i>u</i> ²	<i>v</i> ²	Resid- ual, <i>S_{nn}</i>	mean	std. dev.
<u>Tap 50101</u>									
C081	0.5345	0.5406	25.9	24.2	22.4	28.6	-1.1	0.95	0.45
C709	0.1361	0.1352	24.7	23.5	25.1	26.1	0.6	0.99	0.41
C478	0.1819	0.1833	26.4	24.0	26.8	23.6	-0.8	0.97	0.40
<u>Tap 50501</u>									
C081	1.6488	1.6289	24.5	33.5	19.6	21.2	1.2	1.04	0.47
C709	1.4486	1.4625	25.0	30.1	21.2	24.7	-1.0	1.01	0.41
C478	1.2255	1.2310	31.7	24.1	21.0	23.7	-0.5	1.01	0.42
<u>Wind tunnel: 50501</u>									
WT1*	0.9331	0.5173	29.9	-	25.5	-	44.6	-	-
WT2*	0.9784	0.5564	30.0	-	26.9	-	43.1	-	-
WT3*	0.8973	0.509	29.8	-	26.9	-	43.9	-	-
<u>Tap 50505</u>									
C081	0.0742	0.0753	27.4	24.9	22.9	26.2	-1.4	0.94	0.44
C478	0.0132	0.0135	31.1	25.6	23.4	21.8	-1.9	1.00	0.41
<u>Tap 50901</u>									
C081	0.5119	0.5157	38.9	22.2	17.1	22.7	-0.9	1.01	0.46
C709	0.4660	0.4577	26.3	24.5	23.2	24.2	1.8	1.01	0.41
C478	0.3389	0.3407	32.0	25.1	22.3	21.1	-0.5	1.02	0.42
<u>Tap 50905</u>									
C081	0.0509	0.0506	26.0	21.0	21.6	30.8	0.6	0.95	0.44
C478	0.0911	0.0930	29.5	25.2	25.8	21.5	-2.0	0.99	0.41
<u>Tap 50907</u>									
C081	0.0191	0.0185	30.9	19.5	21.5	25.1	3.0	0.93	0.45
C478	0.0142	0.0144	27.9	26.0	26.0	21.9	-1.8	1.00	0.41

* Only *u* velocity time history data was available from the wind tunnel.

Pressure tap 50501 is located about 1.5 m (5 ft) away from the corner along the southern edge of the roof. Tap 50501 experiences the highest rms and peak pressures on the test building. The pressure at this tap is strongly influenced by the conical vortices. The transfer functions for this tap for a typical record, C081, are shown in Figure 6.6. The output prediction and spectral decomposition for this tap are shown in Figures 6.7 and 6.8, respectively. The predicted spectrum was found to match the measured one closely. The input and output spectra used in the identification of transfer functions for this tap are shown in Figure 6.9. The coherence function for this tap shown in Figure 6.11 has a mean and standard deviation of 1.04 and 0.46, respectively. The coherence function has the same form as any others presented so far.

The bispectrum for tap 50501, shown in Figure 6.10, has a sharp peak at the very low frequency end. It can be seen from Table 6.2 that the linear terms in the model contribute 55 to 60 percent to the pressure variance. This means the pressures at this tap are more influenced by modification of flow. Also, it is the linear v term that has the most significant contribution. This indicates that changes in wind direction, that aid in rotating the fluid elements, contribute significantly to the formation of the delta-wing vortices producing high suctions at this tap. Among the quadratic terms, the one associated with lateral velocity contributes higher in the dissipation process than the along wind component. It is observed from the analysis of record C478 ($\theta = 214^\circ$) that, as the mean angle of attack becomes less skewed to the roof edges, the along wind component undergoes modification to produce the more significant contribution to the pressures. The transfer functions of all the three records were of similar form, but exhibited variability in the quantitative sense.

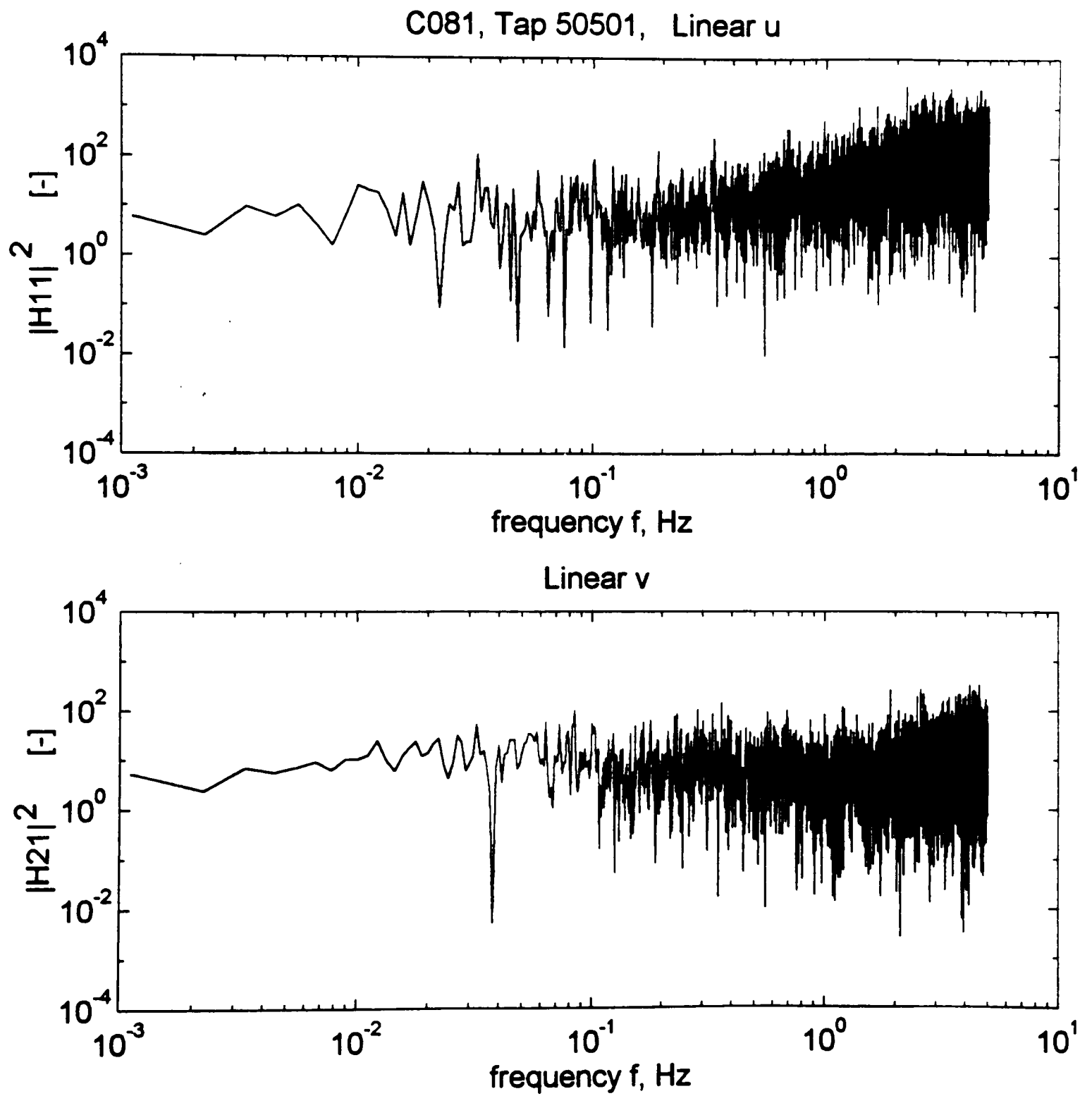


Figure 6.6. Transfer functions for tap 50501 (C081). (a) Linear.

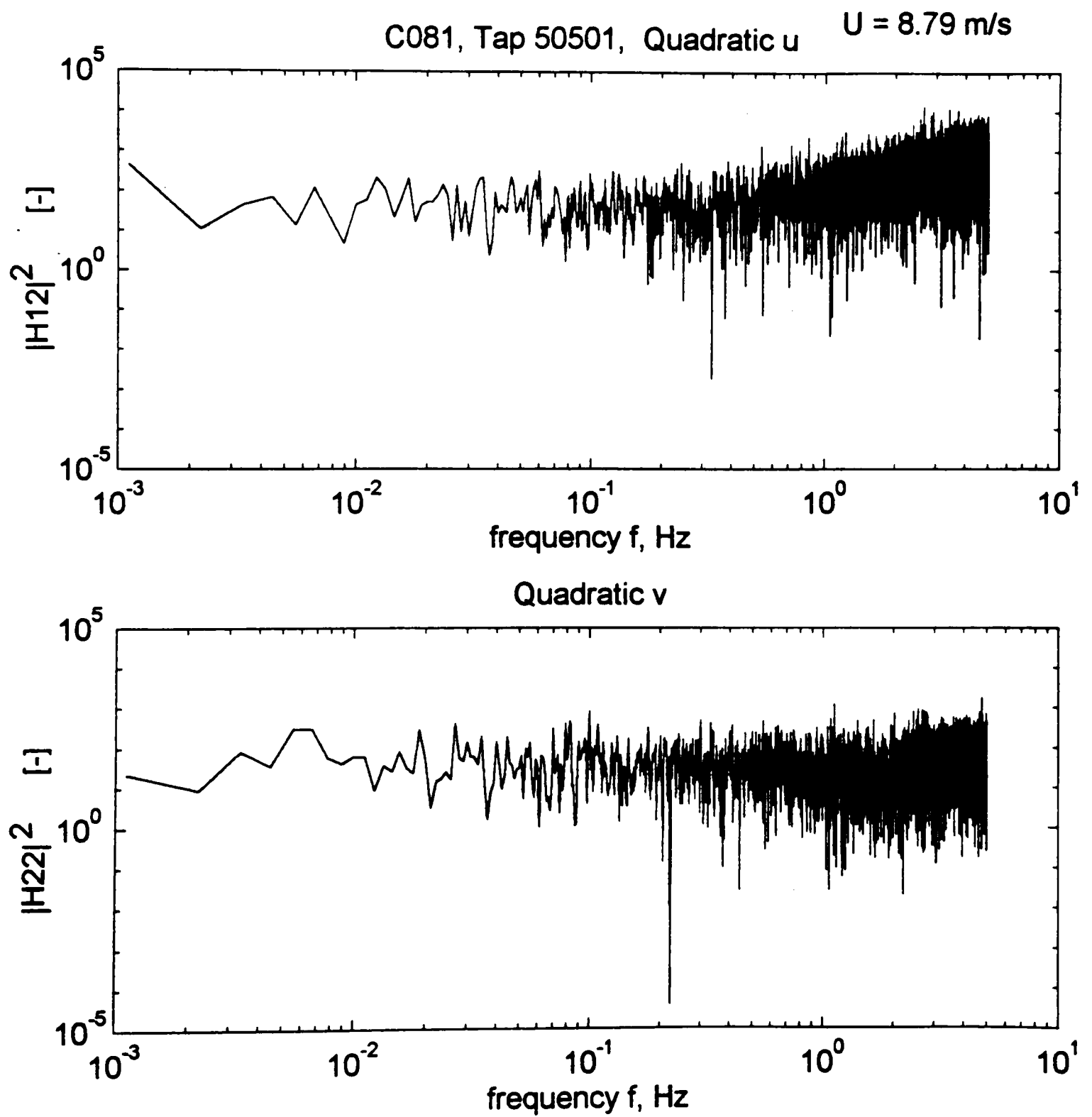


Figure 6.6. Continued. (b) Quadratic.

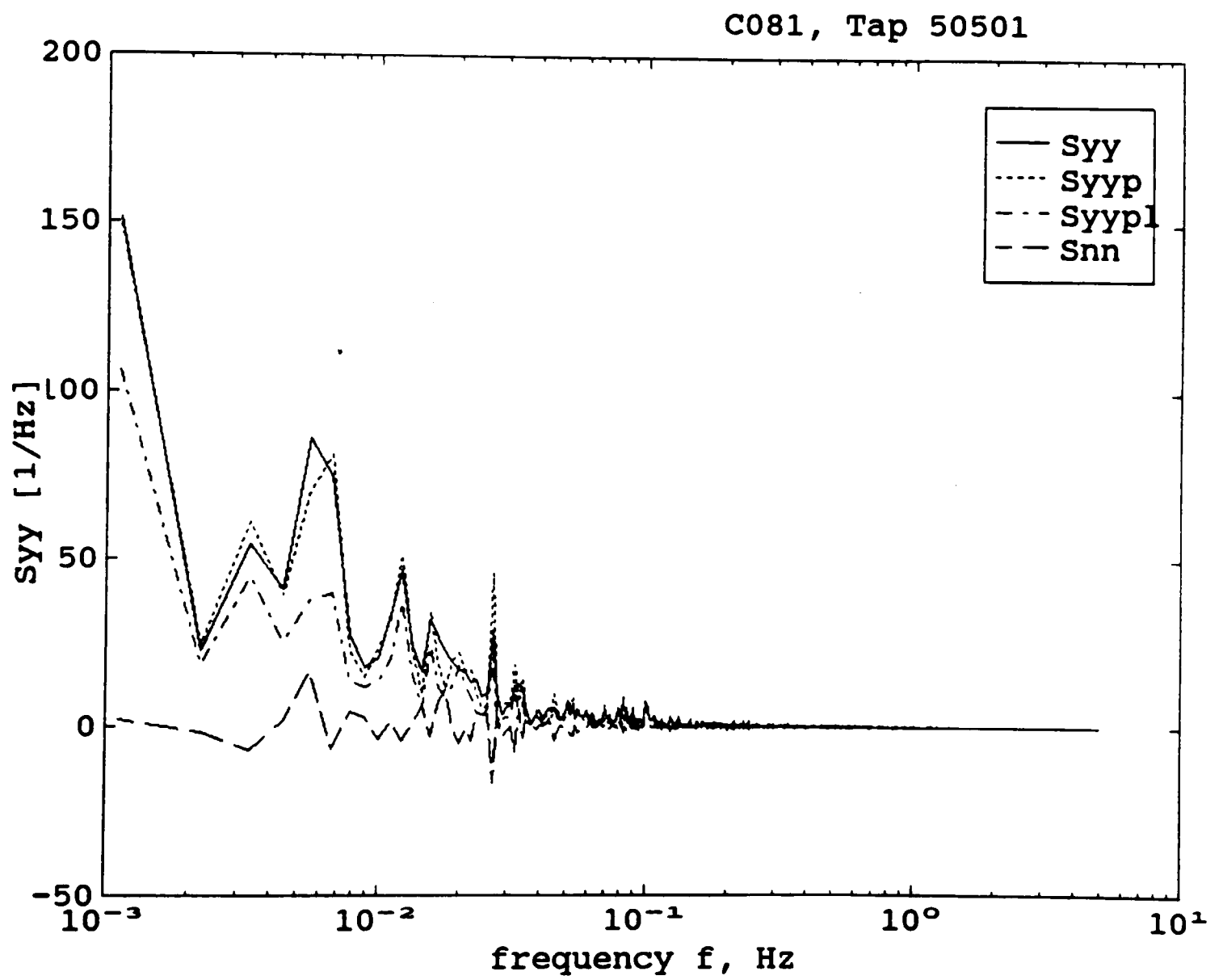


Figure 6.7. Output prediction for tap 50501 (C081).

C081: Tap 50501

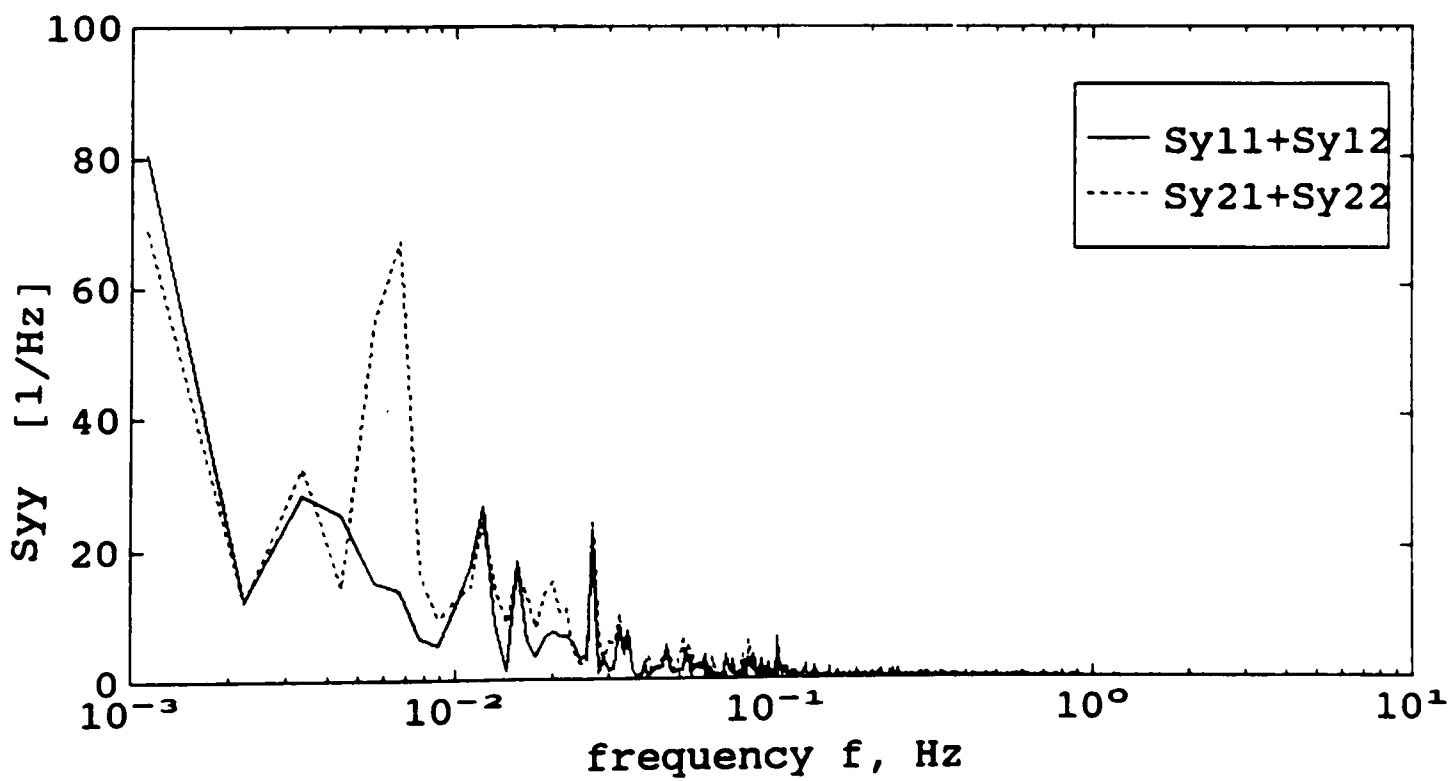
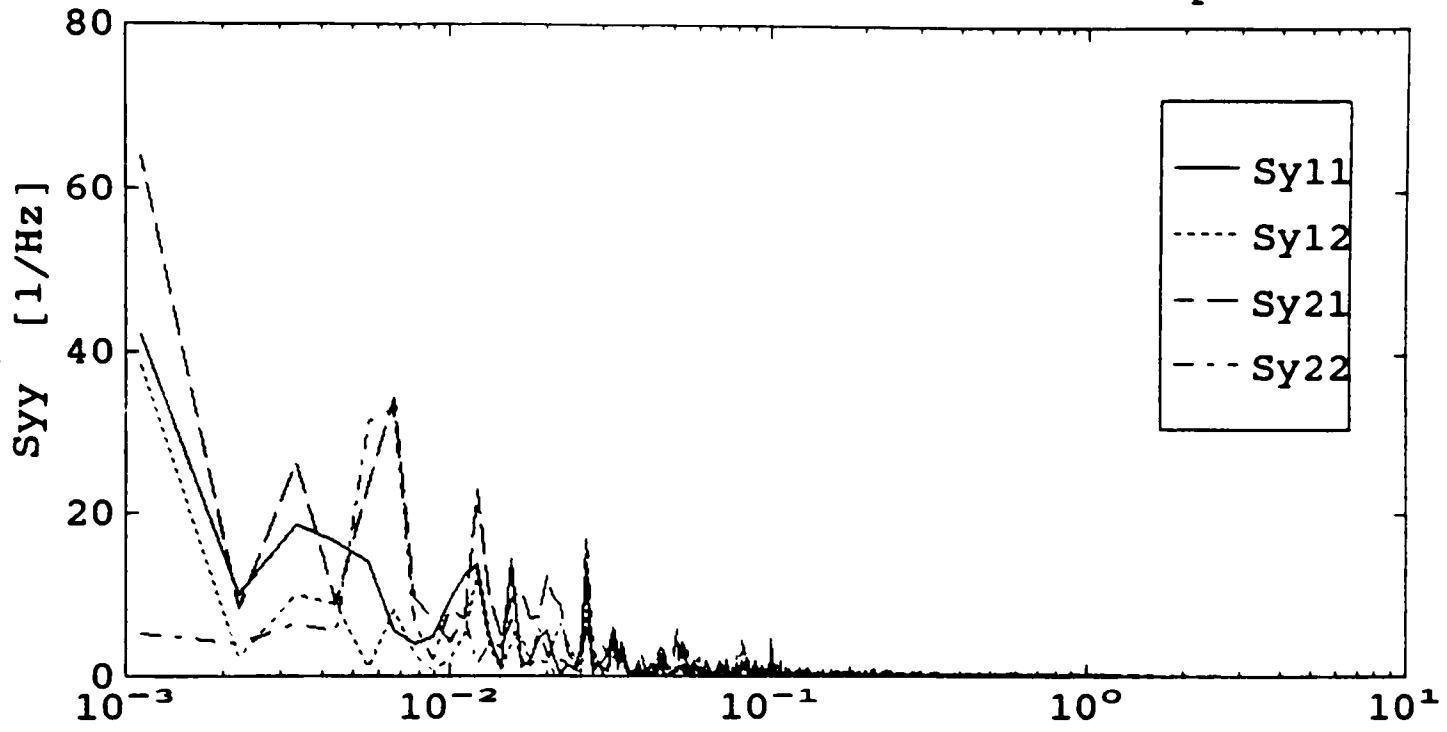
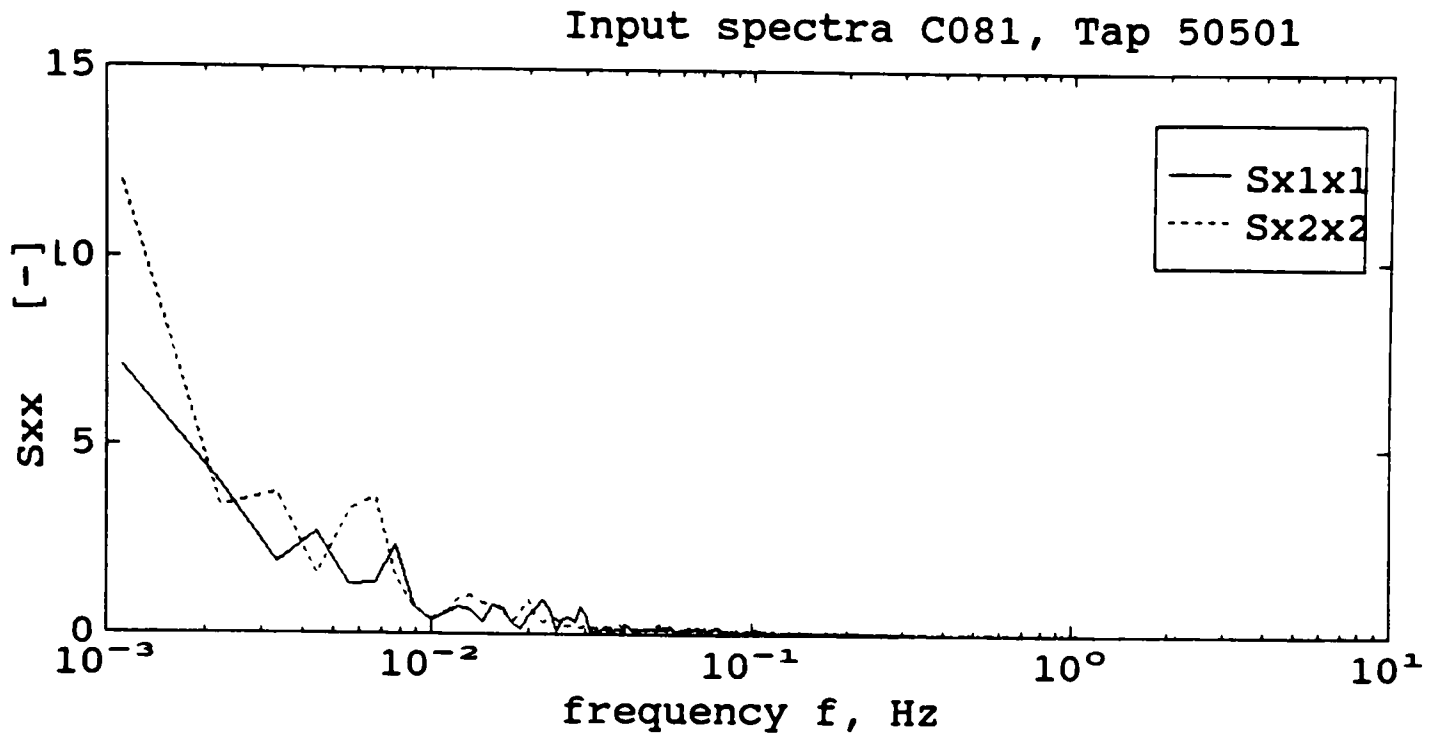
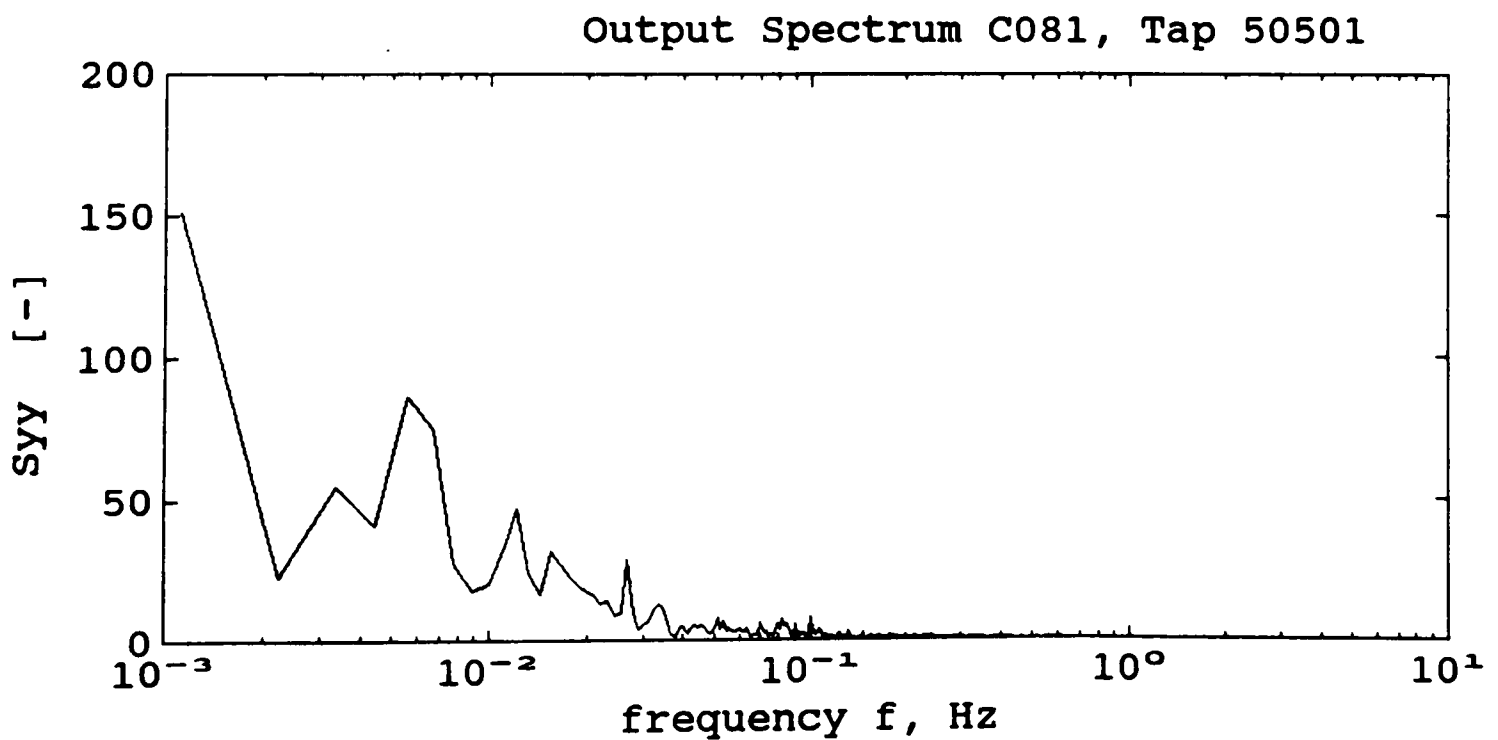


Figure 6.8. Decomposition of pressure-coefficient spectrum for tap 50501 (C081).



(a) Input velocity spectra.



(b) Output pressure-coefficient spectrum.

Figure 6.9. Input and output spectra for tap 50501 (C081).

Bispectrum of $y=C_p$: Tap 50501, M15N086, $\theta=228.1$, dyn. pr.= 5.1 kg/m^2

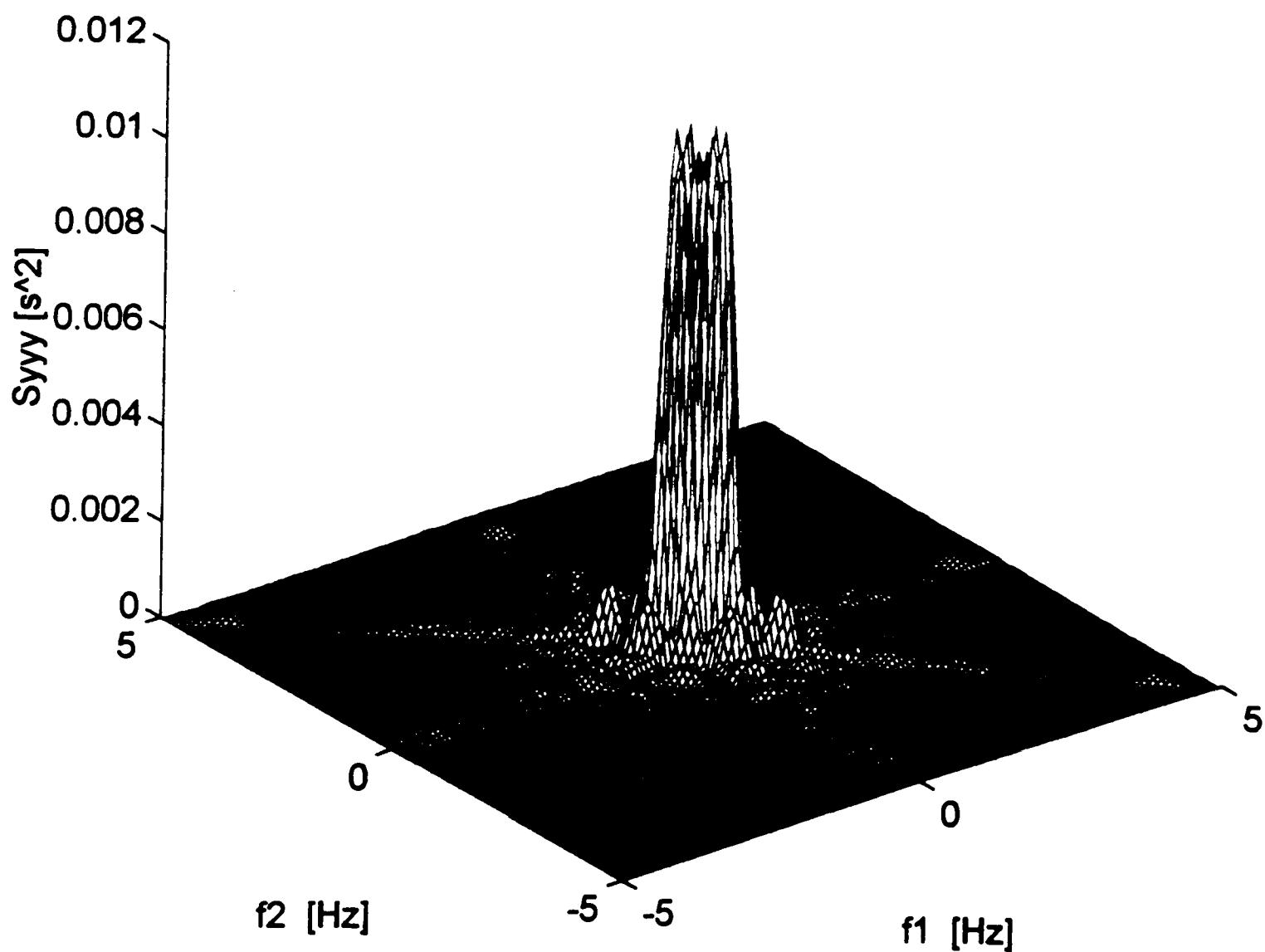


Figure 6.10. Bispectrum of pressure-coefficients for tap 50501 (M15N086).

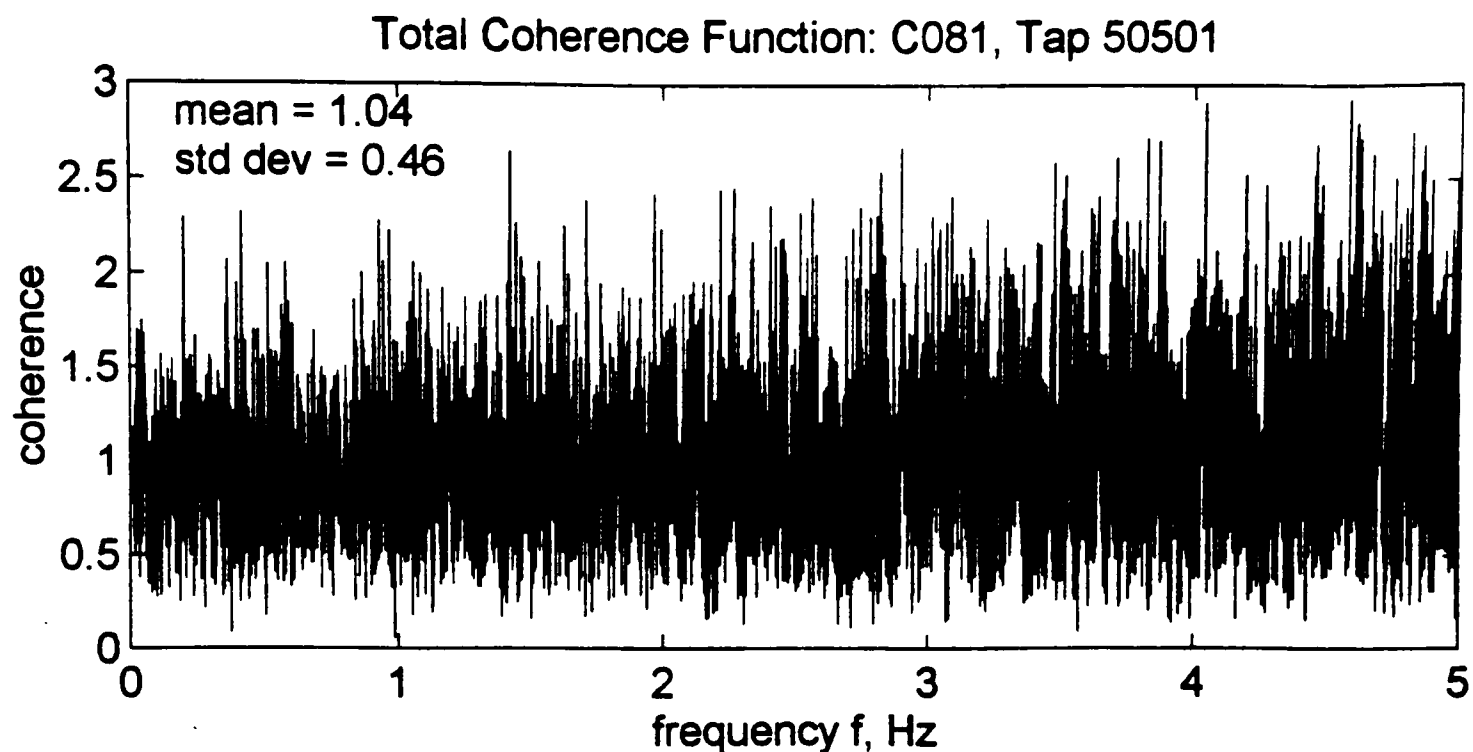


Figure 6.11. Total coherence function for tap 50501 (C081).

Three records of simultaneous measurements of velocity and pressures collected in the meteorological wind tunnel (MWT) at CSU were examined for tap 50501. These records are designated WT1, WT2 and WT3 in the results presented here. The MWT and the data are briefly described in Section 3.4. The data were collected on a 1:50 model of the test building for the angle of attack of 225° at a sampling frequency of 400 Hz (i.e., 8 Hz full-scale). However, simultaneous measurements of only the longitudinal component of velocity were available. Hence, only the transfer functions associated with the linear and quadratic u terms can be identified. Each record consisting of 32767 points, was divided into sub-records consisting of 7200 points representing a full scale time duration of 15 minutes.

The transfer functions for record WT3 are shown in Figure 6.12 in comparison with the full-scale one for record C709. It can be seen that the transfer functions obtained from the wind-tunnel and field data are quite similar up to about 0.5 Hz. The upward trend seen at the higher frequency end in the field transfer functions is again due to the

insufficient frequency response of the 3-cup anemometer beyond about 0.5 Hz. The predicted output pressure-coefficient spectrum due to only the linear and quadratic u terms (S_{yypu}) and the measured one (S_{yy}) are shown in Figure 6.13. The spectral decomposition for the wind-tunnel record WT3 is shown in 6.14. The total coherence function associated with the u terms, shown in Figure 6.15, has a standard deviation of 0.28 about a mean of 0.52. The form of the coherence function is also indicative of random errors, as seen for the field records, in spite of more controlled conditions under which the data are collected in the wind tunnel. Hence, noise in the input is not the primary cause of the random errors. Further discussion of the errors and variability is continued in Section 6.3 where simulation of the pressure spectrum, due to the u terms only, is attempted using the wind tunnel data.

It is observed from Table 6.2 that the contribution from the u terms are consistent for all the three records. It is also seen from that the contribution from the u terms account for about 56 percent for all the wind tunnel records, with the linear u term having the more significant contribution (30 percent). On the contrary, the field records have a contribution of only about 46 percent from the u terms. This seems to indicate that the lateral turbulence, which has a more dominant contribution and seen to play an important role in producing fluctuating pressures in the field, is not being simulated well in the wind tunnel. This could possibly be the reason for deficiency in the peak and rms pressures observed in the wind tunnel at the roof corner by Cochran (1992). The similarity observed between the field and wind-tunnel the transfer functions suggests that the transfer functions essentially capture the physical mechanism which results in producing surface pressures. This mechanism is the same for the field and wind tunnel. Thus, there is an indication that the deficiency observed in the wind tunnel is possibly due to a deficiency in the input velocity spectra. This seems to be specifically true for the lateral velocity component.

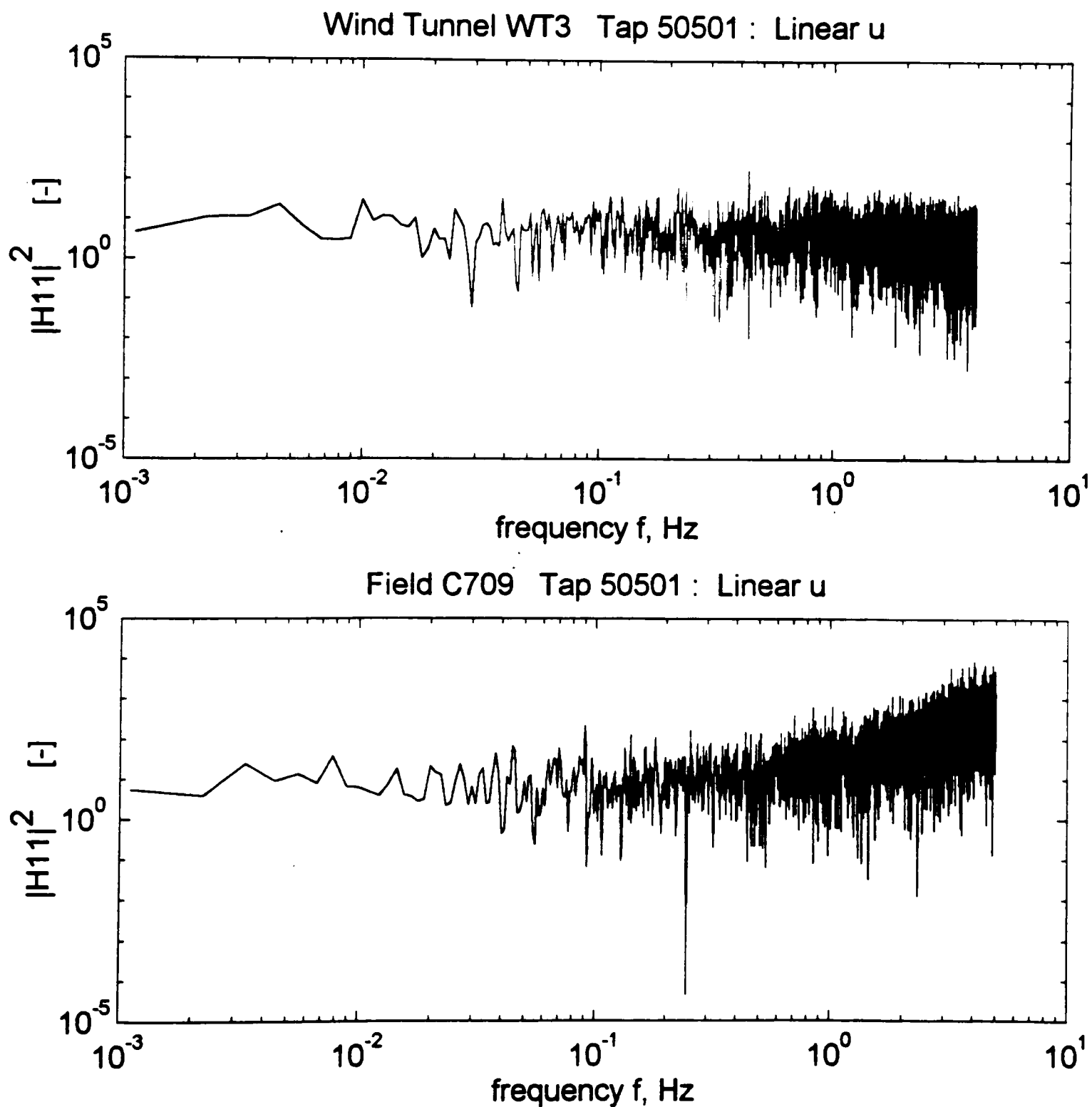


Figure 6.12. Comparison of transfer functions between field and wind tunnel for tap 50501. (a) Linear u .

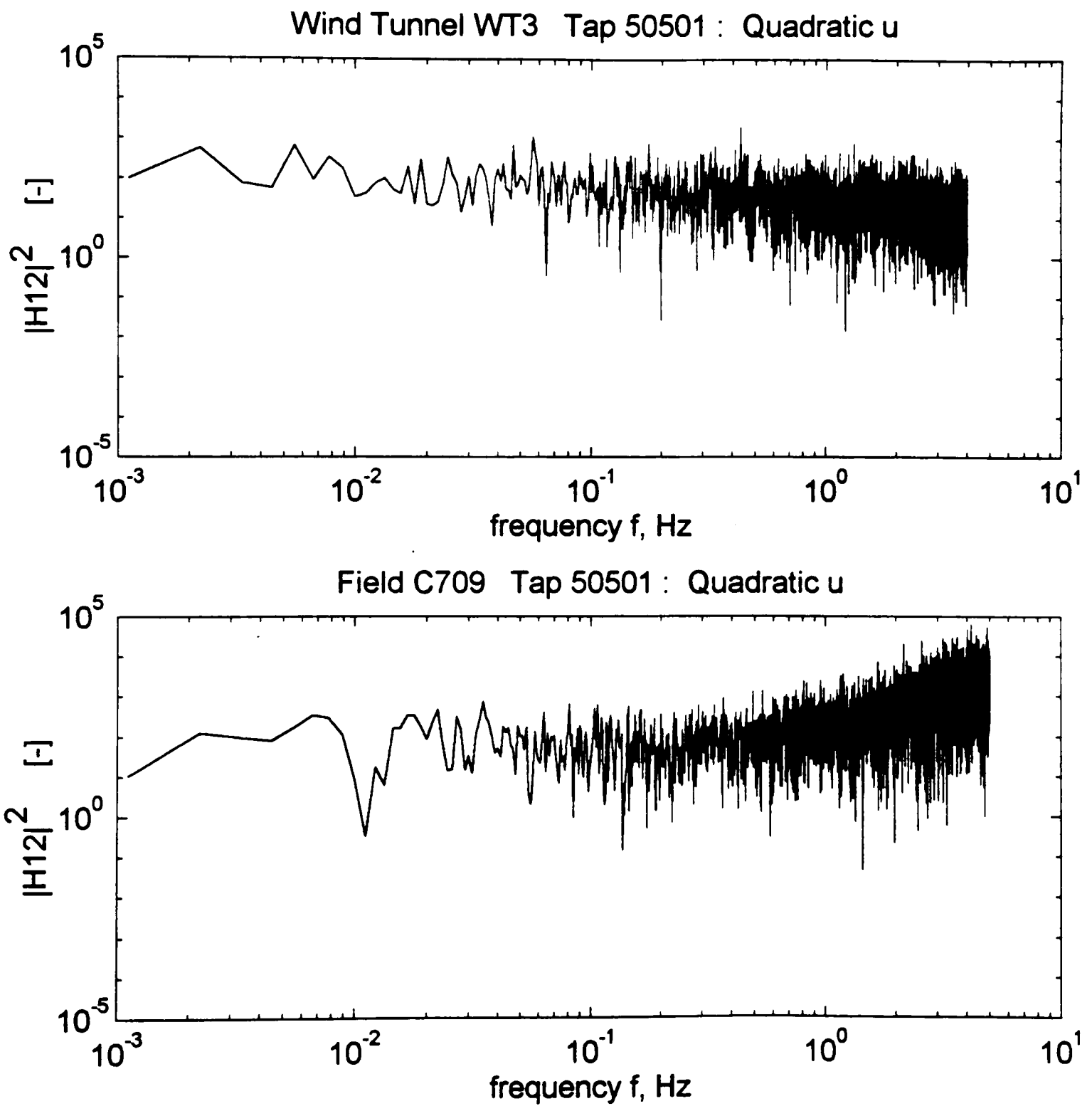


Figure 6.12. Continued. (b) Quadratic u .

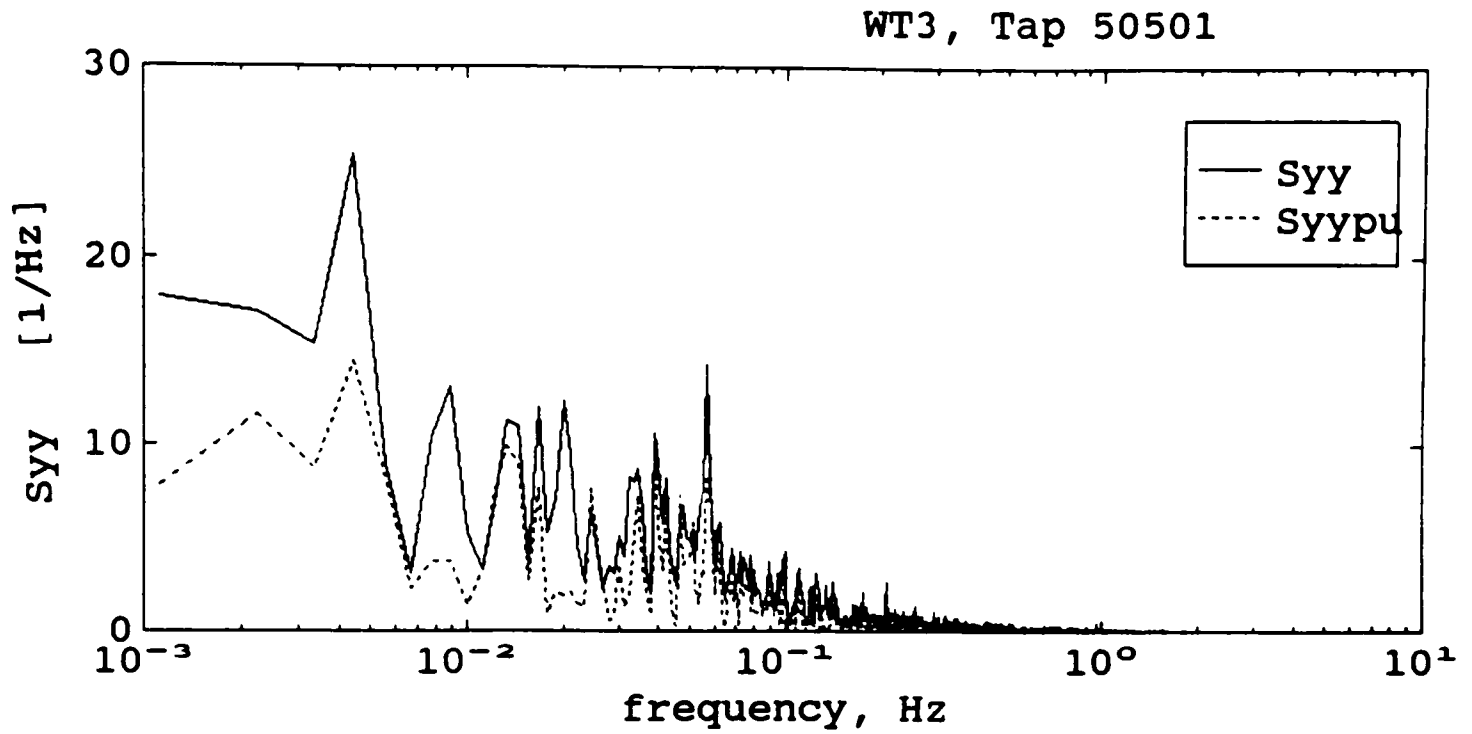


Figure 6.13. Output prediction for tap 50501 for wind-tunnel data (WT3).

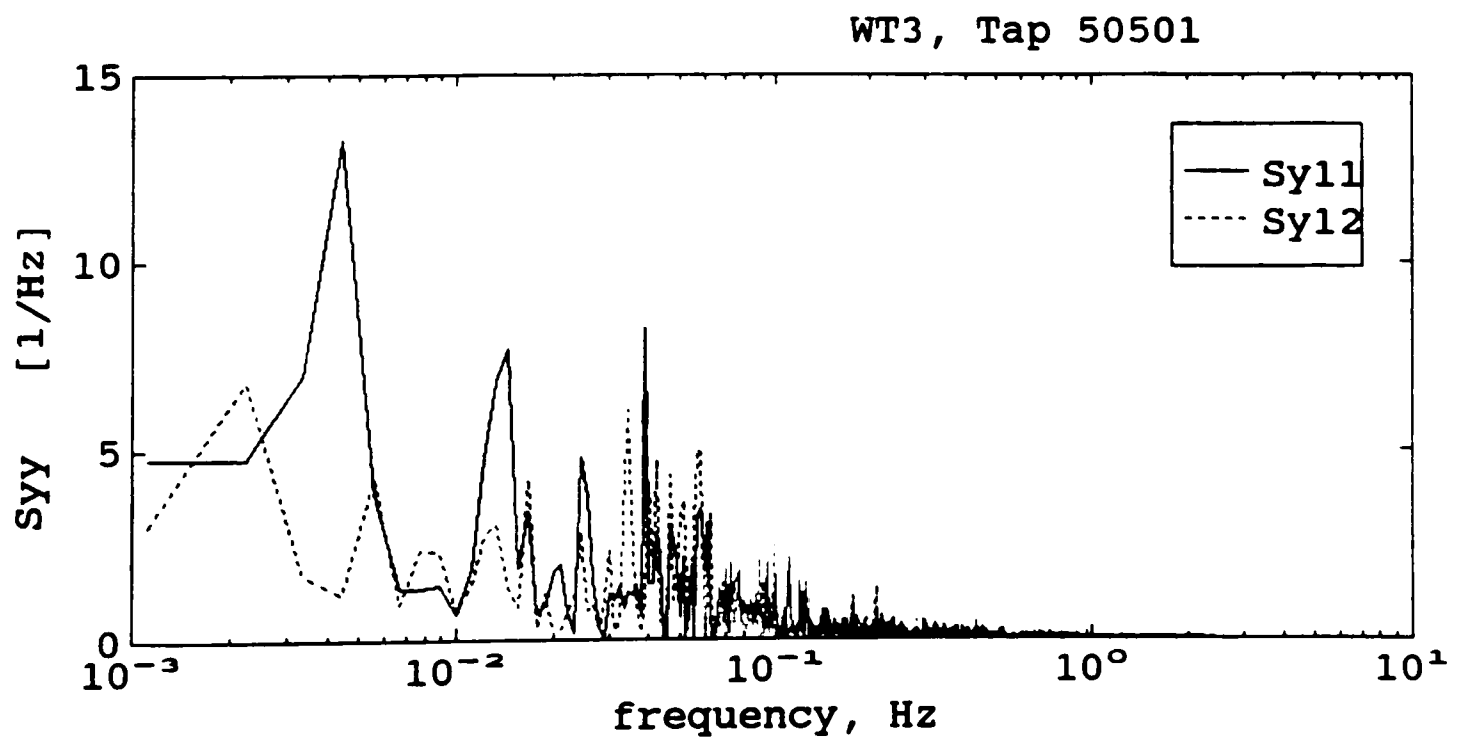


Figure 6.14. Decomposition of pressure-coefficient spectrum for tap 50501 for wind-tunnel data (WT3).

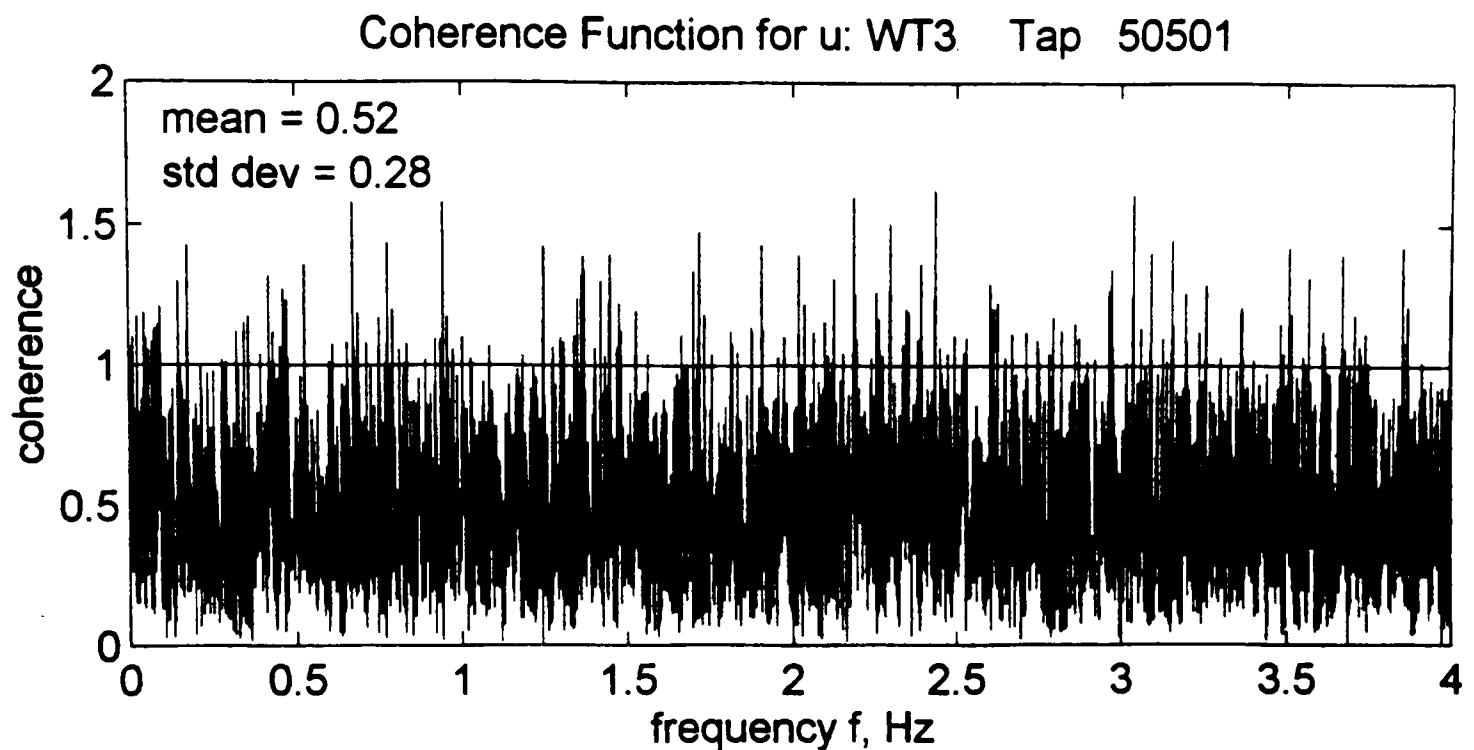


Figure 6.15. Coherence function for the u terms for tap 50501 for the wind-tunnel data (WT3).

Pressure tap 50901 is again located along the southern roof edge about 2.7 m (9 ft) from the corner. It is at the downstream end of the conical vortex. The transfer functions for tap 50901 are shown in Figure 6.16. The output prediction and spectral decomposition are shown in Figures 6.17 and 6.18, respectively. The coherence function was found to have a mean of 1.01 and a standard deviation of 0.46. It appears from Table 6.2 and Figure 6.18 that the modification of the along wind flow has the most significant contribution to the pressure variance. The linear terms contribute about 55 to 60 percent. The bispectrum for tap 50901 is shown in Figure 6.19. The bispectrum is seen to show a sharp peak at the very low frequency end and smaller perturbations along the two frequency axes and the line where $f_1 = -f_2$.

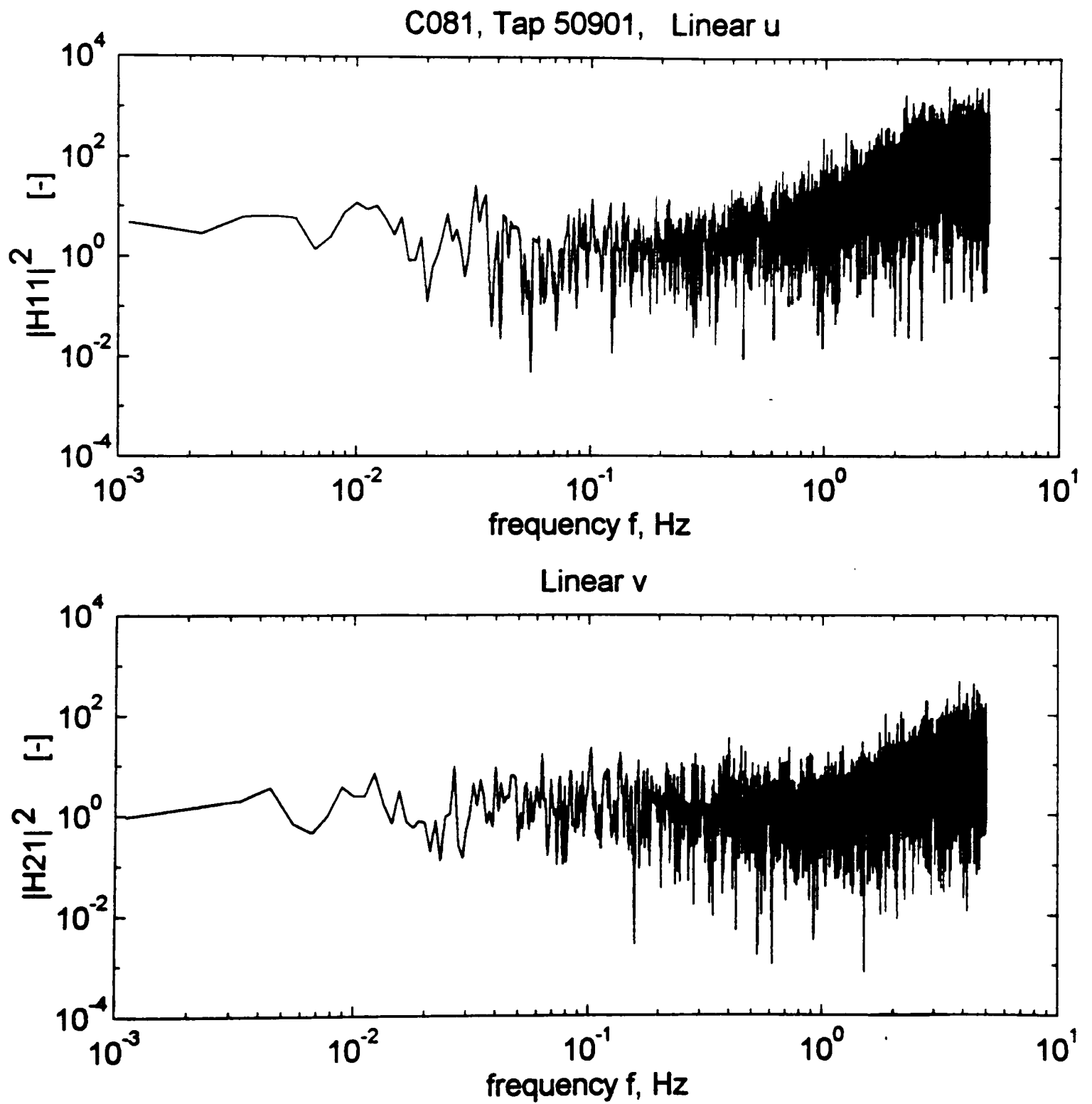


Figure 6.16. Transfer functions for tap 50901 (C081). (a) Linear.

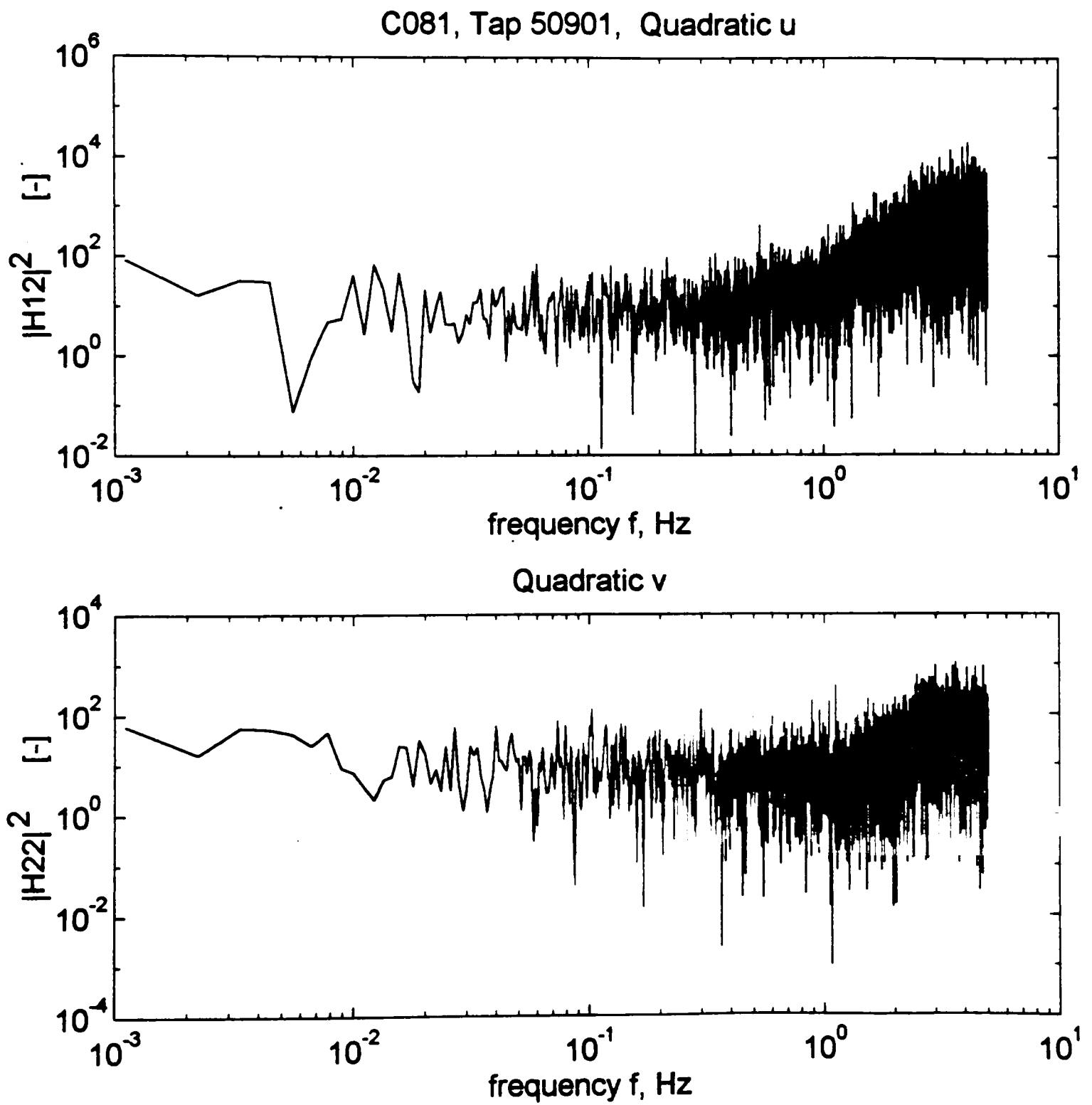


Figure 6.16. Continued. (b) Quadratic.

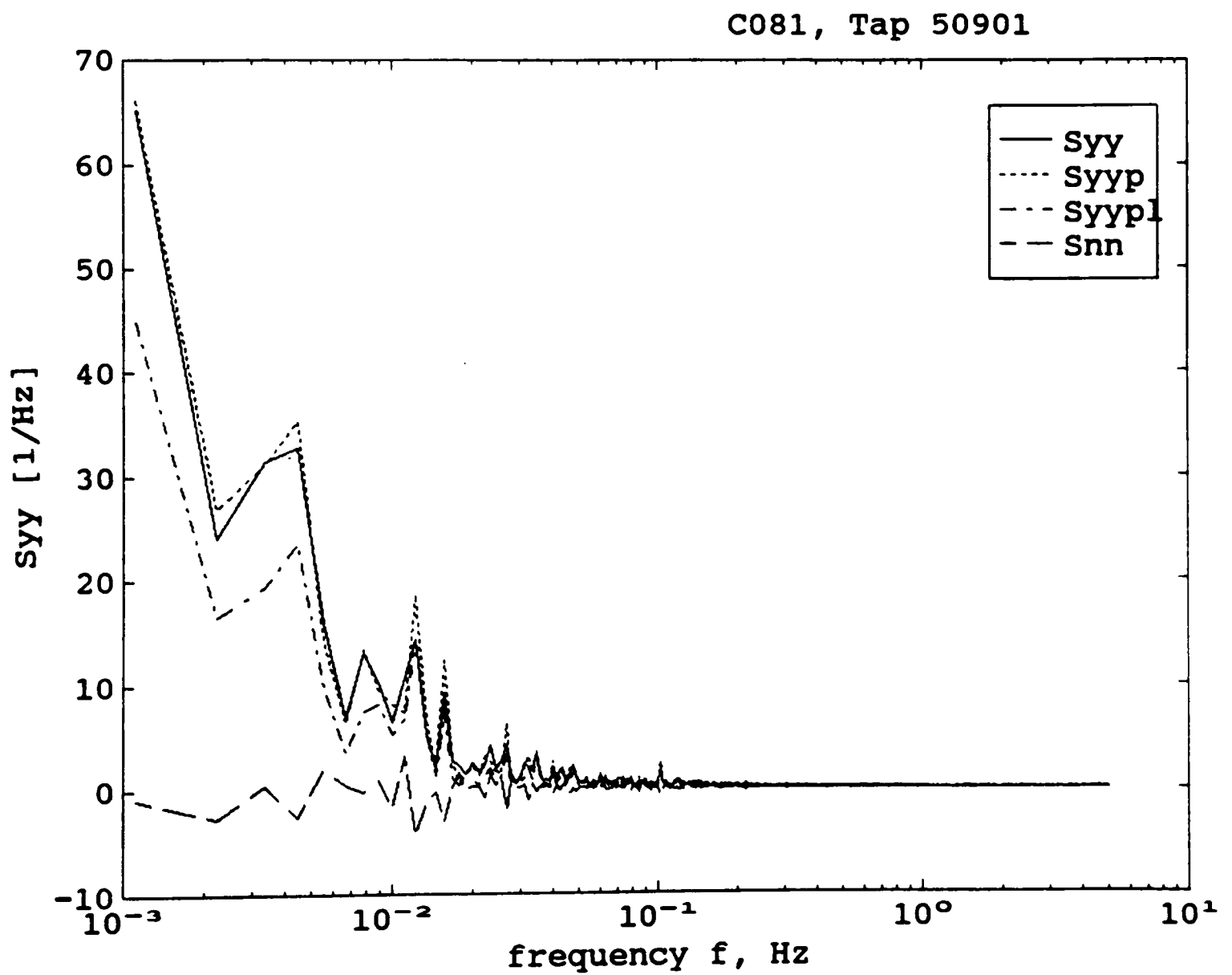


Figure 6.17. Output prediction for tap 50901 (C081).

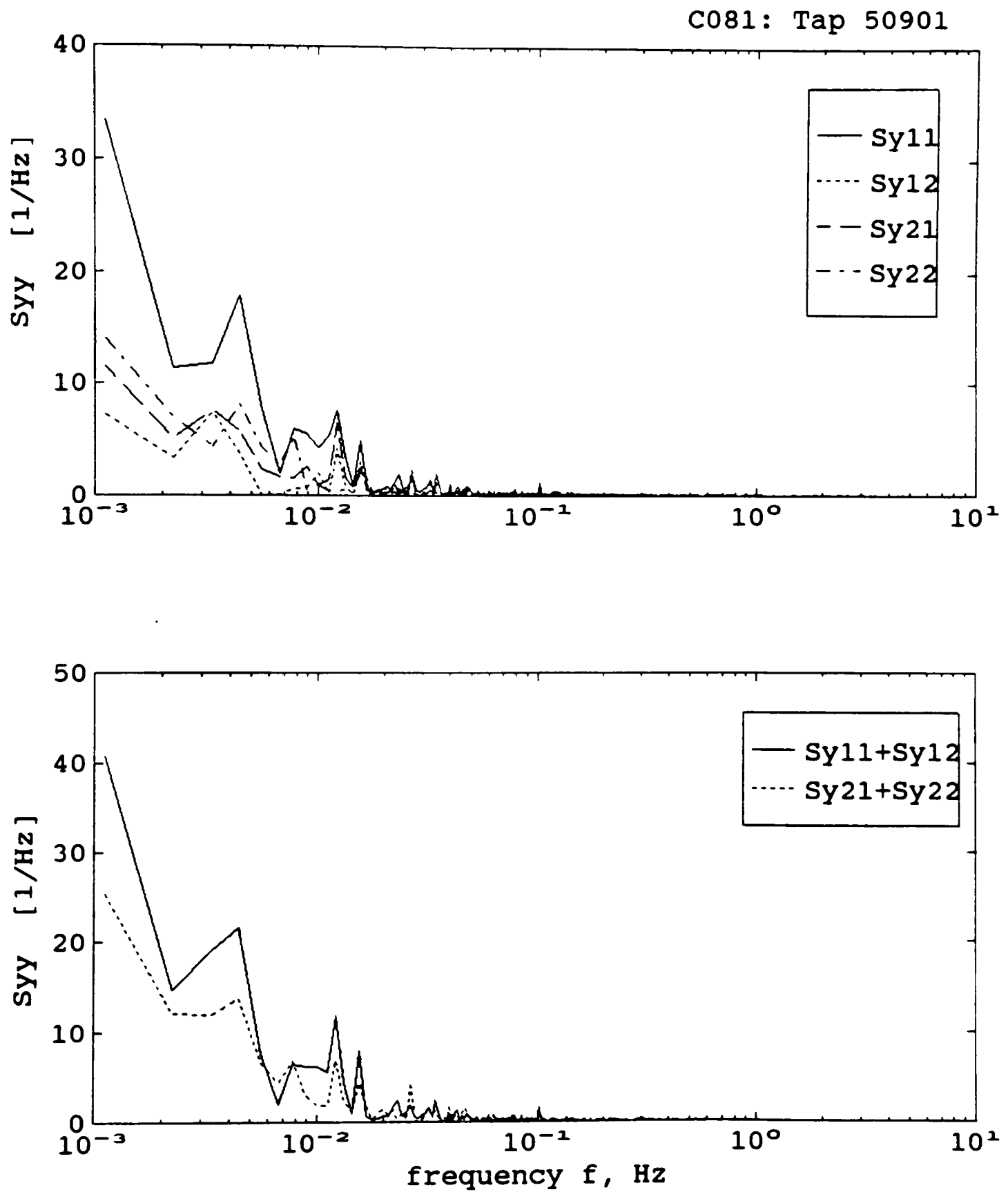


Figure 6.18. Decomposition of pressure-coefficient spectrum for tap 50901 (C081).

Bispectrum of $y=C_p$: Tap 50901, M15N086, $\theta=228$, dyn. pr.=5.1 kg/m²

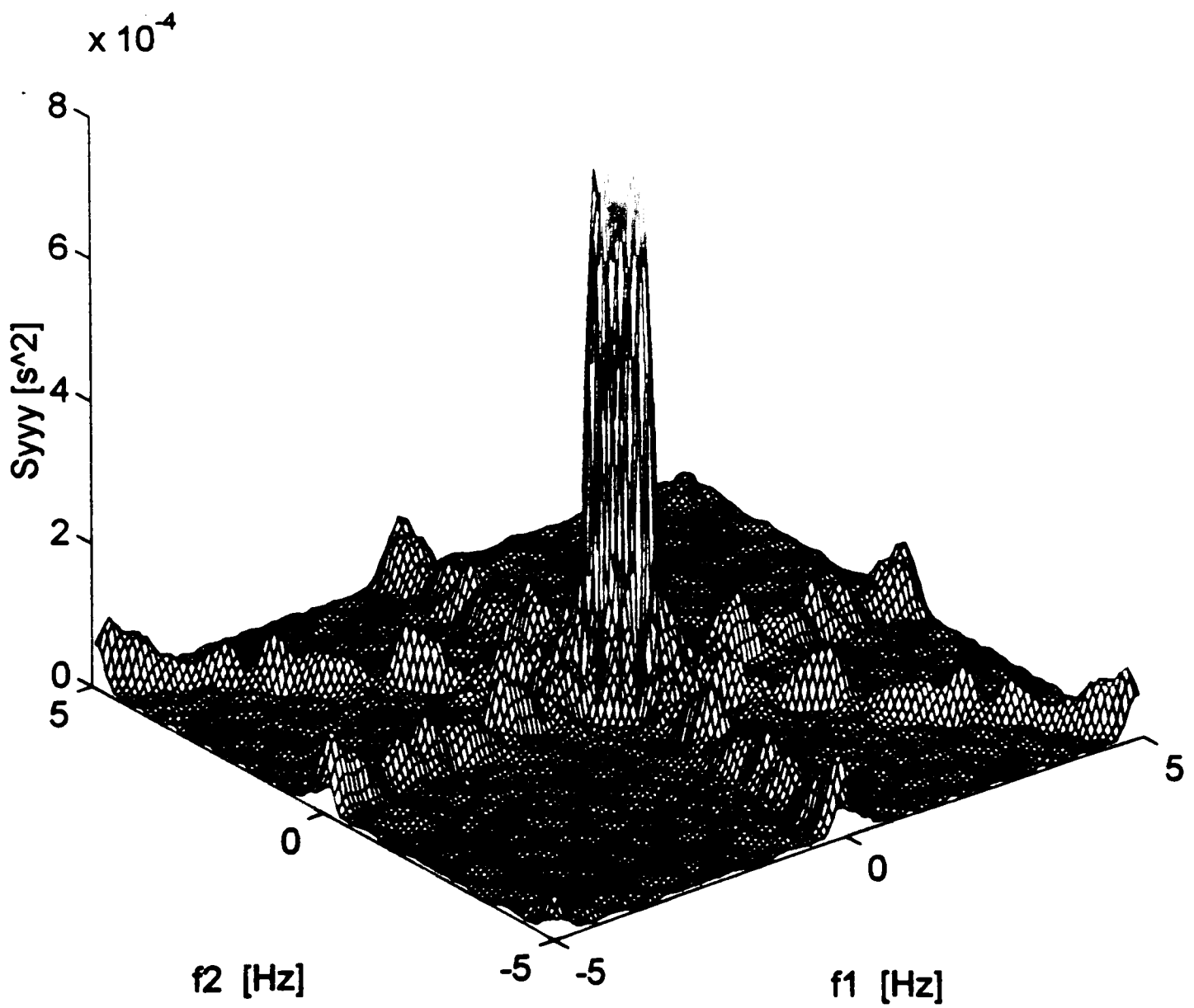


Figure 6.19. Bispectrum of pressure-coefficients for tap 50901 (M15N086).

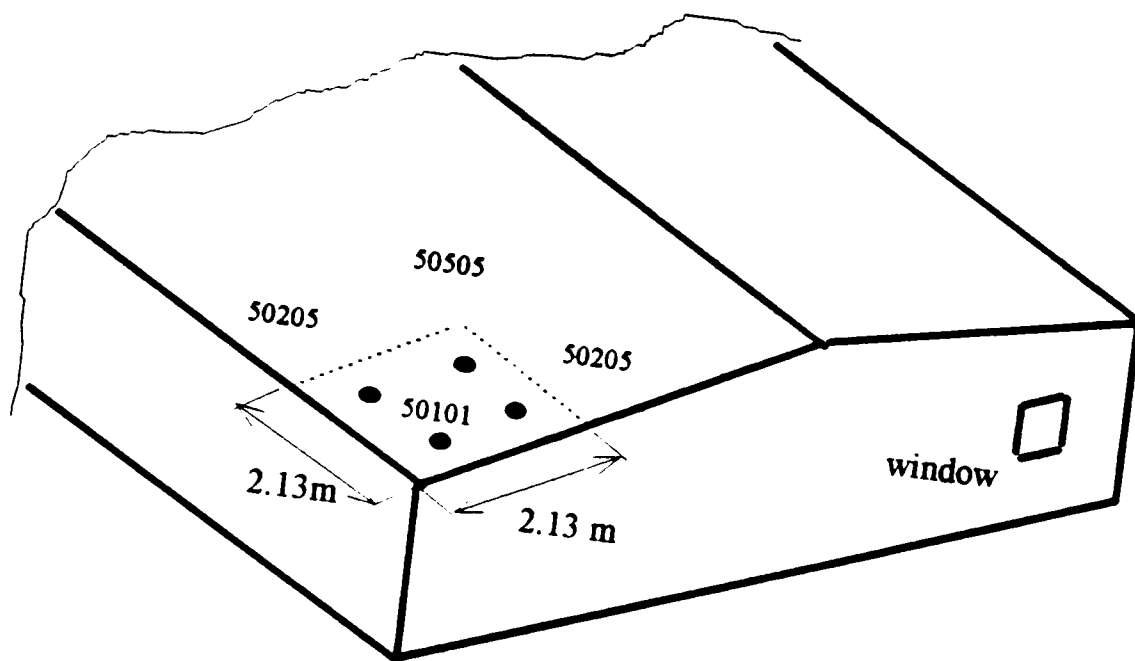
Transfer functions were also identified for taps 50505, 50905 and 50907 located in the V-wedge of attached flow discussed earlier. These taps have much lower rms values. The relative contribution of the different terms of the model and the total coherence for these taps are tabulated in Table 6.2. All the terms do have a comparable contribution.

6.2.2 Area-averaged Cases for the Roof Corner

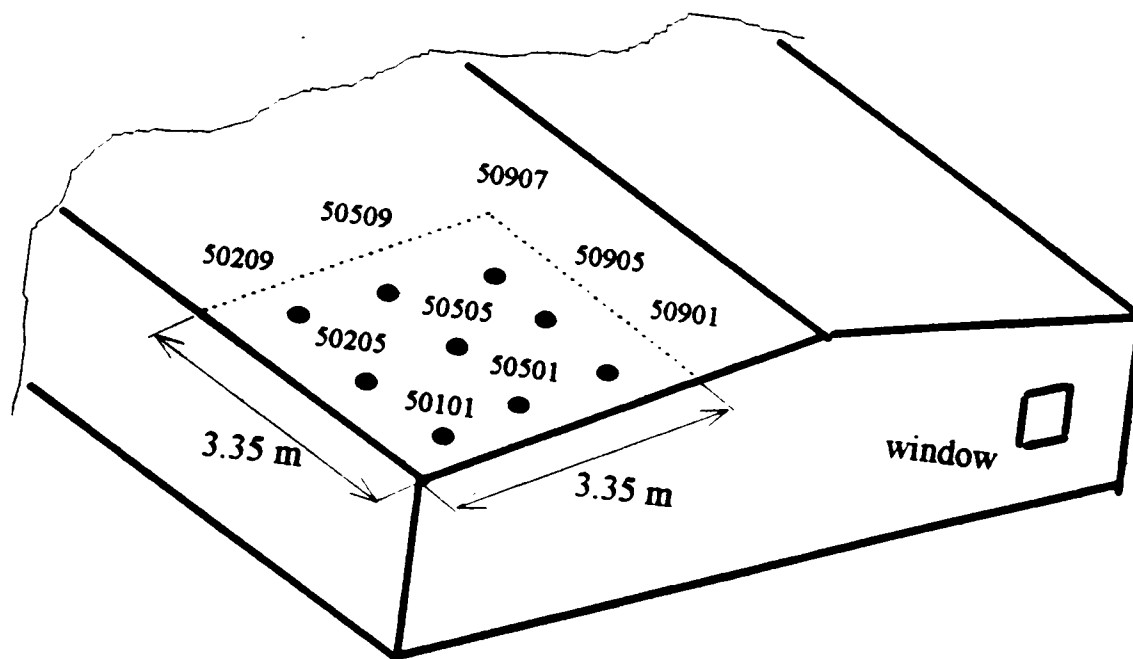
Nine pressure taps, approximately evenly spaced over an area of 3.35 m (11 ft) x 3.35 m (11 ft) area, were instrumented. Two cladding areas of 11.2 m² and 4.5 m² were considered. Since the taps are evenly spaced, equal weights were assigned to each of the taps in the area-averaging process. The pressure taps whose measurements were averaged for the two cases are shown in Figure 6.20. Two angles of attack of $\theta \approx 225^\circ$ and $\theta \approx 270^\circ$ were analyzed.

The transfer functions for a typical area-averaged case (11.2 m², $\theta \approx 225^\circ$) are shown in Figure 6.21 for record C081. The output prediction and spectral decomposition are shown in Figures 6.22 and 6.23, respectively. The coherence function has a mean of 1.0 and a standard deviation of 0.46. The relative contributions of the different components of the model to the pressure variance and the total coherence for all the area-averaged cases are tabulated in Table 6.3 for two sets of records.

It is seen from Table 6.3 that for the quartering wind case the linear terms contribute about 57 to 62 percent for both the cases. The contribution is slightly higher for the 11.2 m² case. The linear u term has the most significant contribution. For the normal wind case, the contribution from the linear terms is in the range 51 to 55 percent. The more the wind is skewed to the normal, the higher the contribution of the linear u term. Hence, the modification of the upstream flow plays a more significant role in the pressure variance for the corner case. However, the dissipation terms are also important.



(a) Cladding area of 4.5 m^2 .



(b) Cladding area of 11.2 m^2 .

Figure 6.20. Pressure taps used for area-averaging for cladding at roof corner.

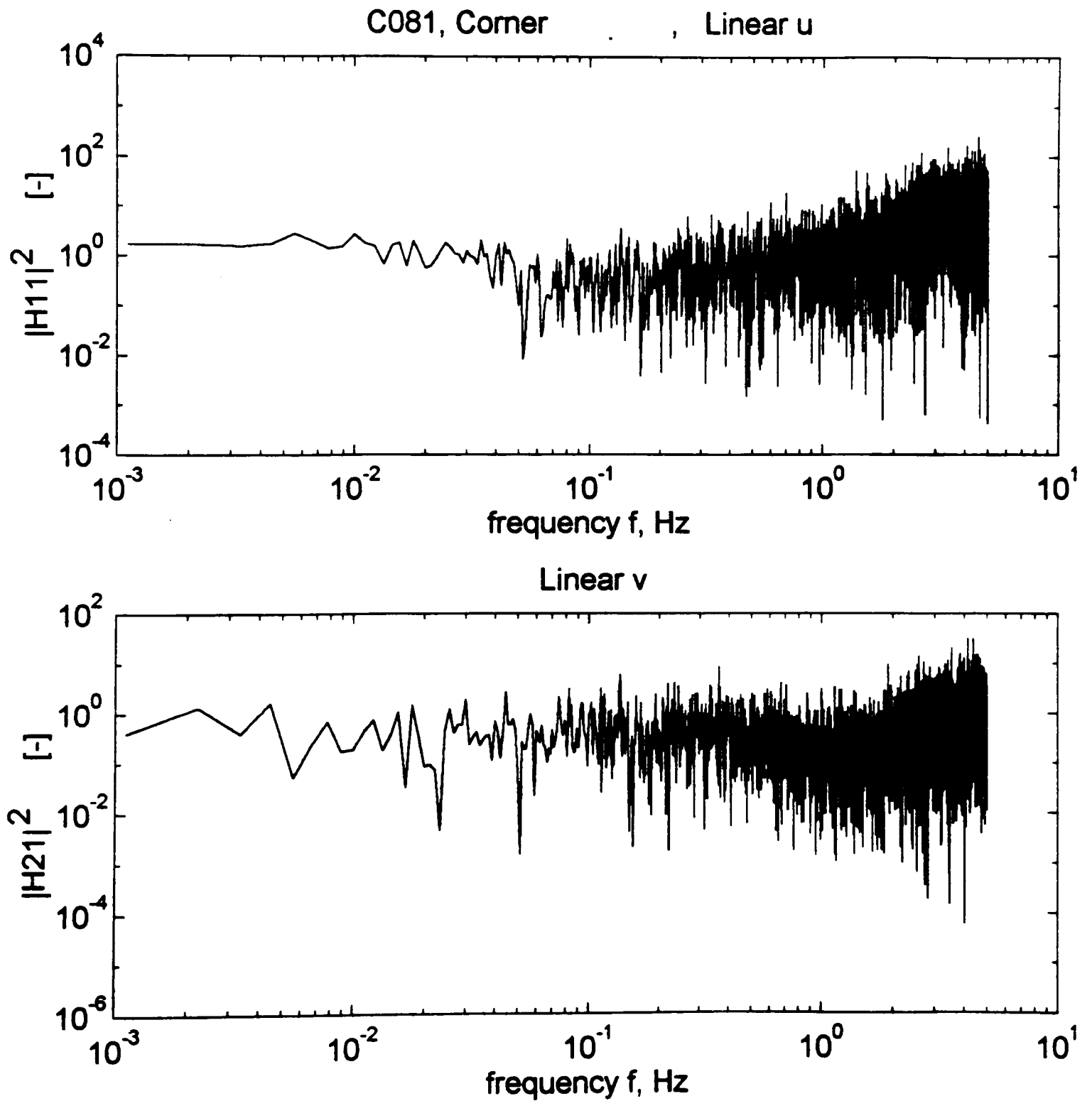


Figure 6.21. Transfer functions for the 11.2 m² area-averaged case (C081). (a) Linear.

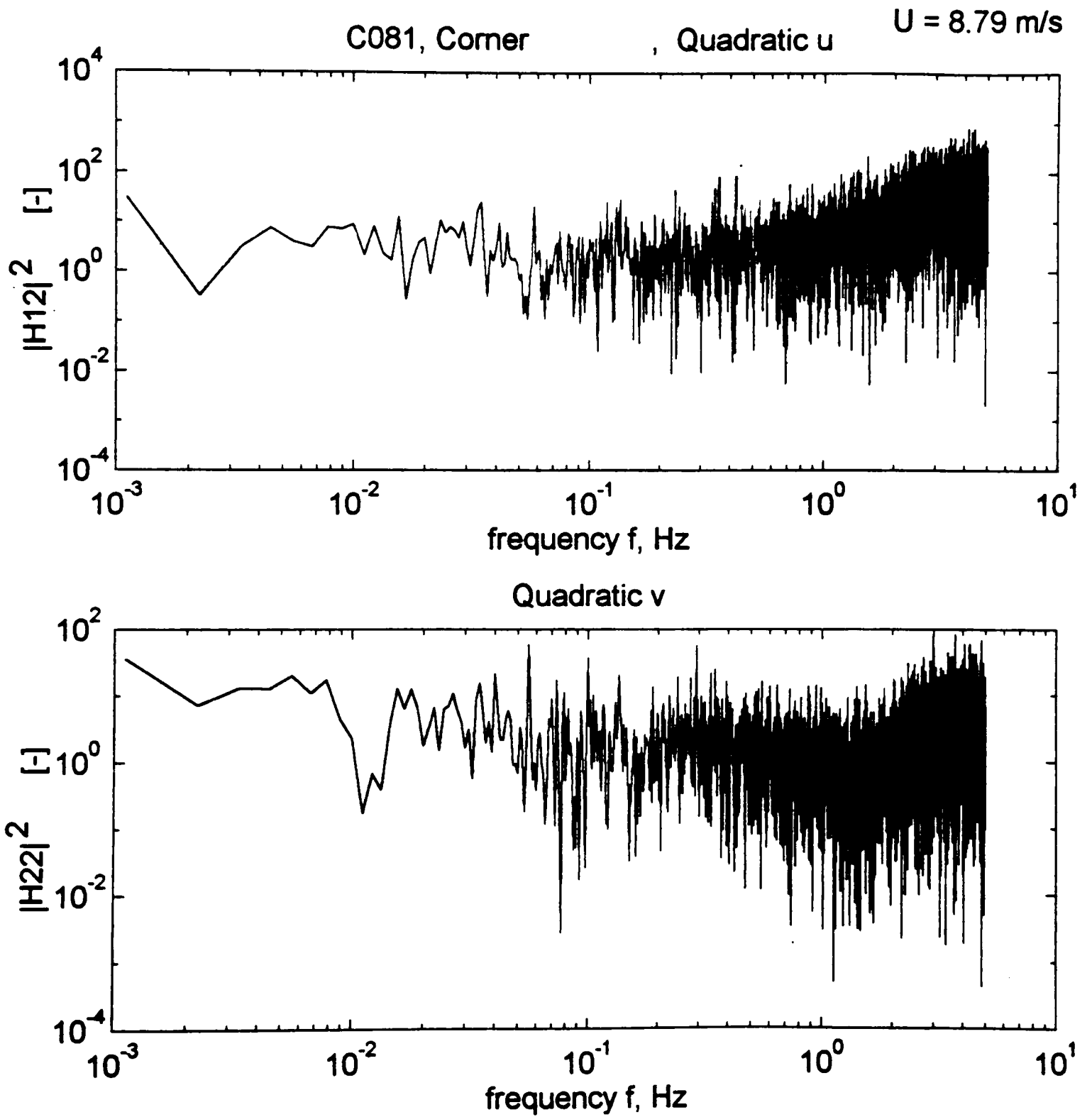


Figure 6.21. Continued. (b) Quadratic.

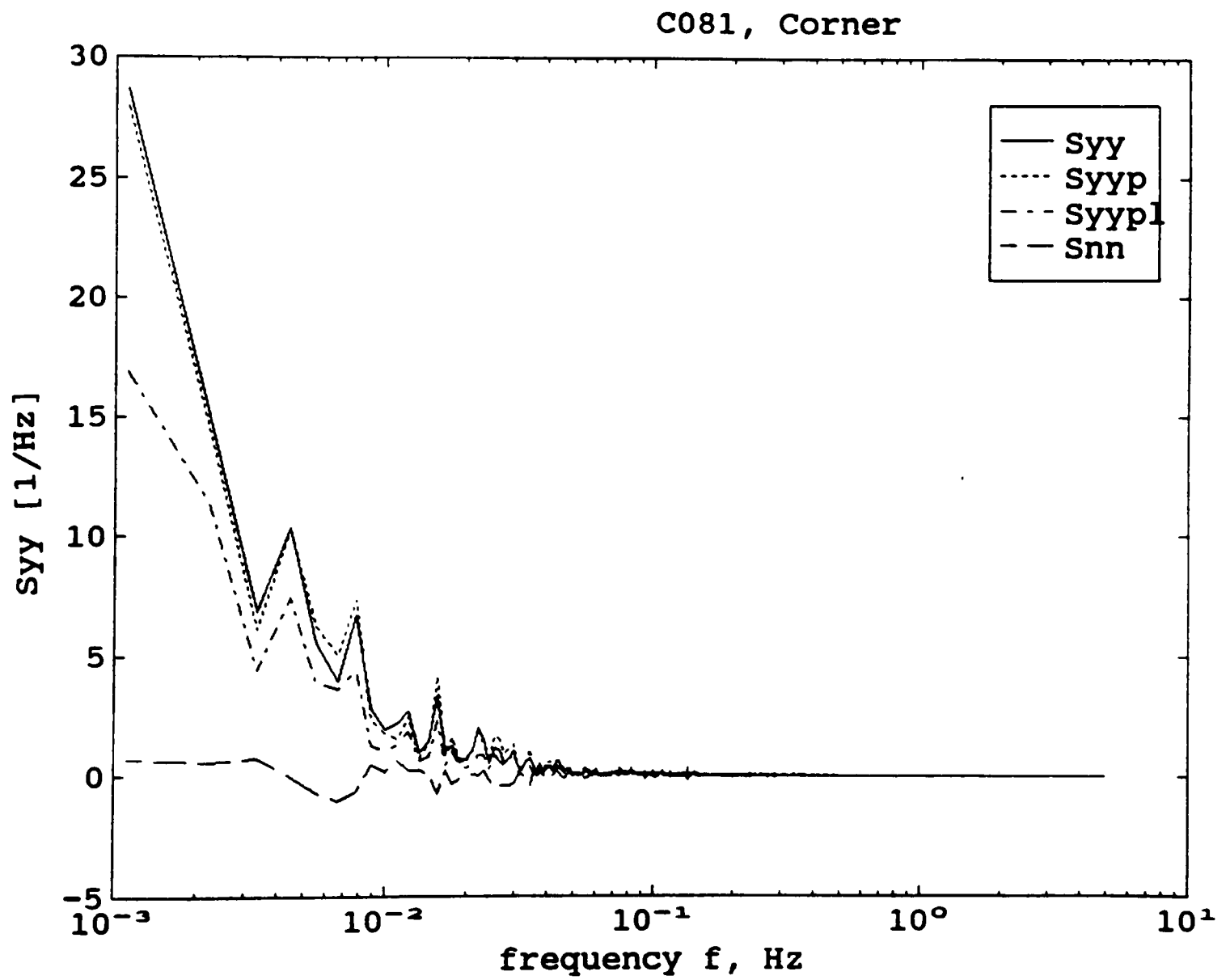


Figure 6.22. Output prediction for the 11.2 m² area-averaged case (C081).

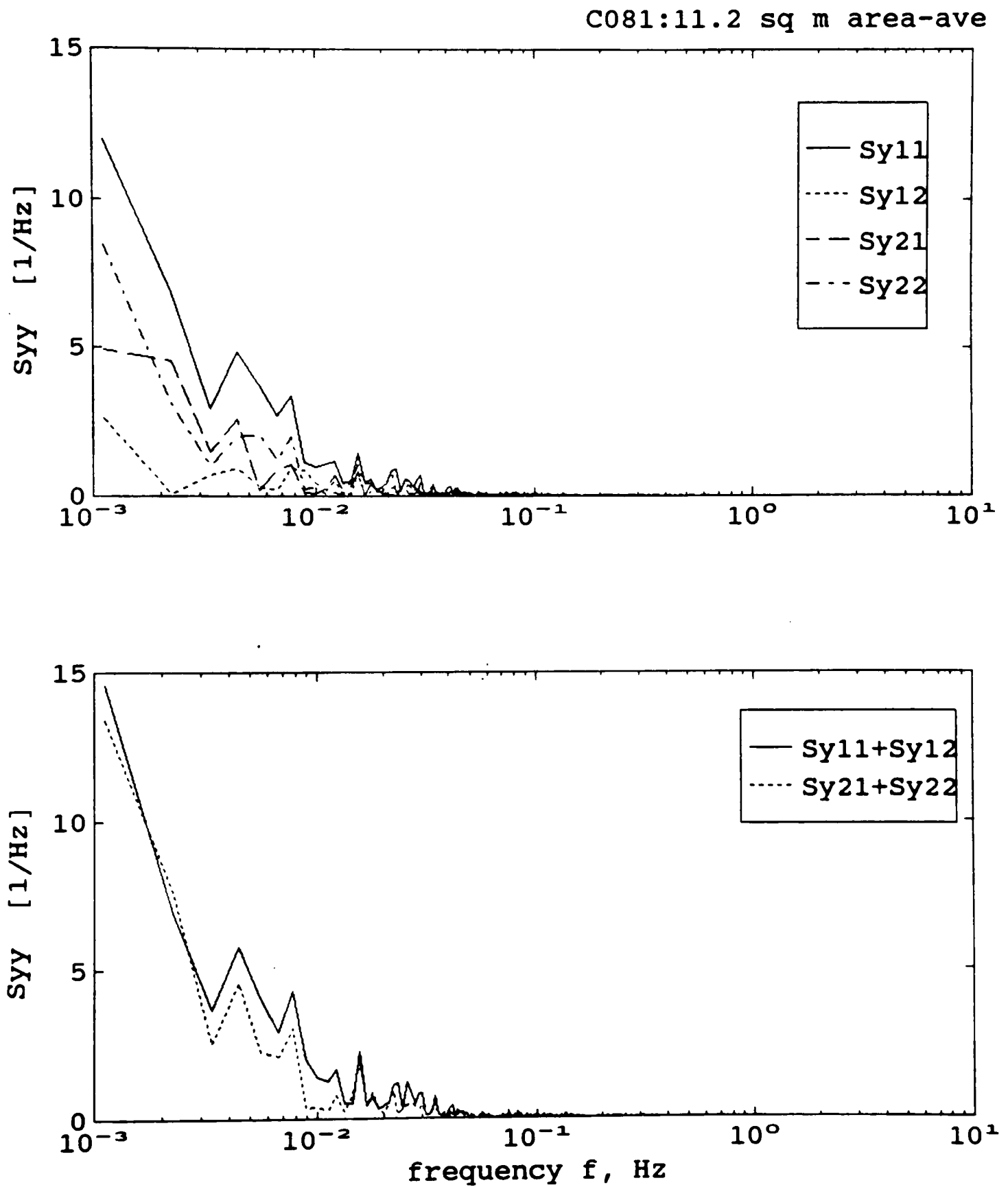


Figure 6.23. Decomposition of pressure-coefficient spectrum for the 11.2 m² area-averaged case (C081).

Table 6.3. Contribution from different components of the model to area-averaged pressures at the roof corner.

Record	Cp_variance		Contribution, as % of measured spectrum, from					Total Coherence	
	meas- ured	pred- icted	<i>u</i>	<i>v</i>	<i>u</i> ²	<i>v</i> ²	Resid- ual, <i>S_{mn}</i>	mean	std. dev.
<u>11.2m²</u> <u>area:</u>	<u>~225⁰</u>								
C081	0.1527	0.1530	42.2	19.7	13.9	24.5	-0.2	1.00	0.46
C478	0.0778	0.0764	30.3	29.0	21.3	17.7	1.8	1.00	0.42
	<u>~270⁰</u>								
C539	0.1023	0.1057	33.5	20.7	22.8	26.3	-3.4	1.04	0.42
C544	0.0894	0.0918	24.6	26.3	24.6	27.2	-2.6	1.01	0.41
<u>4.5 m²</u> <u>area</u>	<u>~225⁰</u>								
C081	0.2427	0.2471	38.8	20.6	16.5	25.9	-1.8	1.01	0.46
C478	0.1275	0.1247	30.9	26.1	22.2	18.7	2.1	1.00	0.41
	<u>~270⁰</u>								
C539	0.1786	0.1826	34.6	20.5	22.2	25.0	-2.2	1.02	0.41
C544	0.1701	0.1756	25.6	26.2	23.6	27.8	-3.2	1.01	0.41

6.2.3 Confidence Interval for Mean Coherence

The mean and standard deviation of the total coherence for each data case analyzed is tabulated in the last two columns of Tables 5.2 through 5.6, 5.8, 6.2 and 6.3. The total number, *n*, of all such field data cases listed in the above tables is 62. It may be recalled that a measure of the goodness of fit of the model is obtained by observing how close the total coherence is to one. Since point estimates cannot really be expected to coincide with the quantities they are intended to estimate, it is preferable to replace them with *interval estimates*, that is, intervals for which one can assert with a reasonable degree of certainty that they contain the parameter (the mean coherence herein) under consideration. Hence,

a 95 percent confidence interval is constructed for the mean value of the total coherence on the basis of the data tabulated in the tables listed above.

The $100(1-\alpha)\%$ confidence interval for the mean μ of a variable y using the t statistic is given by (Ott, 1988)

$$\bar{y} \pm t_{\alpha/2} \frac{s}{\sqrt{n}}, \quad (6.1)$$

where \bar{y} and s are the sample mean and standard deviation, respectively, n is the sample size and $(1-\alpha)$ is the confidence coefficient.

For the coherence data tabulated in the tables mentioned earlier, $\bar{y} = 1.01$, $s = 0.42$, $\alpha = 0.05$ (for 95% confidence), $t_{\alpha/2} = t_{0.025} = 2.0$ (Table 4 on pp. A-5; Ott, 1988), and $n = 62$. It may be noted that the value of s was obtained as the square root of the mean-square value of the numbers tabulated in the last column of the tables listed earlier in this section. Using Eq. 6.1, the 95 percent confidence interval for the mean coherence is given by

$$\bar{y} \pm t_{0.025} \frac{s}{\sqrt{n}} \quad \text{or} \quad 1.01 \pm \frac{2.0(0.42)}{\sqrt{62}},$$

which is the interval 1.01 ± 0.11 , or 0.90 to 1.12. Hence, it may be asserted with 95 percent confidence that the mean coherence will lie in the interval [0.90, 1.12] which is an interval whose lower and upper limits are close to one. This further strengthens the goodness-of-fit of the proposed model.

6.2.4 Frequency Distribution of the Variance of Measured Pressures at the Roof Corner

It was observed in Section 4.2.8 that there may not be any significant frequencies above 5 Hz in the pressure time histories. This was generally found to be true from the measured spectra for different pressure taps presented earlier in this chapter. The average frequency distribution of the variance between 0 and 5 Hz for these roof corner taps are

tabulated in Table 6.4 for an angle of attack of approximately 225° , unless noted otherwise.

It is seen from Table 6.4 that more than 90 percent of the pressure variance is contained in frequencies below 2 Hz for all the taps except 50901. For the area-averaged cases this figure is 95 percent. However, more than 97 percent of the variance is contained in frequencies below 4 Hz and more than 70 percent is contained in frequencies below 0.5 Hz for all the cases. Hence, it is reasonable to conclude that there are no significant frequencies beyond 5 Hz for the point or area-averaged pressures even at the roof corner. It is also observed that the lower frequencies are much more predominant in the area-averaged cases than for the individual taps.

Table 6.4 Average frequency distribution of measured pressures for the roof corner.

Flow Region	Pressure Tap	variance, as % of measured, from 0 Hz to					
		0.05 Hz	0.1 Hz	0.5 Hz	1 Hz	2 Hz	4 Hz
Roof corner	50101	41.0	51.4	71.3	81.5	90.2	97.4
	50501	58.2	68.2	86.2	92.0	96.0	99.0
	50501 WT	44.3	63.0	89.6	95.4	98.6	100.0
	50505	49.6	60.0	80.5	87.3	92.8	97.8
	50901	56.7	64.0	77.4	82.1	87.7	96.4
	50905	40.6	55.9	82.5	88.6	93.4	98.2
	50907	42.9	53.5	76.4	84.3	90.8	97.7
Corner area averaged	<u>11.2 m²</u> $\theta \sim 225^{\circ}$	<u>area</u> 74.0	80.3	92.1	95.4	97.4	99.3
	$\theta \sim 270^{\circ}$	67.8	78.3	93.8	96.8	98.2	99.5
	<u>4.5 m²</u> $\theta \sim 225^{\circ}$	62.2	68.5	84.2	90.7	95.5	98.9
	$\theta \sim 270^{\circ}$	61.5	71.9	89.5	94.2	97.0	99.1

Note: Area under spectrum from 0 to 5 Hz is the measured variance, except for wind tunnel in which case it is 0 to 4 Hz. $\theta \sim 225^{\circ}$, unless noted.

6.2.5 Phase of Transfer Functions and Pressure Spectra

The phase associated with the transfer functions for a critical roof corner tap 50501 are shown in Figure 6.24, for a typical field record. These functions are shown only for the frequency range 0-1 Hz for clarity. It is seen from these figures that the phase angles associated for all the transfer functions were uniformly distributed between $-\pi$ and $+\pi$ radians with a mean and standard deviation of approximately 0 and 1.8, respectively.

The phase function of the pressure spectrum for tap 50501 is shown in Figure 6.25 for a typical field record. The corresponding probability density function (pdf) is shown in Figure 6.26. It can be observed from these figures that the phase angles are uniformly distributed between $-\pi$ and $+\pi$ radians. The mean of the phase angles was found to be approximately zero and the standard deviation was found to be in the range 1.8 to 1.9, as was observed for the cases in Chapter 5.

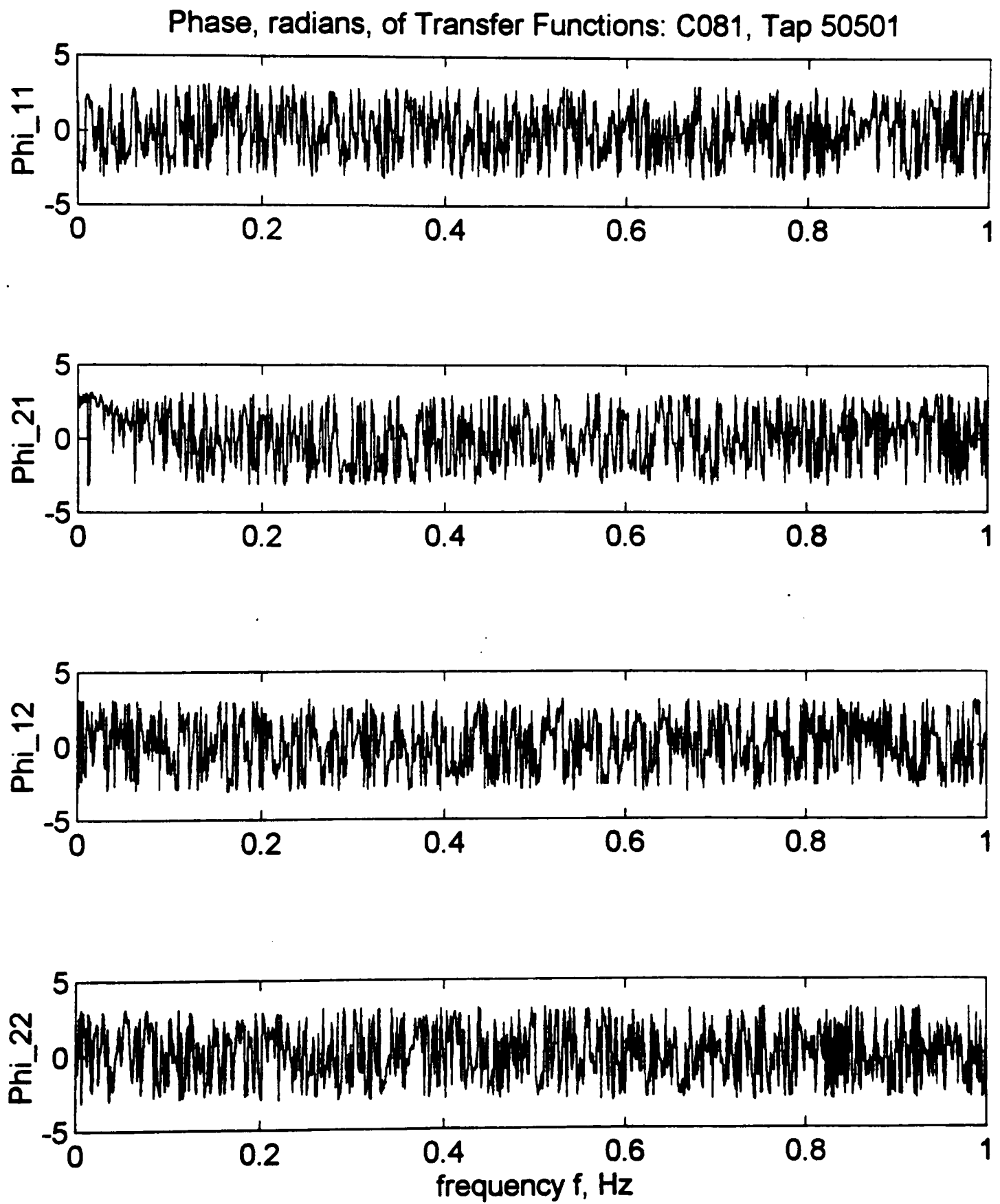


Figure 6.24. Phase of transfer functions for tap 50501 (C081).

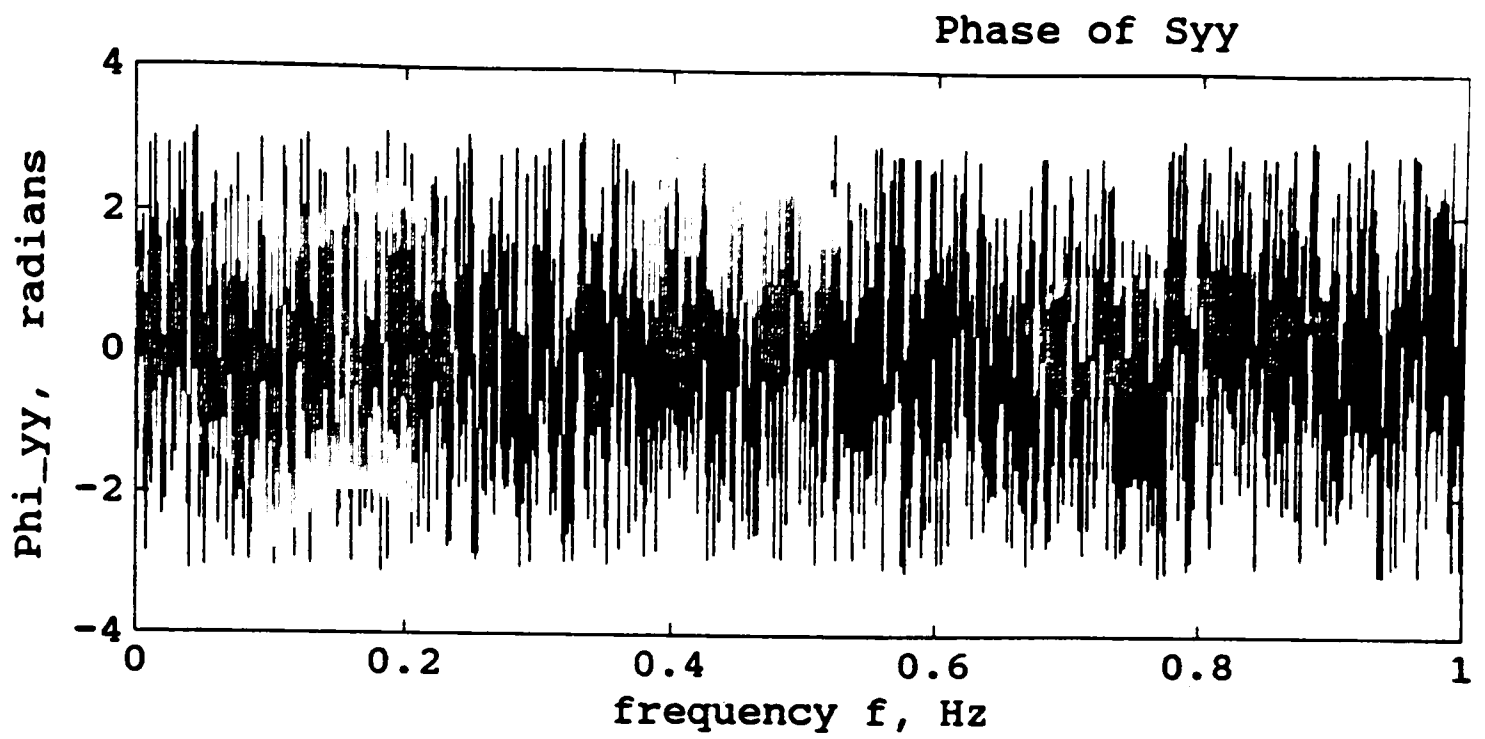


Figure 6.25. Phase of pressure spectra for tap 50501 (C081).

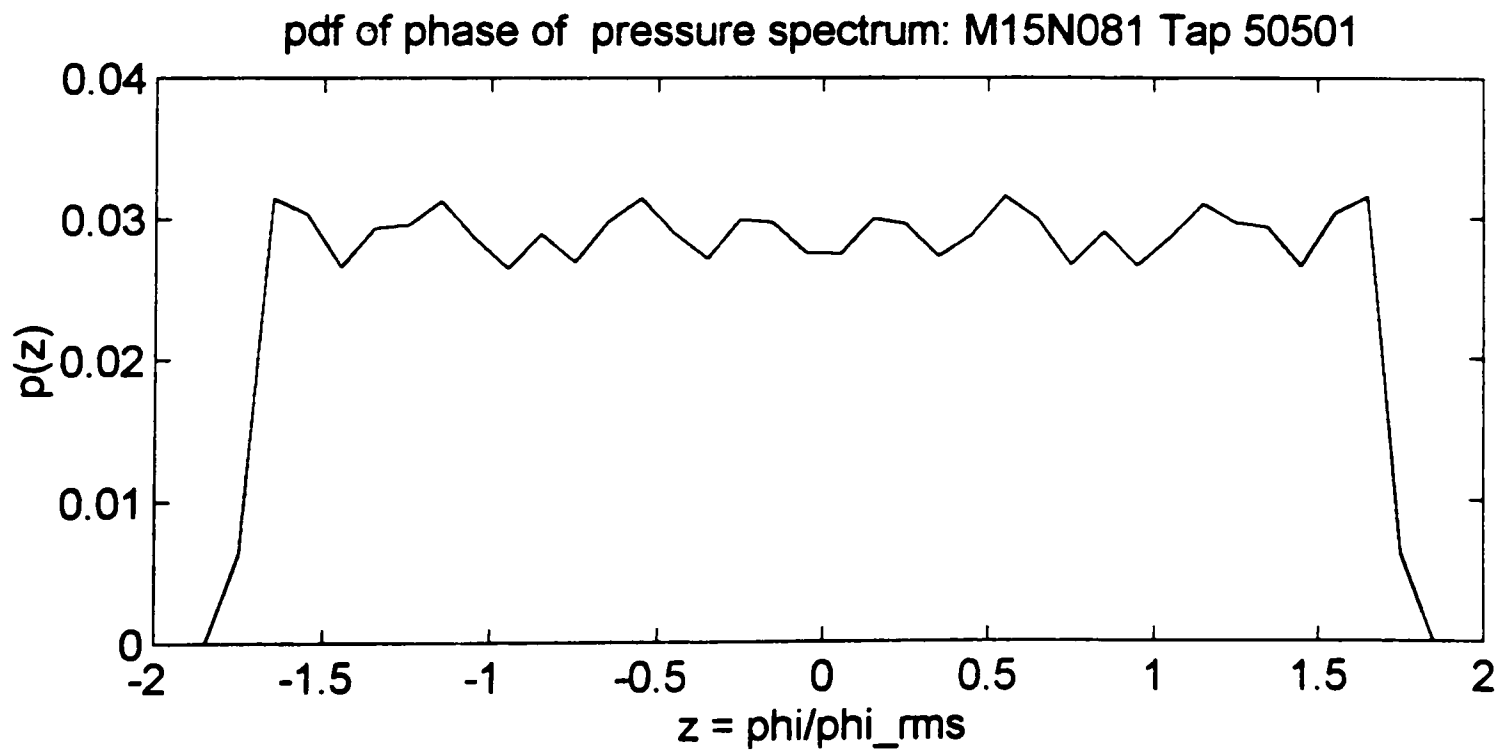


Figure 6.26. Pdf of phase of pressure spectra for tap 50501 (C081).

6.3 Simulation of Pressure-coefficient Spectra

In this section, a comparison will be first made between the transfer functions obtained from different records with approximately similar mean angles of attack for a critical tap, 50501, at the roof corner for both field and wind-tunnel cases. A simulation exercise, as presented in Section 5.3, will then be performed for some typical roof corner cases using transfer functions from other similar records.

A comparison of the transfer functions for tap 50501 obtained from field records C081 ($\theta = 227.6^\circ$) and C709 ($\theta = 222.1^\circ$) with approximately similar mean angles of attack is shown in Figure 6.27. It is seen that the transfer functions are very similar in form, both qualitatively and quantitatively. Some quantitative variability observed could be attributed to the same reasons discussed in earlier in Section 5.3 of Chapter 5. A similar comparison of transfer functions, associated with the linear and quadratic u terms only, for tap 50501 from the three wind tunnel records (WT1, WT2 and WT3) is shown in Figure 6.28. The wind tunnel transfer functions are also similar with some quantitative variation. Since the transfer functions from both the wind-tunnel and the field data exhibit similar kind of variability, another possible reason for the variability could be the apparent non-stationary nature of the pressure signals. However, the similarity observed in the transfer functions points to the fact that the transfer functions essentially capture the mechanism that transforms wind velocity to pressures on building surfaces, irrespective of the record used.

Now the transfer functions of C709 and C081 will be used with the input velocity spectra of C478 in order to simulate the pressure-coefficient spectrum of C478 for tap 50501. Two cases are examined: (i) the transfer functions of only C709 were used, and (ii) the averaged transfer functions of C709 and C081 were used. The comparison of the simulated pressure spectrum (S_{yyp}) and the measured one (S_{yy}) for record C478 for tap 50501 for the two cases is shown in Figure 6.29. The simulated and measured pressure variances are also indicated therein. It is seen from Figure 6.29 that the simulated or predicted pressure variance was about 1.31 (1.14, in terms of rms values) times the measured one for the first case. The predicted rms value was found to be 1.27 as against

the measured value of 1.11. This is well within the range of rms values (1.05 to 1.8, Mehta et al., 1992) observed in the field for tap 50501 for approximately quartering winds. It is seen, however, that the prediction improved significantly, to 1.07 times the measured variance, for the second case where averaged transfer functions were used. Figure 6.29 shows that the frequency content is also predicted reasonably well for both cases.

Figure 6.30 shows the simulation of the pressure-coefficient spectrum for tap 50501 for record C709 using the averaged transfer functions of records C081 and C478. It is again seen that the predicted pressure spectrum compares reasonably well with the measured one. The predicted pressure variance was found to 1.08 times the measured one.

A simulation of the pressure-coefficient spectrum for the 11.2 m² area-averaged case at the roof corner is shown in Figure 6.31. The simulation was carried out using transfer functions of record C081 to predict the spectrum of record C478. The simulated and measured pressure variances are indicated in the figure. It is again seen that predicted spectrum reasonably matches the frequency content of measured spectrum. The predicted pressure variance was found to 1.06 times the measured one.

A simulation of the pressure-coefficient spectrum associated with only the linear and quadratic u terms (since v velocity data was not available) in the model using the wind-tunnel records is shown in Figure 6.32. The averaged transfer functions of records WT2 and WT3 were used to simulate the pressure spectrum (S_{yysu}) of record WT1. The comparison made here is with the predicted pressure spectrum (S_{yypu}) of WT1 obtained using both the transfer functions and input spectra from record WT1 itself. It is seen that the match is very good. The pressure variance from S_{yysu} was found to be 1.11 times that from S_{yypu} , which is an excellent match.

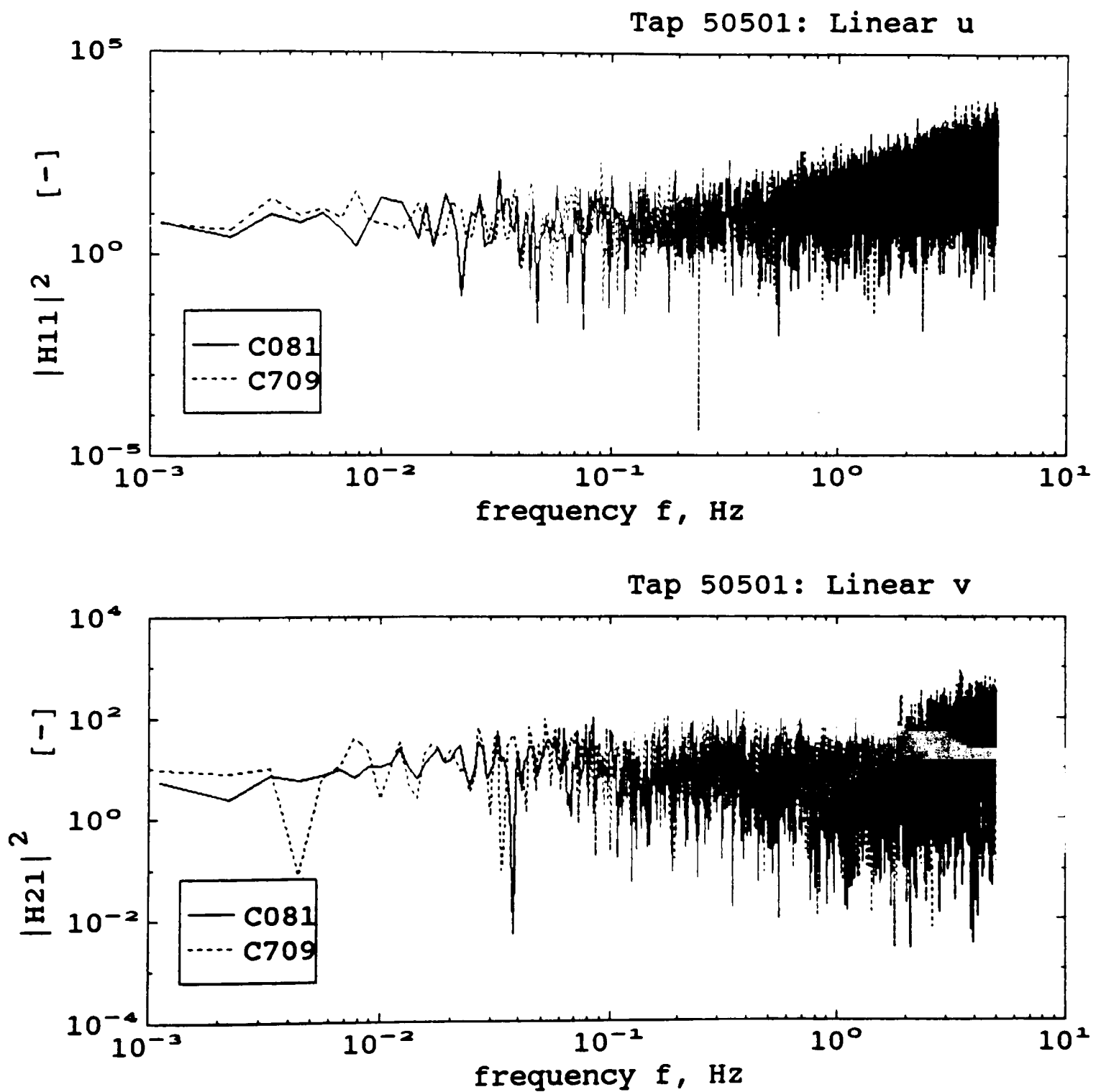


Figure 6.27. Comparison of transfer functions from two field records for tap 50501. (a) Linear.

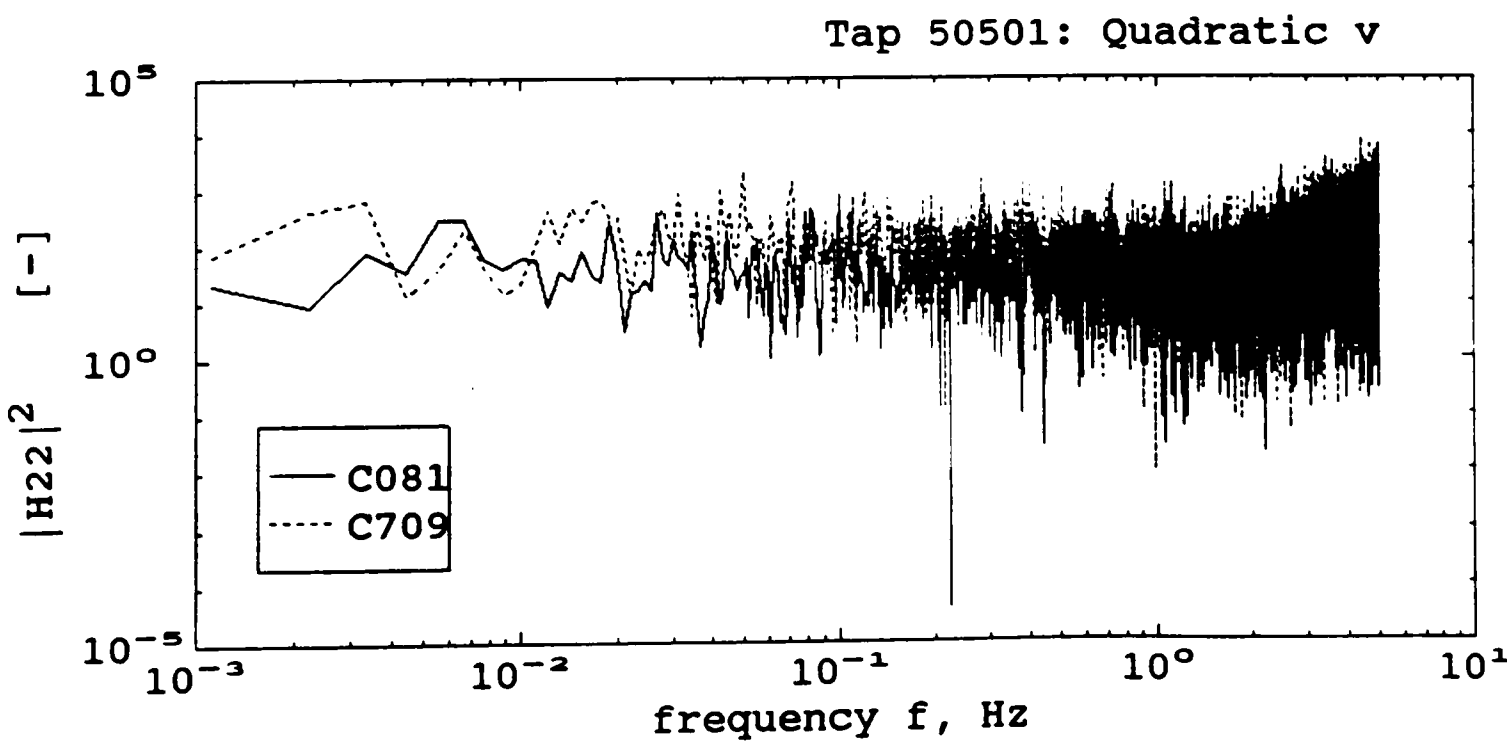
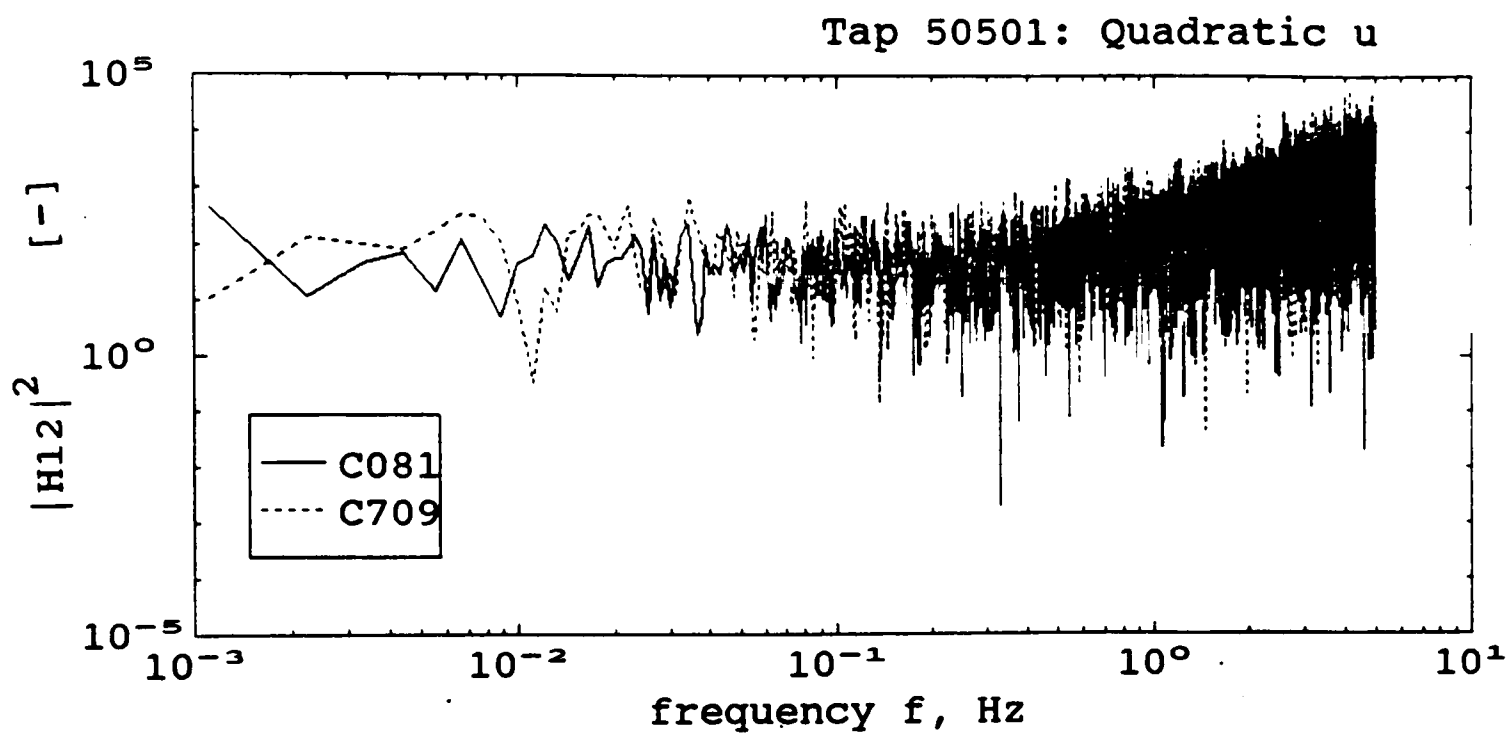


Figure 6.27. Continued. (b) Quadratic.

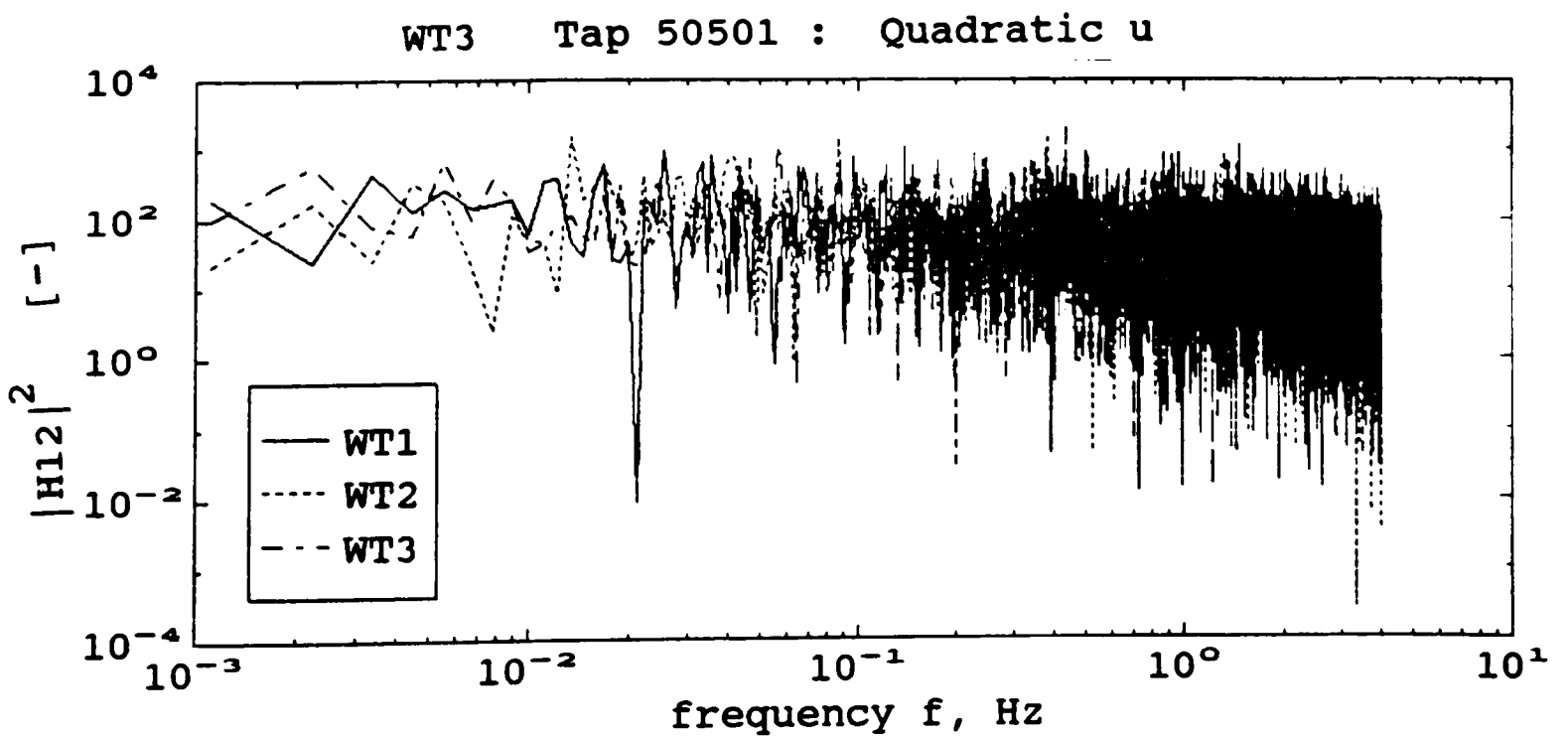
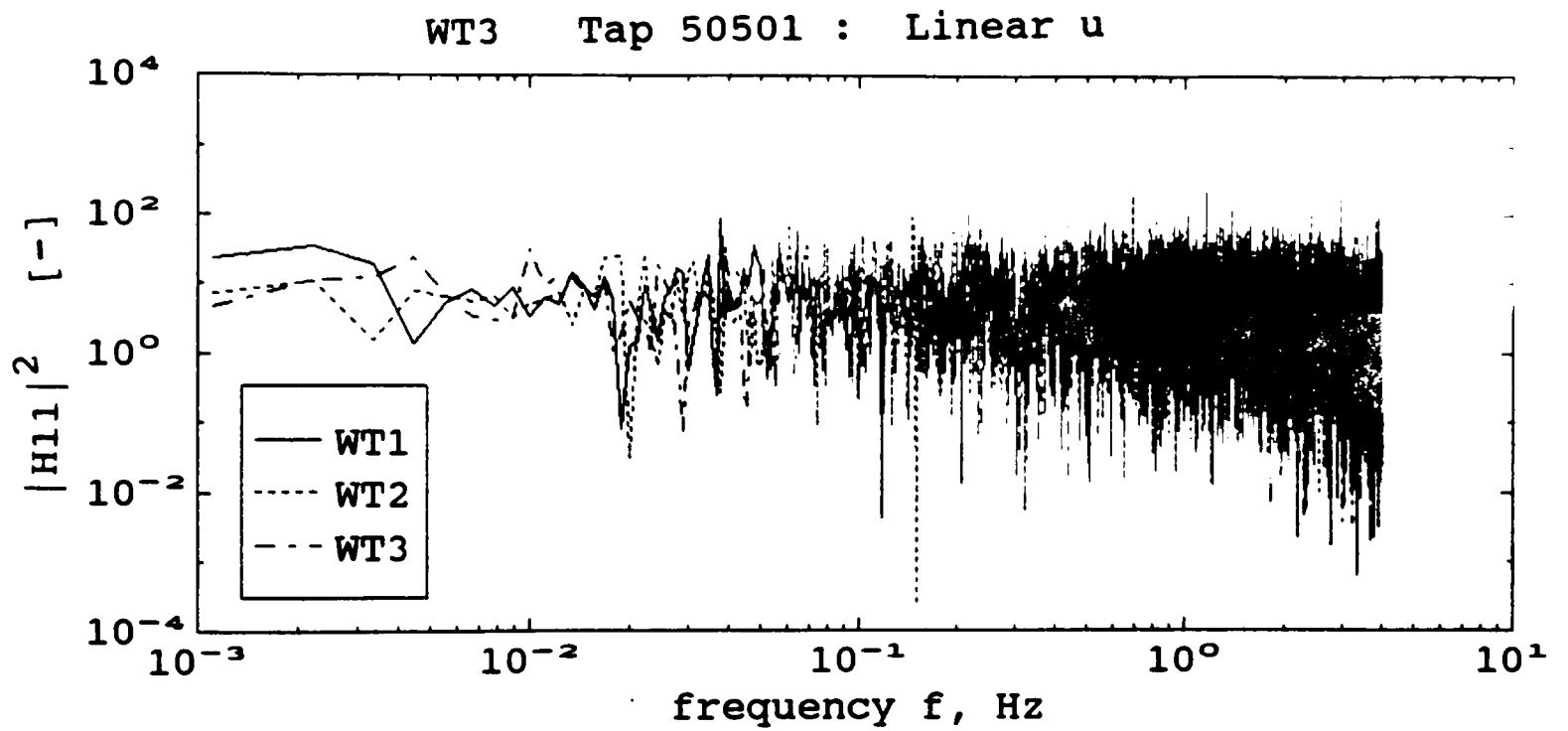
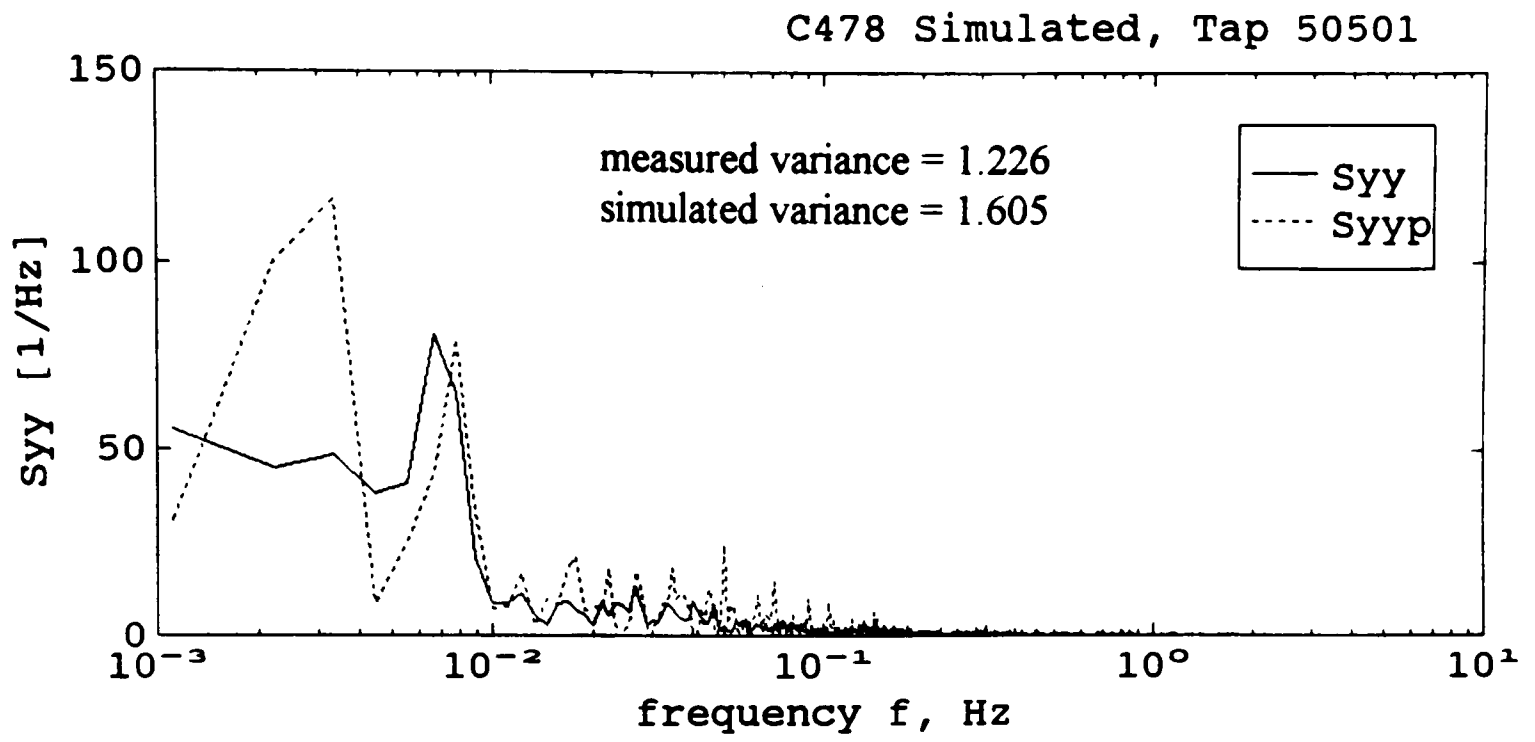
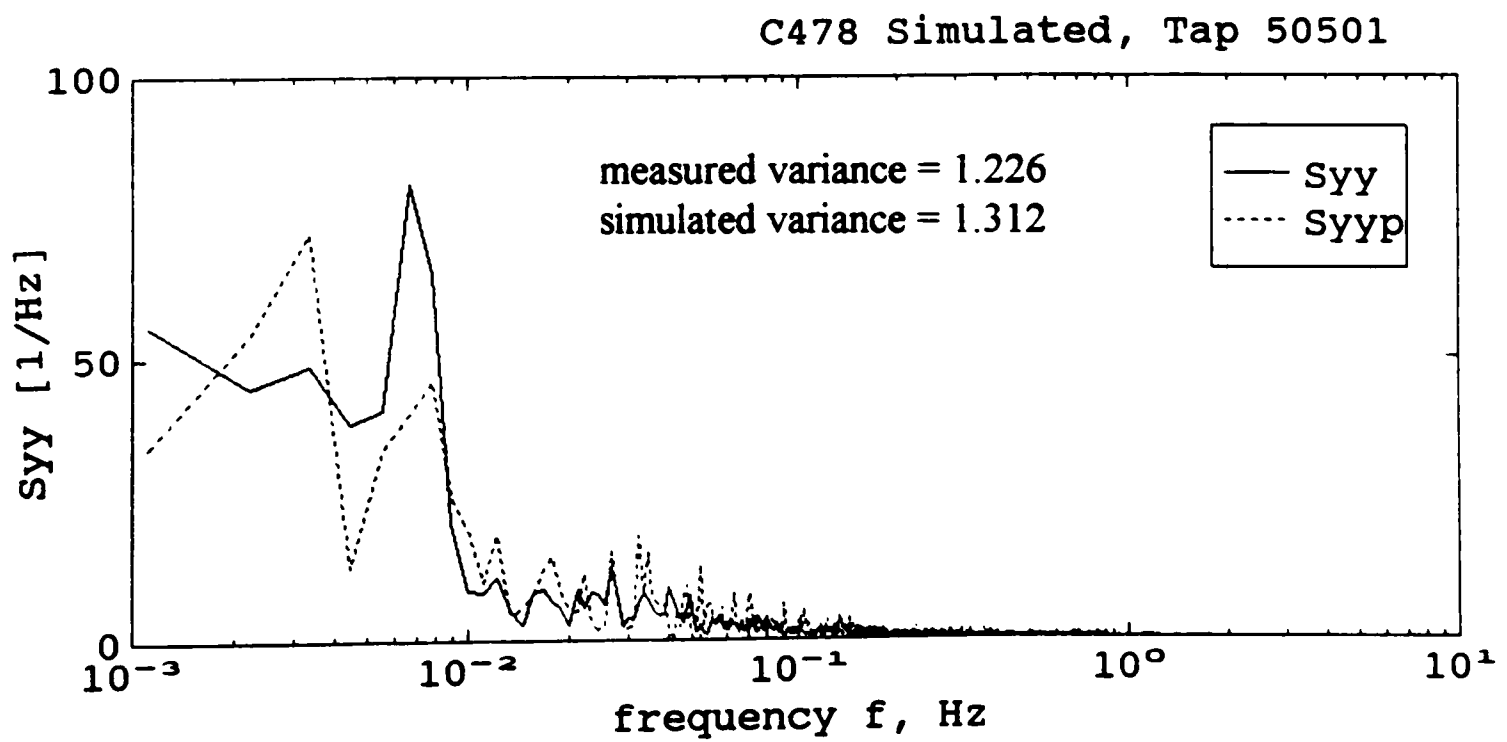


Figure 6.28. Comparison of transfer functions from wind-tunnel records for tap 50501.



(a) Using transfer functions of C709 only.



(b) Using averaged transfer functions of C081 and C709.

Figure 6.29. Simulated pressure-coefficient spectrum for tap 50501 for record C478.

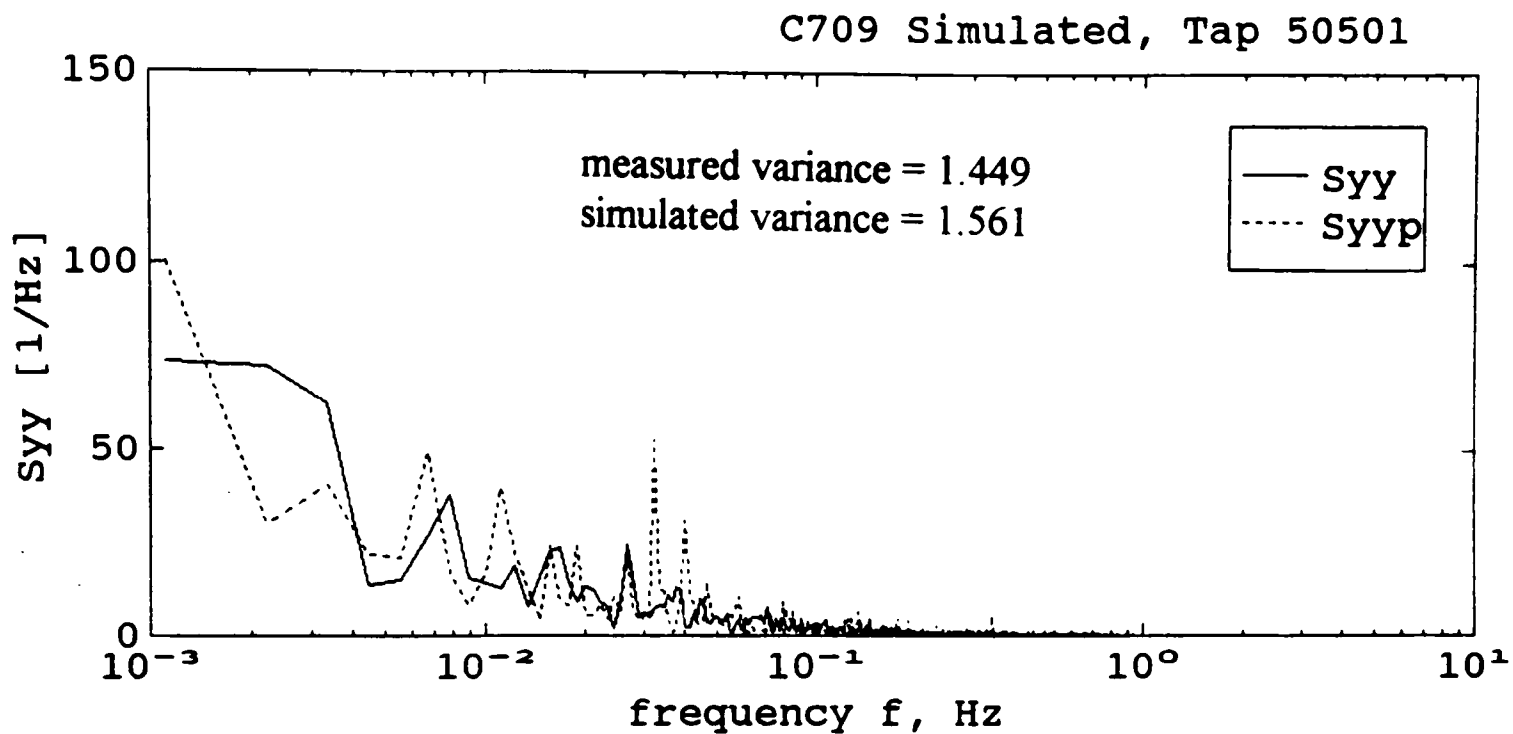


Figure 6.30. Simulated pressure-coefficient spectrum for tap 50501 for record C709 using averaged transfer functions of C081 and C478.

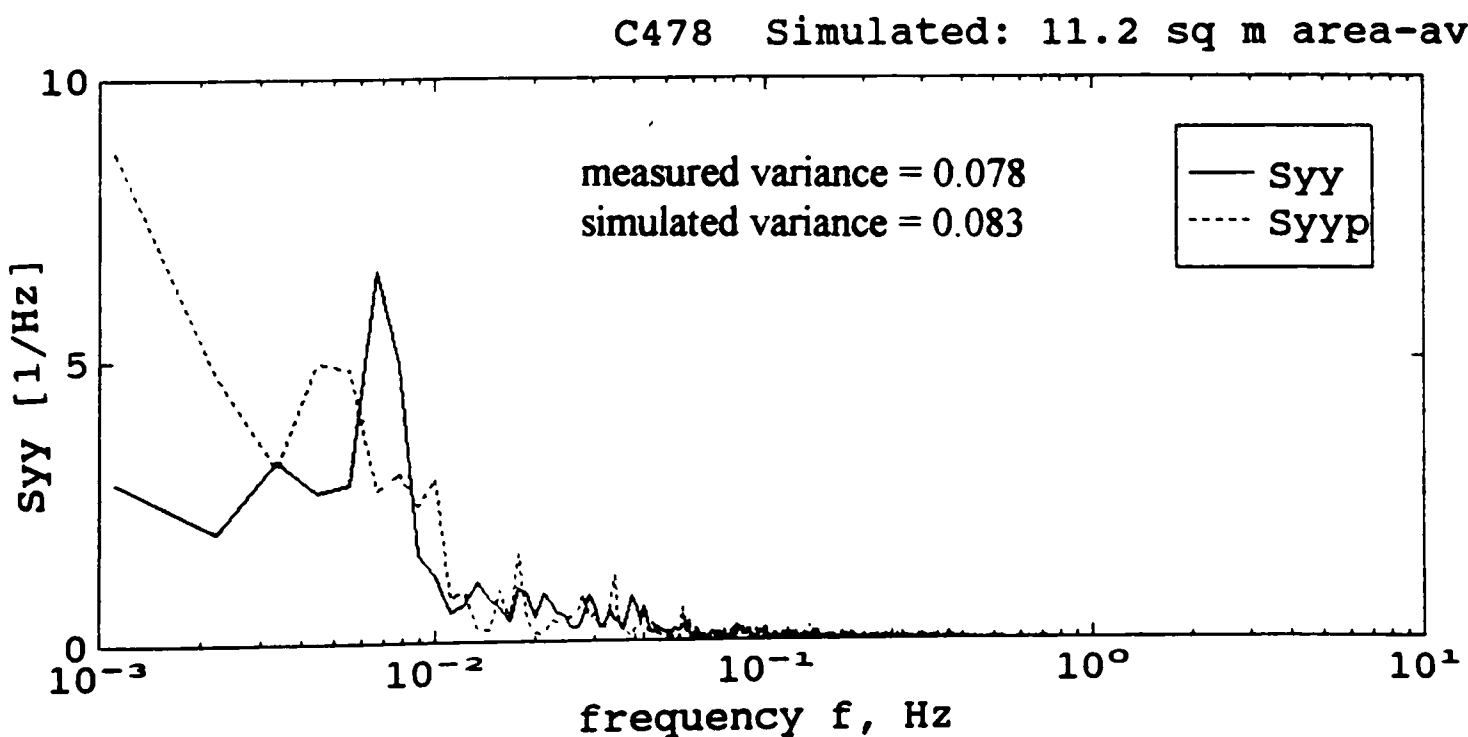


Figure 6.31. Simulated pressure-coefficient spectrum for C478 using transfer functions of C081 for the 11.2 m² area-averaged case at roof corner.

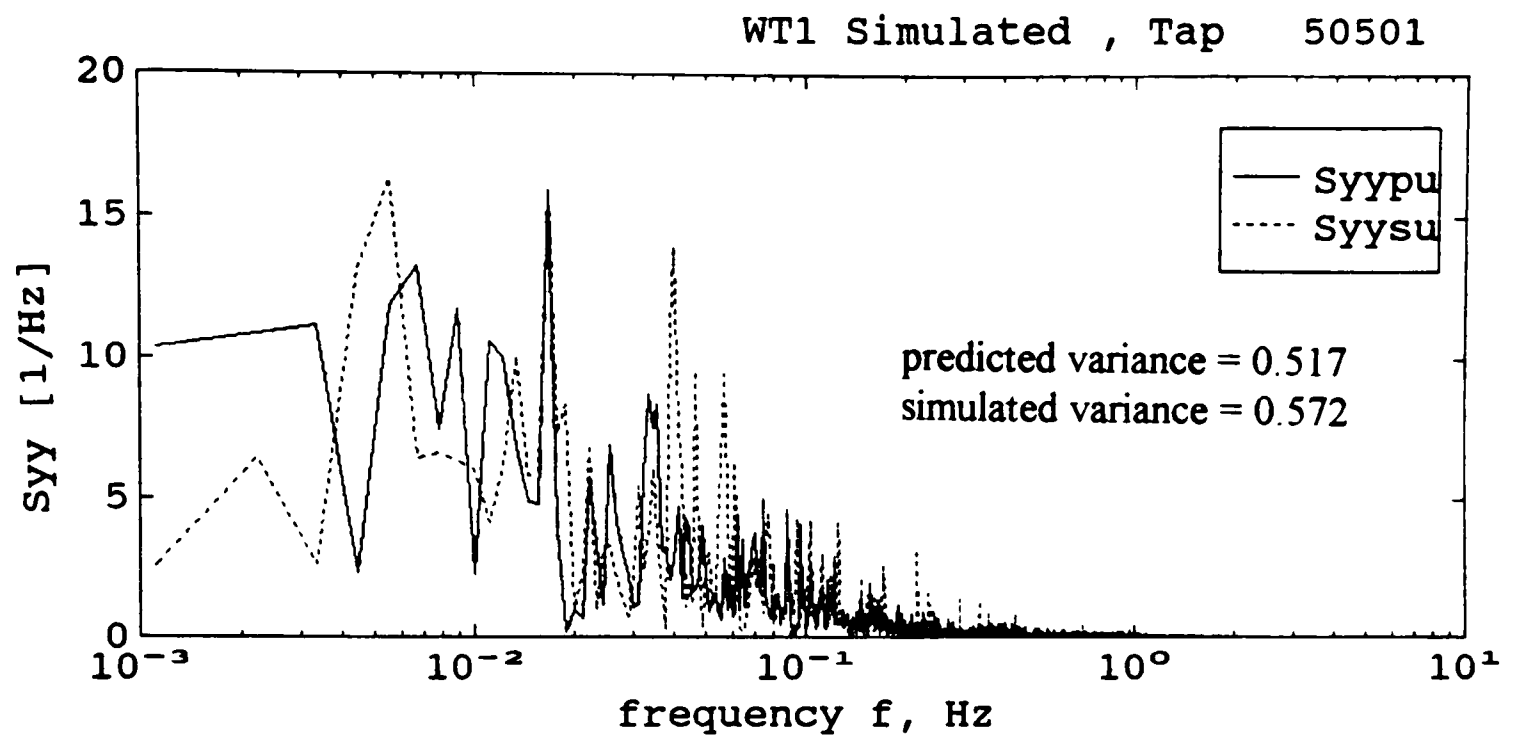


Figure 6.32. Simulated pressure-coefficient spectrum for tap 50501 for wind-tunnel record WT1 using averaged transfer functions from WT2 and WT3.

Although the transfer functions presented in this work did exhibit some variability, it must be realized that they were identified based on a very limited number of data records with similar mean angle of attack. Improvements seem possible if a very large number of records are used. The simulation results presented in Section 5.3 and in this section are found to be encouraging. It may be concluded that reasonably good simulations of the pressure spectrum are obtained from both field and wind-tunnel records. The predictions, although not exact, fall well within the range of rms values observed in the field for a particular tap from different records with similar angle of attack. Hence, practical applications of the proposed model seem promising.

6.4 Applicability of the Proposed Model

The transfer functions identified in the current work can be applied to prismatic low buildings of similar overall shape to predict the pressure-coefficient spectrum, and hence the pressure variance, at the appropriate flow region from the representative velocity

spectra at eave height of the building. From the simulations performed in this work, it was found that the model was successful in reasonably predicting the frequency content and pressure rms values within the range observed in the field. It was observed earlier that the transfer functions essentially capture the mechanism which results in producing wind pressures on building surfaces. The effect of other terrain conditions or more severe turbulence conditions are accounted for in the model by the appropriate input velocity spectra.

In the case of wind loads on tall buildings, aeroelastic forces due to the motion (structural dynamics) of the building are also present in addition to aerodynamic forces. Based on the limited wind-tunnel data examined in this work, it was found that the transfer functions obtained from wind-tunnel data were quite similar to the corresponding ones from field data. The proposed model is a general formulation and may be applied to determine transfer functions for wind pressures on tall buildings or other building types provided wind-tunnel or full-scale data are available for that building.

The pressure spectrum predicted using the model can be used as the target spectrum for the digital synthesis of fluctuating wind-pressure time histories. This can be achieved by applying an effective digital synthesis technique proposed by Seong (1993). The proposed technique makes use of the organization and shift of the phase part of the Fourier representation of the signal in generating the fluctuating character and peak events observed in wind-pressure time histories. The characteristics of the phase of the pressure spectra presented in this work also finds use in applying the digital synthesis technique. A quantitative treatment of the application of the technique is beyond the scope of this work and may be obtained from Seong (1993). The time histories so generated may be used to develop credible loading criteria for fatigue testing of cladding and fastener elements under severe wind events.

6.5 Summary

In this chapter, transfer functions, spectral decomposition and simulation results obtained from full-scale data were presented for individual taps and area-averaged cases at

the roof corner primarily for quartering winds. A comparison with results from wind-tunnel data was shown for tap 50501. The proposed model was found to predict and simulate the pressure spectrum from the upstream velocity spectra reasonably well. The residuals were small and the predictions were seen to fall well within the range of variability observed in the field data. It can be said with 95 percent confidence that the mean coherence will fall in the interval 0.90 to 1.12.

The transfer functions for the roof corner were similar in form, but exhibiting quantitative variation, for all the cases. The transfer functions from two different records with similar mean angle of attack were found to be quite similar, both in the qualitative and quantitative sense, with some quantitative variation. Also, the corresponding transfer functions from field and wind-tunnel data were found to be quite similar. These similarities suggest that the transfer functions essentially capture the mechanisms which produce pressures on building surfaces. The phase angles of the transfer functions the pressure spectra were again found to be uniformly distributed between $-\pi$ and $+\pi$ radians, with a mean of zero and a standard deviation in the range 1.8 to 1.9.

The spectral decomposition results show that the contribution from all the components are comparable for the tap closest to the edge of the corner (50101). For all the other taps the linear terms have a higher contribution (52 to 60 percent). For taps along the middle of the wedge of reattached flow, the linear u term has a more dominant contribution (about 27 to 30 percent). For taps well under the conical vortex, the linear v term has the most significant contribution (30 to 34 percent), indicating the strong influence of change in direction on the formation of the conical vortices. For the area-averaged case with quartering wind, the linear u and v terms have a total contribution of 57 to 61 percent, indicating that modification of the upstream flow plays a more important role in producing overall loads at the roof corner. For the area-averaged case with wind normal to the building, the contributions from different components are comparable. When the mean angle of attack is slightly skewed, the linear u term becomes more significant.

Analysis of the wind-tunnel data for tap 50501 showed a contribution of about 56 percent associated with the linear and quadratic u terms. However, the field data showed an even contribution to be associated with the linear and quadratic v terms. This again seems to indicate that lateral turbulence is not being properly simulated in the wind tunnel.

The bispectra of wind pressures again indicate that the non-Gaussian and hence the non-linear character of wind pressures are associated with low frequencies for almost all the roof corner cases. There are no significant frequencies beyond 5 Hz in the pressure spectra for all the cases. More than 90 percent (95 percent for area-averaged cases) of the pressure variance was contained in frequencies less than 2 Hz for most of the cases. In fact, more than 70 percent of the pressure variance is contained in frequencies below 0.5 Hz for all the cases.

The simulation results show that practical applications of the model seem promising. The effect of other terrain conditions or more severe turbulence conditions are accounted for in the model by the appropriate input velocity spectra. The pressure spectrum predicted using the model can be used as the target spectrum for the digital synthesis of fluctuating wind-pressure time histories. The time histories so generated may be used to develop credible loading criteria for fatigue testing of cladding and fastener elements under severe wind events.

CHAPTER 7

CONCLUDING REMARKS

7.1 The Proposed Model

A general linear-quadratic (bilinear) model (Bendat, 1990; Bendat and Piersol, 1982) is proposed herein to relate the spectral characteristics of the fluctuating longitudinal (u) and lateral (v) components of the upstream wind velocity to the spectral characteristics of the fluctuating point or area-averaged pressures on building surfaces. The model is non-parametric, time-invariant and adopts the concept of multiple transfer functions. Four transfer functions are defined: one each associated with the linear and quadratic terms of the u and v velocity components. The bilinear model consists of a linear system in parallel with a finite-memory square-law system for each input (u and v). The finite-memory square-law system is modeled as a zero-memory square-law system followed by a linear system (Case 1 model in Bendat, 1990; Bendat and Piersol, 1982).

The proposed approach groups the boundary layer and the structure together for the assessment of wind pressures. It enables a weighted decomposition of the measured output pressure spectrum into components representing contributions from the linear and quadratic terms of the input velocity components and the remaining uncorrelated residual and/or noise effects. The model provides physical insight into the influence of the upstream turbulence in producing pressures on building surfaces. The four transfer functions are optimally identified from cross-spectra of the velocity terms and surface pressure fluctuations by minimizing the residual/noise spectrum. The transfer functions (frequency response functions) so identified are Fourier transforms of the corresponding impulse response functions in the time domain. Physically, these response functions accumulate the effects of all past fluctuations of wind velocity. There are no assumptions made regarding the form of the transfer functions. The transfer functions, so identified, essentially capture the mechanism that results in producing wind pressures on building surfaces. The effect of terrain conditions or more severe turbulence conditions are

accounted for in the model by the appropriate input velocity spectra. The proposed model is, thus, more rational and an improvement over the modified quasi-steady theory.

The model has the following physical interpretation. In the physical sense, wind pressures on building surfaces are a result of two mechanisms: (1) the modification of the upstream flow, which results in change in momentum, due to interaction with the structure and the flow around it, and (2) the dissipation of kinetic energy in the upstream turbulence when it encounters the structure. The linear terms in the model represent the contribution to the pressures due to the modification or change in momentum of the upstream flow. The quadratic terms in the model represent the contribution to the pressures due to direct dissipation of the fluctuating kinetic energy in the upstream wind when it encounters the structure. The v terms represent the effect of local changes in wind direction.

A disadvantage of the proposed model is that the magnitudes of the identified transfer functions, in the higher frequency range, depend on the frequency response characteristics of the anemometer used in measuring the input velocities. However, these transfer functions give the correct output prediction when used with input data from the same type of anemometer as used for the identification work.

7.2 Conclusions

The present research is primarily based on full-scale wind velocity data at roof height (4 m) and pressure data collected on a 13.7 m x 9.1 m x 4 m flat-roof metal test building, located on a flat open terrain, at the Texas Tech Wind Engineering Research Field Laboratory. A very limited amount of wind-tunnel data obtained from Colorado State University was also used. The proposed model was applied to the data: (a) to solve the system identification problem; and (b) to solve the spectral decomposition and output prediction (including simulation) problem. The field velocity data used were measured with either a 3-cup/vane anemometer or a sonic anemometer. Analyses were presented and discussed for typical flow regions on the building: windward wall, roof separation and reattachment zones, leeward wall, side walls, roof corner and area-averaged cases. The important conclusions that can be drawn from the present research are as follows.

1. The proposed model is able to predict and simulate the pressure spectrum from the upstream velocity spectra reasonably well, with respect to both variance (or rms) and frequency content, for field and wind-tunnel records. The predictions fall well within the range of rms values observed in the field for the particular tap from different records with similar angle of attack of the wind. It can be said with 95 percent confidence that the mean coherence will fall in the interval 0.90 to 1.12.
2. The quadratic terms of wind velocity are important and they have comparable contributions as the linear terms to the surface pressures on low-rise buildings.
3. The lateral velocity terms play an equally vital role as the longitudinal velocity terms in producing surface pressures. This signifies the importance of local changes in wind direction in producing fluctuating pressures on building surfaces.
4. The study supports the hypothesis presented by other researchers (e.g., Tieleman, 1995b; Tieleman, 1994; Tieleman et al., 1994) that improper simulation of lateral turbulence in the upstream wind is, perhaps, the primary reason for deficiencies observed in wind-tunnel model pressures.
5. All the terms in the model have a comparable contribution to the pressures for most cases. The effect of changes in wind direction is more significant under the delta-wing vortices and on the side and leeward walls. The linear u component is more significant for area-averaged pressures.
6. The similarity between the transfer functions obtained from the field and corresponding wind-tunnel data and from different field records with approximately same mean angle of attack suggests that the transfer functions essentially capture the mechanism that transforms wind velocity to pressure. This mechanism is the same in the field and in the wind tunnel. The wind tunnel is, hence, an effective tool in capturing flow mechanisms and hence can be used to determine transfer functions for different types of buildings.
7. The transfer functions for different flow regions are similar in form but show quantitative variation.

8. The transfer functions obtained from the 3-cup anemometer showed an upward trend in the higher frequency end, beyond about 0.5 Hz for u and 1 Hz for v , in comparison to the more realistic ones obtained using data from the sonic anemometer. This is due to insufficient frequency response of the 3-cup anemometer at higher frequencies. However, these transfer functions give the correct output prediction when used with input data from the same type of anemometer as used for the identification work.
9. The phase of the pressure spectra and the transfer functions are uniformly distributed between $-\pi$ and $+\pi$ radians, with a mean of approximately zero and a standard deviation in the range 1.8 to 1.9. This information is useful for the digital synthesis of fluctuating wind-pressure time histories from pressure spectra.
10. There are practically no significant frequencies beyond 5 Hz in the velocity spectra. More than 75 percent of the velocity variance is contained in frequencies below 0.5 Hz.
11. There are practically no significant frequencies beyond 5 Hz in the pressure spectra for all the flow regions. More than 70 percent of the pressure variance is contained in frequencies below 0.5 Hz for all the cases except the reattachment zone where higher frequencies are more significant.
12. The bispectra of pressures show that the non-linear and non-Gaussian character of pressures are mainly associated with the low frequencies, the reattachment zone being the only exception.
13. The model presented in this research can be proposed as an alternative to the modified quasi-steady theory for predicting the spectra of fluctuating wind pressures on building surfaces.

7.3 Scope for Further Work

The present work has demonstrated the feasibility of the proposed model to predict the pressure spectrum from the velocity spectra. The transfer functions for a particular record did exhibit variability over the entire frequency range. This variability can be attributed to reasons such as deviations from Gaussian behavior of the input, noise in the

input instrumentation, computational noise, variability in input and output spectra observed in the field due to changes in wind direction, full-scale non-stationary effects, and the very limited number of similar records that were available for the identification process. There is scope for significant improvement in the transfer function estimates if a very large number (over a 100) of similar records obtained from the field or wind tunnel are used for averaging. A quantitative analysis of errors may also be performed on the transfer function estimates.

It would be worthwhile to investigate the use of the pressure spectrum predicted from the model for the digital synthesis of fluctuating wind-pressure time histories (Seong, 1993). This would form the basis for the development of a credible loading criteria for fatigue testing of cladding and fastener elements under severe wind events.

The proposed model, which is a general formulation, may be used to determine transfer functions for wind pressures on tall buildings or other building types provided wind-tunnel or full-scale data is available for that building.

REFERENCES

- ASCE Committee on Wind Effects (1987), *Wind Loading and Wind-Induced Structural Response*, A state-of-the-art report, ASCE Structural Division, New York, pp. 32-96.
- Bearman, P.W. (1978), Turbulence Effects on Bluff Body Mean Flow, *Proceedings of the Third U.S. National Conference on Wind Engineering Research*, University of Florida, Gainesville, February 26-March 1, pp. 265-272.
- Bearman, P.W. (1971), An Investigation of the Forces on Flat Plates Normal to a Turbulent Flow, *Journal of Fluid Mechanics*, Volume 46, Part 1, pp. 177-198.
- Bendat, J.S. (1990), *Nonlinear System Analysis and Identification from Random Data*, John Wiley & Sons, Inc., New York.
- Bendat, J.S., and Piersol, A.G. (1986), *Random Data: Analysis and Measurement Procedures*, Second Edition, John Wiley & Sons Inc., New York.
- Bendat, J.S., and Piersol, A.G. (1982), Spectral Analysis of Non-linear Systems Involving Square-law Operations, *Journal of Sound and Vibration*, Volume 81(2), pp. 199-213.
- Bendat, J.S., and Piersol, A.G. (1980), *Engineering Applications of Correlation and Spectral Analysis*, John Wiley & Sons Inc., New York.
- Carter, G.C., Knapp, C.H., and Nuttall, A.H. (1973), Estimation of the Magnitude-Squared Coherence Function Via Overlapped Fast Fourier Transform Processing, *IEEE Transactions on Audio and Electroacoustics*, Volume AU-21, No. 4, pp. 337-344.
- Cermak, J.E. (1993), Wind Engineering--Engineering for Wind Damage Mitigation, *Structural Engineering in Natural Hazards Mitigation*, Structures Congress, Irvine, California, April 19-21, pp. 37-58.
- Choi, D.W., Miksad, R.W., Powers, E.J., and Fischer, F.J. (1985), Application of Digital Cross-Bispectral Analysis Techniques to Model the Non-linear Response of a Moored Vessel System in Random Seas, *Journal of Sound and Vibration*, Volume 99, No. 3, pp. 309-326.
- Chok, C.V. (1988), *Wind Parameters of Texas Tech University Field Site*, Master's Thesis, Department of Civil Engineering, Texas Tech University, Lubbock.

- Cochran, L.S. (1992), *Wind-Tunnel Modelling of Low-Rise Buildings*, Ph.D Dissertation, Fluid Mechanics and Wind Engineering Program, Department of Civil Engineering, Colorado State University, Fort Collins.
- Cook, N.J. (1985), *The Designer's Guide to Wind Loading of Building Structures Part 1: Background, Damage Survey, Wind Data and Structural Classification*, Building Research Establishment and Butterworths, London.
- Cook, N.J. (1990), *The Designer's Guide to Wind Loading of Building Structures Part 2: Static Structures*, Building Research Establishment and Butterworths, London.
- Dalglish, W.A., Templin, J.T., and Cooper, K.R. (1979), Comparison of Wind Tunnel and Full-Scale Building Surface Pressures with Emphasis on Peaks, *Wind Engineering --Proceedings of the Fifth International Conference* (J.E. Cermak, editor), Fort Collins, Colorado, July 1979, pp. 553-565.
- Davenport, A.G., Surry, D., and Stathopoulos, T. (1977), *Wind Loads on Low-Rise Buildings: Final Report of Phases I and II--Parts 1 and 2*, BLWT--SS8-1977, The University of Western Ontario, London, Canada.
- Davenport, A.G. (1971), On the Statistical Prediction of Structural Performance in the Wind Environment, ASCE National Structural Engineering Meeting, Baltimore, Maryland, April 19-23.
- Davenport, A.G. (1961), The Application of Statistical Concepts to the Wind Loading of Structures, *Proceedings of the Institution of Civil Engineers*, Volume 19, pp. 449-471.
- DeFatta, D.J., Lucas, J.G., and Hodgkiss, W.S. (1988), *Digital Signal Processing: A System Design Approach*, John Wiley & Sons, New York.
- Drabble, M.J., Grant, I., Armstrong, B.J., and Barnes, F.H. (1990), The Aerodynamic Admittance of a Square Plate in a Flow with a Fully Coherent Fluctuation, *Physics of Fluids A : Fluid Dynamics*, Volume 2, No. 6, pp. 1005-1013.
- Eykhoff, P. (1974), *System Identification--Parameter and State Estimation*, John Wiley & Sons, New York.
- Gerhardt, H.J., and Kramer, C. (1992), Effect of Building Geometry on Roof Wind Loading, *Journal of Wind Engineering and Industrial Aerodynamics*, Volumes 41-44, pp. 1765-1773.

- Gurley, K., and Kareem, A. (1994), On the Analysis and Simulation of Random Processes Utilizing Higher Order Spectra and Wavelet Transforms, *Computational Stochastic Mechanics* (P. D. Spanos, editor), Proceedings of the Second International Conference on Computational and Stochastic Mechanics, Athens, Greece, June 12-15, pp. 315-324.
- Harris, F.J. (1978), On the Use of Windows for Harmonic Analysis with the Discrete Fourier Transform, *Proceedings of the IEEE*, Volume 66, No. 1, pp.51-83.
- Holmes, J.D. (1982), *Wind Loads on Low Rise Buildings—A Review*, Technical Report, Division of Building Research, CSIRO, Australia.
- Holmes, J.D. (1981), Non-Gaussian Characteristics of Wind Pressure Fluctuations, Short Communication, *Journal of Wind Engineering and Industrial Aerodynamics*, Volume 7, pp. 103-108.
- Holmes, J.D., Melbourne, W.H., and Walker, G.R. (1990), *Commentary on the Australian Standard for Wind Loads*, Australian Wind Engineering Society.
- Holscher, N. (1995), Spectral Decomposition of Turbulence Induced Pressure Fluctuations into Linear and Non-linear Components by Means of a Multivariate Aerodynamic Admittance, *Summary Papers for the Ninth International Conference on Wind Engineering*, New Delhi, India, January 9-13, 1995, pp. 86-87.
- Holscher, N. (1993), *Eine multivariater Ansatz für die aerodynamische Übertragungsfunktion der Winddrucke in atmosphärischer Grenzschichtströmung*, Ph.D thesis, Institut für Konstruktiven Ingenieurbau, Ruhr-Universität Bochum, Germany.
- Holscher, N., and Niemann, H.J. (1992a), Multiple Aerodynamic Pressure Admittance - Concept and Related Experiments, *Journal of Wind Engineering and Industrial Aerodynamics*, Volumes 41-44, pp. 715-726.
- Holscher, N., and Niemann, H.J. (1992b), Turbulence and Separation Induced Pressure Fluctuations on a Finite Circular Cylinder--Application of a Multiple Aerodynamic Admittance, *Second International Colloquium on Bluff Body Aerodynamics and Applications*, Volume II, Melbourne, Australia, December 7-10.
- Horlock, J.H. (1968), Fluctuating Lift Forces on Aerofoils Moving Through Transverse and Chordwise Gusts, *Transactions of the ASME, Journal of Basic Engineering*, December 1968, pp. 494-500.

- Hunt, J.C.R., Kawai, H., Ramsey, S.R., Pedrizetti, G., and Perkins, R.J. (1990), A Review of Velocity and Pressure Fluctuations in Turbulent Flows Around Bluff Bodies, *Journal of Wind Engineering and Industrial Aerodynamics*, Volume 35, pp. 49-85.
- Imai, H., Yun, C.B., Maruyama, O., and Shinozuka, M. (1989), Fundamentals of System Identification in Structural Dynamics, A Review Paper, *Probabilistic Engineering Mechanics*, Volume 4, No. 4, pp. 162-173.
- Jancauskas, E.D., and Sankaran, R. (1992), The Coherence of Cross-wind Velocity and Pressure on Two-Dimensional Rectangular Cylinders in Turbulent Flows, *Journal of Wind Engineering and Industrial Aerodynamics*, Volumes 41-44, pp. 809-810.
- Jancauskas, E.D., and Melbourne, W.H. (1986), The Aerodynamic Admittance of Two-Dimensional Rectangular Section Cylinders In Smooth Flow, *Journal of Wind Engineering and Industrial Aerodynamics*, Volume 23, pp. 395-408.
- Jones, N.P., Reed, D.A., and Cermak, J.E. (1993), Wind Hazards Reduction Program, *Structural Engineering in Natural Hazards Mitigation*, Structures Congress, Irvine, California, April 19-21, pp. 827-830.
- Kanai, H., Hori, T., Chubachi, N, and Ono, T. (1994), Delayed Block Transfer Function in the Frequency Domain, *IEEE Transactions on Signal Processing*, Volume 42, No. 7, pp.1669-1684.
- Kareem, A. (1987), Wind Effects on Structures: A Probabilistic Viewpoint, *Probabilistic Engineering Mechanics*, Volume 2, No. 4, pp. 166-200.
- Kareem, A., Gurley, K., and Tognarelli, M. (1995), Advanced Analysis and Simulation Tools for Wind Engineering, *Wind Engineering--Retrospect and Prospect*, Ninth International Conference on Wind Engineering, New Delhi, January 9-13, Volume V.
- Kareem, A., and Li, Y. (1988), On Modelling the Nonlinear Relationship Between Random Fields By Means of Higher-Order Spectra, *Probabilistic Methods in Civil Engineering* (Edited by P.D. Spanos), ASCE, New York, pp. 384-387.
- Kawai, H. (1983), Pressure Fluctuations on Square Prisms--Applicability of Strip and Quasi-steady Theories, *Journal of Wind Engineering and Industrial Aerodynamics*, Volume 13, pp. 197-208.
- Kim, K.I., and Powers, E.J. (1988), A Digital Method of Modelling Quadratically Nonlinear Systems with a General Random Input, *IEEE Transactions on Acoustics, Speech and Signal Processing*, Vol. 36, No. 11, pp. 1758-1769.

- Krishna, P. (1995), Wind Loads on Low Rise Buildings--A Review, *Journal of Wind Engineering and Industrial Aerodynamics*, Volumes 54/55, pp. 383-396.
- Letchford, C.W. (1995), Simultaneous Flow Visualization and Pressure Measurements on the Texas Tech Building, *Wind Engineering--Retrospect and Prospect*, Proceedings of the Ninth International Conference on Wind Engineering, New Delhi, January 9-13, Volume I, pp. 524-535.
- Letchford, C.W., and Mehta, K.C. (1993), The Distribution and Correlation of Fluctuating Pressures on the Texas Tech Building, *Journal of Wind Engineering and Industrial Aerodynamics*, Volume 50, pp. 225-234.
- Letchford, C.W., Iverson, R.E., and McDonald, J.R. (1993), The Application of the Quasi-steady Theory to Full Scale Measurements on the Texas Tech Building, *Journal of Wind Engineering and Industrial Aerodynamics*, Volume 48, pp. 111-132.
- Letchford, C.W., Sandri, P., Levitan, M.L., and Mehta, K.C. (1992), Frequency Response Requirements for Fluctuating Wind Pressure Measurements, *Journal of Wind Engineering and Industrial Aerodynamics*, Volume 40, pp. 263-276.
- Levitan, M.L., and Mehta, K.C. (1992a), Texas Tech Field Experiments for Wind Loads Part 1: Building and Pressure Measuring System, *Journal of Wind Engineering and Industrial Aerodynamics*, Volumes 41-44, pp. 1565-1576.
- Levitan, M.L., and Mehta, K.C. (1992b), Texas Tech Field Experiments for Wind Loads Part 2: Meteorological Instrumentation and Terrain Parameters, *Journal of Wind Engineering and Industrial Aerodynamics*, Volumes 41-44, pp. 1577-1588.
- Lin, J.X., Surry, D., and Tieleman, H.W. (1995), The Distribution of Pressure Near Roof Corners of Flat Roof Low Buildings, *Journal of Wind Engineering and Industrial Aerodynamics*, Volume 56, pp. 235-265.
- Little, J.N., and Shure, L. (1992), *Signal Processing Toolbox for Use with Matlab: Users Guide*, The Mathworks Inc., Natick, Massachusetts.
- Ljung, L. (1987), *System Identification: Theory for the User*, Prentice Hall Inc., Englewood Cliffs, New Jersey.
- Matlab: User's Guide*, The Math Works Inc., Natick, Massachusetts, 1992.
- Matlab: Reference Guide*, The Math Works Inc., Natick, Massachusetts, 1992.

- Mendel, J.M. (1991), Tutorial on Higher-Order Statistics (Spectra) in Signal Processing and System Theory: Theoretical Results and Some Applications, *Proceedings of the IEEE*, Volume 79, No. 3, pp. 278-305.
- Mehta, K.C., Levitan, M.L. Iverson, R.E., and McDonald, J.R. (1992), Roof Corner Pressures Measured in the Field on a Low Building, *Journal of Wind Engineering and Industrial Aerodynamics*, Volumes 41-44, pp. 181-192.
- Nam, S.W., and Powers, E.J. (1994), Application of Higher Order Spectral Analysis to Cubically Nonlinear System Identification, *IEEE Transactions on Signal Processing*, Volume 42, No. 7, pp. 1746-1765.
- Nikias, C.L., and Petropulu, A.P. (1993), *Higher-Order Spectral Analysis: A Nonlinear Signal Processing Framework*, PTR Prentice Hall, New Jersey.
- Nikias, C.L., and Raghuveer, M.R. (1987), Bispectrum Estimation: A Digital Signal Processing Framework, *Proceedings of the IEEE*, Volume 75, No. 7, pp. 869-891.
- Oppenheim, A.V., and Schaffer, R.W. (1975), *Digital Signal Processing*, Prentice Hall Inc., Englewood Cliffs, New Jersey.
- Ott, L. (1988), *An Introduction to Statistical Methods and Data Analysis*, PWS Kent Publishing Company, Boston, Massachusetts, pp. 156 & A-5.
- Peterka, J.A., Meroney, R.N., and Kothari, K.M. (1985), Wind Flow Patterns about Buildings, *Journal of Wind Engineering and Industrial Aerodynamics*, Volume 21, pp. 21-38.
- Peterka, J.A., and Cermak, J.E. (1975), Wind Pressures on Buildings--Probability Densities, *Journal of the Structural Division, ASCE*, Volume 101, No. ST6, pp. 1255-1267.
- Reed, D.A. (1980), *Time Series Analysis of Wind Loadings on Hyperbolic Cooling Towers*, Ph.D. Dissertation, Department of Civil Engineering, Princeton University.
- Rice, H.J., and Fitzpatrick, J.A. (1988), A Generalized Technique for Spectral Analysis of Non-linear Systems, *Mechanical Systems and Signal Processing*, 2(2), pp. 195-207.
- Sandri, P. (1992), *Frequency Response Requirements for Measuring Fluctuating Wind Pressures on Buildings*, Master's Thesis, Department of Civil Engineering, Texas Tech University, Lubbock.

- Sankaran, R., and Jancauskas, E.D. (1992), Direct Measurement of the Aerodynamic Admittance of Two-dimensional Rectangular Cylinders in Smooth and Turbulent Flows, *Journal of Wind Engineering and Industrial Aerodynamics*, Volumes 41-44, pp. 601-611.
- Sarkar, P.P., Scanlan, R.H., and Jones, N.P. (1994), Aerodynamic Transfer Functions for Bridge Buffeting, *Proceedings of the 80th Birthday Symposium in Honor of Professor Robert H. Scanlan*, Department of Civil Engineering, The Johns Hopkins University, October 28-29, pp. 295-307.
- Sarkar, P.P. (1992), *New Identification Methods Applied to the Response of Flexible Bridges to Wind*, Ph.D. Thesis, Department of Civil Engineering, The Johns Hopkins University, Baltimore, Maryland.
- Scanlan, R.H. (1993), Problemetics in the Formulation of Wind Force Models for Bridge Decks, *Journal of Engineering Mechanics, ASCE*, Volume 119, pp. 1353-1375.
- Schetzen, M. (1980), *The Volterra and Weiner Theories of Nonlinear Systems*, John Wiley & Sons Inc., New York.
- Schueller, G.I. Editor (1991), *Structural Dynamics: Recent Advances*, Springer-Verlag, Berlin.
- Seong, S.K. (1993), *Digital Synthesis of Wind Pressure Fluctuations on Building Surfaces*, Ph.D Dissertation, Department of Civil Engineering, Colorado State University, Fort Collins, Colorado.
- Smith, D.A., Mehta, K.C., Yeatts, B.B., and Bhavaraju, S.V. (1994), Area-averaged and Internal Pressure Coefficients Measured in the Field, *Journal of Wind Engineering and Industrial Aerodynamics*, Volume 53, pp. 89-103.
- Standards Association of Australia (1989), *S.A.A Loading Code - Part 2: Wind Loads AS 1170.2-1989*, Sydney, Australia.
- Stathopoulos, T. (1984), Wind Loads on Low-Rise Buildings: A Review of the State of the Art, *Engineering Structures*, Volume 6, April, pp. 119-135.
- Stathopoulos, T., Surry, D., and Davenport, A.G.(1978), Some General Characteristics of Turbulent Wind Effects On Low-Rise Structures, *Proceedings of the Third Colloquium on Industrial Aerodynamics*, Aachen, West Germany, June 14-16, pp.211-225.

- Synopsis of the Discussions (1975), Symposium on Full Scale Measurements of Wind Effects on Tall Buildings and other Structures, *Journal of Industrial Aerodynamics*, Volume 1, pp. 18-23.
- Thomas, G., Sarkar, P.P., and Mehta, K.C. (1995), Identification of Admittance Functions for Wind Pressures from Full-Scale Measurements, *Wind Engineering--Retrospect and Prospect*, Proceedings of the Ninth International Conference on Wind Engineering, New Delhi, January 9-13, Volume III, pp. 1219-1230.
- Thomas, G., Cochran, L.S., Cermak, J.E. and Mehta, K.C. (1993), Comparison of Field and Wind-Tunnel Measured Spectra, *Proceedings of the 7th U.S. National Conference on Wind Engineering*, UCLA, June 27-30, pp. 793-802.
- Tieleman, H.W. (1995a), Universality of Velocity Spectra, *Journal of Wind Engineering and Industrial Aerodynamics*, Volume 56, No. 1, pp. 55-69.
- Tieleman, H.W. (1995b), Simulation of Surface Winds for Assessment of Extreme Wind Loads on Roofs, *Wind Engineering--Retrospect and Prospect*, Proceedings of the Ninth International Conference on Wind Engineering, New Delhi, January 9-13, Volume III, pp. 1162-1169.
- Tieleman, H.W. (1994), Model/Full Scale Comparison of Pressures on the Roof of the TTU Experimental Building, *East European Conference on Wind Engineering, Preprints*, Part 1, Volume 3, Warsaw, Poland, July 4-8, pp. 185-194.
- Tieleman, H.W. (1993), Wind Loads on Roofs of Low Rise Structures: Buffeting or Interaction, *Hurricanes of 1992, Proceedings of Symposium Organized by ASCE*, Miami, December 3-5, pp. B 1 V 1-12.
- Tieleman, H.W., Surry, D., and Lin, J.X. (1994), Characteristics of Mean and Fluctuating Pressure Coefficients under Corner (delta wing) Vortices, *Journal of Wind Engineering and Industrial Aerodynamics*, Volume 52, pp. 263-275.
- Tieleman, H.W., and Tavoularis, S.C. (1977), An Instrumentation System for the Measurement of Atmospheric Turbulence, *Journal of Wind Engineering and Industrial Aerodynamics*, Volume 2, pp. 49-63.
- Tseng, Y.C., and Linebarger, D.A. (1995), Linear-Quadratic System Identification with Completed Frequency Domain Region of Support, *IEEE Transactions on Signal Processing*, Volume 43, No. 1, pp. 254-261.
- Vaicaitis, R., and Simiu, E. (1977), Nonlinear Pressure Terms and Alongwind Response, *Journal of the Structural Division, ASCE*, Volume 102, No. ST4, pp. 903-906.

- Van der Hoven, I. (1957), Power Spectrum of Horizontal Wind Speed in the Frequency Range from 0.0007 to 900 Cycles per Hour, *Journal of Meteorology*, Volume 14, pp. 160-164.
- Vickery, B.J. (1976), Wind Loads on Low-Rise Buildings, presented at DRC Seminar, Darwin, Australia, March 30.
- Vickery, B.J. (1966), Fluctuating Lift and Drag on a Long Cylinder of Square Cross-Section in a Smooth and in a Turbulent Stream, *Journal of Fluid Mechanics*, Volume 25, pp. 481-494.
- Wagaman, S.A. (1993), *Full-Scale Flow Visualization Over a Low-Rise Building*, Master's Thesis, Department of Civil Engineering, Texas Tech University, Lubbock, TX.
- Yin, J. (1996), *Probabilistic Study of Wind Pressures on Buildings*, Ph.D. Dissertation, Department of Civil Engineering, Texas Tech University, Lubbock.
- _____, *Operator's Manual for SWS 503/2KZ Two-Axis Sonic Wind System Anemometer*, Revision B, Applied Technologies Inc., Boulder, Colorado.

APPENDIX
SUMMARY STATISTICS OF DATA USED

Table A.1 Summary statistics of velocity data.

Record	Wind azimuth α°	Angle of attack θ°	U at 4 m m/s	I_u	I_v	$0.5\rho U^2$ kg/m ²
M15N024	278.0	294.0	10.10	0.170	0.240	6.10
M15N081	270.8	225.8	8.32	0.229	0.306	4.16
M15N082	273.9	228.9	8.59	0.234	0.269	4.35
M15N086	273.1	228.1	9.48	0.217	0.201	4.61
M15N325	253.0	358.0	7.96	0.257	0.217	3.82
M15N326	258.1	3.1	8.45	0.216	0.229	4.30
M15N327	259.2	4.2	9.35	0.229	0.194	5.20
M15N478	301.3	211.3	13.01	0.161	0.138	9.67
M15N479	304.4	214.4	11.98	0.153	0.158	8.26
M15N482	306.3	216.3	9.70	0.171	0.210	5.47
M15N539	353.1	263.1	9.55	0.197	0.191	5.33
M15N540	349.8	259.8	8.86	0.183	0.206	4.61
M15N541	356.6	266.4	8.95	0.191	0.162	4.64
M15N544	356.5	266.5	8.94	0.202	0.150	4.66
M15N545	358.1	268.1	10.04	0.157	0.144	5.93
M15N546	358.6	268.6	9.09	0.189	0.136	4.89
M15N709	25.8	220.8	10.33	0.180	0.188	6.12
M15N710	29.5	224.5	9.70	0.210	0.171	5.31
M15N711	29.0	224.0	9.61	0.188	0.223	5.36
M15N728	168.8	3.8	7.38	0.191	0.180	3.09
M15N729	170.2	5.2	7.74	0.239	0.158	3.37
M15N730	169.9	4.9	8.27	0.213	0.153	3.86

Table A.1 Continued.

Record	Wind azimuth α°	Angle of attack θ°	U at 4 m m/s	I_u	I_v	$0.5\rho U^2$ kg/m ²
SA070	253.9	268.9	10.73	0.213	0.224	7.14
SA071	251.1	266.1	9.50	0.239	0.211	5.50
SA072	252.7	267.7	9.91	0.230	0.200	5.99
SA073	248.8	263.8	9.87	0.198	0.202	5.94
SA074	257.9	272.9	10.07	0.215	0.179	6.18
SA075	260.9	275.9	8.65	0.231	0.263	4.56
SA077	271.6	271.6	9.90	0.244	0.221	5.94
SA078	270.7	270.7	9.38	0.230	0.210	5.33
SA079	268.7	268.7	8.55	0.244	0.226	4.44
M38N070	253.9	268.9	11.49	0.209	0.201	8.19
M38N071	251.7	266.7	10.64	0.198	0.167	6.89
M38N072	252.1	267.1	10.64	0.211	0.168	6.91
M38N077	268.4	268.4	10.82	0.212	0.156	7.10
M38N078	267.0	267.0	10.69	0.191	0.133	6.93
M38N079	265.1	265.1	9.79	0.202	0.140	5.82
WT1	-	225.0	10.32	0.192	-	6.50
WT2	-	225.0	10.19	0.201	-	6.33
WT3	-	225.0	10.11	0.203	-	6.23

Notes:

1. I_u and I_v are longitudinal and lateral turbulence intensities, respectively.
2. All M15 records were measured with a 3-cup/vane anemometer.
3. All SA records were measured with a two-axis sonic anemometer and was synchronized with M38 records with identical numbers.
4. All M38 records were measured with a propellor type UVW anemometer.
5. All records designated WT were collected in the CSU Wind Tunnel.
6. All records are of 15 minutes duration except the wind tunnel records.
7. An average value of 1.2 kg/m³ may be taken for air density ρ .

Table A.2 Summary statistics of pressure-coefficient data.

Location/ Pressure Tap	Record	Cp_mean	Cp_rms	Cp_max	Cp_min
<u>Windward Wall:</u>					
42206	C539	0.65	0.307	1.65	-1.32
	C544	0.66	0.301	1.96	-0.90
	CS070	0.53	0.342	2.25	-1.06
	CS077	0.50	0.295	1.98	-0.96
42212	C539	0.58	0.345	2.21	-1.53
	C544	0.63	0.339	1.68	-1.18
	CS070	0.48	0.362	2.46	-1.51
	CS077	0.47	0.340	2.24	-1.27
	CS073	0.57	0.402	2.98	-1.95
<u>Leeward Wall:</u>					
22306	C539	-0.15	0.096	0.29	-0.90
	C544	-0.12	0.074	0.28	-0.38
	CS070	-0.26	0.087	0.25	-0.33
	CS077	-0.25	0.075	0.28	-0.53
22312	C539	-0.16	0.101	0.32	-0.70
	C544	-0.13	0.081	0.36	-0.44
<u>Side Wall:</u>					
11407	C539	-0.46	0.278	1.15	-1.19
	C544	-0.37	0.296	1.05	-1.94
	CS070	-0.40	0.245	0.81	-1.43
	CS077	-0.40	0.236	0.82	-1.70
31407	C539	-0.14	0.280	0.99	-1.74
	C544	-0.20	0.271	0.94	-1.46
	CS070	-0.38	0.345	1.29	-1.79
	CS077	-0.38	0.320	1.11	-2.08
<u>Roof Separation:</u>					
50123	C539	-1.11	0.451	0.96	-3.65
	C544	-1.11	0.431	0.94	-3.37

Table A.2 Continued.

Location/ Pressure Tap	Record	Cp_mean	Cp_rms	Cp_max	Cp_min
50523	C539	-1.08	0.442	1.21	-3.52
	C544	-1.06	0.430	1.41	-3.26
50823	C539	-0.89	0.395	1.18	-3.42
	C544	-0.84	0.400	1.25	-2.51
<u>Roof Reattachment:</u>					
51423	C539	-0.42	0.262	1.05	-1.74
	C544	-0.37	0.263	0.87	-2.68
52323	C539	-0.17	0.150	0.66	-1.13
	C544	-0.16	0.153	0.64	-1.60
52923	C539	-0.12	0.107	0.49	-0.97
	C544	-0.11	0.102	0.58	-1.02
<u>Roof Corner:</u>					
50101	C081	-0.89	0.732	1.41	-7.89
	C478	-0.74	0.429	1.04	-5.75
	C709	-0.63	0.370	0.97	-5.75
50501	C081	-1.85	1.284	2.10	-8.27
	C478	-2.86	1.113	2.88	-8.86
	C709	-2.36	1.210	2.35	-7.34
	WT1	-1.86	0.978	2.15	-5.97
	WT2	-1.89	1.016	2.24	-4.58
	WT3	-1.88	0.972	2.21	-4.83
50505	C081	-0.44	0.275	0.89	-3.77
	C478	-0.38	0.115	0.56	-1.92
50901	C081	-1.68	0.716	1.72	-5.19
	C478	-1.95	0.587	1.74	-4.73
	C709	-1.86	0.688	1.75	-5.03
50905	C081	-0.42	0.226	0.78	-2.12
	C478	-0.41	0.303	0.73	-3.45
50907	C081	-0.34	0.140	0.59	-1.16
	C478	-0.31	0.121	0.56	-1.67

Table A.2 Continued.

Location/ Pressure Tap	Record	Cp_mean	Cp_rms	Cp_max	Cp_min
<u>Roof Corner</u>					
<u>Area-averaged:</u>					
11 m ² area	C081	-1.12	0.392	0.88	-2.04
	C478	-1.05	0.283	0.77	-1.65
	C539	-0.97	0.320	0.77	-1.46
	C544	-0.92	0.304	0.72	-1.63
4.5 m ² area	C081	-1.28	0.495	1.18	-3.01
	C478	-1.23	0.362	1.20	-2.51
	C539	-1.20	0.419	0.99	-2.22
	C544	-1.14	0.416	0.95	-3.11
<u>Purlin</u>					
<u>Area-averaged:</u>					
	C539	-0.65	0.245	0.60	-1.33
	C544	-0.59	0.235	0.55	-1.40
	C325	-0.78	0.244	0.63	-1.51
	C728	-0.60	0.220	0.64	-1.32